MECHANISMS OF ENERGY CONSERVATION IN *PYROCOCCUS FURIOSUS*

by

DOMINIK KRZYSZTOF HAJA

(Under the Direction of Michael W. W. Adams)

ABSTRACT

The model hyperthermophilic archaeon, *Pyrococcus furiosus*, grows optimally at 100 °C by fermentation. This generates ATP through substrate-level phosphorylation and reduced ferredoxin (Fd), which is used by a membrane-bound hydrogenase, MBH, to reduce protons to H_2 and generate a Na^+ gradient. This is used by ATP synthase to generate additional ATP through electron transport phosphorylation. Herein, we used deletion strains of MBH and a related multiple resistance and pH (Mrp) antiporter to demonstrate the different mechanisms by which the Na^+ gradient is generated and utilized by the cell. During growth in the presence of elemental sulfur (S^0), the expression of genes encoding MBH rapidly decreases and expression of the membrane-bound sulfane sulfur reductase (MBS) increases. MBS oxidizes Fd and reduces sulfane sulfur derived from S^0 and generates a Na^+ gradient. However, the catalytic mechanism remains unknown. Herein, we determined the cryo-EM structure of MBS and showed that it uses a novel [4Fe-4S] cluster to directly catalyze the reduction of sulfane sulfur. Additionally, the structure provided insights into the evolution of both MBS and MBH and established their close relationship

with Complex I of the mitochondrial respiratory chain. We also took advantage of the robust genetic system of *P. furiosus* in order to heterologously express respiratory systems from other hyperthermophiles. A thiosulfate reductase (Tsr) and arsenate respiratory reductase (Arr) were heterologously expressed from the hyperthermophile *Pyrobaculum aerophilum*. Both Tsr and Arr were the first characterized archaeal examples of their respective enzyme families, and both were shown to utilize molybdenum instead of tungsten in their active sites, the first examples of active molybdoenzymes being expressed by and purified from *P. furiosus*. The Arr-expressing strain was also able to utilize arsenate as a terminal electron acceptor, the first example of *P. furiosus* using non-native substrates as terminal electron acceptors.

Index words: *Pyrococcus furiosus*, Hyperthermophile, Anaerobe, Energy Conservation, Sodium, Respiration, Hydrogenase, Evolution, Elemental Sulfur, Cryo-EM

MECHANISMS OF ENERGY CONSERVATION IN *PYROCOCCUS FURIOSUS*

By

Dominik Krzysztof Haja

B.S., Wake Forest University 2010

A Dissertation Submitted to the Graduate Faculty of The University of Georgia, in Partial Fulfillment of the Requirements for the Degree

DOCTOR OF PHILOSOPHY

ATHENS, GEORGIA

2021

MECHANISMS OF ENERGY CONSERVATION IN *PYROCOCCUS FURIOSUS*

By

Dominik Krzysztof Haja

Major Professor: Michael W. W. Adams

Committee: Michael K Johnson
William N Lanzilotta
Jorge C Escalante-Semerena

Electronic Version Approved:

Ron Walcott
Dean of the Graduate School
The University of Georgia
May 2021

DEDICATION

This dissertation is dedicated to my family, for their love and support while I spent years playing with proteins, and to my friends, especially those I met in Athens, that made my years at UGA special. Long live the Caledonia Lounge!

ACKNOWLEDGEMENTS

I would like to thank Dr. Michael W. W. Adams for his support and mentorship, not just in conducting research but how to write and review scientific manuscripts and give a great seminar. I would also like to thank my committee members Dr. Michael Johnson, Dr. Bill Lanzilotta, and Dr. Jorge Escalante-Semerena for helpful discussions and suggestions over the years. In addition, I would like to than the members of the Adams lab for their support and for the many entertaining discussions around the coffee pot over the years. In particular, I would like to thank Farris Poole, Gerti Schut, and Perry Wu for all their training and advice.

TABLE OF CONTENTS

Page

LIST OF TABLES

Page

LIST OF FIGURES

Page

CHAPTER ONE

INTRODUCTION AND LITERATURE REVIEW

Archaea and Hyperthermophiles

Since 1990, all living things have been categorized into three different domains: Bacteria, Eukarya, and Archaea[1]. The Archaebacteria were first classified as Bacteria before being reclassified as Archaea, and were known to contain at least two different phyla, Euryarchaeota and Crenarchaeota[1,2]. The domains were first separated according to ribosomal RNA sequences, with the Archaea being phylogenetically more similar to Eukaryotes than Bacteria (Figure 1.1)[1]. Unlike Eukaryotes, Archaea and Bacteria are prokaryotes, lacking a nucleus and organelles. Additionally, Archaeal genomes encode more proteins that have bacterial homologues, especially those involved in metabolism, metabolic uptake systems, cell wall biosynthesis, and transcriptional regulation[3,4]. However, Archaeal transcription, translation, and DNA replication are all much more complicated than in Bacteria and share significant homology with Eukaryotic systems[3-6]. In contrast to both Bacteria and Eukarya, the hydrophobic component of Archaeal membranes consists of isoprenoid lipids rather than phospholipids[7].

The domain Archaea was initially proposed to contain two different phyla[1,2]. Significantly more varied are the Euryarchaeota, which include methanogens, extreme

halophiles, sulfate reducers, and (extreme) thermophiles, while the Crenarchaeota are a more homogenous group of sulfur-reducing, extremely thermophilic organisms. As the number of sequenced archaeal genomes has increased, additional (super)phyla, including DPANN (the most well studied of which are Nanoarchaeota, obligate symbionts with highly reduced genomes), TACK (containing Thaumarchaeota, some members of which undergo aerobic oxidation of ammonia, Aigarchaeota, Crenarchaeota and Korarchaeota) and Asgard Archaea (a proposed superphylum that is thought to be the ancestor of the eukaryotic cell) have been proposed (Figure 1.2)[8-14].

Archaea have been isolated from ocean water and sediments, freshwater lakes, soil, plant roots, petroleum-contaminated aquifers, and the human mouth and gut, among other examples, and typically occupy ~10% of the total microbiota present in these environments[15-21]. They are now known to occupy a large number of ecological roles in both aerobic and anaerobic environments, including methane metabolism, hydrocarbon and organic matter degradation, and sulfur, nitrogen, and iron cycling[14].

One of the characteristics common to all the Archaeal (super)phyla is thermophily. Hyperthermophiles are organisms with an optimal growth temperature at least 80℃; in fact, some hyperthermophiles, such as *Pyrolobus fumarii*, will not grow below 90 ℃[22,23]. When grown under high-pressure (20 MPa) conditions simulating deep-ocean water pressure, the methanogen *Methanopyrus kandlera* was able to grow at 122 ℃, the highest ever recorded[24]. Hyperthermophiles are found in a number of different environments, both natural (hot springs, solfataric fields, shallow hydrothermal systems, abyssal hot vents or black smokers, active seamounts, and heated oil reserves) and artificial (coal refuse piles, uranium mines, hot outflow from nuclear power plants) [25-32]. They have been proposed as

the last universal common ancestor, with both modelled and experimental evidence supporting this hypothesis [33-36]. Hyperthermophiles have many adaptations to survive at elevated temperatures, most important of which positive supercoiling of the DNA helix by reverse gyrase[37-39]. The metabolic flexibility of hyperthermophiles and the remarkable heat resistance and temperature stability of their enzymes has spurred interest in their use for a number of biotechnological applications[40].

The most numerous and most frequently isolated of the archaeal hyperthermophiles are representatives from the order Thermococcales. All members of Thermococcales are obligate anaerobic organotrophic thermophiles with a fermentative metabolism that uses peptides or polysaccharides as carbon sources. Additionally, elemental sulfur is either required or stimulatory for their growth[41]. The order contains three genera: *Thermococcus*[42], *Paleococcus*[43], and *Pyrococcus*[44]. Unlike *Thermococcus* species, which have been isolated from terrestrial freshwater sources, among others, *Pyrococcus* species have solely been isolated from marine hydrothermal vents[44-48].

Pyrococcus furiosus

P. furiosus was first isolated from thermally-heated marine sediments in Vulcano, Italy[44]. It grows between 70-103℃, with a 37-minute doubling time at an optimal growth temperature of 100℃. Its genome (1.91 MB) has been sequenced and predicted to contain 2,065 open reading frames[49]. The organism is spherically shaped and highly motile due to the presence of the archaeal motility structure the archaellum (Figure 1.3) [50,51]. It is able to utilize yeast extract, peptone, tryptone, meat extract, casein, starch, and maltose, as well as other sugar polymers and disaccharides, as carbon sources, but is unable to utilize monosaccharides or amino acids. Starch is first degraded extracellularly by an

amylopullylase to smaller α-linked oligosaccharides, which are imported to the cell by the MalII importer, while maltose is imported by the maltose-specific importer MalI[52]. This import specificity likely explains the inability of *P. furiosus* to utilize monosaccharides. Once inside the cell, maltose and starch degradation products are converted to glucose by α-amylase[53]. *P. furiosus* can also utilize various β-linked sugars, including cellobiose, laminarin, and chitin. Cellobiose uptake is facilitated by a binding protein-dependent ABC transporter with broad β-glucosidase specificity. Expression of this transporter is induced by the presence of cellobiose[54]. Laminarin, a β-1,3-glucoside polymer, is degraded extracellularly to smaller oligosaccharides by the endo-beta-1,3-glucanase LamA before import into the cell[55]. Chitin, a β-1,4-linked glucosamine, is cleaved by two chitinases, one extracellular and one intracellular[56]. Once imported, β-linked sugars are converted to glucose by β-glucosidase and β-mannosidase[57].

Fermentation of glucose is carried out by a modified Embden-Meyerhoff (EM) glycolytic pathway, with acetate, CO_2, alanine, and hydrogen (H_2) as primary end products of fermentation[58]. Increasing partial pressure of H_2 has been shown to be inhibitory to growth; this can be alleviated by addition of elemental sulfur (S^0), in which case H_2 formation is replaced by hydrogen sulfide (H_2S) formation. Both H_2 and H_2S were predicted to function as a sink for reducing equivalents generated during glycolysis[59]. Glucose is first phosphorylated to glucose-6-phosphate by an ADP-dependent glucokinase, the discovery of which was key to the identification of the EM pathway in *P. furiosus*. It is highly specific to glucose and ADP, which no activity using fructose, mannose, galactose, ATP, GDP, PEP, or pyrophosphate, and its expression is strictly regulated to glycolysis, with no activity detected in cell extracts when grown on peptides[60]. Glucose-6-phosphate

is converted to fructose-6-phosphate by a novel archaeal phosphoglucose isomerase that shows no sequence similarity to the conserved bacterial and eukaryotic enzymes[61]. Fructose-6-phosphate is further phosphorylated by an ADP-dependent phosphofructokinase[62]. ATP and AMP are competitive inhibitors of the enzyme activity, which is highest with ADP. The two ADP-dependent enzymes represent the first difference between the classical EM pathway and the modified EM pathway used by *P. furiosus*. One possibility for the preference for ADP over ATP is the increased thermostability of the former (measured half-lives at 90 °C of 750 and 115 minutes for ADP and ATP, respectively). Whatever the reason, the ADP-dependent enzymes are found in most hyperthermophilic Archaea[63]. Next, aldolase converts fructose-1,6-bisphosphate to dihydroxyacetone phosphate (DHAP) and glyceraldehyde-3-phosphate (GAP), which are interconverted by triose phosphate isomerase[64,65]. In the classical EM pathway, GAP is oxidized to glycerate-1,6-bisphosphate by an NAD(P) dependent GAP dehydrogenase and further converted to 3-phosphoglycerate by phosphoglycerate kinase in an ATP-generating step. The *P. furiosus* genome encodes a copy of GAP-dehydrogenase, but expression and kinetic data suggest that it is involved in gluconeogenesis[66]. Instead, the novel tungstoenzyme GAP:ferredoxin oxidoreductase (GAPOR) oxidizes GAP directly to 3-phosphoglycerate. GAPOR does not utilize aldehydes as substrates, nor does it use NAD(P) as an electron acceptor, instead using ferredoxin (Fd), a small molecular weight protein that is the primary electron carries in *P. furiosus*[67,68]. A consequence of the GAPOR reaction is that there is no ATP generated by substrate-level phosphorylation during the conversion of GAP to 3-phosphoglycerate, and GAPOR thus constitutes the second major difference between the classical and modified EM pathways.

The rest of the pathway from 3-phosphoglycerate to pyruvate follows the classical EM pathway. Phosphoglycerate mutase converts 3-phosphoglycerate to 2-phosphoglycerate, enolase converts 2-phosphoglycerate to phosphoenolpyruvate, and pyruvate kinase converts phosphoenolpyruvate to pyruvate[69-71] The final step represents the sole ATP-generating reaction in glycolysis by *P. furiosus.* Pyruvate sits at a branch point in glucose metabolism. It can be reductively aminated to form alanine, which serves to dispose of excess reducing equivalents formed during glycolysis[72]. The more favorable, ATP-generating pathway involves oxidative decarboxylation of pyruvate to acetyl-CoA by the pyruvate ferredoxin oxidoreductase POR[73]. The enzyme contains thiamine pyrophosphate and requires CoA-SH as a cofactor. Finally, acetyl-CoA is converted to acetate by two distinct ADP-dependent acetyl-CoA synthetases, which results in formation of an additional ATP molecule[74].

In addition to carbohydrates, *P. furiosus* is also capable of growth on peptides, including casein, tryptone, and peptone. Peptide fermentation begins by proteolysis into individual amino acids[75]. The amino acids are transformed into their corresponding 2-keto acids by transaminases that utilize 2-ketoglutarate as a substrate[76]. The glutamate generated by the transamination reaction is recycled to 2-ketoglutarate by glutamate dehydrogenase, which produces NAD(P)H[77]. In addition to POR, *P. furiosus* contains an additional three oxidoreductases that act on 2-keto acids: indole-pyruvate ferredoxin oxidoreductase (IOR), which acts on aromatic acids; keto-valine ferredoxin oxidoreductase (VOR), which acts on branched-chain acids; and 2-ketoglutarate ferredoxin oxidoreductase (KGOR), which utilizes 2-ketoglutarate[78-80]. The four oxidoreductases reduce Fd and convert the keto-acids to their corresponding acetyl-CoA derivatives, which are utilized by the two acetyl-CoA

synthetases to generate ATP[74]. Additionally, aldehydes produced during peptidolysis are oxidized to their corresponding acids by the tungstoenzyme aldehyde ferredoxin oxidoreductase AOR, generating additional reduced Fd in the process[81]. Interestingly, growth on peptides appears to require S^0, as little growth is observed when *P. furiosus* is incubated on peptides in the absence of S^0. Additionally, peptides appear to have little effect when cells are grown on carbohydrates in the absence of S^0. Finally, the growth rate of *P. furiosus* is fastest on peptides + S^0 independent of the presence of carbohydrates, suggesting that glycolysis occurs independently of peptidolysis[82]. It is possible that peptides are the preferred carbon source because they eliminate the need for energy-requiring synthesis of amino acids during growth on carbohydrates. Most *Pyrococcus* species are unable to utilize carbohydrates and can only grow on peptides + S^0, suggesting that *P. furiosus* is unique in that it is able to grow to high cell densities using glycolytic pathways. Studies have shown that the maximum cell yield per maltose in the presence of S^0 are twice that when S^0 is omitted, suggesting that reduction of S^0 may be an energy conserving process, and not simply a method to dispose of excess reductant as initially proposed[83].

During both glycolysis and peptidolysis, the only ATP generating step is in the conversion of acyl-CoA derivatives to their corresponding acids. However, the growth yields of *Pyrococcus furiosus* are much higher than could be accounted for from this single substrate-level phosphorylation step. This was explained with the purification and characterization of the membrane bound hydrogenase MBH, a 14-subunit respiratory complex that established *P. furiosus* as a respiratory as well as a fermentative organism[84,85]. At least eight of the fermentative enzymes expressed in *P. furiosus* generate reduced Fd as

a product, which is oxidized by MBH to reduce protons to H_2 and generate a sodium ion gradient[85]. The resulting Na^+ gradient is used by a novel Na^+-dependent ATP synthase to generate an additional 1.2 moles of ATP per glucose, in addition to the 2 moles per glucose generated by substrate level phosphorylation[86]. Initial transcriptomics experiments showed that in the presence of S^0, expression of the 14 MBH genes, among others, were downregulated over 5-fold, while a 13 gene operon encoding a homologous NADH dehydrogenase were significantly upregulated[87]. This complex has since been identified as a Membrane Bound Sulfane sulfur reductase, or MBS, which couples the oxidation of reduced Fd to reduction of linear polysulfides to (indirectly) produce H_2S and generate a Na^+-gradient (Figure 1.4)[88]. Genome-wide transcriptional analysis showed that the response to S^0 can be separated into a primary (within 10 minutes) and secondary (within 30 minutes) response[89]. When S^0 is added to growing cells, H_2S formation begins following a 10 minute lag in growth and all H_2 production ceases within an hour. Indeed, the primary S^0 response sees a downregulation of 34 ORFs (fold >3), including the 14 ORFs encoding MBH, 8 encoding two 4-subunit soluble hydrogenases (SHI and SHII), and 2 involved in maturation of the NiFe active site, while 19 ORFs are upregulated (fold > 3), including the 13 ORFs encoding MBS. The secondary S^0 response sees the upregulation of an additional 27 ORFs, including genes involved in glutamate and branch-chain amino acid biosynthesis, ferrous iron transport, and iron sulfur cluster synthesis. Surprisingly, the most highly upregulated ORFs (400- and 26-fold) were relegated to the secondary S^0 response. It is now known that the genes encode the proteins Iron Sulfur Storage Protein A and B (IssA and IssB), which store iron and sulfur as thioferrate and can reconstitute iron sulfur clusters *in vitro*[90]. Additionally, they are regulated not by S^0 but by sulfide in an iron-dependent

manner and their presence is not required for growth on sulfur, so the physiological function remains unknown[91,92]. More detail on IssA is included in Appendix B. The primary S^0 response is mediated by the Sulfur Response Regulator SurR. SurR binds specifically to the $GTTn_3AAC$ promoter sequence found near all genes involved in the primary S^0 response, acting as both an activator of hydrogenases and associated maturation genes and a repressor of genes involved in S^0 metabolism[93]. The helix-turn-helix DNA binding domain of SurR contains a CxxC motif. In the absence of S^0, reduced SurR is able to bind DNA in order to act as an activator and repressor. When S^0 is present, SurR is oxidized, leading to formation of a disulfide bond in the CxxC motif, and the resulting conformational change lowers the affinity of SurR for DNA, resulting in *de*activation of hydrogenase genes and *de*repression of genes involved in S^0 metabolism[94]. Mutational studies on SurR deletion strains as well as those expressing a constitutively active form of SurR have confirmed its role as a master regulator in *Thermococcus* species, not only for electron pools but also for membrane lipid biosynthesis, nucleotide metabolism, and others[95].

Hydrogenases and Respiratory Complexes in *Pyrococcus furiosus*

Hydrogenases are metalloenzymes that catalyze one of the simplest reactions in nature – the reversible oxidation of hydrogen gas to protons and electrons (equation 1)[96].

$$H_2 (\leftrightarrow H^+ + H^-) \leftrightarrow 2H^+ + 2e^- \qquad \text{(Equation 1)}$$

They are found in bacteria, archaea, and eukaryotes and can be found in the cytoplasm, periplasm, and membrane as soluble and membrane bound enzymes[97-99]. In eukaryotes, they are often found in specialized compartments inside the cell[100]. Their primary functions

are to provide redox balance in the cell, oxidizing H_2 to deliver electrons or removing reducing equivalents by generating molecular hydrogen. Many hydrogenases are tuned for either uptake or removal depending on their location inside the cell and the bioenergetic needs of the organism *in vivo*, although some retain a bidirectional function[101]. *In vitro*, all hydrogenases catalyze reversible reactions, to varying degrees. Hydrogenases can also be used to establish a transmembrane ion gradient[85]. Additionally, they can be used as sensory or regulatory mechanisms, with H_2 binding at the active site serving as a trigger for transcriptional regulation[102,103].

Hydrogenases can be divided based on the metal composition of their active site into three classes Fe-only, FeFe-, and NiFe-hydrogenases[96,104]. The *hmd* gene encoding the Fe-only hydrogenase is found in most methanogens, where it is upregulated under nickel-limited conditions[97,105]. Unlike FeFe- and NiFe- hydrogenases, Fe-only hydrogenases do not contain additional FeS clusters, and do not exhibit dye-linked activity, instead reversibly coupling the oxidation of H_2 to a secondary methenyltetrahydromethanopterin (methylene-H_4MPT$^+$) cofactor to methylene-H_4MPT and H^+[106,107]. They contain a novel iron-guanylylpyridinol (Fe-GP) cofactor that is bound to the enzyme only through the thiol group of a cysteine residue in the active site (Figure 1.5A)[108-110]. The cofactor can be added to apoenzymes purified from *Escherichia coli* to produce the active holoenzyme, which enabled the study of Fe-only hydrogenases from difficult-to-cultivate methanogens[111]. The crystal structure of the methylene-H_4MPT-bound enzyme from *Methanocaldococcus jannaschii* was solved in 2006, showing that the mononuclear Fe is coordinated by two CO-ligands, one C(O)CH_2, one S-CH_2, and the sp^2-hybridized nitrogen of the pyridinol ring[112]. Similar to the other classes of hydrogenases, the biosynthesis of the active site

requires dedicated maturation enzymes. While the genes encoding the maturation machinery have not been identified for Fe-only hydrogenases, each methanogen encoding an *hmd* gene also contains seven conserved *hmd*-co-occurring genes (*hcg*) that are likely involved in synthesis of the active site cofactor[97].

FeFe-hydrogenases are found in anaerobic prokaryotes, including clostridia and S^0 reducers, as well as some anaerobic eukaryotes, fungi, and green algae, but not archaea[100]. Recent phylogenetic analyses have shown that they can be divided into three groups, with the group A1 or "prototypical" FeFe-hydrogenases being the most well studied[104]. They couple oxidation of Fd to fermentation or photobiological production of H_2. Many are composed of a single subunit that contains the catalytically active metal center known as the H cluster, but there are examples of up to heterotetramers. Crystal structures of the FeFe-hydrogenase have been solved from *Clostridium pasteuranium* (a monomer that contains an additional three [4Fe-4S] clusters and one [2Fe-2S] cluster), *Desulfovibrio desulfuricans* (a heterodimer consisting of a small subunit lacking any metal centers and a large subunit with the H cluster and an additional two [4Fe-4S] cluster), and *Chlamydomonas reinhardtii* (which was purified as an apoenzyme from *E. coli*)[113-115]. The structures were used to build a consensus model of the H-cluster binding site, consisting of a di-iron (2Fe) subcluster connected to a [4Fe-4S] cluster through the thiolate of a bridging cysteine residue[116]. Similar to Fe-only hydrogenases, this represents the sole covalent bond between the metal center and the protein surface. The proximal and distal Fe in the diiron center share a bridging CO ligand and have one additional CN^- ligand bound each, and the H-cluster domain is highly conserved and identified by three binding motifs (Figure 1.5B)[117]. Similar to the NiFe-hydrogenases, the H-cluster in FeFe-hydrogenases is buried

deep inside the protein, which necessitates pathways for gas transport and proton and electron transfer. The H-cluster requires three maturation factors, HydE, HydF, and HydG, to assemble and insert into the protein, and while the entire maturation mechanism is unresolved, several essential steps have been identified using structural and spectroscopic *in vitro* experiments using the enzymes[118-121].

The second most well-studied class of FeFe-hydrogenases are the group A3 bifurcating hydrogenases, first identified from the hyperthermophilic bacterium *Thermotoga maritima*[104,122]. During oxidation of glucose, *T. maritima* generates both reduced Fd and NADH as reducing equivalents which must be oxidized to H_2 in order to regenerate the electron acceptors, but the purified hydrogenase did not catalyze Fd-linked or NADH-linked H_2 production. However, H_2 was produced in the presence of both substrates in a process now known as electron bifurcation, which represents the third mechanism of energy conservation. The *T. maritima* bifurcating FeFe-hydrogenase couples the exergonic oxidation of Fd to the unfavorable oxidation of NADH to produce H_2 and conserve energy.

The remaining groups of FeFe-hydrogenases are, for the most part, putative and predicted from phylogenetic and bioinformatic analyses. Group A2 FeFe-hydrogenases are predicted to be linked to glutamate synthase, transferring electrons from H_2 to NAD and generating reducing equivalents for glutamate synthase[104]. Group A4 FeFe-hydrogenases are linked to formate dehydrogenase; the NADP-specific FeFe-hydrogenase from *Clostridium autoethanogenum* was purified in a complex with formate dehydrogenase and couples formate oxidation to H_2 production, while also exhibiting electron bifurcating activity[123]. Group B ancestral FeFe-hydrogenases are uncharacterized and predicted solely

from phylogenetic analyses and their exact function is unknown, while the group C sensory hydrogenases are predicted to sense H_2 and induce regulatory cascades of kinases and phosphatases[104,124].

The third and most diverse type of hydrogenase is the NiFe-hydrogenase, which is widespread throughout bacteria and archaea [100,104]. The minimal composition of the NiFe-hydrogenase is a heterodimeric molecule, with the two subunits characterized as the Large (NiFe-L) and small (NiFe-S) subunits, where NiFe-L contains the NiFe active site and NiFe-S contains three [4Fe-4S] clusters[125]. The NiFe cluster is coordinated by 4 sulfurs from 4 highly conserved cysteine residues, two as terminal ligands to the Ni and 2 as bridging ligands to the Fe, which is also coordinated by one CO and two CN^- ligands. There is also a third bridging ligand that changes with the redox state of the cluster (Figure 1.5C)[126]. The three [4Fe-4S] clusters in the NiFe-S subunit are named the proximal, medial, and distal clusters, depending on their proximity to the active site, and they are arranged in a linear fashion approximately 12Å apart to enable efficient electron tunneling from the donor to the active site [127]. As with the FeFe-hydrogenases, the NiFe active site is buried deep within the protein structure and thus the enzymes have extensive gas transport channels and proton and electron pathways. The overall structure of this heterodimeric module is almost identical for most of the NiFe-hydrogenases. The maturation process of NiFe-hydrogenases is the most elaborate and extensive of the three classes of hydrogenases, involving at least 6 maturation genes and four major steps that have been extensively studied in *E. coli*[96,128-131]. Generally, the steps are 1: maturation of the NiFe active site, which itself can be broken down into CN^- synthesis, Fe-CN formation, CO insertion and Ni insertion into the apoenzyme by the proteins HypA-F; 2: cleavage of the

C-terminus of NiFe-L by hydrogenase-specific proteases, which is a checkpoint for assembly of the NiFe center before attachment of NiFe-S; 3: delivery of assembled FeS clusters to the NiFe-S subunit; and 4: translocation or localization of the complete NiFe-hydrogenase to the correct cellular compartment.

NiFe-hydrogenases can be separated into 4 groups, each containing between 4 and 8 subgroups. Generally, the groups are Group 1 membrane-bound H_2 uptake NiFe-hydrogenases, Group 2 cytoplasmic H_2 uptake NiFe-hydrogenases, Group 3 cytosolic bidirectional NiFe-hydrogenases, and Group 4 membrane bound H_2 evolving NiFe-hydrogenases (Figure 1.6)[96,104]. The group 1 H_2 uptake hydrogenases oxidize hydrogen gas to generate reducing equivalents for a variety of respiratory systems. Group 1A, or the ancestral hydrogenases, liberate electrons for sulphate, metal, organohalide, and methanogenic heterodisulfide respiration, and include NiFeSe variants, such as that from *Desulfovibrio vulgaris* in which one of the cysteine residues coordinating the NiFe site is replaced by a selenocysteine[132]. It is thought that the selenocysteine substitution increases the oxygen tolerance of these hydrogenases by allowing for a novel non-oxide bridging ligand that shields the active site from O_2. Group 1B are the prototypical H_2 uptake NiFe-hydrogenases, providing electrons for sulphate, fumarate, and nitrate respiration. For example, the trimeric hydrogenase from *Wollinella succinogenes* oxidizes H_2 to reduce menaquinone in the membrane-anchored subunit HydC, which is used as an electron donor by fumarate reductase or polysulfide reductase to reduce fumarate or polysulfide, respectively[133]. Group 1C or "Hyb" type NiFe-hydrogenases are found in pathogenic bacteria such as *Salmonella enterica*, where they consume H_2 produced by other microbiota to provide electrons for fumarate formation and are essential for pathogenesis[134]. Group

1D NiFe-hydrogenases are O_2 tolerant and involved in aerobic respiration and oxygen-tolerant anaerobic respiration. The crystal structure of the *Ralstonia eutropha* hydrogenase revealed a novel [4Fe-3S] proximal cluster that is coordinated by six cysteine residues, which along with a series of extensive water cavities that serve to eliminate water produced during active site attack by O_2 contributes to its ability to maintain activity in the presence of O_2[135]. Group 1e or Isp type NiFe-hydrogenases, such as that from *Allochromatium vinosum* are thought to be bidirectional and involved in sulfur respiration[136]. The functions of group 1f (oxygen-protecting) and 1g (Crenarchaeota type) NiFe-hydrogenases are still unknown. The group 1f NiFe-hydrogenase from *Geobacter sulfurreductens* has been shown to be essential for growth in the presence of reactive oxygen species after exposure to oxidative stress, while the group 1g NiFe-hydrogenase from *Acidianus ambivalens* is involved in sulfur respiration[137,138]. The group 1h actinobacterium-type NiFe-hydrogenases are sometimes classified instead as group 5 NiFe-hydrogenases and are involved in oxygen-dependent H_2 uptake from the atmosphere in order to sustain growth under starvation conditions. They are found in soil bacterium, including *Mycobacterium smegmatis*, and are proposed to be a major atmospheric H_2 sink[139].

Group 2 NiFe-hydrogenases are cytosolic enzymes involved in H_2 uptake for respiration, H_2 recycling, and H_2 sensing; there are two characterized subgroups. The group 2a Cyanobacteria type, such as that from the nitrite-oxidizing bacterium *Nitrospira moscoviensis*, enables the organism to utilize H_2 instead of nitrite as an energy source in the presence of oxygen to support growth. *N. moscoviensis* represents a widely distributed lineage of nitrite-oxidizing bacteria and suggests an alternative lifestyle for these organisms outside the nitrogen cycle, as well as a broader distribution[140]. The group 2b hydrogenases

are linked to a histidine kinase and control expression of other hydrogenases. In *Rhodobacter capsulatus*, the HupUV sensory hydrogenase controls autophosphorylation of its partner HupT histidine kinase, which under H_2-conditions transfers a phosphate group to the HupR regulator, activating transcription of the HupSL group 1 uptake hydrogenase[141]. There are also two putative group 2 NiFe-hydrogenases, the uncharacterized group 2c DGC-linked NiFe-hydrogenase, predicted to sense H_2 and induce cyclic di-GMP production, and the 2d Aquificae type NiFe-hydrogenase, such as that from *Aquifex aeolicus*, which may be involved in carbon fixation or have a simple regulatory role[104].

Group 3 NiFe-hydrogenases are cytoplasmic, bidirectional hydrogenases that contain a third subunit with additional cofactor biding sites, such as for NADPH or F_{420}, and they provide a variety of roles in controlling electron flux in the cell. The group 3a F_{420} NiFe-hydrogenases are found in methanogens, where they couple oxidation of H_2 to the reduction of F_{420} to supply electrons for methanogenesis. A cryo-EM structure of the FrhABG hydrogenase from *Methanothermobacter marburgensis* revealed that the FrhB subunit contains an FAD binding site that binds the F_{420} cofactor [142]. Group 3b NADP-dependent NiFe-hydrogenases include soluble hydrogenase I and II (SHI and SHII) from *P. furiosus* and directly couple oxidation of NADPH to H_2 evolution. Their physiological role in *P. furiosus* remains unknown, but it is proposed that they function in the reverse direction, oxidizing H_2 produced by MBH during glycolysis and regenerating NADPH for biosynthesis; they also exhibit sulfhydrogenase activity[143]. Group 3c NiFe-hydrogenases are trimeric methyl-viologen reducing hydrogenases (MvhAGD) found mostly in methanogenic archaea that form a complex with heterodisulfide dehydrogenase (HdrABC).

The complex couples the exergonic reduction of heterodisulfide with the endergonic reduction of Fd, using H_2 as the electron donor, and is another example of a bifurcating mechanism of energy conservation, one that is likely highly important to many methanogens[144]. Group 3d contains bidirectional NAD-linked NiFe-hydrogenases, which directly interconvert electrons between H_2 and NADH[104].

Group 4 NiFe-hydrogenases are membrane-bound, energy-conserving complexes, and represent the only group whose primary function is in H_2 evolution. Sequence homology of group 4 NiFe-hydrogenases is low compared to that of other groups, except for the residues coordinating the NiFe site and the proximal cluster; it is also the only group to contain non-hydrogenases. Group 4a contains the bacterial formate hydrogen lyase (FHL) complex, which couples the reduction of formate to CO_2 with the concomitant reduction of protons to H_2. The complex consists of the NiFe subunit HycE, FeS cluster-containing subunits HycGFB, a molybdopterin-type formate dehydrogenase subunit FdhF, as well as the membrane anchoring subunits HycCD that are thought to generate a proton gradient[145]. Group 4b is represented by *P. furiosus* MBH and links cytoplasmic hydrogenase activity to sodium-ion pumping through the membrane-anchored Mrp module[85]. The detailed structure of MBH is described in Appendix A. Group 4b also includes the archaeal FHL complex from *Thermococcus onnurineus*, which contains additional electron input modules to couple oxidation of formate to CO_2 and H_2, as well as the MBS complex from *P. furiosus*[88,146]. Group 4c contains an FHL-type CODH-linked NiFe-hydrogenase, in which the FdhF subunit is replaced by the CooF, which contains FeS clusters, and CooS, the catalytic subunit of CO dehydrogenase, which allows the complex to catalyze the conversion of CO to CO_2 and H_2 and generate a proton gradient[147]. Group

4d contains the Ech-like Eca and Ecb hydrogenases, which consume an ion gradient to couple H_2 oxidation to Fd reduction for anaplerotic and anabolic purposes, respectively[148,149]. Finally, group 4e complexes are simple, 6 subunit energy conserving hydrogenases (Ech), which couple Fd oxidation to H_2 generation and generate a proton gradient for ATP synthesis[150]. The main difference between Ech-type group 4 NiFe-hydrogenases and MBH-type group 4 hydrogenases is the presence of the Mrp module, which allows MBH-type enzymes to generate a Na^+ gradient, instead of the H^+ gradient generated by Ech.

Evolution and Homology of complex I, MBH, MBS, and Mrp

Respiratory complex I (NADH quinone oxidoreductase, NUO) is the first enzyme in the aerobic electron transport chain, catalyzing electron transfer from NADH to quinone and subsequently pumping protons across the membrane that are used to conserve energy by ATP synthesis. While the composition can vary in size, extending to more than 40 subunits in mitochondria, complex I contains a 14-subunit core for redox catalysis and ion translocation that is highly conserved[151,152]. Several structures have been solved from bacteria, yeast, and mammalian cells that allow for insight into the exact mechanism and function of the complex, although the coupling mechanism of redox activity to ion translocation remained unknown[153-155]. Interestingly, the group 4b NiFe-hydrogenases, especially *P. furiosus* MBH and MBS, share significant sequence and structural homology to complex I (Figure 1.7). Specifically, the catalytic subunit of complex I NuoD has significant sequence homology to the catalytic MbhL and MbsL subunits. The structure of *P. furiosus* MBH was solved in 2018 (see appendix A for a detailed description), but it offered a number of insights into the evolution of respiratory complexes. Specifically, it

highlighted three conserved structural features: a three-loop system connecting the active site to the membrane, the similarity of the NiFe active site to the quinone binding site in the catalytic pocket of complex I, and a long lateral helix connecting the ion-pumping membrane subunits. The three-loop system connects the redox active site to a central charged axis spanning the membrane arm; this includes discontinuous transmembrane helices that are known features of proton translocating modules in complex I. It was proposed that conformational changes that occur during H^+ and quinone reduction in MBH and complex I, respectively, are propagated through the membrane arm to drive ion translocation; this was confirmed in a recent publication in which the structure of mitochondrial complex I was determined for 5 stages in the catalytic cycle, showing clear movement of the loops and conformational changes in the proton pumping subunits that allowed for translocation of protons[156].

Unlike complex I, which only contains subunits homologous to the proton-pumping subunits of Mrp (Multiple Resistance and pH antiporters), the structure of MBH also provided insights into the structure and function of Mrp. Mrp was first identified from an alkaline sensitive *Bacillus halodurans* strain in 1990[157]. The seven-subunit operon is widespread among bacteria and archaea, and the Mrp antiporter system generally utilizes the proton motive force to efflux intracellular Na^+ ions[158,159]. In addition to its role in cytoplasmic pH and Na^+ homeostasis, the Mrp antiporter has a number of varied physiological roles, including bile acid resistance, sporulation, plant infection, pathogenesis, and arsenic resistance[160-167]. The two largest subunits in the Mrp operon are MrpA and MrpD, and their sequences, along with NuoLMN, MbhH, and MbsHH', are highly conserved. MrpA and D are therefore predicted to contain the proton translocation

pathways, although the ion pumping stoichiometry and location of the Na^+ pathway remains unknown. Extensive mutagenesis have been performed to analyze the role of each subunit in complex formation[168]. Single gene deletions of the *Bacillus pseudoformas* Mrp complex showed that the MrpD subunit is necessary for complex formation. Additionally, extensive site-directed mutagenesis studies were performed on highly conserved residues along the entire Mrp complex, as well as those conserved in complex I. The mutations were classified into 8 categories depending on the effects of the mutations[169,170]. Category 1 mutations totally disrupted complex formation and abolished Na^+/H^+ antiporter activity; category 2 mutations retained Na^+/H^+ antiport activity but failed to show formation of the full Mrp complex on SDS-PAGE gels, suggesting to disrupt the interaction between the MrpABCD subcomplex and the MrpEFG subunits. Mutations in categories 3-7 all retained complex formation, but Na^+/H^+ antiport activity was affected to varying degrees, from total loss of activity to reduced activity and increases in the apparent K_m for Na^+. These mutational studies were instrumental in identifying the ion translocation pathways in the structures of both complex I and MBH.

In the last year, structures of two Mrp complexes were solved – the group 1 Mrp from *Anoxybacillus flavithermus* and the group 2 Mrp from *Dietzia* sp. DQ12-45-1b[171,172]. The structures are highly homologous, with the exception of the overall charged residues on the surface of the proteins. While group 1 Mrp contains two separate MrpA and MrpB subunits, each containing 2 MrpB domains, group 2 Mrp contains a fusion of MrpA and B, with the resulting MrpA protein retaining two copies of the MrpB domain. These structures also highlight one of the main differences between the Mrp antiporter and the Mrp domain of MBH – namely, Mrp contains two copies of the predicted proton pumping subunits,

while MBH only contains one. The ion pumping stoichiometry must therefore be different between the complexes, but the exact ratio is still unknown. Additionally, the Mrp complex does not conserve any of the three loop structures necessary for energy transduction in MBH, suggesting that Mrp couples ion pumping to the proton motive force through an as-yet unknown mechanism. Interestingly, the *P. furiosus* genome encodes a copy of a stand-alone Mrp that has sequence homology to MBH, i.e., only one predicted proton pumping subunit. The exact physiological role of this stand-alone group 3 Mrp in *P. furiosus* is unknown and is the focus of chapter 2 of this work.

A theoretical ancestral respiratory complex (ARC) has been proposed that likely arose from the combination of a cytoplasmic NiFe-hydrogenase and an Mrp antiporter to couple oxidation of Fd to reduce protons and generate a sodium ion gradient[173]. The evolutionary path between MBH, MBS, and complex I can likely be ascribed to changes in energy yield and rising electrochemical potentials as the Earth's atmosphere and oceans became more oxidized due to photosynthesis[174]. The difference in free energy of the Fd/H^+, Fd/S^0, and NADH/quinone redox couples is -12, -41, and -81 kJ/mol, respectively, with the switch to the oxygen-stable NADH from the oxygen-sensitive Fd as an electron donor due to increasing levels of atmospheric oxygen (Figure 1.8). This could also have been the driving force between the number of proton pumps, as MBH, MBS, and complex I are predicted to pump 1, 2, and 4 H^+ per 2 e^-, respectively, although this remains to be experimentally proven for any complex.

There are two notable differences between the sequences of MBH and MBS. The first is the presence of two predicted proton pumping subunits MbsH and MbsH', in which MbsH is homologous to MbhH and MbsH' appears to be a fusion of MbhH and the lateral helix

MbhI, which could contribute to different proton pumping stoichiometry between the two complexes. Consequently, while MBH is homologous to the Mrp antiporter lacking the second proton pumping MrpA subunit, MBS is likely homologous to the full Mrp antiporter complex. The second difference is in the conserved cysteine residues in the active site of the complexes. While MbhL contains four conserved cysteine residues that coordinate the NiFe active site, MbsL only contains two (complex I has subsequently lost all four cysteine residues to allow for quinone binding in the active site). Site-directed mutagenesis of these cysteine residues in MBS have shown that they are not essential for H_2S production and growth on elemental sulfur. While the exact role of MBS in S^0 respiration has recently been elucidated (see below), the exact mechanism of H_2S production was unknown and is the primary goal of chapter 3 of this work.

Sulfur Respiration and the role of MBS

There is extensive evidence to suggest that not only was S^0 prevalent during the early Archaean, but that it was the preferred sulfur source for microorganisms that disproportionate sulfur[175]. Sulfur derivatives are one of the most abundant components in volcanic gases and sulfidic ores that make up the rock in volcanic environments, and therefore sulfur compounds are the most abundant source of electron donors and acceptors used by microorganisms in these environments to support growth[176]. The solubility of S^0 in water at 25℃ is only 5 μg l^{-1}, and its solubility at higher temperatures is unknown. S^0 can occur in many forms, but is predominantly found as S_8 rings[177]. The addition of sulfide to S^0 leads to its dissolution into polysulfide by nucleophilic attack of the S_8 ring, and at neutral pH the maximum amount dissolved is approximately equal to the sulfide concentration[178]. At pH > 6, the predominant species of polysulfide are tetrasulfide (S^{2-}_4)

and pentasulfide (S^{2-}_5), with the pK of proton dissociation falling well below 7. Because of the low solubility of S^0 and its reactivity with sulfide, polysulfides are thought to be possible intermediates of S^0 respiration.

Anaerobic reduction of S^0 is a widespread ability in archaea, with at least four known mechanisms utilized by various genera[179]. The first is respiration of S^0 utilizing H_2 as an electron donor, and it involves two membrane bound enzymes – a sulfur or polysulfide reductase (SR/PSR) and a group 1 NiFe-hydrogenase. The SR complex of *Acidianus ambivalens* is similar to the bacterial system found in *W. succinogenes* and is composed of three subunits: the large subunit SreA, the FeS subunit SreB, and the membrane anchor SreC. SreAB share sequence homology with DMSO reductase family enzymes and likely contain molybdopterin and FeS clusters[180]. Electron transfer between the complexes is likely mediated by the applicable, organism-specific quinone. The crystal structure of a related PSR was solved from *Thermus thermophilus*, and it provided a detailed mechanism of polysulfide reduction in which the polysulfide chain is coordinated in the active site to an arginine residue near the molybdenum center, giving the molybdenum full coordination by six sulfur residues (four from the molybdopterin substrate and 2 from the polysulfide chain). Binding of the polysulfide therefore cleaves the sulfur, releasing a terminal $S_{(n-1)}^{2-}$ and leaving a $Mo[S]_6$ core; subsequent delivery of electrons and protons generates H_2S and leaves a $Mo[S]_5$ core (equation 2)[181].

$$S_n^{2-} + 2\ e^- + 2\ H^+ \rightarrow S_{n-1}^{2-} + H_2S \qquad (2)$$

The second mechanism is likely similar to the first but uses organic compounds as electron donors. The third mechanism involves assimilatory reduction of S^0 to H_2S in methanogens, but this is not an energy-conserving mechanism. The final mechanism is the fermentation

of organic compounds to reduce S^0, such as that performed by MBS in *P. furiosus*. MBS is phylogenetically distinct from DMSO reductases and does not contain a molybdopterin binding site, so the mechanism must be different than that of SR/PSR. The activity of MBS was unknown for many years because of the significant background activity due to the non-specific reactivity of S^0 derived compounds; however, the substrate dimethyltrisulfide (DMTS, CH_3-S-S-S-CH_3) was identified as a model substrate for MBS using reduced methyl viologen as an electron donor[88]u. Surprisingly, no H_2S was detected in MBS assays with DMTS, suggesting that the mechanism does not result in the cleavage of terminal sulfur to produce H_2S. MS analysis showed that the products of the reaction are methanethiol (CH_3SH) and methyl hydrogen disulfide (CH_3S-SH). These data suggested that MBS catalyzes the two-electron reduction of organic polysulfides (equation 3, where $n \geq 3$ and R and R' are alkyl, not aryl) and anionic polysulfides (equation 4, where $n \geq 4$); when $n \leq 3$ the polysulfides spontaneously disproportionate to H_2S and S^0 at physiologically relevant pH (equation 5).

$$R\text{-}S_n\text{-}R' + 2e^- \rightarrow RS^-_{n-x} + R'S^-_x \quad (3)$$

$$S^{2-}_n + 2\ e^- \rightarrow S^{2-}_{n-x} + S^{2-}_x \quad (4)$$

$$S^{2-}_n + 2e^- + 2H^+ \rightarrow S^{2-}_{n-1} + H_2S \quad (5)$$

Answering how MBS catalyzes this reaction seemingly without any metal centers in the active site in place of the NiFe-site found in MBH is the goal of chapter 3.

Genetic Engineering in *Pyrococcus furiosus*

One of the most important advances in the biochemical study of any microorganism is the development of a genetic system. While a number of Archaea are difficult to grow in

isolation under lab conditions, there is a growing number of organisms that are both easily cultivatable and have a robust genetic system available[182]. A genetically tractable strain of *P. furiosus*, COM1, was developed that takes advantage of the natural competence for DNA of the organism; a deletion of the *pyrF* uracil biosynthesis gene allows for selection and counterselection of both linear and plasmid DNA using uracil auxotrophy[183]. The genome of COM1 was sequenced and revealed that the *P. furiosus* genome is dynamic, and further analysis revealed that it contains several intergenic regions with little to no transcriptional activity that can be targets for inserting DNA constructs[184,185]. COM1 has been used extensively to study native processes and enzymes from *P. furiosus*, both using deletion mutants and expression of affinity tagged proteins[91,183,186-195].

In addition to native enzymes, COM1 has been genetically engineered to express individual proteins and full metabolic pathways from other organisms[196-199]. The versatility of the genetic system makes *P. furiosus* especially useful in studying heterologously expressed enzymes from other organisms that do not have genetically tractable strains, particularly other hyperthermophilic archaea. The membrane bound FHL complex from the euryarchaea *T. onnurineus*, an 18 subunit type 4b NiFe-hydrogenase complex related to MBH, was expressed in *P. furiosus* and allowed the strain to utilize formate as an H_2 source, both at 95°C and 80°C (near the optimum growth temperatures of *P. furiosus* and *T. onnurineus*, respectively)[200]. A more striking result was achieved with the expression of the *T. onnurineus* CODH complex (also a group 4b NiFe-hydrogenase complex), which not only allowed for production of H_2 from CO by the strain but also enabled the use of CO as an energy source and allowed the strain to grow on limiting sugar concentrations as well as peptides in the absence of S^0 [201]. *T. onnurineus* is closely related to *P.* furiosus, so

these studies are representative of horizontal gene transfer events. A major goal of this work, and the focus of chapters 4 and 5, is the expansion of the phylogenetic origins of heterologously expressed genes in *P. furiosus* from Euryarchaea to Crenarchaea.

Pyrobaculum aerophilum is a crenarchaeon with an optimal growth temperature of 100°C that undergoes both aerobic respiration as well as dissimilatory nitrate reduction using both organic and inorganic compounds as carbon sources; its growth is inhibited by the presence of S^0 [202]. Its genome (2.2 Mb) was sequenced and found to contain 2,578 ORFs[203]. Microarray experiments provided insights into the remarkable respiratory versatility of the organism. The *P. aerophilum* genome encodes two operons that encode aerobic cytochrome oxidase (Sox) complexes, SoxB and SoxM, that are differentially expressed under suboxic and oxic conditions respectively, suggesting that the SoxB cluster encodes an oxygen scavenger or sensor and that the SoxM cluster represents the primary aerobic respiratory complex[204]. Under anaerobic conditions, *P. aerophilum* can reduce nitrate to dinitrogen during growth, and reductase activities for each step (nitrate, nitrite and nitric oxide) have been identified in membrane fractions[205,206]. Additionally, the *P. aerophilum* genome contains genes encoding a respiratory NarG-type reductase, a cd_1-type nitrite reductase, and a heme O-containing nitric oxide reductase[207]. These genes were all found to be upregulated up to 15-fold upon the addition of nitrate to the growth medium, with the gene encoding the nitrate reductase catalytic subunit expressed under all growth conditions, suggesting that reduction of nitrate is the preferred respiratory pathway. The NarGHI respiratory nitrate reductase is a DMSO reductase family enzyme, where NarG contains the molybdopterin cofactor that is the site of nitrate reduction, NarH contains FeS clusters, and NarI is a membrane anchor that contains a heme-o_p and the likely

menaquinone binding site[208]. Unlike in bacteria, in which the cytoplasmic NarGHI directly generates a proton gradient, the *P. aerophilum* NarGHI is directed to the periplasm by a TAT signal peptide. It has been proposed that formate is used as an electron source by a DMSO reductase-type formate dehydrogenase, and that reduction of menaquinone and H^+ uptake on the cytoplasmic side of the membrane by FDH and its oxidation and release of H^+ by Nar on the periplasmic side is used to indirectly generate the PMF. Similar models of PMF generation have been proposed for other DMSO reductase respiratory complexes, including the thiosulfate reductase of *Salmonella enterica*[209]. Under anoxic conditions, a three gene operon encoding a putative PSR is upregulated, while a three gene operon encoding a respiratory arsenate reductase (ARR) is upregulated in the presence of Arsenat[204]. Both operons are predicted to encode DMSO reductase type complexes, with a catalytic molybdopterin subunit (PsrA and ArrA), an FeS subunit (PsrB and ArrB), and a membrane anchor with a menaquinone binding site (PsrC and ArrC). Unlike NarI, the sequences of the Psr and Arr membrane anchors do not contain consensus sequences for heme binding sites. It is likely that these complexes function similarly to NarGHI in creating a PMF for ATP generation. Because of their relative simplicity and lack of heme cofactors (*P. furiosus* does not contain heme and the genome does not encode the biosynthetic genes), Psr and Arr were chosen as targets for heterologous expression in *P. furiosus*. However, a fundamental question that needs to be addressed is what metal will the heterologously-expressed enzymes contain in their pyranopterin active site? *P. furiosus* encodes five pyranopterin containing enzymes and only inserts tungsten (W) into their active sites, even when grown in the presence of molybdenum (Mo) and the absence of W[210]. Meanwhile, while W is required for anaerobic growth by *P. aerophilum* and it is

inhibited by Mo, its nitrate reductase has been purified containing both metals in the active site, with similar affinity for nitrate but 2-fold higher turnover with Mo[205,208].

Molybdenum and Tungsten Enzymes

Mo and W are transition metals with very similar chemical properties, including analogous valence electron configurations in all oxidation states and similar atomic radii[211]. While Mo is present in all three domains of life, W is only relevant in prokaryotic organisms[212]. The most biologically available form of Mo is the molybdate (MoO_4^{4-}) oxyanion, while that of W is tungstate (WO_4^{2-}); molybdate is present at lower concentrations in oceans, and forms insoluble salts under anoxic and sulfuric conditions, such as those in hydrothermal marine vents. Tungstate, on the other hand, forms soluble salts which remain available for microorganisms and could therefore explain the dependence on many hyperthermophilic archaea on W[213]. Mo is found in nature as two different cofactors: the iron-molybdenum cofactor FeMoCo that is essential for and specific to bacterial nitrogenases, and the pterin-based MoCo cofactors, which is utilized by all domains of life[214]. Based on their similar properties, W was often assumed to act as a general inhibitor of MoCo enzymes, but in recent years it has been proven that WCo is an essential cofactor to many bacterial and archaeal systems[215]. Enzymes containing the metallopterin (MPT) cofactor can be divided into four unrelated families: 1: sulfite oxidases (SO), 2: xanthine oxidases (XO), 3: dimethyl sulfoxide reductases (DMSOR), and 4: aldehyde oxidoreductases (AOR). MoCo is found in XO, SO, and DMSOR families, while WCo is found both in DMSOR and AOR families. While Mo in XO and SO families is coordinated by a single MPT, W in AOR family enzymes is always coordinated by two MPTs, referred to as W-bis-MPT, while the

MPT in DMSOR family enzymes is further modified with guanine dinucleotide moieties, and the metal center is referred to as the Mo-/W-bis-MGD cofactor (Figure 1.9)[215].

The biosynthesis of Mo/WCo has been widely studies in *E. coli*, and it is thought that all steps are conserved (with slight differences) in all prokaryotes. While the cofactor is modified further in DMSO reductases, the initial steps of cofactor synthesis are conserved for all Mo/WCo enzyme families. The general steps are the conversion of GTP to the four-ringed intermediate cyclic monophosphate pyranopterin (cPMP), introduction of the two thiols of the dithiolene group, adenylation to MPT-AMP, and metal insertion and release of AMP[215-217]. A second MPT is ligated to the metal center for the bis-MPT cofactors found in AOR family enzymes. The Mo-/W-bis-MPT is further modified by addition of two GMP moieties from GTP to form the Mo-/W-bis-MGD cofactor of DMSO reductase family enzymes[218].

The SO family of molybdopterin enzymes is present in all three domains of life as sulfite oxidase in both animals and plants and sulfide dehydrogenase in bacteria, as well as assimilatory nitrate reductase in plants[219]. Structures from all four sources show that the Mo center of the MPT is connected to the protein exclusively by a cysteine of the polypeptide chain, while also being coordinated by two oxo groups and the two thiol ligands of the MPT[216]. The XO family of molybdopterin enzymes is also found in both eukaryotes and prokaryotes and contain a single MPT cofactor that coordinates Mo through the sulfurs of the dithiolene ligand, an oxo group, a hydroxo group, and, depending on the enzyme, an additional sulfo-, seleno-, oxo-, or S-Cu-S(Cys) group[220]. The most well-known and characterized enzymes from this family are xanthine oxidoreductases, aldehyde oxidases, and aldehyde oxidoreductases[216].

The AOR family of obligately W-dependent enzymes can be broken down into three classes. The most well studied of these is the AOR family of aldehyde oxidoreductases, five of which are present in *P. furiosus,* all but one of which (the tungsten-dependent oxidoreductase WOR4) have been characterized[67,81,221-223]. An additional bacterial member of the family, the bacterial GAP ferredoxin oxidoreductase GOR, was recently characterized[224]. All characterized members of both archaeal and bacterial AOR families oxidize a variety of aldehydes to their corresponding carboxylic acids, with the main physiological function thought to be detoxification of aldehydes that accumulate during various metabolic processes. The catalytic subunit contains a W-bis-MPT cofactor with the W coordinated by four sulfur ligands, as well as an additional [4Fe-4S] cluster[225]. While the archaeal AORs occur as homodimers with a bridging iron and utilize Fd as electron acceptors, bacterial AORs are typically found with a $\alpha_2\beta_2\gamma_2$ composition, with the β and γ subunits harboring additional [4Fe-4S] clusters and FAD binding sites, respectively, that allow them to use a broader range of electron acceptors[226].

Less well characterized AOR family members are the Benzoyl-CoA Reductases (BCR), key enzymes involved in degradation of aromatic compounds in anaerobic prokaryotes[227]. The reaction is catalyzed by two phylogenetically unrelated classes of BCRs; Class I BCRs are found in facultative anaerobes and utilize FeS clusters as their only cofactors, with reduced Fd as the electron donor[228]. The unfavorable reaction is coupled to ATP hydrolysis. Class II BCRs are ATP-independent and found in obligately anaerobic bacteria and have been purified from both Fe(III)- and sulfate-respiring organisms[229,230]. Both are composed of the eight subunits $Bam[(BC)_2DEFGHI]_2$ and represent one of the most complicated metalloenzyme machineries known, containing four

W-bis-MPTs, four zinc, >50 FeS clusters, four selenocysteines, and six FADs. BamB contains the W-MPT active site, while BamC is an FeS cluster containing subunit that transfers electrons into the remaining BamDEFGHI complex, which is driven by flavin-based electron bifurcation, the third example of this energy conserving reaction.

Unlike the XO, SO, and AOR families, which (with few exceptions) utilize solely Mo- or W-MPT, the DMSOR family of enzymes is unique in that they utilize both Mo or W, which appears to be based solely on adaptation of the organism to their environments and not on differences in enzyme function. The most widely abundant family of DMSOR enzymes are the metal-dependent FDHs that are involved in formate-dependent respiration, methanogenesis, acetogenesis, and fermentation as part of FHL complexes[200,231-233]. Unlike other DMSOR family members, which can incorporate either Mo or W into the catalytic site, most FDHs are specific to one of the two metals and growth of the organism is inhibited by the other; for example, *E. coli* requires Mo for growth and is inhibited by W, likely because of the formation of an inactive FDH[234-237]. In contrast, *Desulfovibrio alaskensis* incorporates either Mo or W into its FDH, while *Desulfovibrio vulgaris* Hildenborough produces a specific Mo or W FDH depending on which metal is present in the growth medium[238,239]. Formylmethanofuran dehydrogenases catalyze the FDH-related reduction of CO_2 to formate bound to an activated methanofuran cofactor[233]. Some methanogens, such as *Methanosarcina acetivorans* encode multiple putative formylmethanofuran dehydrogenases with varying W and Mo specificities[240]. The respiratory nitrate reductases, including the NarGHI from *P. aerophilum* discussed previously, can utilize both Mo and W depending on the growth conditions; however, most are inactivated by W, with tungstate preventing assembly of MoCo into the catalytic

subunit of the complex[208,234]. DMSOR and trimethylaminoxide reductase (TMAOR) are required to use DMSO or TMAO as terminal electron acceptors in aerobic respiration. When W was substituted for Mo in the *Rhodobacter capsulatus* DMSOR, the resulting WCo enzyme was more active at reducing DMSO but was unable to catalyze the reverse reaction, likely due to the generally lower redox potential of WCo to MoCo[241,242]. (Per)chlorate reductases reduce perchlorate to chlorate and then chlorite and are found in facultative anaerobes and denitrifiers and use MoCo in the active site. While enzymes isolated from perchlorate-respiring bacteria are active with both perchlorate and chlorate, those isolated from chlorate-reducing bacteria cannot utilize perchlorate[243,244]. Arsenate and arsenite, while both toxic to life, can also be utilized by some prokaryotes as electron donors or acceptors for respiratory arsenate reductase and two different classes of arsenite oxidase. While the composition of the complexes differs among the three types, all contain Mo[245,246]. Finally, there are a number of DMSOR family enzymes involved in reduction of various S-containing compounds, including S^0, polysulfide, thiosulfate, and tetrathionate; all exclusively contain Mo[138,181,209,247].

Figure 1.1

Phylogenetic tree of the three domains of life based on rRNA sequence analysis. Modified from (1).

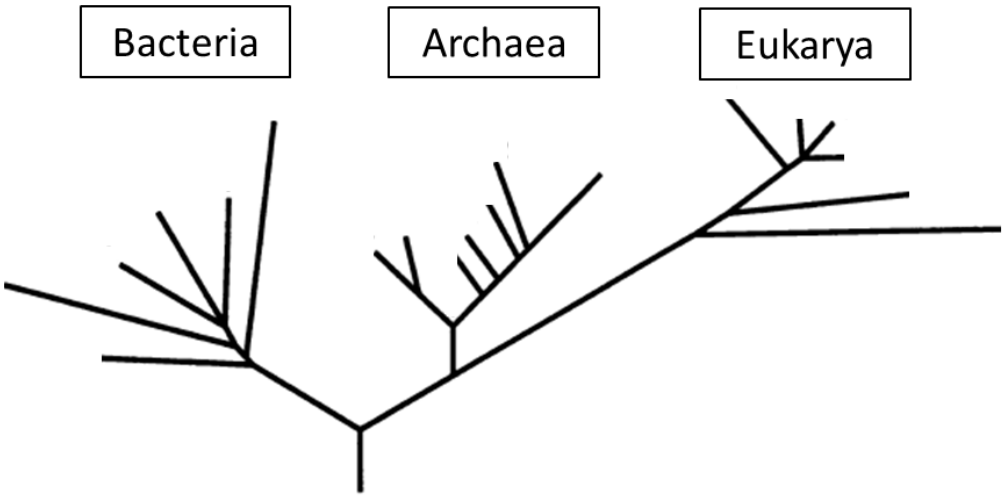
Bacteria
Archaea
Eukarya

Figure 1.2

Phylogenetic tree, including proposed Phyla, of Archaea based on 36 conserved marker proteins. The tree was generated using 3,549 archaeal genomes. Adapted from (14).

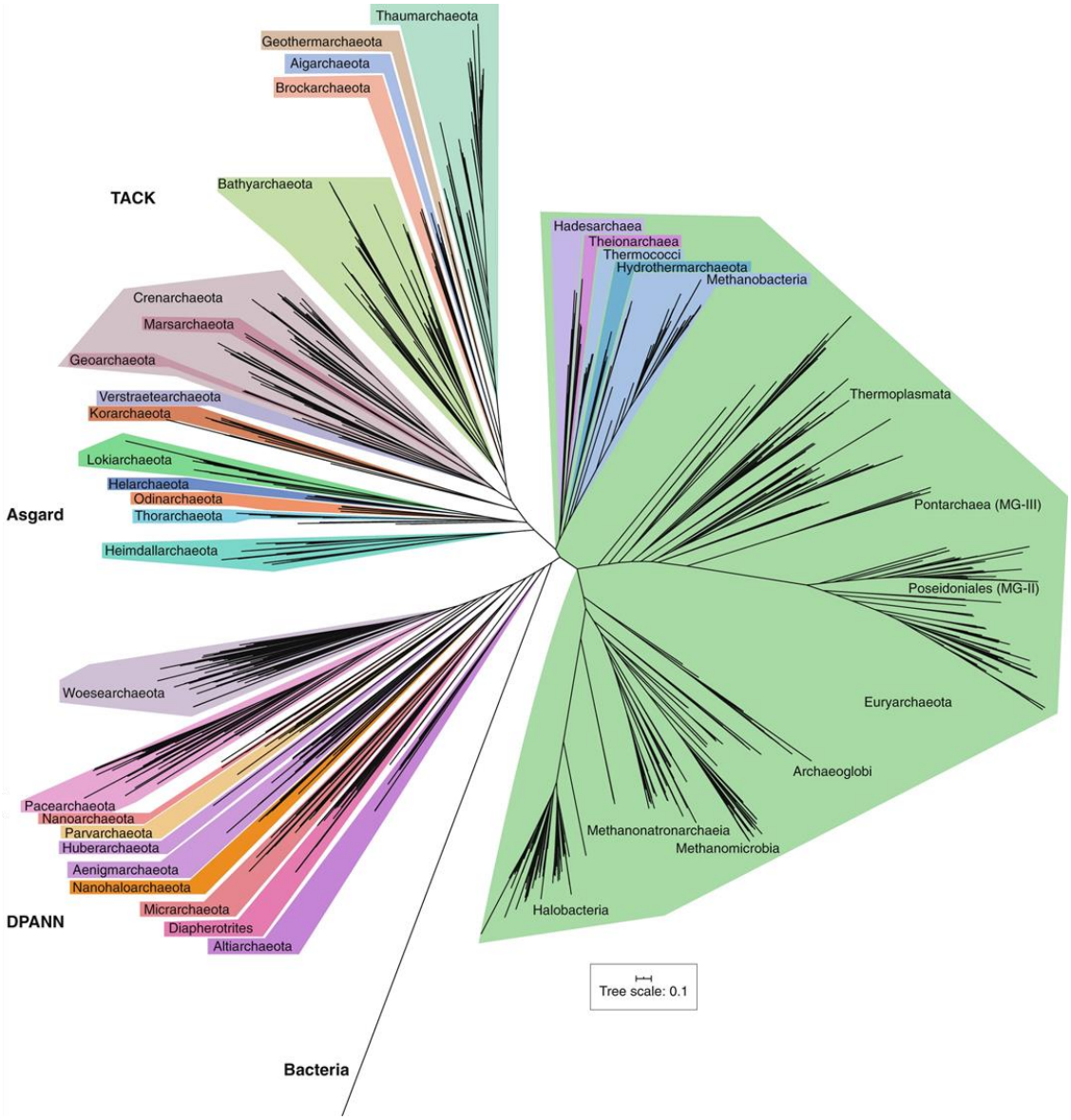
Thaumarchaeota
Geothermarchaeota
Aigarchaeota
Brockarchaeota
TACK
Bathyarchaeota
Crenarchaeota
Marsarchaeota
Geoarchaeota
Verstraetearchaeota
Korarchaeota
Lokiarchaeota
Helarchaeota
Odinarchaeota
Thorarchaeota
Asgard
Heimdallarchaeota
Hadesarchaea
Theionarchaea
Thermococci
Hydrothermarchaeota
Methanobacteria
Thermoplasmata
Pontarchaea (MG-III)
Poseidoniales (MG-II)
Euryarchaeota
Archaeoglobi
Methanonatronarchaeia
Methanomicrobia
Halobacteria
Woesearchaeota
Pacearchaeota
Nanoarchaeota
Parvarchaeota
Huberarchaeota
Aenigmarchaeota
Nanohaloarchaeota
Micrarchaeota
Diapherotrites
Altiarchaeota
DPANN
Tree scale: 0.1
Bacteria

Figure 1.3

Electron micrograph of *Pyrococcus furiosus*. Taken from (44).

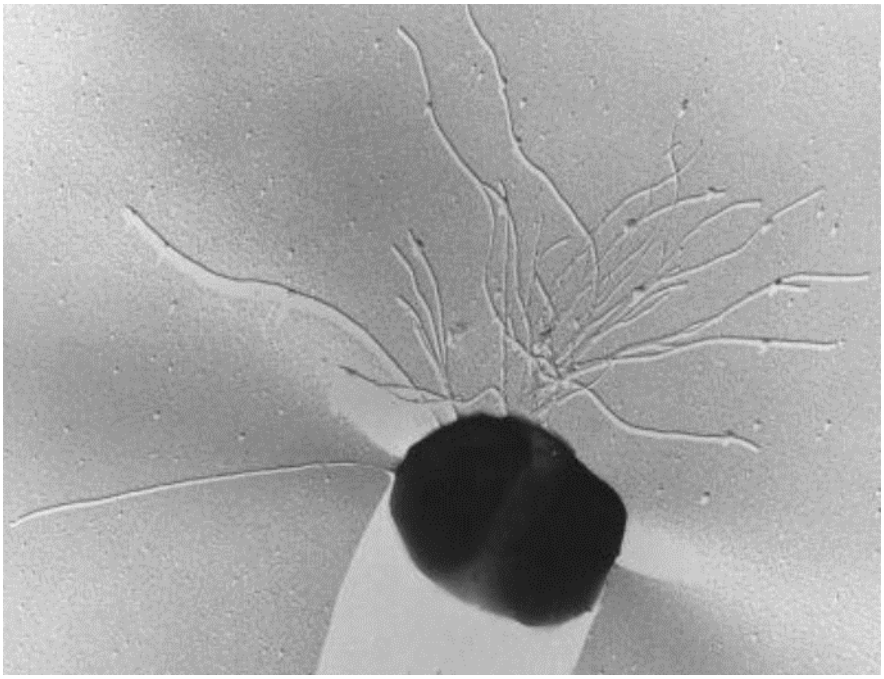

Figure 1.4

Proposed physiological roles of MBH and MBS in hydrogen and sulfur metabolism. MBH: membrane-bound hydrogenase; MBS: membrane-bound sulfane sulfur reductase; Fd_{red}: reduced form of ferredoxin; Fd_{ox}: oxidized form of ferredoxin. Modified from (185).

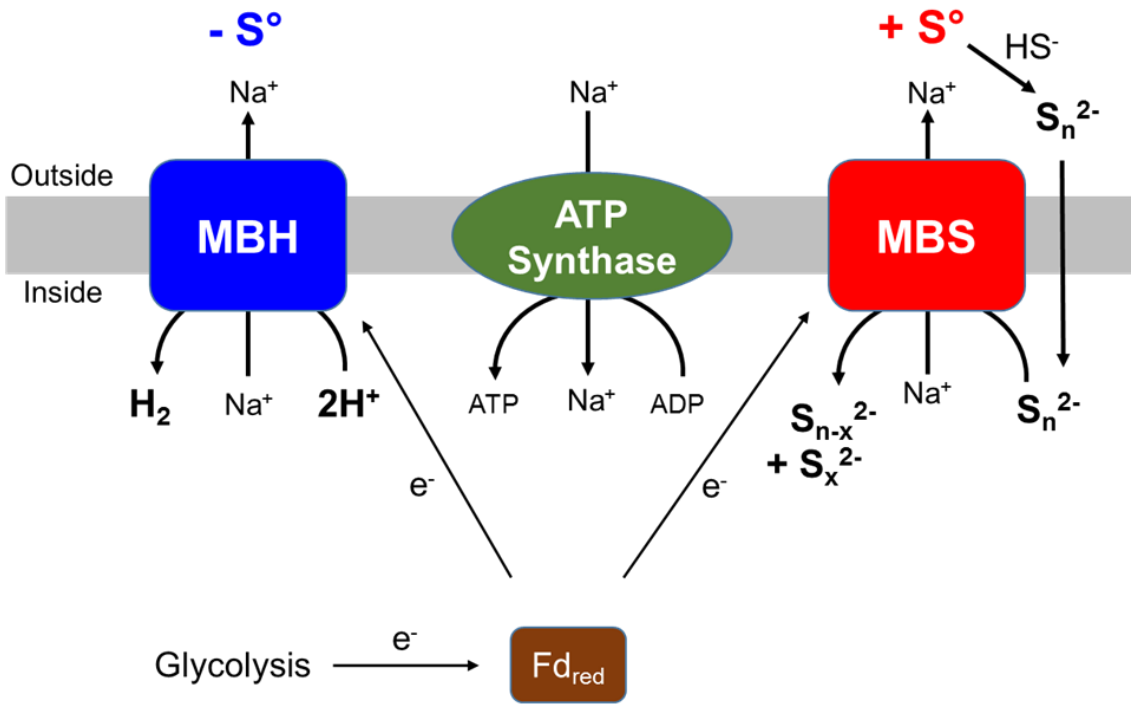
- S°
+ S°
HS-
Na+
Na+
Na+
Outside
Inside
MBH
ATP Synthase
MBS
S_n^{2-}
H_2
Na+
$2H^+$
ATP
Na+
ADP
S_{n-x}^{2-} + S_x^{2-}
Na+
S_n^{2-}
e-
e-
Glycolysis
e-
Fd_{red}

Figure 1.5

Metal cofactors of hydrogenases. (A) The iron-guanylylpyridinol cofactor of Fe-only hydrogenases; (B) the H cluster of FeFe-hydrogenases; and (C) the NiFe center of NiFe-hydrogenases. Modified from (110). Reprinted with permission from AAAS.

A

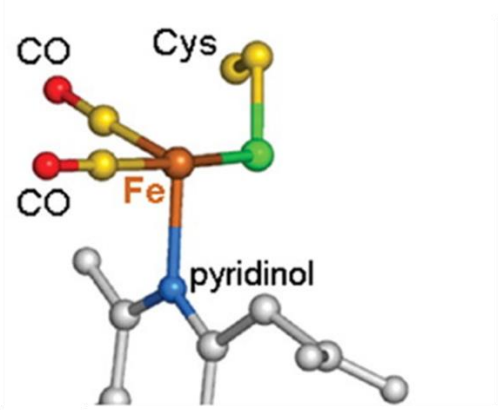

B

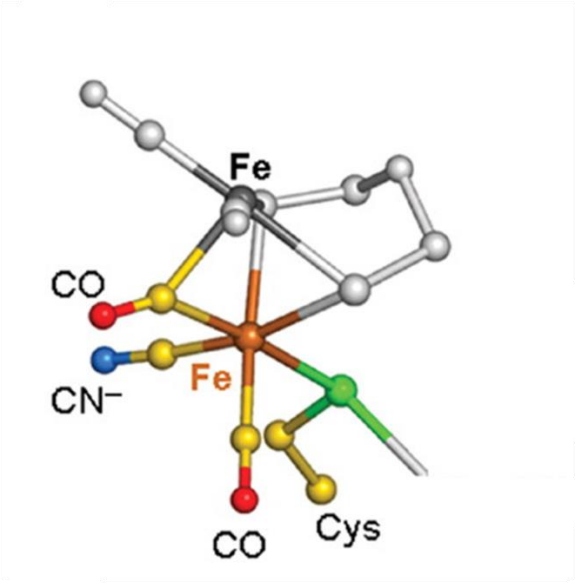

C

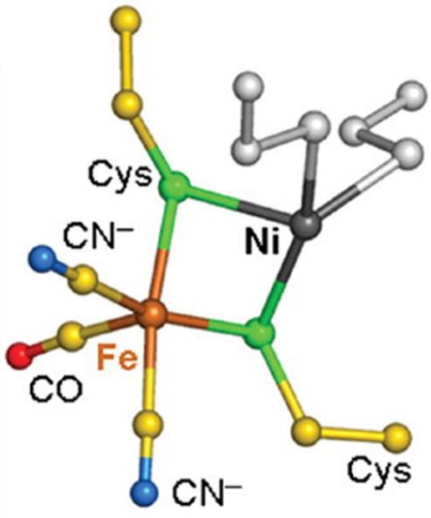

Figure. 1.6

Phylogenetic tree of NiFe hydrogenases based on sequence analysis of the catalytic subunits. MBH: membrane-bound hydrogenase; MBS: membrane-bound sulfane sulfur reductase. Group 4, containing MBH, MBS, and complex I, is the only group to contain non-hydrogenases. Modified from (185).

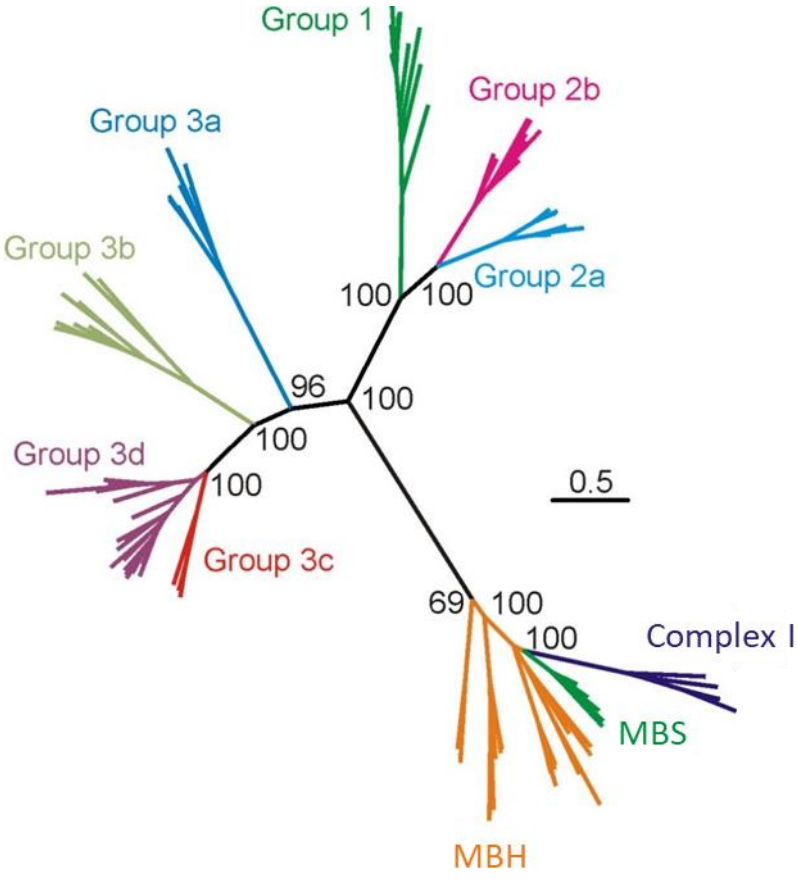
Group 1
Group 2b
Group 3a
Group 3b
Group 2a
100
100
96
100
100
Group 3d
100
0.5
Group 3c
69
100
100
Complex I
MBS
MBH

Figure 1.7

Homology models of MBH, MBS, Mrp, and complex I. Homologous subunits between complexes are shown in the same colors. Mrp: multiple resistance and pH antiporter; MBH: membrane-bound hydrogenase; MBS: membrane-bound sulfane sulfur reductase. Modified from (185).

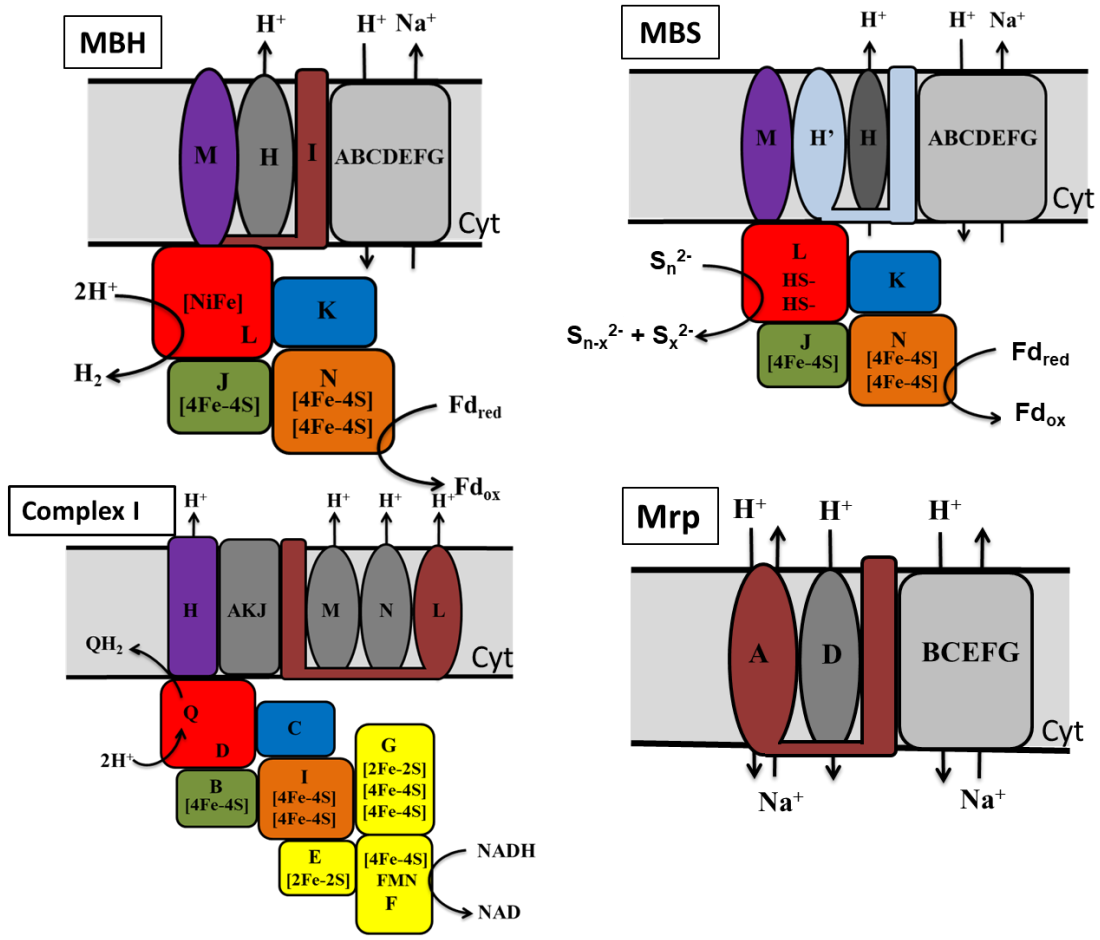
MBH
H+
H+ Na+
M
H
I
ABCDEFG
Cyt
2H+
[NiFe]
L
K
H2
J
[4Fe-4S]
N
[4Fe-4S]
[4Fe-4S]
Fdred
Fdox
MBS
H+
H+ Na+
M
H'
H
ABCDEFG
Cyt
Sn2-
L
HS-
HS-
K
Sn-x2- + Sx2-
J
[4Fe-4S]
N
[4Fe-4S]
[4Fe-4S]
Fdred
Fdox
Complex I
H+
H+
H+
H+
H
AKJ
M
N
L
Cyt
QH2
Q
D
C
2H+
B
[4Fe-4S]
I
[4Fe-4S]
[4Fe-4S]
G
[2Fe-2S]
[4Fe-4S]
[4Fe-4S]
E
[2Fe-2S]
[4Fe-4S]
FMN
F
NADH
NAD
Mrp
H+
H+
H+
A
D
BCEFG
Cyt
Na+
Na+

Figure 1.8

Bioenergetics driving the evolution of respiratory complexes. MBH: membrane-bound hydrogenase; MBS: membrane-bound sulfane sulfur reductase; Fd: ferredoxin; MQ: menaquinone; UQ: ubiquinone. Modified from (174).

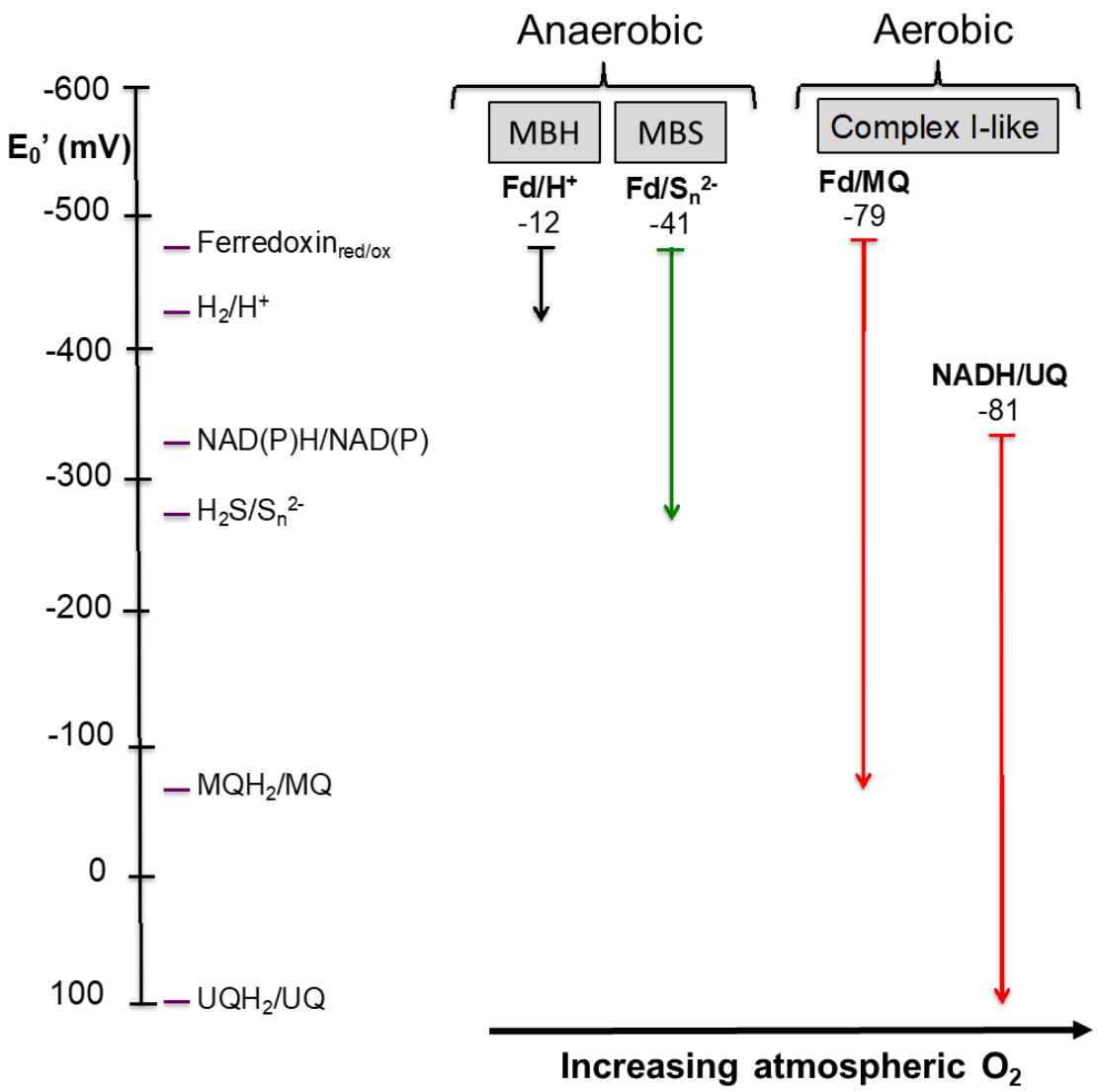
Anaerobic
Aerobic
MBH
MBS
Complex I-like
Fd/H+
-12
Fd/Sn2-
-41
Fd/MQ
-79
NADH/UQ
-81
E0' (mV)
-600
-500
-400
-300
-200
-100
0
100
Ferredoxinred/ox
H2/H+
NAD(P)H/NAD(P)
H2S/Sn2-
MQH2/MQ
UQH2/UQ
Increasing atmospheric O2

Figure 1.9

Structures of the molybdo- or tungsto-metallopterin (MPT) cofactors from DMSOR and AOR family enzymes. DMSOR: dimethylsulfoxide reductase; AOR: aldehyde oxidoreductase. DMSOR enzymes typically use the Mo/W-bis-MPT (mgd) cofactor, while AOR family enzymes are predominated by W-bis-MPT. Taken from (215).

DMSOR family

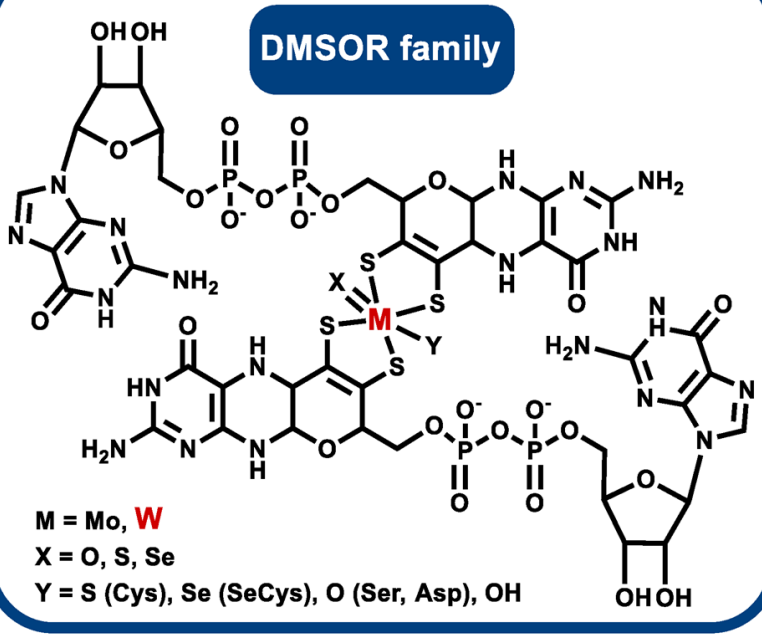

M = Mo, W
X = O, S, Se
Y = S (Cys), Se (SeCys), O (Ser, Asp), OH

AOR family

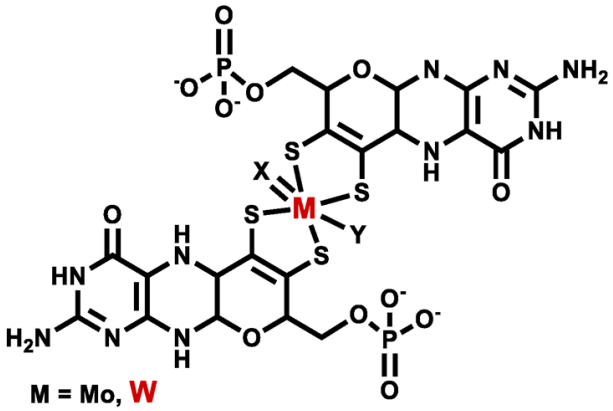

M = Mo, W
X = O, ?
Y = S (Cys), OH (H_2O)

CHAPTER TWO

SODIUM ION PUMPING BY MRP IN *Pyrococcus furiosus*[1]

[1]Haja, D.K. and Michael W. W. Adams. Submitted to *Frontiers in Microbiology*

Abstract

Multiple Resistance and pH (Mrp) antiporters are seven-subunit complexes that couple transport of ions across the membrane in response to a proton motive force and have various physiological roles, including sodium ion sensing and pH homeostasis. The hyperthermophilic archaeon *Pyrococcus furiosus* encodes three copies of Mrp genes in its genome. Two are found as part of the respiratory complexes, membrane bound hydrogenase (MBH) and the membrane bound sulfane sulfur reductase (MBS), that couple redox activity to sodium pumping, while the third Mrp copy is stand-alone. Sequence alignments show that this Mrp does not contain an energy-input (pmf) module but contains all other predicted functional Mrp domains. The *P. furiosus* Mrp deletion strain exhibits no significant changes in optimal pH or sodium ion concentration for growth but is more sensitive to changes in media pH. Cell suspension hydrogen gas production assays using the deletion strain show that Mrp uses sodium as the coupling ion. Mrp likely maintains cytoplasmic pH by pumping protons out of the cell in exchange for sodium. Deletion of the MBH sodium-pumping module demonstrate that hydrogen gas production is uncoupled from ion pumping and provide insights into the evolution of this Mrp-containing respiratory complex.

Introduction

Multiple resistance and pH adaptation (Mrp) antiporters are multi-subunit complexes that transport of Na^+ (or K^+) ions across the membrane in response to the proton motive force (PMF) (1). They are part of a larger group of Na^+/H^+ antiporters including Eukaryotic NHE families (2) and bacterial NhaA families (3) and are the only subgroup that is comprised of multiple subunits. Mrp complexes perform a number of different physiological roles, including maintaining pH and Na^+ homeostasis, Na^+ tolerance, pathogenesis, and arsenic tolerance (4-9). The typical Mrp operon is composed of a seven gene *mrpABCDEFG* cluster, and each gene is predicted to encode a membrane protein. Mrp complexes can be further divided into three groups depending on the arrangement of the A and B genes (1, 10). Group 1 *mrp* operons encode separate *mrpA* and *mrpB* genes, with *mrpA* containing a second C-terminal *mrpB* domain. Group 2 *mrp* operons lack an *mrpB* gene, but *mrpA* contains two *mrpB* domains. Group 3 *mrp* operons are characterized by the lack of an *mrpA* gene, containing only *mrpD*, sometimes with multiple copies. The proteins encoded by *mrpA* and *mrpD* are homologous to each other and are both predicted to contain H^+ pumps (11). Homologues of MrpA/D are found in a number of various respiratory complexes, ranging from bacterial and mitochondrial complex I to the Membrane Bound Hydrogenase (MBH) and Membrane Bound Sulfane reductase (MBS) of the hyperthermophilic archaeon *Pyrococcus furiosus*. These complexes are proposed to have evolved from the fusion of an Mrp-like membrane antiporter with a cytoplasmic NiFe hydrogenase and couple ion pumping to cytoplasmic redox activity. Structures of complex I, MBH, and MBS have all been recently determined (12-15).

Until recently, Mrp complexes were studied primarily through mutagenesis and homology modeling using respiratory complexes as templates. However, two Mrp structures, the group 1 Mrp from *Anoxibacillus flavithermus* and the group 2 Mrp from Dietzia sp. DQ12-45-1b, were very recently determined (16, 17). While the subunit organization between the two complexes differs as described above, the overall structures are very similar. The major difference between the two clusters lies in a highly negatively charged cavity between MrpA and MrpF in the *A. flavithermus* Mrp, proposed to be part of the Na^+ translocation path, that is absent in the *Dietzia* Mrp, suggesting that the Na^+ pathways are distinct between various Mrp complexes.

Pyrococcus furiosus is a hyperthermophilic archaeon isolated from a marine environment with an optimal growth temperature of 100 °C (18). Its genome encodes for three copies of a group 3 Mrp operon. Two copies are associated with MBH and MBS, which, in the absence and presence of elemental sulfur, couple reduction of protons and polysulfide, respectively, to Na^+ pumping across the membrane (19, 20). The resulting Na^+ gradient is used by a Na^+-dependent ATP synthase to produce ATP (21). The third copy encodes a stand-alone *mrp* operon with the structure *mrpEFGBB'CD*, where *mrpB* and *mrpB'* are homologous to group 1 and 2 MrpB subunits. Interestingly, this operon lacks the *mrpA* gene, which is proposed to have a proton-translocating pump and to be the primary driving force for Na^+ pumping by the remaining subunits. In MBH, MrpA has been replaced by the membrane-anchored hydrogenase domain, and Na^+ pumping is driven by coupling redox activity, rather than by pmf as in Mrp (14). The operon encoding the stand alone Mrp is unique in that it does not contain any energy-input module. However, the operon retains a single proton-pumping subunit, as well as all the genes that contain the

predicted Na^+ channel, suggesting that this Mrp complex retains its role in either pH or Na^+ sensing or homeostasis.

In this study, we have used deletion strains to determine the physiological functions of two of the Mrp complexes in *P. furiosus,* the stand-alone Mrp and the Mrp of MBH. While many organisms contain multiple copies of the Mrp gene cluster, *P. furiosus* is unique in that it contains both a stand-alone Mrp as well as one associated with respiratory complexes, allowing for a direct comparison of the roles it plays between various types of complexes.

Materials and Methods

Deletion of Mrp

The genetically tractable *P. furiosus* strain COM1 was used to delete *Pf1147-53*. 500 bp flanking regions were amplified from *P. furiosus* genomic DNA for the UFR and DFR, and the selection marker (*pyrF*-P_{gdh}) was amplified by using pGL021 as the template (22). Table S2.1 contains primers used in this study. The knock-in cassette was assembled using overlapping PCR (23). The genomic DNA was prepared using Zymobead Genomic DNA Kit (Zymo Research).

P. furiosus transformants were grown in defined maltose media as previously described (Lipscomb et al., 2011). The medium for *P. furiosus* growth was composed of 1x base salt, 1x trace minerals, 1x vitamin solution, 2x 19-amino-acid solution, 0.5% (wt/vol) maltose, 10 µM sodium tungstate, and 0.25 mg/ml resazurin, with added cysteine at 0.5 g/liter, sodium sulfide at 0.5 g/liter, sodium bicarbonate at 1 g/liter, and 1 mM sodium phosphate buffer (pH 6.8). The 5x base salts stock solution contained (per liter) 140 g of NaCl, 17.5 g of $MgSO_4 \cdot 7H_2O$, 13.5 g of $MgCl_2 \cdot 6H_2O$, 1.65 g of KCl, 1.25 g of NH_4Cl,

and 0.70 g of $CaCl_2 \cdot 2H_2O$. The 1000x trace mineral stock solution contained (per liter) 1 ml of HCl (concentrated), 0.5 g of Na_4EDTA, 2.0 g of $FeCl_3$, 0.05 g of H_3BO_3, 0.05 g of $ZnCl_2$, 0.03 g of $CuCl_2 \cdot 2H_2O$, 0.05 g of $MnCl2 \cdot 4H_2O$ 0.05 g of $(NH4)_2MoO_4$, 0.05 g of $AlK(SO_4) \cdot 2H_2O$, 0.05 g of $CoCl2 \cdot 6H_2O$, and 0.05 g of $NiCl2 \cdot 6H_2O$. The 200x vitamin stock solution contained (per liter) 10 mg each of niacin, pantothenate, lipoic acid, *p*-aminobenzoic acid, thiamine (B_1), riboflavin (B_2), pyridoxine (B_6), and cobalamin (B_{12}) and 4 mg each of biotin and folic acid. The 25x 19-amino-acid solution contained (per liter) 3.125 g each of arginine and proline; 1.25 g each of aspartic acid, glutamine, and valine; 5.0 g each of glutamic acid and glycine; 2.5 g each of asparagine, histidine, isoleucine, leucine, lysine, and threonine; 1.875 g each of alanine, methionine, phenylalanine, serine, and tryptophan; and 0.3 g tyrosine. A solid medium was prepared by mixing an equal volume of liquid medium at a 2x concentration with 1% (wt/vol) Phytagel (Sigma) previously autoclaved to solubilize, and both solutions were maintained at 95°C just prior to mixing. The medium was poured into glass petri dishes immediately after mixing.

Aliquots of *P. furiosus* culture typically grown to mid-log phase (2x 10^8 cells/ml) in defined liquid medium were mixed with DNA at a concentration of 2 to 10 ng DNA per µL of culture, spread in 30-µL aliquots onto defined solid medium and plates were placed inverted in anaerobic jars and incubated at 90°C for ~64 h. Colonies were picked into 4 mL of defined medium in Hungate tubes and incubated anaerobically overnight at 90°C.

The genomic DNA isolated by Zymobead Genomic DNA Kit (Zymo Research) was used for PCR screening, which was carried out by using GXL polymerase (Takara, ClonTech). PCR screening was performed using a pair of primers outside the Mrp locus in order to confirm that the transformation cassette recombined into the correct locus. After

PCR confirmation of a deletion, the resulting strain was passaged twice on solid medium for colony purification. Upon colony purification, the resulting strain MW0576 saved as a glycerol stock and subsequently used as the parent for the double deletion of Mrp and *Pf1423-25*. 5-FOA counterselection was used to pop-out the selection marker for a second round of transformation. 30 µl of culture was plated directly onto solid medium plates containing 8 mM 5-FOA. Plates were placed inverted in anaerobic jars and incubated at 90 °C for ~64 h. Colonies were picked into 4 mL of defined medium in Hungate tubes and incubated anaerobically overnight at 90°C.The resulting strain was passaged twice on solid medium for colony purification, and the transformation was repeated as described above. All strains used and created in this study are listed in Table 2.1.

Growth Studies

Strains were grown in defined maltose media in 50 mL cultures contained in 100 mL bottles at 90 ˚C with shaking. Where indicated 50 mM 3-(N-morpholino)propanesulfonic acid (MOPS) was added to the growth medium. 1 mL culture samples were taken at desired time intervals. pH was measured using an Orion Dual Star pH/ISE meter (Thermo Scientific). Cell protein was measured using the Bradford method. H_2 production was measured by taking 1 mL headspace samples from growing cultures and analyzed in a 6850 Network Gas Chromatograph (Agilent Technologies).

Preparation of Cell Suspensions

Strains were grown in defined maltose media in 1L culture bottles at 90 ˚C with shaking. Cells were harvested by centrifugation at 18,000 xg for 10 minutes in a Beckman-Coutler Avanti J-30i centrifuge. Cell suspensions were created by washing harvested cells with an anaerobic resuspension buffer containing 20 mM imidazole, 30 mM $MgCl_2 \cdot 6H_2O$, 0.5 M

KCl, 2 mM cysteine-HCl, pH 6.5 and resuspending them in the same buffer at cell densities of OD_{600} = 0.6.

H_2 Production Assays

H_2 production assays are modified from that reported previously(24). Cell suspensions (final volume, 2 mL) were added to rubber-sealed glass 8 ml vials and the headspace was flushed with argon. Samples were incubated at 80 ˚C for 3 minutes and the reaction was initiated by the addition of the desired concentration of NaCl from an anaerobic 2 M stock solution. At various time intervals, gas samples were taken and analyzed in a 6850 Network Gas Chromatograph (Agilent Technologies). H_2 production was normalized to cellular protein concentrations determined by the Bradford method.

Results

Amino acid sequence alignments (Supplemental Figure S2.1) derived from the seven *P. furiosus* Mrp-related genes with the homologous genes in MBH, MBS, and the *Bacillus subtilis* Mrp provide insights into the structure and function of the stand-alone Mrp operon. First, *P. furiosus* MrpB and MrpB' are homologous to the transmembrane (TM) helices 17-21 of *B. subtilis* MrpA (containing one copy of the MrpB motif) and *B. subtilis* MrpB, respectively. The two MrpB motifs are homologous to the MbhD and E subunits, which form the secondary proton pathway at the junction between the proton pumping module and the sodium pumping module. Additionally, *P. furiosus mrpB* is homologous to a fusion of the *mbhD* and *mbhE* genes, while *mrpB'* is homologous to *mbhF*. The reason for this gene fusion is unknown, but the *P. furiosus mbsE* gene (of MBS) represents a fusion of *mbhE* and *mbhF* (of MBH). These gene fusions are additional evidence that the subunit composition between various Mrp groups is not important to the function of the complex,

which is determined by the presence of the required domains. Finally, several of the amino acids proposed to be involved in both H^+ pumping and Na^+ translocation pathways are highly conserved between *P. furiosus* Mrp, MBH, and MBS, suggesting that Mrp plays a role in H^+/Na^+ exchange. A full comparison of all *P. furiosus* Mrp, MBH, and MBS subunits, as well as the *B. subtilis* Mrp, is shown in Table 2.2.

The operon structures of *P. furiosus* MBH and Mrp are shown in Figure 2.1. MBH can be divided into three modules: the membrane-anchored hydrogenase module, which includes the NiFe active site in MbhL, the proton translocation module, and the sodium translocation module. MBH catalyzes the oxidation of reduced ferredoxin, a low molecular weight protein that is the primary electron carrier in the cell, and the reduction of protons to generate H_2 (19). The redox activity in the hydrogenase module is coupled to conformational changes in the proton translocation module that generates a H^+ gradient. This H^+ gradient is exchanged for a Na^+ gradient by the sodium translocation module (14). A ΔMbhABC deletion strain was shown to have diminished Na^+-dependent H_2 production activity, demonstrating that the Na^+ ion pathway is located in MbhABC. Additionally, hydrogenase-catalyzed H_2 production activity in membrane fractions was unchanged between ΔMbhABC and the parent strain, suggesting that redox activity is independent from Na^+ pumping. Without Na^+ pumping driving additional ATP synthesis by the Na^+-dependent ATP synthase in *P. furiosus*, ATP is only generated through glycolysis in ΔMbhABC. This difference in energy yield can be seen in a decreased growth rate of ΔMbhABC compared to the parent (Figure 2.2A). Maximum cell yield (based on intracellular protein concentrations, used for all growth experiments) and H_2 production (Figure 2.2B) is unchanged between the two strains.

The *P. furiosus* Mrp operon (Figure 2.1) is missing the membrane-anchored hydrogenase module or indeed any other energy-input module, but it does contain both the proton translocation module and the Na^+ translocation module. This homology to MBH suggests that Mrp also contains Na^+ pumping activity. Hence, a ΔMrp strain was generated to determine the effects that Mrp has on Na^+ pumping in *P. furiosus*. ΔMbhABC, as well as a double deletion strain (ΔMrp/ΔMbhABC) were used to compare the Na^+ pumping effects between the two Mrp complexes. All strains were first grown in a defined maltose medium with a "normal" NaCl concentration of 500 mM, typical for a marine microorganism like *P. furiosus* (Figure 2.2A). Both ΔMrp and the double deletion strain appear to have a shorter lag phase and faster growth rate than the parent strain. Specific hydrogen production rates were similar for all strains (Supplemental Figure 2.2). As anticipated, both ΔMrp and ΔMrp/ΔMbhABC appear to be significantly more sensitive to changes in pH than the parent strain. The primary end products of glycolysis in *P. furiosus* are H_2, acetate, and CO_2, and production of the latter causes a rapid drop in the pH of the growth medium (from a starting pH of 6.7 to 4.4 by 15 hours) (25). At low pH, cells begin to lyse, increasing soluble protein but decreasing total cellular protein; cell lysis is therefore represented by a drop in total cellular protein concentrations.

In order to investigate the effects of pH on growth, the 500 mM NaCl growth was repeated with the addition of 50 mM MOPS buffer to the growth medium in order to lessen the effect of CO_2 production on medium pH. As seen in Figure 2.3, while ΔMrp and ΔMrp/ΔMbhABC still have a shorter lag phase than the parent strain, once in exponential phase the parent strain has a slightly faster growth rate than the other strains. Additionally, there is no difference in maximum cell density (~120 μg/mL) between any of the strains.

To determine whether or not *P. furiosus* Mrp is involved in Na^+ homeostasis, all strains were grown under both low (Figure 2.4A) and high (Figure 2.4B) NaCl concentrations. At decreasing Na^+ concentrations, similar trends persist, with ΔMrp and ΔMrp/ΔMbhABC having a shorter lag phase than the parent strain or ΔMbhABC (9 vs 12 hours). However, when the Na^+ concentration is decreased to 50 mM, the parent strain no longer grows faster than ΔMbhABC, suggesting that at low sodium concentrations MBH is no longer able to generate a sufficient gradient for additional ATP synthesis. There is no significant difference in growth rate or maximum cell yield among the strains at higher Na^+ concentrations; no growth was observed in any strains at 1M Na^+ (data not shown). Taken together, the data show that the presence of Mrp in the cells does not significantly expand the range of Na^+ concentrations suitable for growth of *P. furiosus*, suggesting that its physiological role is not in Na^+ homeostasis.

In order to test the role of Mrp in the pH response, ΔMrp and the parent strain were grown under varying starting pH regimes (Figure 2.5). When the pH was lowered (pH 6.0) from the pH for optimum growth (7.0), both strains showed a significantly longer lag phase (~15 hours), but the maximum protein yield was only ~30% that of cells grown at the optimum. When the pH was raised (pH 8.0), both strains grew poorly, only reaching ~15% of the maximum protein yield at optimum pH. However, the change in pH (ΔpH = 1 and 0.5 for cells grown at pH 8 and 6, respectively) was insignificant under suboptimal pH conditions, and neither strain underwent cell lysis upon reaching stationary phase. However, while the pH stays relatively stable through 12 hours when starting at the optimum pH of 7.0, it drops rapidly (ΔpH =2.4) when cells reach stationary growth phase. Once the pH drops to ~4.5, ΔMrp begins to lyse more quickly than the parent. Both strains

produce similar levels of acetate during growth (equivalent to CO_2 production, which leads to the change in pH), suggesting that product formation is not different between the strains and that a different response to pH is the sole contributor to cell lysis. These data together suggest that the *P. furiosus* Mrp is involved in pH response. As the pH in the cell drops, Mrp likely maintains the cytoplasmic pH at the physiological value by pumping protons outside the cell at the cost of the Na^+ gradient. In order to confirm that Na^+ is the coupling ion used by Mrp, Na^+-dependent H_2 production assays were performed and show that, compared to the parent strain, H_2 production in ΔMrp is less stimulated by the presence of Na^+, producing only 45% the H_2 after 3 hours (Figure 2.5); thus, Mrp likely used Na^+ as a coupling ion for H^+ pumping. Surprisingly, while the deletion of Mrp does not have any effect on the growth of the strain at varying Na^+ concentrations, the ΔMrp strain shows a more significant decrease in Na^+-dependent H_2 production than the ΔMbhABC strain.

Discussion

The results presented in this paper show that the *P. furiosus* group 3 stand-alone Mrp is involved in the pH dependency of cell growth. H_2 production assays using cell suspensions show that, like MBH, Mrp uses Na^+ as the coupling ion. As the pH drops, Mrp brings in Na^+ in exchange for pumping protons outside the cell in order to maintain cytoplasmic pH near optimum levels for growth. The marine environment inhabited by *P. furiosus* is advantageous for Mrp function, with close to 500 mM Na^+ ions (compared to 10 μM protons at pH 5) available to balance pH. However, this pH homeostasis by Mrp comes at a cost to ATP synthesis, as Mrp "competes" for Na^+ flux with the ATP synthase of *P. furiosus*. This is best seen in the growth rates of ΔMrp and the parent strain under different buffer conditions. In the standard unbuffered medium (pH 6.7, Figure 2.2), the parent strain

has a slower growth rate than ΔMrp (4.1 vs 5.7 μg protein / hour for the parent and ΔMrp, respectively) because it attempts to correct for the changes in pH that occur as growing cells produce CO_2 during glycolysis. ΔMrp is not able to utilize the Na^+ gradient to maintain pH, so all Na^+ flux goes through ATP synthase and the cells quickly lyse upon reaching low pH. In buffered medium (pH 6.7, Figure 2.3) the parent strain no longer requires Mrp to maintain pH, so the growth rate is faster than that of ΔMrp (13.7 vs 12.7 μg protein / hour for the parent and ΔMrp, respectively). By slightly shifting the starting pH toward the optimum growth pH of *P. furiosus* (pH 7.0, Figure 2.5), the difference in growth rate is even more dramatic (30.7 vs 21.6 μg protein / hour for the parent and ΔMrp, respectively). This suggests that Mrp is able to act in the reverse direction, pumping Na^+ outside the cell and contributing to the Na^+ gradient utilized by ATP synthase, when pH is able to be maintained by a different mechanism, such as additional buffer in the medium. In fact, the results of Na^+-dependent H_2 production assays, which showed that ΔMrp is more sensitive to changes in Na^+ concentration than the parent, suggest that under optimal pH conditions Mrp has a greater contribution to the Na^+ gradient than the sodium pumping module of MBH.

As a marine organism, *P. furiosus* likely is specially adapted to life under high salt concentrations. However, it appears that while Mrp may contribute to the Na^+ gradient, it is not involved in maintaining Na^+ homeostasis inside the cell, as deletion of Mrp does not affect the range of Na^+ concentrations that support growth like Mrp complexes from other organisms. For example, expression of the group 1 Mrp from the halophile *Halomonas zhaodongensis* in *E. coli* increases the range of suitable Na^+ concentrations from 100 mM to almost 1 M NaCl (26). However, the genome of *P. furiosus* encodes a number of

predicted Na^+ pumping genes (Supplementary Table 2.2), including four homologues of the single subunit NapA Na^+/H^+ antiporter, one copy of the single subunit NhaC Na^+/H^+ antiporter, a Ca^+/Na^+ cation antiporter, the sodium-dependent acr3 arsenical resistance gene, and multiple amino acid symporters and bacterial homologues of Na^+-dependent neurotransmitters (27-31). *P. furiosus* likely has a number of redundant systems in order to maintain cellular Na^+ homeostasis in a high-salt environment.

Interestingly, the Mrp of *P. furiosus* is an active Na^+/H^+ antiporter even though it does not contain an energy-input module. For example, the MrpA subunit from *B. subtilis* has been found to be essential for Na^+-dependent pH homeostasis, with various mutations showing no pmf-dependent Na^+ efflux (32). MrpA has therefore been proposed to act as an energy-input module for Na^+/H^+ exchange. In respiratory complexes such as MBH and MBS, the MrpA module is replaced as an energy input by the peripheral hydrogenase and sulfane sulfur reductase modules, respectively, which couple redox activity in the cytoplasm to ion pumping (14, 15). While various models for coupling the PMF to ion pumping in Mrp have been proposed, the exact mechanism remains unknown (16, 17). The lack of an energy-input module represents an opportunity to compare *P. furiosus* Mrp to those that contain the additional MrpA subunit and could provide valuable insight into the coupling mechanism of the pmf to ion pumping.

There are multiple examples of organisms that contain multiple Mrp gene clusters. *Staphylococcus aureus* has two sets of group 1 *mrp* gene clusters, one encoding a Na^+/H^+ antiporter and the other encoding an Mrp of unknown function (33). The marine bacterium *Oceanobacillus iheyensis* has two sets of *mrp* gene clusters, while *Microbacterium* sp. TS-1 has three *mrp* gene clusters, two belonging to group 2 and the third to group 3. However,

their physiological functions remain unknown (34, 35). The marine hyperthermophile *Thermococcus onnurineus* NA1, a close relative of *P. furiosus*, encodes three group 3 *mrp* gene clusters, although all three are associated with respiratory complexes (36). *P. furiosus* is therefore the perfect organism in which to study Mrp complexes, as it is one of the few examples of an organism that contains both a respiratory and a stand-alone Mrp.

In addition to elucidating the role of the stand-alone Mrp in *P. furiosus*, the experiments in this work conducted with the ΔMbhABC strain provide additional insights into the function of MBH. While the growth rate of the ΔMbhABC strain was slower than that of the parent strain, the specific H_2 production rates were the same for both strains, suggesting that hydrogenase activity is uncoupled from Na^+ pumping in MBH. This is consistent with the proposed coupling mechanism of MBH, in which redox activity is coupled to the formation of a H^+ gradient across the membrane, which is passively exchanged by the Na^+ pumping module in order to generate a gradient for ATP generation (14, 21). Additionally, deletion of the catalytic MbhL subunit has been shown to abolish growth in the absence of elemental sulfur (37). Together, these data suggest that the primary role of MBH in *P. furiosus* is not as an energy conservation mechanism but simply as a method for disposing of reductant and recycling reduced ferredoxin generated by glycolysis, and provide additional support for the theory that MBH and related respiratory complexes evolved from the coupling of a simple NiFe hydrogenase with an Mrp antiporter (38). *P. furiosus* Mrp likely contributes to the Na^+ gradient for ATP synthesis under ideal conditions and might represent an artifact of the evolution of the respiratory MBH complex.

Acknowledgements

This work was funded by a grant from the Division of Chemical Sciences, Geosciences and Biosciences, Office of Basic Energy Sciences of the U.S. Department of Energy (DE-FG02-95ER20175 to MWWA.).

References

1. Ito M, Morino M, Krulwich TA. 2017. Mrp Antiporters Have Important Roles in Diverse Bacteria and Archaea. *Front Microbiol* 8.2325:1-12.

2. Brett CL, Donowitz M, Rao R. 2005. Evolutionary origins of eukaryotic sodium/proton exchangers. *Am J Physiol Cell Physiol* 288:C223-239.

3. Lentes CJ, Mir SH, Boehm M, Ganea C, Fendler K, Hunte C. 2014. Molecular characterization of the Na+/H+-antiporter NhaA from *Salmonella Typhimurium*. *PLoS One* 9:e101575-e101575.

4. Hamamoto T, Hashimoto M, Hino M, Kitada M, Seto Y, Kudo T, Horikoshi K. 1994. Characterization of a gene responsible for the Na+/H+ antiporter system of alkalophilic *Bacillus* species strain C-125. *Mol Microbiol* 14:939-946.

5. Kudo T, Hino M, Kitada M, Horikoshi K. 1990. DNA sequences required for the alkalophily of *Bacillus* sp. strain C-125 are located close together on its chromosomal DNA. *J Bacteriol* 172:7282-7283.

6. Padan E, Bibi E, Ito M, Krulwich TA. 2005. Alkaline pH homeostasis in bacteria: New insights. *Biochimica et Biophysica Acta (BBA) - Biomembranes* 1717:67-88.

7. Padan E, Schuldiner S. 1996. Chapter 22 Bacterial Na+/H+ antiporters — Molecular biology, biochemistry and physiology, p 501-531. *In* Konings WN, Kaback HR, Lolkema JS (ed), Handbook of Biological Physics, vol 2. North-Holland.

8. Kosono S, Haga K, Tomizawa R, Kajiyama Y, Hatano K, Takeda S, Wakai Y, Hino M, Kudo T. 2005. Characterization of a multigene-encoded sodium/hydrogen antiporter (sha) from *Pseudomonas aeruginosa*: its involvement in pathogenesis. *J Bacteriol* 187:5242-5248.

9. Kashyap DR, Botero LM, Lehr C, Hassett DJ, McDermott TR. 2006. A Na+:H+ antiporter and a molybdate transporter are essential for arsenite oxidation in *Agrobacterium tumefaciens*. *J Bacteriol* 188:1577-1584.

10. Swartz TH, Ikewada S, Ishikawa O, Ito M, Krulwich TA. 2005. The Mrp system: a giant among monovalent cation/proton antiporters? *Extremophiles* 9:345-354.

11. Morino M, Ogoda S, Krulwich TA, Ito M. 2017. Differences in the phenotypic effects of mutations in homologous MrpA and MrpD subunits of the multi-subunit Mrp-type Na(+)/H(+) antiporter. *Extremophiles* 21:51-64.

12. Sharma LK, Lu J, Bai Y. 2009. Mitochondrial respiratory complex I: structure, function and implication in human diseases. *Curr Med Chem* 16:1266-1277.

13. Baradaran R, Berrisford JM, Minhas GS, Sazanov LA. 2013. Crystal structure of the entire respiratory complex I. *Nature* 494:443-448.

14. Yu H, Wu CH, Schut GJ, Haja DK, Zhao G, Peters JW, Adams MWW, Li H. 2018. Structure of an Ancient Respiratory System. *Cell* 173:1636-1649.e1616.

15. Yu H, Haja DK, Schut GJ, Wu C-H, Meng X, Zhao G, Li H, Adams MWW. 2020. Structure of the respiratory MBS complex reveals iron-sulfur cluster catalyzed sulfane sulfur reduction in ancient life. *Nature Communications* 11:5953.

16. Steiner J, Sazanov L. 2020. Structure and mechanism of the Mrp complex, an ancient cation/proton antiporter. *eLife* 9:e59407.

17. Li B, Zhang K, Nie Y, Wang X, Zhao Y, Zhang XC, Wu X-L. 2020. Structure of the *Dietzia* Mrp complex reveals molecular mechanism of this giant bacterial sodium proton pump. *Proceedings of the National Academy of Sciences* 117:31166-31176.

18. Fiala G, Stetter KO. 1986. *Pyrococcus furiosus* sp. nov. represents a novel genus of marine heterotrophic archaebacteria growing optimally at 100°C. *Archives of Microbiology* 145:56-61.

19. Sapra R, Verhagen MFJM, Adams MWW. 2000. Purification and characterization of a membrane-bound hydrogenase from the hyperthermophilic archaeon *Pyrococcus furiosus*. *J Bacteriol* 182:3423-3428.

20. Wu C-H, Schut GJ, Poole FL, 2nd, Haja DK, Adams MWW. 2018. Characterization of membrane-bound sulfane reductase: A missing link in the evolution of modern day respiratory complexes. *J Biol Chem* 293:16687-16696.

21. Pisa KY, Huber H, Thomm M, Müller V. 2007. A sodium ion-dependent A1AO ATP synthase from the hyperthermophilic archaeon *Pyrococcus furiosus*. *FEBS J* 274:3928-3938.

22. Lipscomb GL, Stirrett K, Schut GJ, Yang F, Jenney FE, Scott RA, Adams MWW, Westpheling J. 2011. Natural competence in the hyperthermophilic archaeon *Pyrococcus furiosus* facilitates genetic manipulation: construction of markerless deletions of genes encoding the two cytoplasmic hydrogenases. *Applied and Environmental Microbiology* 77:2232-2238.

23. Bryksin AV, Matsumura I. 2010. Overlap extension PCR cloning: a simple and reliable way to create recombinant plasmids. *Biotechniques* 48:463-465.

24. Lim JK, Mayer F, Kang SG, Müller V. 2014. Energy conservation by oxidation of formate to carbon dioxide and hydrogen via a sodium ion current in a hyperthermophilic archaeon. *Proceedings of the National Academy of Sciences* 111:11497-11502.

25. Mukund S, Adams MW. 1995. Glyceraldehyde-3-phosphate ferredoxin oxidoreductase, a novel tungsten-containing enzyme with a potential glycolytic role in the hyperthermophilic archaeon *Pyrococcus furiosus*. *Journal of Biological Chemistry* 270:8389-8392.

26. Meng L, Hong S, Liu H, Huang H, Sun H, Xu T, Jiang J. 2014. Cloning and identification of Group 1 mrp operon encoding a novel monovalent cation/proton antiporter system from the moderate halophile Halomonas zhaodongensis. *Extremophiles* 18:963-972.

27. Furrer EM, Ronchetti MF, Verrey F, Pos KM. 2007. Functional characterization of a NapA Na(+)/H(+) antiporter from Thermus thermophilus. *FEBS Lett* 581:572-578.

28. Ito M, Guffanti AA, Zemsky J, Ivey DM, Krulwich TA. 1997. Role of the nhaC-encoded Na+/H+ antiporter of alkaliphilic Bacillus firmus OF4. *J Bacteriol* 179:3851-3857.

29. Yamato I, Anraku Y. 1990. Mechanism of Na+/proline symport in Escherichia coli: reappraisal of the effect of cation binding to the Na+/proline symport carrier. *J Membr Biol* 114:143-151.

30. Androutsellis-Theotokis A, Goldberg NR, Ueda K, Beppu T, Beckman ML, Das S, Javitch JA, Rudnick G. 2003. Characterization of a Functional Bacterial Homologue of Sodium-dependent Neurotransmitter Transporters *. *Journal of Biological Chemistry* 278:12703-12709.

31. Haja DK, Wu C-H, Ponomarenko O, Poole FL, George GN, Adams MWW. 2020. Improving Arsenic Tolerance of Pyrococcus furiosus by Heterologous Expression

of a Respiratory Arsenate Reductase. *Applied and Environmental Microbiology* 86:e01728-01720.

32. Ito M, Guffanti AA, Oudega B, Krulwich TA. 1999. Mrp, a multigene, multifunctional locus in *Bacillus subtilis* with roles in resistance to cholate and to Na+ and in pH homeostasis. *J Bacteriol* 181:2394-2402.
33. Swartz TH, Ito M, Ohira T, Natsui S, Hicks DB, Krulwich TA. 2007. Catalytic properties of *Staphylococcus aureus* and *Bacillus* members of the secondary cation/proton antiporter-3 (Mrp) family are revealed by an optimized assay in an *Escherichia coli* host. *J Bacteriol* 189:3081-3090.
34. Krulwich TA, Ito M. 2013. Alkaliphilic Prokaryotes, p 441-469. *In* Rosenberg E, DeLong EF, Lory S, Stackebrandt E, Thompson F (ed), The Prokaryotes: Prokaryotic Communities and Ecophysiology. Springer Berlin Heidelberg, Berlin, Heidelberg.
35. Fujinami S, Takeda K, Onodera T, Satoh K, Sano M, Narumi I, Ito M. 2013. Draft Genome Sequence of Sodium-Independent Alkaliphilic *Microbacterium* sp. Strain TS-1. *Genome Announc* 1:e01043-01013.
36. Lim JK, Kang SG, Lebedinsky AV, Lee J-H, Lee HS. 2010. Identification of a novel class of membrane-bound [NiFe]-hydrogenases in *Thermococcus onnurineus* NA1 by *In Silico* analysis. *Appl Environ Microbiol* 76:6286-6289.
37. Schut G, Nixon W, Lipscomb G, Scott R, Adams M. 2012. Mutational analyses of the enzymes involved in the metabolism of hydrogen by the hyperthermophilic archaeon *Pyrococcus furiosus*. *Front Microbiol* 3.

38. Schut GJ, Zadvornyy O, Wu C-H, Peters JW, Boyd ES, Adams MWW. 2016. The role of geochemistry and energetics in the evolution of modern respiratory complexes from a proton-reducing ancestor. *Biochimica et Biophysica Acta (BBA) - Bioenergetics* 1857:958-970.

Table 2.1. Strains generated and used in this study.

Trivial Name	**Lab Name**	**Phenotype**	**Source**
Parent	MW0003	Δ*pyrF*::*pyrF*	(22)
ΔMrp	MW0576	Δ*mbhABC*::P_{gdh}*pyrF*	This work
ΔMbhABC	MW0574	Δ*mrpEFGBB'CD*::P_{gdh}*pyrF*	(14)
ΔMrp/ΔMbhABC	MW0582	Δ*mbhABC*Δ*mrpEFGBB'CD*::P_{gdh}*pyrF*	This work

Table 2.2. Subunit homology of *P. furiosus* MBH, MBS, and Mrp and *B. subtilis* Mrp.

Proposed MBH module	***P. furiosus* MBH complex**	***P. furiosus* MBS complex**	***B. subtilis* Mrp complex**	***P. furiosus* Mrp Complex**
-	-	-	-	-
-	-	-	-	-
Membrane-anchored hydrogenase module	MbhJ	MbsJ	-	-
	MbhK	MbsK	-	-
	MbhL	MbsL	-	-
	MbhN	MbsN	-	-
	MbhM	MbsN	-	-
-	-	MbsH' N-terminal TM1-14	MrpA TM1-16	-
-	MbhI N-terminal[a]	MbsH' C-terminal TM 15-16	-	-
-	MbhI C-terminal[b]		-	-
Proton translocation module	MbhD[c]	MbsD	MrpA TM17-21	MrpB
	MbhE[c]	MbsE N-terminal		
	MbhG	MbsG	MrpC	MrpC
	MbhH	MbsH	MrpD	MrpD
Sodium translocation module	MbhF	MbsE C-terminal	MrpB	MrpB'
	MbhA	MbsA	MrpE	MrpE
	MbhB	MbsB	MrpF	MrpF
	MbhC	MbsC	MrpG	MrpG

Figure 2.1

Operon structure of *P. furiosus* MBH and Mrp.

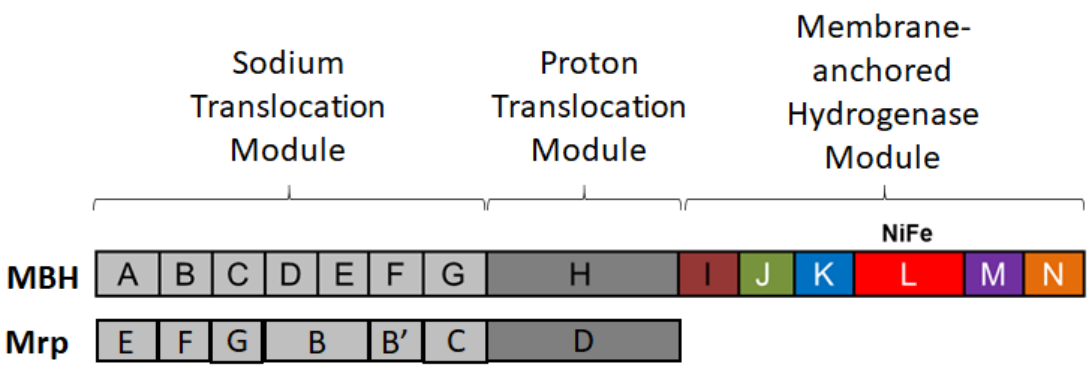
Sodium Translocation Module
Proton Translocation Module
Membrane-anchored Hydrogenase Module
NiFe
MBH
A
B
C
D
E
F
G
H
I
J
K
L
M
N
Mrp
E
F
G
B
B'
C
D

Figure 2.2

Growth and pH (A) and H_2 production (B) of deletion strains in unbuffered medium. Yellow, Parent strain; blue, ΔMbhABC; orange, ΔMrp; gray, ΔMrp/ΔMbhABC. Black triangles represent average measured pH values. Error bars represent standard deviation of biological triplicate samples.

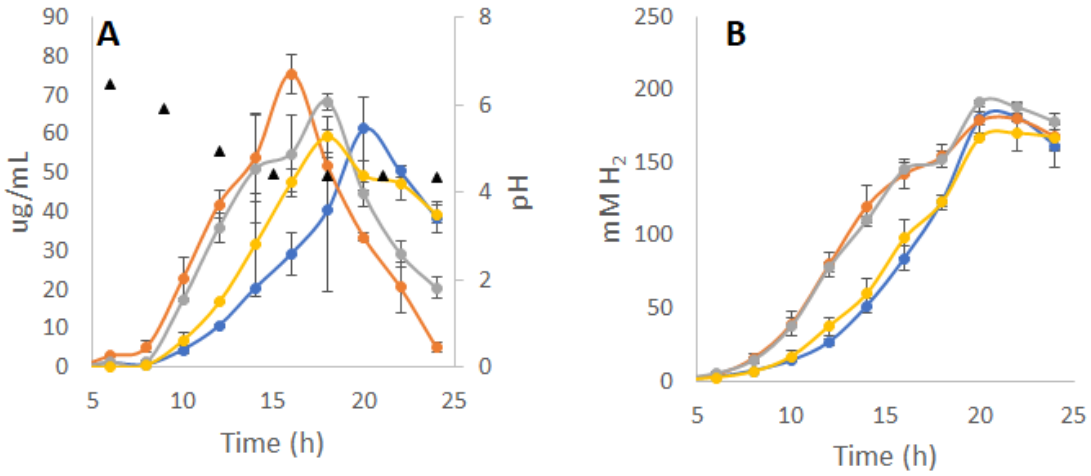
A
ug/mL
pH
Time (h)
B
mM H2
Time (h)

Figure 2.3

Growth of deletion strains in buffered medium. Yellow, Parent strain; blue, ΔMbhABC; orange, ΔMrp; gray, ΔMrp/ΔMbhABC. Error bars represent standard deviation of biological triplicate samples.

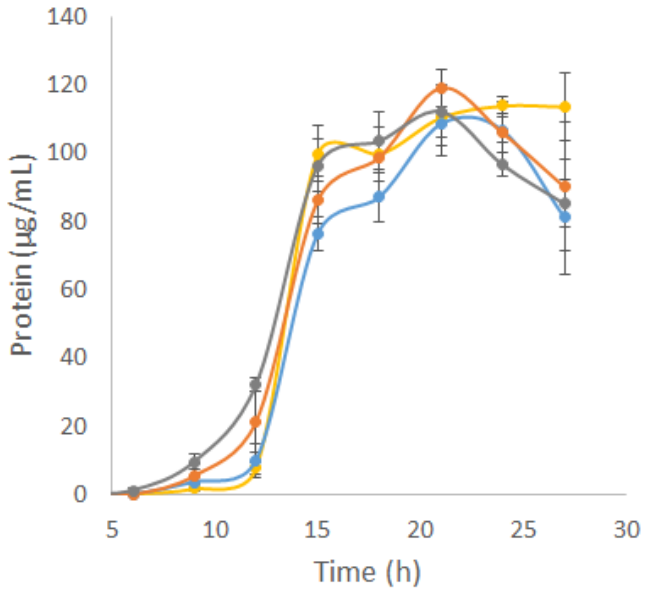
140
120
100
80
60
40
20
0
Protein (µg/mL)
5
10
15
20
25
30
Time (h)

Figure 2.4

Growth of deletion strains in buffered medium containing 50 mM (A) and 750 mM (B) NaCl. Yellow, Parent strain; blue, ΔMbhABC; orange, ΔMrp; gray, ΔMrp/ΔMbhABC. Black triangles represent average measured pH values. Error bars represent standard deviation of biological triplicate samples.

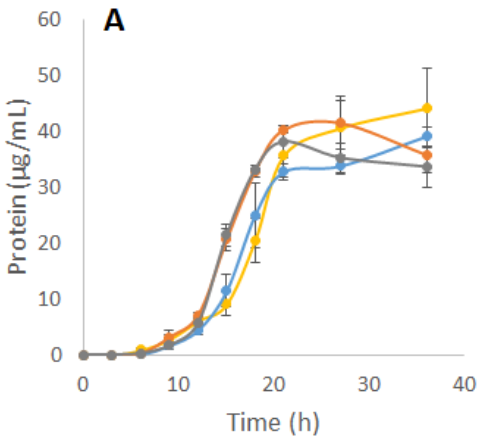
A
Protein (µg/mL)
Time (h)
0
10
20
30
40
50
60

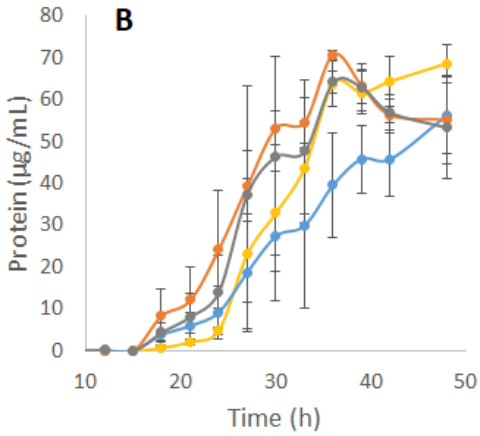
B
Protein (µg/mL)
Time (h)
0
10
20
30
40
50
60
70
80

Figure 2.5

Growth and pH of ΔMrp and the parent strain at different starting pH values. Filled circles represent protein concentration, while filled triangles of the same color represent the corresponding pH. Blue, Parent pH 7; red, Parent pH 6; orange, Parent pH 8; gray, ΔMrp pH 7; green, ΔMrp pH 6, yellow, ΔMrp pH 8. Error bars represent standard deviation of biological triplicate samples.

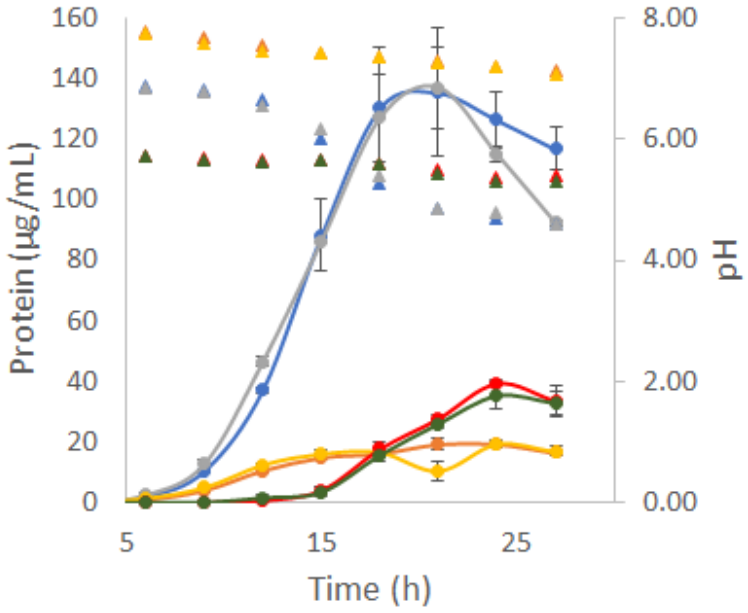
160
140
120
100
80
60
40
20
0
Protein (µg/mL)
8.00
6.00
4.00
2.00
0.00
pH
5
15
25
Time (h)

Figure 2.6

Na^+-dependent H_2 production in cell suspensions after 3 hours. Error bars represent standard deviation of technical triplicate samples.

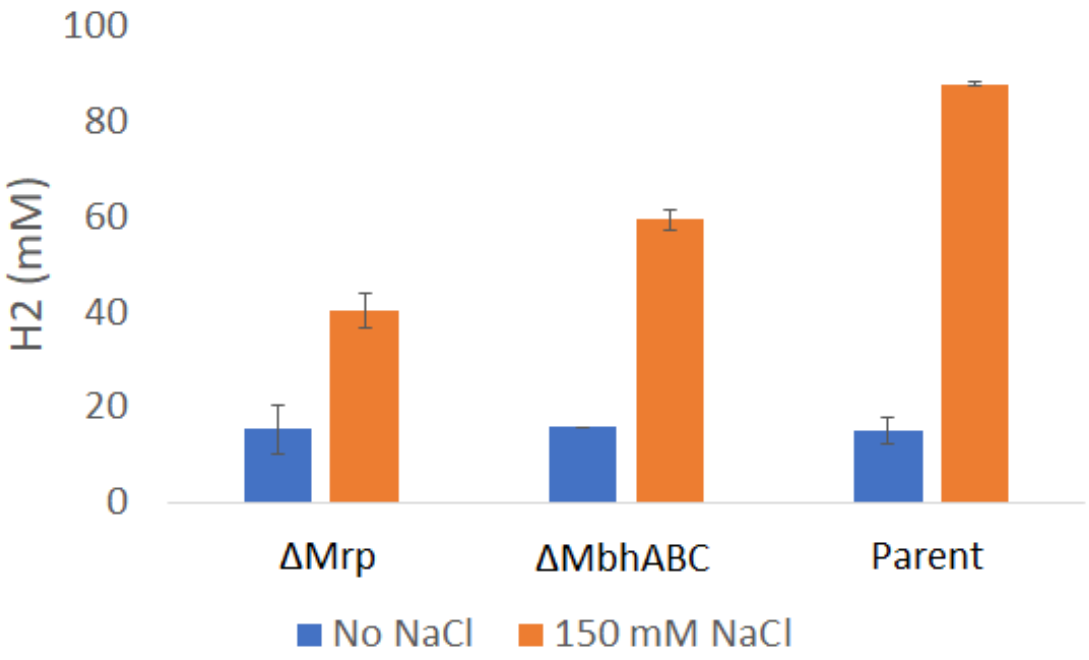
100
80
60
40
20
0
H2 (mM)
ΔMrp
ΔMbhABC
Parent
No NaCl
150 mM NaCl

Table S2.1 Primers used in this study.

Primer	**Sequence**
ΔMrp UFR F	agagtggccagctcattagagagtgttggaggattagcgacaattacaattttctttcta
ΔMrp UFR R	cctctagaatgttctccttcctccccccccattacaagggc
ΔMrp DFR F	actcagctcactccattttcaatccgggtatttggatacttctgg
ΔMrp DFR R	gaggcatcagtgaggaatactagcccaagtattattccaatcattcctcc

Table S2.2. Predicted single-subunit Na^+ transporters in *P. furiosus.*

GM number	Annotation	Predicted Function
PF1603	hypothetical Na+ antiporter	NapA/CPA2/Kef-type K^+ ion importer
PF1164	probable Na+/H+ antiporter	
PF0268	Na+/H+ antiporter homolog	
PF0275	Na+/H+ antiporter	
PF2032	conserved hypothetical protein	NhaC-like Na^+ antiporter
PF0350	putative cation antiporter	Ca^+/Na^+ antiporter
PF0429	putative proline permease	Amino Acid symporter
PF0514	d-alanine glycine permease	
PF1469	glutamate/aspartate transport protein	
PF0552	arsenical-resistance protein acr3	Arsenical resistance
PF0371	putative transporter	Na^+-dependent neurotransmitter transporter
PF1254	probable sodium dependent transporter	
PF1726	conserved hypothetical protein	

Figure S2.1

Sequence alignments of *P. furiosus* Mrp subunits. A-H: sequence alignments of *P. furiosus* Mrp subunits with homologous subunits in *P. furiosus* MBH and MBS; I: sequence alignment of *P. furiosus* MrpB and the C terminus of *B. subtilis* MrpA. Boxed residues represent proposed ion channels and conserved structural elements based on the MBH structure in (14). Black: identity; blue: highly conserved; green: similarity; red: not conserved. Red asterisks represent amino acids with previously published mutations.

A

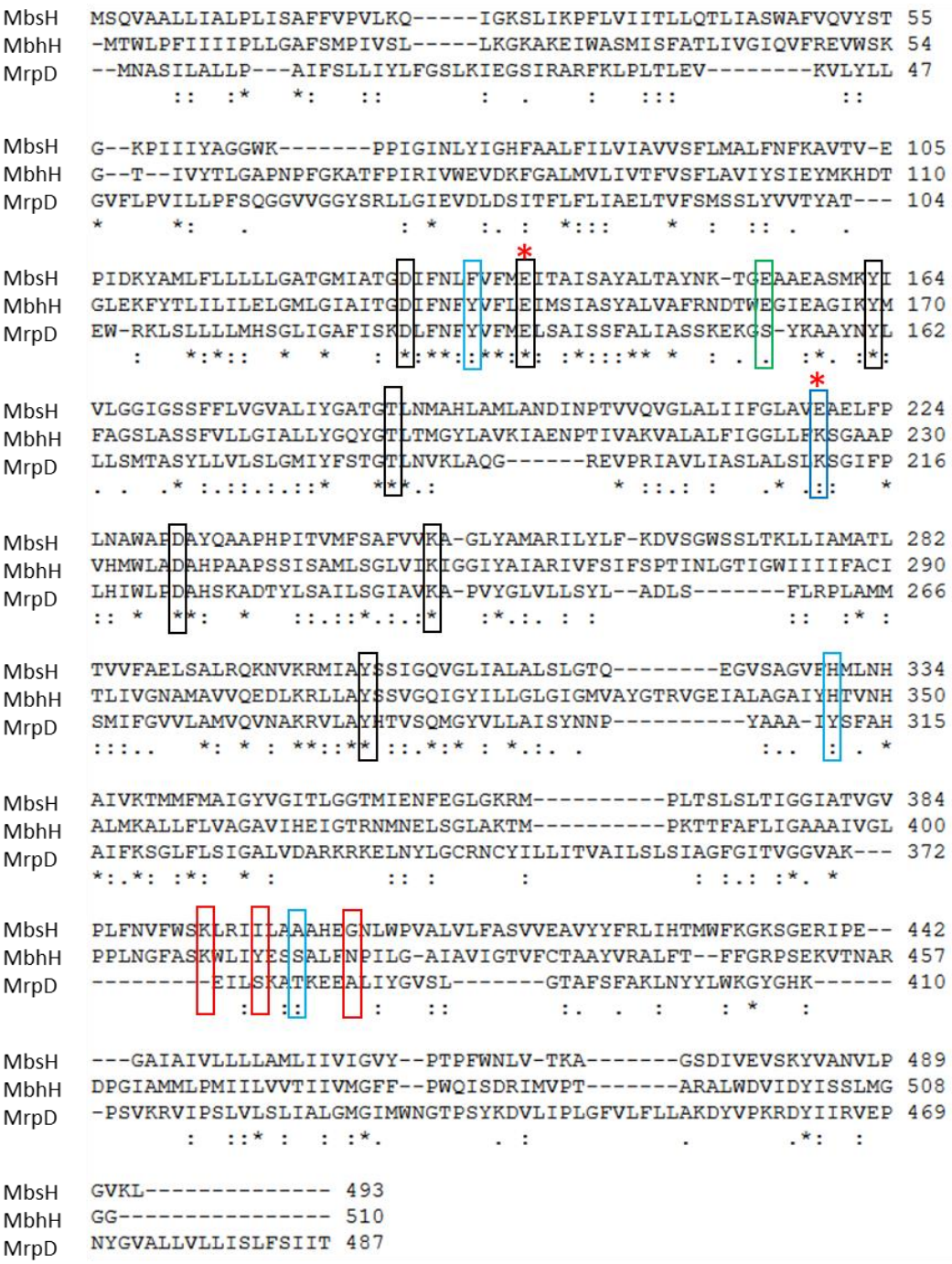
MbsH MSQVAALLIALPLISAFFVPVLKQ-----IGKSLIKPFLVIITLLQTLIASWAFVQVYST 55
MbhH -MTWLPFIIIIPLLGAFSMPIVSL-----LKGKAKEIWASMISFATLIVGIQVFREVWSK 54
MrpD --MNASILALLP---AIFSLLIYLFGSLKIEGSIRARFKLPLTLEV--------KVLYLL 47
MbsH G--KPIIIYAGGWK-------PPIGINLYIGHFAALFILVIAVVSFLMALFNFKAVTV-E 105
MbhH G--T--IVYTLGAPNPFGKATFPIRIVWEVDKFGALMVLIVTFVSFLAVIYSIEYMKHDT 110
MrpD GVFLPVILLPFSQGGVVGGYSRLLGIEVDLDSITFLFLIAELTVFSMSSLYVVTYAT--- 104
MbsH PIDKYAMLFLLLLLGATGMIATGDIFNLFVFMEITAISAYALTAYNK-TGEAAEASMKYI 164
MbhH GLEKFYTLILILELGMLGIAITGDIFNFYVFLEIMSIASYALVAFRNDTWEGIEAGIKYM 170
MrpD EW-RKLSLLLLMHSGLIGAFISKDLFNFYVFMELSAISSFALIASSKEKGS-YKAAYNYL 162
MbsH VLGGIGSSFFLVGVALIYGATGTLNMAHLAMLANDINPTVVQVGLALIIFGLAVEAELFP 224
MbhH FAGSLASSFVLLGIALLYGQYGTLTMGYLAVKIAENPTIVAKVALALFIGGLLFKSGAAP 230
MrpD LLSMTASYLLVLSLGMIYFSTGTLNVKLAQG------REVPRIAVLIASLALSIKSGIFP 216
MbsH LNAWAPDAYQAAPHPITVMFSAFVVKA-GLYAMARILYLF-KDVSGWSSLTKLLIAMATL 282
MbhH VHMWLADAHPAAPSSISAMLSGLVIKIGGIYAIARIVFSIFSPTINLGTIGWIIIIFACI 290
MrpD LHIWLPDAHSKADTYLSAILSGIAVKA-PVYGLVLLSYL--ADLS-------FLRPLAMM 266
MbsH TVVFAELSALRQKNVKRMIAYSSIGQVGLIALALSLGTQ--------EGVSAGVFHMLNH 334
MbhH TLIVGNAMAVVQEDLKRLLAYSSVGQIGYILLGLGIGMVAYGTRVGEIALAGAIYHTVNH 350
MrpD SMIFGVVLAMVQVNAKRVLAYHTVSQMGYVLLAISYNNP----------YAAA-IYSFAH 315
MbsH AIVKTMMFMAIGYVGITLGGTMIENFEGLGKRM----------PLTSLSLTIGGIATVGV 384
MbhH ALMKALLFLVAGAVIHEIGTRNMNELSGLAKTM----------PKTTFAFLIGAAAIVGL 400
MrpD AIFKSGLFLSIGALVDARKRKELNYLGCRNCYILLITVAILSLSIAGFGITVGGVAK--- 372
MbsH PLFNVFWSKLRIILAAAHEGNLWPVALVLFASVVEAVYYFRLIHTMWFKGKSGERIPE-- 442
MbhH PPLNGFASKWLIYESSALFNPILG-AIAVIGTVFCTAAYVRALFT--FFGRPSEKVTNAR 457
MrpD ---------EILSKATKEEALIYGVSL-------GTAFSFAKLNYYLWKGYGHK------ 410
MbsH ---GAIAIVLLLLAMLIIVIGVY--PTPFWNLV-TKA-------GSDIVEVSKYVANVLP 489
MbhH DPGIAMMLPMIILVVTIIVMGFF--PWQISDRIMVPT-------ARALWDVIDYISSLMG 508
MrpD -PSVKRVIPSLVLSLIALGMGIMWNGTPSYKDVLIPLGFVLFLLAKDYVPKRDYIIRVEP 469
MbsH GVKL-------------- 493
MbhH GG---------------- 510
MrpD NYGVALLVLLISLFSIIT 487

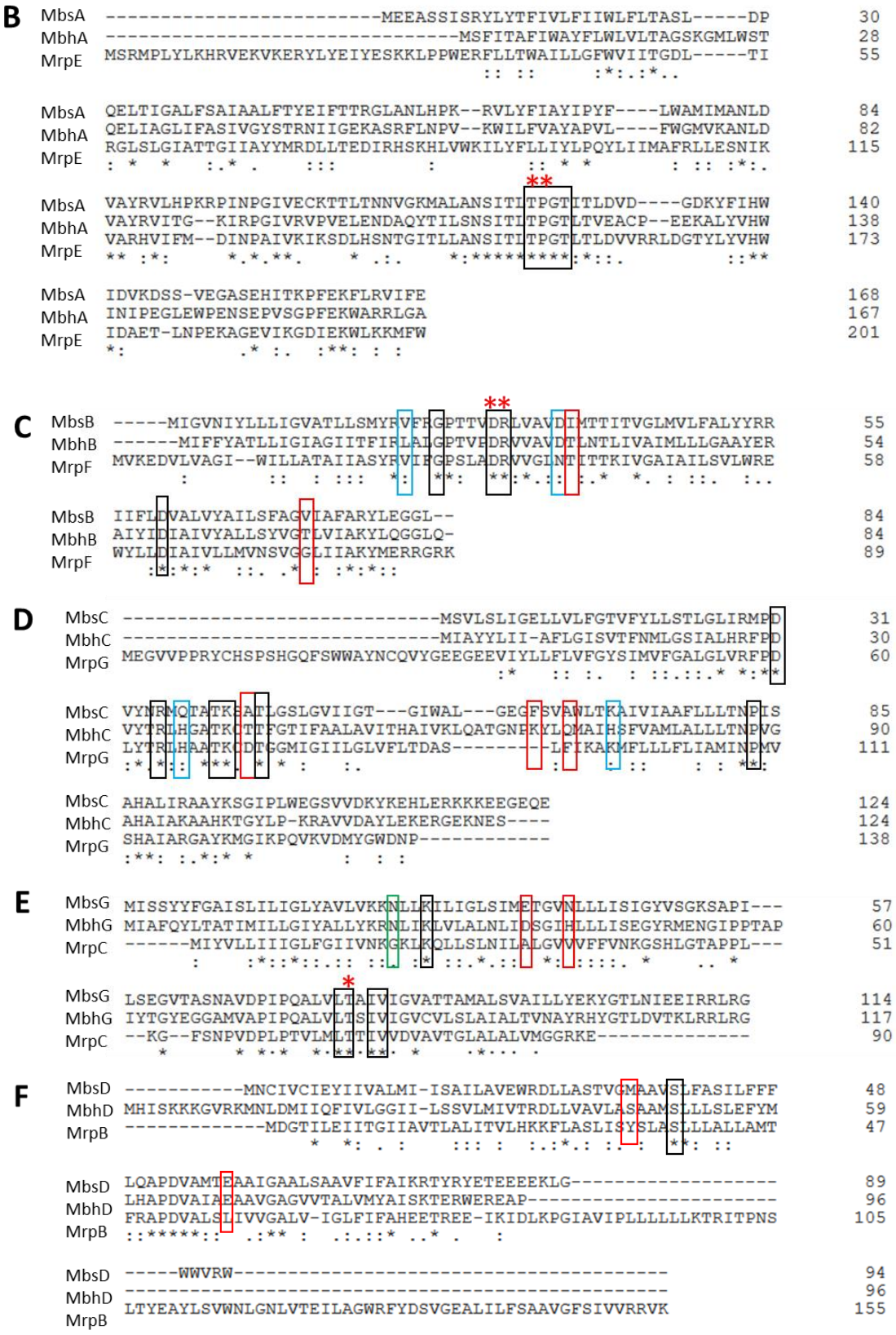
B
MbsA
MbhA
MrpE
C
MbsB
MbhB
MrpF
D
MbsC
MbhC
MrpG
E
MbsG
MbhG
MrpC
F
MbsD
MbhD
MrpB

G

```
MbsE  ----------------------------------------MVGMLKRVLA-ILTILVI   17
MbhE  ----------------------------------------MKRALG-FLSLLVI   13
MrpB  MDGTILEIITGIIAVTLALITVLHKKFLASLISYSLASLLLALLAMTFRAPDVALSLIVV   60
                                                *.    *:::*:

MbsE  G-------------------YWLAQGLADVPFGQ---DKMVV-GKYYLEHVKEETGAVNA   54
MbhE  FAS-----LL----VALSPEYGIKFGVGGEDWL----KYRYT-DNYYIEHGIEEVGGTNI   59
MrpB  GALVIGLFIFAHEETREEIKIDLKPGIAVIPLLLLLLKTRITPNSLTYEAYLSVWNLGNL   120
                          :  *:.         .  . ..  *   .  .  *

MbsE  VTAVVVNYRGLDTLGEVTVLFIASTGVAALLWKKKRERTAKTEGSVVLTTGARLLFPFIA   114
MbhE  VTDIVFDYRGYDTLGEATVLFTAIAGAVALLRPWRREENE--------------------   99
MrpB  VTEILAGWRFYDSVGEALILFSAAVGFSIVVRRVK-------------------------   155
      ** :: .:*  *::**. :** * .*   ::   :

MbsE  LFGMYIFIHGHLTPGGGFPGGATIATAFLLMYLAFTIYEIPHRGFEVTEGLAGMGYVITG   174
MbhE  ------------------------------------------------------------   99
MrpB  ------------------------------------------------------------   155

MbsE  LIGLAIGGYFLFDWIWQTWGWGHENIGRLFSGGFIPIIYTLIGIKVGTELSGIVDNMLKE   234
MbhE  ------------------------------------------------------------   99
MrpB  ------------------------------------------------------------   155

MbsE  EVKE                                                           238
MbhE  ----                                                           99
MrpB  ----                                                           155
```

H

```
MbsE  MVGMLKRVLAILTILVIGYWLAQGLADVPFGQDKMVVGKYYLEHVKEETGAVNAVTAVVV   60
MbhF  ------------------------------------------------------------   0
MrpB' ------------------------------------------------------------   0

MbsE  NYRGLDTLGEVTVLFIASTGVAALLWKKKRERTAKTEGSVVLTTGARLLFPFIALFGMYI   120
MbhF  ---------------------------------MNEDMGVIVRTNARALIPFIGIFGAYI   27
MrpB' ---------------------------------MKMSIVARTTTKLVAPFLTTYAAYL   25
                                         . .::  * :: : **:  :. *:
         * *  *
MbsE  FIHGHLTPGGGFPGGATIATAFLLMYLAFTIYE----IPHRGFEVTEGLAGMGYVITGLI   176
MbhF  VTHGHLTPGGGFQGGATIAGAGVLFLIAFGVKAAKEKINKNLYSALEGLGGLVFLGAAML   87
MrpB' MIYTTQSPGGGFQAGVILAVALILLITSHGYKSVRKYFRKRVASSLESVGGLATITIFF-   84
      . :  :  :***** .*. :* * :*:  :.        : :.  .  *.:.*:  :   :

MbsE  GLAIGGYFLFDWIWQTWGWGHENIGRLFSGGFIPIIYTLIGIKVGTELSGIVDNMLKEEV   236
MbhF  GLSV--AFFYNILWHEGPIFNSSPGTLLSAGFLPIMNLGVGLKVFTGLV---SALFALSV   142
MrpB' ---------LTVLLFLRP----------SEVYVVPANVFIGLKVGAAFTLMFYALISV--   123
                 :               *  ::      :*:** : :      ::

MbsE  KE----                                                         238
MbhF  FRRWKS                                                         148
MrpB' LERD--                                                         127
       .
```

I

```
B. subtilus MrpA  GFIILIGGAFAIKGGFSFKTEGMAKIGVYEIILTLVMISATVATVFARSRLTAIIALGVV   660
P. furiosus MrpB  ----------------------MDGTILEIITGIIAVTLALITVLHKKFLASLISYSLA   37
                                         .  : ***  :: :: :: **: :. *:::*: .:.

B. subtilus MrpA  GYTLALFFVIFRAPDLALTQLVIETISVALFLLCFYHLPKLRLKTKTRTFRMTNFIISLG   720
P. furiosus MrpB  SLLLALLAMTFRAPDVALSLIVVGALVIGLFIFAHEETRE---EI--------KIDLKPG   86
                  .  ***: : *****:**: :*: :: :.**::.. .  :   :         :: :. *

B. subtilus MrpA  VGVIVTLLGIASSSQRTKDSIASFFVKHSHDLGGGDNVVNVILVDFRGFDTMFEITVLTI   780
P. furiosus MrpB  IAVIPLLLLLLKT-RITPNSLT---YEAYLSVWNLGNLVTEILAGWRFYDSVGEALILFS   142
                  :.**  ** : .: : * :*::    :   .: . .*:*. **..:* :*:: *  :*

B. subtilus MrpA  AALGIYSMIKTKVKEEGKSGE                                   801
P. furiosus MrpB  AAVGFSIV-VRRVK-------                                   155
                  **:*:  :   :**
```

Figure S2.2

Calculated specific H_2 production rates corresponding to the growth data in Figure 2.1. Yellow, Parent strain; blue, ΔMbhABC; orange, ΔMrp; gray, ΔMrp/ΔMbhABC.

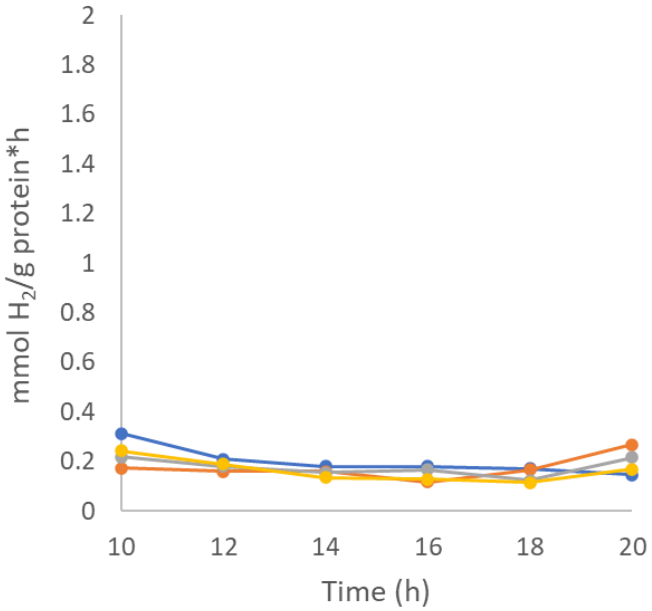
2
1.8
1.6
1.4
1.2
1
0.8
0.6
0.4
0.2
0
mmol H2/g protein*h
10
12
14
16
18
20
Time (h)

Figure S2.3

Acetate production of ΔMrp (gray) and the parent strain (blue) at pH 7. Corresponds to growth data in Figure 2.4. Error bars represent standard deviation from biological triplicate samples.

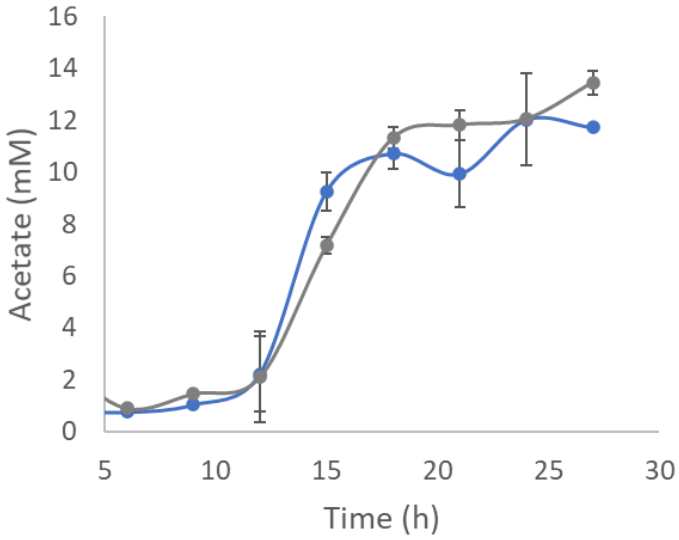
16
14
12
10
8
6
4
2
0
Acetate (mM)
5
10
15
20
25
30
Time (h)

CHAPTER THREE

STRUCTURE OF THE RESPIRATORY MBS COMPLEX REVEALS IRON-SULFUR CLUSTER CATALYZED SULFANE SULFUR REDUCTION IN ANCIENT LIFE[2]

[2] Haja, D.K.*, Yu, H*., Schut, G.J. *et al.* 2020. *Nature Communications.* 11, 5953.

*The authors contributed equally to this work

Abstract

Modern day aerobic respiration in mitochondria involving complex I converts redox energy into chemical energy and likely evolved from a simple anaerobic system now represented by hydrogen gas-evolving hydrogenase (MBH) where protons are the terminal electron acceptor. Here we present the cryo-EM structure of an early ancestor in the evolution of complex I, the elemental sulfur (S^0)-reducing reductase MBS. Three highly conserved protein loops linking cytoplasmic and membrane domains enable scalable energy conversion in all three complexes. MBS contains two proton pumps compared to one in MBH and likely conserves twice the energy. The structure also reveals evolutionary adaptations of MBH that enabled S^0 reduction by MBS catalyzed by a site-differentiated iron-sulfur cluster without participation of protons or amino acid residues. This is the simplest mechanism proposed for reduction of inorganic or organic disulfides. It is of fundamental significance in the iron and sulfur-rich volcanic environments of early earth and possibly the origin of life. MBS provides a new perspective on the evolution of modern-day respiratory complexes and of catalysis by biological iron-sulfur clusters.

Introduction

Respiratory complexes couple the energy released from spontaneous electron transfer reactions to the generation of chemical gradients. From archaea and bacteria to mammalian mitochondria, modern-day respiratory complex I contains a 14-subunit core[1-6] that oxidizes NADH, reduces quinone and translocates four protons across the membrane, used to drive ATP synthesis thereby conserving energy[7-11]. Such complexes first appeared billions of years ago in an anaerobic environment where, without oxygen, oxidative microbial metabolism ultimately reduced the ubiquitous proton to produce hydrogen gas catalyzed by a membrane-bound [NiFe]-hydrogenase (Fig 3.1A, MBH)[6,12-15]. As the atmosphere became more oxidized, ancestral MBH evolved to reduce elemental sulfur (S^0), now represented by sulfane sulfur reductase or MBS, and ultimately to reducing quinone, as in complex I[12-15] and related NDH[16].

MBH and MBS are found in the anaerobic hyperthermophilic archaeon *Pyrococcus furiosus*[17], which oxidizes the redox protein ferredoxin, produces H_2S or H_2, and conserves energy by pumping Na^+ (Fig 3.1A)[9,12,18,19]. In the presence of S^0, the genes encoding MBS are expressed while those encoding MBH are repressed[19-21], resulting in a microbial cell yield twice that when cells are grown without S^0 [9,22], suggesting that MBS is more efficient in energy conservation although the underlying mechanism is unknown. MBS reductively cleaves linear polysulfide chains (S_n^{2-}, where $n \geq 4$), produced abiotically from the reaction of H_2S and S° (Equation 1) in the hydrothermal vent environments that *P. furiosus* inhabits, into two shorter polysulfides (Equation 2). Further reduction yields unstable di- and trisulfides (Equation 3) that spontaneously convert to S° and H_2S (Equation 4). S-S bond cleavage by MBS does not involve protons (Equations 2 and 3) and H_2S is produced

abiotically (Equation 4). Bacterial polysulfide reductase (PSR, not present in *P. furiosus*) uses a molybdopterin cofactor to reductively cleave the terminal sulfur of polysulfides as H_2S **(**Equation 5)[23,24] so the archaeal MBS must reduce a disulfide bond by a different mechanism.

Abiotic: $S_8 + H_2S \rightarrow {}^{-}S\text{-}S\text{-}S\text{-}S\text{-}S\text{-}S\text{-}S\text{-}S\text{-}S^{-}$ (S_9^{2-}) + $2\,H^+$ (1)

MBS: $S_9^{2-} + 2\,e^- \rightarrow {}^{-}S\text{-}S\text{-}S\text{-}S^{-} + {}^{-}S\text{-}S\text{-}S\text{-}S\text{-}S^{-}$ (S_5^{2-}) (2)

MBS: $S_5^{2-} + 2\,e^- \rightarrow {}^{-}S\text{-}S\text{-}S^{-} + {}^{-}S\text{-}S^{-}$ (S_2^{2-}) (3)

Abiotic: $5\,S_2^{2-} + 4\,H^+ \rightarrow S_8 + 2\,H_2S$ (4)

PSR: $S_n^{2-} + 2\,e^- + 2\,H^+ \rightarrow S_{n-1}^{2-} + H_2S$ (5)

The structure of MBH (298 kDa, 14 subunits) revealed its close evolutionary relationship with complex I. Although MBH contains a single proton pump compared to four in complex I, they have the same structural elements thought to enable transduction of redox energy to an ion gradient[6,7,25-27]. Herein we describe the structure of MBS (357 kDa, 13 subunits), the proposed evolutionary link between them[9], and how a catalytic site evolved from reducing protons to reducing large hydrophobic molecules like S_n^{2-} and cleaving an inorganic sulfur-sulfur bond, a reaction of high significance in the primordial early earth.

Results

Structure of MBS

We determined the cryo-EM structure of MBS in a dimer complex form (Fig. 3.1B-C, Supplementary Figure 3.1, Supplementary Figure 3.2, Supplementary Table 3.1). The

atomic model contained 26 protein subunits and 116 transmembrane helices (TMHs). The MBS monomer consists of a peripheral cytoplasmic arm (MbsJ, K, L and N), anchored to the membrane by MbsM, and coordinates three [4Fe-4S] clusters that transfer electrons from ferredoxin to the substrate polysulfide (Fig 3.1C)[19]. The membrane arm (MbsA, B, C, D, E, G, H, H' and M) has 58 TMHs and contains a module proximal to the peripheral arm (proximal membrane module; MbsH', MbsH, MbsD, MbsG and TMH1-2 of MbsE) and a distal membrane module (MbsA, B and C, and TMH3-6 of MbsE) (Fig. 3.2A, Supplementary Figure 3.3A).

The MBS dimer complex is assembled via extensive contacts at two main places between the proximal membrane module of one MBS and the membrane-anchored peripheral module of the other (Fig. 3.1B, Fig. 3.2A-C). The first contact involves a long amphipathic horizontal helix (termed helix HL) of MbsH' (Fig. 3.2D): the MbsH' helix HL of one MBS interacts extensively with the N-terminal region of MbsN and TMH8 of MbsM in the other MBS, including several hydrophobic interactions and a salt bridge. The 2-fold axis is located between two F566 residues preceding the helix HL in the two MbsH' of the MBS dimer complex. The second contact involves the tryptophan-rich C-terminal extension (W90, W91 and W94) of MbsD of one MBS projecting into a largely hydrophobic cleft in the peripheral domain of the other (Fig. 3.2E). The distal membrane module is not involved in the MBS dimer interface and is likely somewhat dynamic, which may explain the lower local resolution in this region (Supplementary Figure 3.1G).

MbsH and MbsH' each contain a proton pump

In the proximal membrane module, the two largest subunits MbsH and MbsH' are of similar fold, consistent with the idea from sequence comparison that MbsH' is a gene-

duplication product of MbsH [19] (Supplementary Figure **3.**3B) that occurred prior to the evolution of MBH and MBS and, as discussed below, during the evolution of the Na^+/H^+ Mrp antiporter. MbsH and MbsH' are homologous to the antiporter-like subunits of complex I (*T. thermophilus* Nqo12, 13 and 14) proposed for H^+ pumping[1-3,5]. MbsH and MbsH' each contain two five-TMH repeating units: TMHs 4-8 and TMHs9-13 that are superimposable when one repeat is flipped upside down in the membrane (Supplementary Figure 3.3B). Each 5-TMH unit features a discontinuous α-helix – TMH7 in the first repeat and TMH12 in the second repeat with conserved charged residues around the helical kink: E219 and K393 in MbsH, and K217 and K399 in MbsH'. Notably, the arrangement between MbsH and MbsH' as a unit is strikingly similar to Nqo13 and Nqo14 of *T. thermophilus* complex I (Fig. 3.3A-B). As a result, a central charged axis across MbsH and MbsH' (MbsH E138, K250, and H330; MbsH' E128, K248, and H336) is formed that is conserved in complex I (Fig. 3.3C). These features are characteristic of the proton pumps that are found in mammalian and bacterial forms of complex I, which have been supported by structural studies, mutagenesis analysis and recent molecular dynamics simulations[1-3,28-30]. We therefore propose that MbsH and MbsH' each contains a H^+ pump in MBS.

Interestingly, MbsH' contains two extra TMHs (TMH15 and TMH16) that are connected by a long intervening loop ($Loop_{TMH15-16}$) and the horizontal helix HL. The helix HL and its following TMH16 holds MbsH and MbsH' together. This element is conserved across the different respiratory complexes, with the helix HL either shortened in MBH (with one antiporter-like subunit MbhH) or elongated in complex I (with three antiporter-like subunits) (Fig. 3.3A-B, Supplementary Figure 3.4A), strongly supporting the modular evolution of these respiratory machineries[31]. Notably, $Loop^{TMH15-16}$ and TMH15 of the C-

terminal end of MbsH' tie together the membrane anchored peripheral module and the proton pumping module (Supplementary Figure 3.4A). This organization mode is conserved in the MBH complex, though MbsM and MbsH' form a tighter interacting interface than the lipid-filled wide cleft between MbhM and MbhH in the MBH complex (Supplementary Figure 3.4B)[6]. In contrast, in complex I, the membrane anchored peripheral module is located on the opposite side of the membrane arm (Fig. 3.3A). However, in spite of this different architecture, a charged axis within the membrane-anchored peripheral arm (MbsM E203, E211, D196, E193 and E104) extends continuously into the proton-pumping module (MbsH and MbsH') (Fig. 3.3C), similar to that proposed in complex I for energy transduction[1-3,32].

The tentative Na^+/H^+ antiporter module

Except for MbsH and MbsH', the remainder of the proximal membrane module of MBS is composed of two layers of helix bundles next to MbsH: one layer composed of three TMHs of MbsD and the other layer composed of five TMHs – TMH1-2 of MbsE separated by TMH1-3 of MbsG in the middle (Supplementary Figure 3.3A). This sub-region together with MbsH is conserved among MBH and complex I including key elements: charged residues E58 in MbsD, E37 in MbsG, and a π-bulge distortion in TMH3 of MbsD (Supplementary Figure 3.4A and C). These are key features proposed for proton transfer that are conserved in Nqo10 and 11 in complex I and also in MbhD, G and E in MBH[2,3,6,33], although the precise mechanism is still under debate[1,2,33]. This suggests a putative proton translocation path, termed Pc path for composite proton translocator. We note that the assignment of the Pc proton path is based on structural conservation among MBH, MBS, and complex I, and therefore, this path is tentative. The translocation stoichiometry of the

H^+ and Na^+ is currently unknown and has yet to be experimentally determined with either Mrp, MBH, or MBS. The stoichiometry will help to determine if Pc is a functional proton path.

In the distal membrane module of MBS, MbsA at the far end contains two TMHs and a following ferredoxin-like domain and binds to the three 3-TMH subunits MbsB, C and TMH3-6 of MbsE, which in turn are attached to MbsD of the proximal membrane module (Supplementary Figure 3.3A). Notably, MbsB, C and E contain three conserved regions that are rich in charged/polar residues and run across the interior of the membrane arm (Supplementary Figure 3.4E). Additionally, the conserved MbsC P83 introduces a break in the middle of the membrane of MbsC TMH3. These features are conserved in the Na^+-translocation path in MBH and in Mrp, but not in complex I as complex I does not translocate Na^+ ions (Fig. 3.3A, Supplementary Figure 3.4D)[6,34]. This suggests a Na^+-translocation path within this sub-region. This together with the adjacent H^+ path (Pc) likely forms the Na^+/H^+ antiporter module in the distal end of membrane arm (Fig. 3.3C).

During the review of this manuscript, the structure of Mrp antiporter was published[35]. The structure enables a comparison between MBS and Mrp to obtain direct evolutional insights between them (Fig. 3.4A). All subunits of the Mrp Na^+/H^+ antiporter have homologous counterparts in MBS (Supplementary Table 3.2). Consequently, the MBS membrane arm (excluding MbsM, which anchors the peripheral arm) shares a conserved architecture with Mrp (Fig. 3.4A). It is clear that the Mrp structure lacks the membrane-anchored peripheral arm and supports the modular evolution of respiratory Complexes[31]. The emergence of MBS and MBH was likely a result of the combination of the Mrp antiporter and a peripheral module related to a cytoplasmic [NiFe] hydrogenase.

MBH exhibits loss of the MrpA homolog resulting in fewer proton pumps while its peripheral arm retains the proton reduction activity. In contrast, MBS keeps all the Mrp homologs while its peripheral arm shows concomitant changes in the peripheral module to enable catalysis of the reduction of polysulfide rather than protons (Fig. 3.4B). Conceivably, both MBS and MBH are much more efficient in energy conservation as the redox reaction is now physically coupled with the ion translocation across the membrane.

A three-loop system bridges the electron transfer site and the ion-pumping membrane arm

The architecture of the MBS cytoplasmic module closely resembles those of MBH and complex I (Supplementary Figure 3.5). In MBS, a large hydrophobic chamber, similar in size to those in MBH and complex I is formed by cytoplasmic MbsL, MbsJ, and their membrane anchor MbsM (Fig. 3.5A-C, Fig. 3.6A). The openings of the MBS and complex I hydrophobic chamber are wider than that of MBH allowing entry of hydrophobic substrates (polysulfide and quinone; Fig. 3.5D). The end of this chamber in MBS coincides with the binding site of quinone headgroup defined by Nqo4 H38 and Y87 in complex I (Fig. 3.5E)[1]. However, these two residues for quinone headgroup binding and also for protonation in complex I are absent in MBS (Fig. 3.5F). Moreover, MbhL E21, the key residue for proton reduction in MBH complex, is also absent in MBS[6]. These suggest unique catalytic mechanism for MBS despite similar modular overall architecture, as we will cover later in next section.

This hydrophobic chamber containing the catalytic site of MBS in the peripheral arm is defined by three loops originating from MbsH' ($loop_{TMH15\text{-}16}$, now termed Loop 1), MbsL ($loop_{\beta1–\beta2}$, Loop 2), and MbsM ($loop_{TMH5\text{-}6}$, Loop 3) (Fig. 3.6B). The three loop cluster connects the electron-transferring peripheral arm to the ion pumping membrane arm

and is strikingly similar in the three complexes (Fig. 3.6B)[1-3,6]. In MBS, Loop 1 via TM15 and TM16 of MbsH' connects to its horizontal helix HL that spans two proton pumps (MbsH and MbsH') (Supplementary Figure 3.4A). Similarly in MBH, Loop 1 connects TM1 and TM2 of MbhI to its shorter helix HL that spans a single proton pump (MbhH). In complex I, Loop 1 and its preceding TM1 of Nqo7 locate the conserved membrane-anchored peripheral module to a different site of the membrane arm via TM2-3 of Nqo7 while the much longer helix HL of Nqo15 that spans three proton pumps (Nqo12, 13 and 14) is similar to MBS and MBH (Supplementary Figure 3.4A). A central charged axis in MBS extending from the three loops across the membrane arm in parallel to helix HL is also found in both complex I and MBH (Fig. 3.3C, Fig. 3.6C)[1-3,6,32]. Clearly, the structural elements in MBH and complex I necessary for energy conservation are maintained in MBS. Therefore, we suggest that Loop1 and its preceding TM are a key structural feature that has been conserved across evolution in order to sustain the fundamental function of coupling the redox reaction in the peripheral arm with ion translocation in the membrane arm.

The peripheral arm of MBS contains a uniquely coordinated [4Fe-4S] cluster

In MBS, the three [4Fe-4S] clusters form an efficient electron transfer pathway to the chamber from Fd (Fig. 3.1C inset)[36]. MbsN coordinates the distal and the medial [4Fe-4S] clusters (relative to the catalytic chamber; Supplementary Figure 3.6A). The proximal (p-)[4Fe-4S] cluster in MBS and complex I is at the top of the hydrophobic chamber (Supplementary Figure 3.6B) but, in stark contrast to that in complex I (and MBH), the MBS p-[4Fe-4S] is coordinated by only three rather than the expected four cysteines (C28, C93 and C123 of MbsJ; Fig. 3.6D).

The different functions of the p-[4Fe-4S] clusters in these enzymes (Fig. 3.5B**)** are determined by a conserved structural motif containing a short N-terminal α-helix, a β-strand, a variable loop with two cysteines and another short α-helix (in MbsJ for MBS complex) (Supplementary Figure 3.6B-C). In MBH and cytosolic [NiFe] hydrogenases[6,37], the two cysteines are two residues apart and ideally positioned to both coordinate the proximal cluster, which donates electrons to the NiFe-catalytic site. In complex I, the two cysteines (C45 and C46 in Nqo6) are adjacent to each other enabling sequential dissociation upon proximal cluster reduction, which has been proposed to facilitate electron and proton transfer to the quinone although this is under debate [16,38,39]. In MBS, this structural motif is three residues shorter than it is in MBH, leaving one of the cysteines (MbsJ C25) no longer able to participate in cluster coordination (Fig. 3.6D, Supplementary Figure 3.6C). Hence, one iron atom of the p-4Fe-4S] cluster in MBS has non-cysteinyl coordination (Supplementary Figure 3.2J**)** and therefore catalytic potential. Besides the three [4Fe-4S] clusters, MBH has an additional proton-reducing [NiFe]-site, which is coordinated by four cysteines of MbhL (Supplementary Figure 3.6D)[6,40]. Of these four cysteines, two are not present in MBS, leaving the two conserved residues (C85 and C385 in MbsL) adjacent to the proximal cluster (Fig. 3.7A). Complex I has lost all four, supporting the stepwise evolution of MBS and complex I by sequential loss of the four cysteines coordinating the [NiFe] center in MBH[31,41].

In MBS, two potential polysulfide-reducing sites are close (~12 Å) to the p-[4Fe-4S] cluster: MbsJ C25 and MbsL C85/C385 (Fig. 7A). However, they are not involved in catalysis as the C25A MbsJ and the C85A/C385A MbsL mutant enzymes had comparable catalytic activities using the model substrate dimethyltrisulfide (DMTS) to that of the wild-

type (WT) enzyme (1.8 ± 0.4 units/mg) (Fig. 3.7B). Cluster interconversion was used to provide evidence that the p-[4Fe-4S] cluster of MBS is itself reducing polysulfide, and doing so with a specific role for its unique non-cysteinyl coordinated Fe atom. The WT-enzyme was treated with potassium ferricyanide, a well-established procedure to remove non-cysteinyl coordinated Fe atom from an [4Fe-4S] cluster to generate a [3Fe-4S] cluster[21]. This caused an ~98% loss of activity (Fig. 3.7B). Subsequently incubating the enzyme under reducing conditions with ferrous iron, conditions that are known to restore the [4Fe-4S] cluster from a [3Fe-4S] cluster, the MBS activity was restored to its original value (Fig. 3.7B).

Further evidence for the proposed catalytic p-[4Fe-4S] cluster came from EPR spectroscopy. MBS from S^0-grown cells gave rise to an intense free radical EPR signal (g = 2.00) unaffected by chemical reduction (Supplementary Figure 3.7A) but this was a purification artifact because the enzyme from non-S^0 grown cells (in which transcription of the genes encoding MBS was controlled by a non-regulated promoter) did not exhibit this EPR signal (Supplementary Figure 3.7B). Chemical reduction of MBS did lead to the appearance of a broad EPR signal (g ~ 1.94), consistent with three interacting and reduced [4Fe-4S] clusters (Supplementary Figure 3.7B). After treatment with excess ferricyanide, the inactive enzyme (Fig. 3.7B) exhibited a complex EPR signal indicative of an oxidized S=1/2 $[3Fe\text{-}4S]^+$ cluster (g = 2.09, Supplementary Figure 3.7C)[21], supporting the conclusion that the p-[4Fe-4S] cluster is catalytic and that activity is reversibly lost upon removal of its unique iron. Importantly, chemically-reduced *P. furiosus* MBH gave rise to an EPR signal (Supplementary Figure 3.7D) similar to that of reduced MBS (Supplementary Figure 3.7B), but when treated with ferricyanide under the same

conditions used for MBS, no activity was lost and the MBH sample was EPR silent, consistent with the presence of only oxidized [4Fe-4S] clusters (Supplementary Figure 3.7E). Unlike MBS, the p-[4Fe-4S] cluster of MBH is only involved in electron transfer and has full cysteinyl coordination, hence it is not susceptible to inactivation due to iron loss and oxidative cluster conversion.

The proximal [4Fe-4S] cluster uses a novel, ancestral mechanism for sulfur reduction

Reduction of polysulfide by the p-[4Fe-4S] cluster in the hydrophobic pocket of MBS (Fig. 3.7A) is the first example in a biological system of reduction of an inorganic disulfide bond without the release of H_2S (Equations 2 and 3, c.f. Equation 5). Three types of enzymes use iron-sulfur clusters to indirectly facilitate disulfide bond cleavage; heterodisulfide reductase[42], hydrogenase processing protein HydD[43] and ferredoxin thioredoxin reductase (FTR)[44]. Based in part on FTR, we propose a new mechanism for reduction of an internal disulfide (which could be either inorganic or organic) by MBS (Fig. 3.7C). The unique Fe atom of its p-$[4Fe\text{-}4S]^{2+}$ cluster binds polysulfide (S_n^{2-}), accepts an electron from the medial (m-)$[4Fe\text{-}4S]^{1+}$ cluster (Fig. 3.1C) and catalyzes the two electron reduction of an internal disulfide, generating two smaller polysulfides (S_{n-x}^{2-} and S_x^{2-}) and the superoxidized form of p-$[4Fe\text{-}4S]^{3+}$. As in FTR, reduction of the p-$[4Fe\text{-}4S]^{2+}$ cluster actually leads to its superoxidation because two electrons are used to reduce the disulfide. Moreover, the cluster must be in the 3+ (rather than 2+) state to bind the two product polysulfides at the unique Fe site (Fig. 3.7C). The catalytic cycle is completed by reduction of p-$[4Fe\text{-}4S]^{3+}$ by a second electron from m-$[4Fe\text{-}4S]^{1+}$ (after its reduction by the distal $[4Fe\text{-}4S]^{1+}$ cluster) and release of the two smaller polysulfides. This is the simplest mechanism yet proposed for reduction of an S-S bond in either an inorganic or organic sulfide and is the first not

requiring either protons or amino acid residues[42-44]. This reaction is clearly of fundamental significance in iron and sulfur-rich hydrothermal vent environments of the early earth and possibly in the origin of early life[21], as well as in the subsequent evolution and expansion of iron-sulfur cluster functionality in the diverse array of modern day iron-sulfur proteins[22,45].

That catalysis by MBS does not require water or protons (Fig. 3.7C) is consistent with a highly hydrophobic pocket and the absence in MbsL of the well-defined proton transfer pathway to the NiFe site found in MbhL and other hydrogenases[6]. The requirement for binding two polysulfides (Fig. 3.7B) is superoxidation of the p-[4Fe-4S] cluster (3+), which is facilitated by the hydrophobic site, analogous to superoxidation of hydrophobic [4Fe-4S] clusters in high potential iron sulfur proteins (HiPIPs)[46]. The spontaneous breakdown of tri- and disulfides to release H_2S does require protons (Equation 4) and must occur in the cytoplasm rather than the hydrophobic catalytic site (Fig. 3.7C). The di- and trisulfides produced by MBS do not generate H_2S (or HS^-), are stable in the hydrophobic pocket (where there are no protons or water), and H_2S is only generated when they are released from the enzyme (Fig. 3.7C).

Discussion

The standard state ΔG (pH 7.0) of the electron transfer reactions for MBS (41 kJ/mol/$2e^-$) is more than twice that available to MBH (12 kJ/mol/$2e^-$), and half of that available to complex I (81 kJ/mol/$2e^-$)[9], consistent with pumping of two, one and four protons, respectively[1,2,7,8,47]. The MBS structure confirms that the transduction of redox energy into the spatially separated translocation of ions involves the three loop cluster[1-3,31,48] and a central charged axis[1-3,7,32] (Fig. 3.6B-C), all highly conserved across evolution. The

proposed MBS mechanism also shows that there are key fundamental differences in spite of a common overall means of energy transduction. In MBS, oxidation of the reduced m-[4Fe-4S]$^{1+}$ cluster leads to superoxidation of the oxidized p-[4Fe-4S]$^{2+}$ cluster (2+/3+ redox couple) but in MBH and complex I to reduction of the oxidized p-[4Fe-4S]$^{1+}$ cluster (2+/1+ redox couple; Fig. 3.7C). Hence loss of the NiFe site of an ancestral MBH through evolution generated a highly hydrophobic cavity enabling both MBS and complex I to use the p-[4Fe-4S] cluster to directly interact with and reduce hydrophobic substrates, albeit using different charge states of the cluster (Fig. 3.7D).

It is not clear how a change in the redox status of the m-[4Fe-4S] cluster is ultimately coupled to a change in the dynamics of the three loop cluster, nor how the different amounts of free energy released (12 – 81 kJ/mol/2e$^-$) lead to corresponding differences in the proton motive force that is generated (1 - 4 protons). It is interesting to speculate that MBS might conserve more (or less energy) if one proton pump (MbsH' or equivalent, see Fig. 3.3C) were added (or inactivated, by mutagenesis) and that the cell yield of *P. furiosus* growing on S^0 would be correspondingly higher (or lower). Such experiments are in progress. On a more fundamental level, the question yet to be answered is, as illustrated in Fig. 3.7D, how does m-[4Fe-4S]$^{1+}$ oxidation coupled to a change in the conformation of the three loop cluster lead to the conservation of different quantities of energy in these three types of respiratory complex? In any event, the simple aprotic and abiotic catalytic mechanism of S-S bond reduction by MBS might be a modern remnant of an iron-sulfur world[21] as well as the precursor to more complex mechanisms involving iron sulfur clusters[42-44] and those now found in the aerobic world, such as the reduction of quinones by complex I.

Methods

Purification of MBS

The MBS holoenzyme (S-MBS) was solubilized and purified anaerobically from *Pyrococcus furiosus* strain MW0491, in which a His_9-tag had been engineered at the N terminus of the MbhJ subunit[19].. Frozen cells were lysed in 25 mM sodium phosphate, pH 7.5, containing 1 mM DTT and 50 μg/ml DNase I (5 mL per gram of frozen cells). After stirring for one hour, the cell-free extract was centrifuged at 100,000 x g for one hour. The supernatant was removed and the membranes were washed twice using 50 mM EPPS buffer, pH 8.0, containing 5 mM $MgCl_2$, 50 mM NaCl, 10% (v/v) glycerol, 1 mM DTT and 0.1 mM PMSF. The membrane pellet was collected by ultracentrifugation at 100,000 x g for one hour after each wash step. The washed membranes were resuspended in 50 mM Tris-HCl, pH 8.0, containing 5 mM $MgCl_2$, 50 mM NaCl, 5% (v/v) glycerol, 1 mM DTT, and 0.1 mM PMSF. MBS was solubilized by adding n-dodecyl-β-D-maltoside (DDM, Inalco) to 3% (w/v) followed by incubation at 4 °C for 16 hours. The solubilized membranes were centrifuged at 100,000 x g for 1 hour. The supernatant was applied to a 5 mL His-Trap crude FF Ni-NTA column (GE Healthcare) while diluting it 10-fold with buffer A (25 mM sodium phosphate, 300 mM NaCl, pH 7.5, containing 1 mM DTT and 0.03% DDM). The column was washed with 10 column volumes of buffer A and the bound protein was eluted with a 20-column volume gradient from 0 to 100% buffer B (buffer A containing 500 mM imidazole). The eluted protein was further purified by applying it to a 1-mL His-Trap HP Ni-NTA column (GE Healthcare) while diluting it 5-fold with buffer A. A 30-column volume gradient from 0 to 100% buffer B was used to elute the bound protein. The MBS sample was concentrated and further purified using a Superose 6 10/300

GL column (GE Healthcare) equilibrated with 50 mM Tris-HCl, pH 8.2, containing 300 mM NaCl, 2 mM sodium dithionite, and 0.03% DDM.

P. furiosus strain construction

The strains used in this study are summarized in Supplementary Table 3.3. The genetically-tractable *P. furiosus* strain COM1 was used for the genetic manipulation of MBS[49]. An insertion cassette was amplified using overlapping PCR[50]. The upstream flanking region (UFR), which also contained the selection marker (P_{gdh}-*pyrF*) and the promoter of the gene encoding the S-layer protein (P_{slp}), and the downstream flanking region (DFR), were amplified from MW0567 gDNA. Mutagenesis was carried out using site-directed mutagenesis, with primers designed to amplify the MbsJ^{C25A} mutation. The primers used are listed in Supplementary Table 3.4**.** The fragments were assembled using overlapping PCR and the insertion cassette was transformed into the intergenic space between PF0265 and PF0266 of MW0011. The transformants were grown as previously described[49] and the PCR-confirmed colonies were sequence verified using Sanger sequencing (Genewiz).

Purification of C-MBS, activity assays, and EPR methods

The three C-MBS subcomplexes (WT, MbsL$^{C85A/C385A}$, MbsJ^{C25A}) were purified anaerobically as described previously[19]. Frozen cells were lysed in 25 mM sodium phosphate, pH 7.5, containing 1 mM DTT and 50 µg/µL DNase I (5 mL per gram of frozen cells). After stirring for one hour, the cell-free extract was centrifuged at 100,000 x g for one hour. The supernatant was applied directly to a 5 mL His-Trap FF Ni-NTA column (GE Healthcare) by diluting it 10-fold with 25 mM sodium phosphate, pH 7.5 containing

300 mM NaCl and 1 mM DTT (Buffer C). The column was equilibrated with Buffer C before loading the sample. The column was washed with 5 column volumes of Buffer C and the bound protein was eluted with a 20-column volume gradient from 0 to 100% Buffer D (Buffer C containing 500 mM imidazole).

All activity assays were carried out at 80 °C using anaerobic sealed cuvettes as described previously[19]. The dimethyl trisulfide (DMTS) reduction assay used a 2 mL reaction mixture containing 100 mM 3-(N-morpholino) propanesulfonic acid (MOPS), pH 7.5, and 150 mM NaCl. After pre-heating to 80 °C, 1 mM methyl viologen reduced by titanium citrate and 2 mM DMTS were added and the reaction was initiated by the addition of enzyme. For inactivation by cluster conversion, the enzyme (2 mg/mL in 25 mM sodium phosphate, pH 7.5) was incubated anaerobically with potassium ferricyanide (1 mM) for ~90 hr at room temperature. The sample was then buffer exchanged to remove excess ferricyanide before measuring activity. To activate the enzyme, a mixture of sodium dithionite (1 mM) and $FeCl_3$ (1mM) were added and after ~90 hrs at room temperature, the sample was buffer exchanged to remove the excess reagent. Enzyme activity was measured by the reduction of DMTS by monitoring the oxidation of methyl viologen at 600 nm (ε = 8.25 mM^{-1} cm^{-1}) as previously described[19]. One unit of activity is defined as 1 µmol of DMTS reduced per min.

All samples for spectroscopic studies were prepared under strictly anaerobic conditions. X-band (~9.6 GHz) EPR spectra were recorded using a Bruker EMXplus CW EPR spectrometer controlled with a Bruker PremiumX Ultra low noise microwave bridge, equipped with a cryogen free ColdEdge stinger system and a Lakeshore temperature controller.

Cryo-EM analysis and data acquisition

MBS was purified using detergent DDM and was concentrated to approximately 5 mg/ml. Cryo-EM grids were prepared under aerobic condition and the processes took 20 – 30 min (MBS in air has a half-life of 19 hours[19]). Briefly, three-microliter aliquots of the sample were applied to glow-discharged Quantfoil R 1.2/1.3 gold grids (300 mesh). The grids were blotted for 3 s at 10 °C with 100% humidity and were flash-frozen in liquid ethane using an FEI Vitrobot Mark IV device. Cryo-EM data were recorded on a K2 camera positioned post a GIF quantum energy filter in a 300 kV FEI Titan Krios electron microscopy. Two datasets were automatically collected with Serial EM 3.7beta and FEI EPU software package, respectively, containing 8352 and 6355 movies respectively. Micrographs were recorded in counting mode at a nominal magnification of 130,000× with a pixel size of 1.03 Å on sample. Defocus values varied from -1.1 μm to -3 μm. The dose rate was 10 electrons per pixel per second. A total exposure of 6 s was dose-fractionated into 30 sub-frames, resulting in a total accumulated dose of 52 electrons per $Å^2$.

Image processing

The two datasets collected on Titan Krios were processed using similar strategy. Dose-fractionated movies with a physical pixel size of 1.03 Å were motion-corrected and dose-weighted with MotionCor2 1.1[51,52]. Contrast transfer function (CTF) parameter for individual micrograph was estimated by CTFFIND4.1.10[53]. Further processing steps were carried out using RELION-3.0[54]. For each dataset, a small set of particles were manually picked and were subjected to 2D classification. This generated templates for further reference-based automatic particle picking. Particle sorting and reference-free 2D classification were applied to the auto-picked particles for the removal of bad particles,

resulting in 676,320 and 667,428 particles from the two respective datasets. Further 3D classification was performed on these cleaned-up particles using an ab initio map generated by cryoSPARC v2 as the initial model[55]. For each dataset, three of four 3D classes were combined to get 467,320 and 419,868 good particles, respectively. Those were subjected to another round of 3D classification. One 3D class from each dataset with best density features were combined. The combined dataset (203,673 particles) were used for 3D auto-refinement following CTF refinement, resulting in a map with an overall resolution of 4.0 Å when 2-fold symmetry was applied. We note that most regions, particularly in the peripheral arm and the proximal membrane module, are of substantially better resolution in the range of 3.0 to 3.5 Å. Some strategies including applying C1 symmetry, masking out detergent micelle or expanding the symmetry failed to improve the map. We therefore reasoned that the low overall resolution (4 Å) may be due to the partially flexible distal membrane region. The resolution of the reconstructed map was estimated based on the gold-standard Fourier shell correlation 0.143 criterion[56]. The final map was corrected for the modulation transfer function of the detector and sharpened by applying a negative B-factor, estimated by the post-processing procedure in RELION-3.0. Estimate of Local resolution distribution was calculated using ResMap 1.1.5[57].

Model building and refinement

The initial models of the distal module (MbsA-C, MbsE TMH3-6) and membrane-anchored hydrogenase module (MbsJ-N) were generated with the SWISS-MODEL server [58] using the structure of *P. furiosus* MBH complex (PDB ID 6CFW) as the template. The initial model of the proximal module (MbsD, MbsE TMH3-6, MbsG, MbsH and MbsH') were generated using the structure of *T. thermophilus* complex I as a template (PDB ID

4HEA). These models were individually rigid-body docked into the 3D density map using the Fit-in-map function in Chimera 1.8[59]. These fitted models were improved by manual adjustments and rebuilding in Coot 0.8.9[60]. The rebuilding process was aided by the good density features of α helices and many bulky residues such as Phe, Trp, Tyr and Arg. The clusters within the peripheral arm were modelled based on their electron densities and also the homology of cluster-coordinating subunits with complex I and MBH. The real-space refinement of the MBS complex model against the cryo-EM map was performed using the phenix.real_space_refine in PHENIX 1.15[61]. MolProbity 4.1 (Duke University) was used to assess the final model[62]. Chimera and PyMOL 1.8 (Schrödinger, LLC.) were used to prepare the Figures. Statistics of the 3D reconstruction and model refinement were provided in Supplementary Table 3.1. Since all the subunits of Mrp antiporters have their counterparts in MBS (Supplementary Table 3.2), the structure of *B. subtilis* Mrp antiporter was modeled based on the MBS structure using the SWISS-MODEL server[58].

Data Availability

The accession number for the atomic coordinates reported in this paper is PDB ID 6U8Y [https://doi.org/10.2210/pdb6U8Y/pdb]. The accession number for the EM density map reported in this paper is EMD-20692 [https://www.ebi.ac.uk/pdbe/entry/emdb/EMD-20692]. Source data are provided with this paper. Other data are available from the corresponding authors upon reasonable request.

Acknowledgments

Cryo-EM images were collected at the David Van Andel Advanced Cryo-Electron Microscopy Suite in the Van Andel Research Institute. We thank Soshawn A. Blair,

Sydney Hallenbeck, and Michael K. Johnson of the University of Georgia for helpful discussions on the catalytic mechanism of MBS and for assistance in running EPR spectroscopy. This work was funded by grants from the Division of Chemical Sciences, Geosciences and Biosciences, Office of Basic Energy Sciences of the U.S. Department of Energy (DOE; DE-SC0020085 to H.L. and DE-FG02-95ER20175 to M.W.W.A.).

Author Contributions

H.L. and M.W.W.A. conceived and designed experiments. H.Y., D.K.H., G.J.S., C.-H.W., X.M., G.Z. performed experiments. H.Y., D.K.H, G.J.S., M.W.W.A., and H.L. analyzed the data. H.Y., D.K.H., H.L., and M.W.W.A. wrote the manuscript.

Competing Interests

The authors declare no competing interests.

References

1 Baradaran, R., Berrisford, J. M., Minhas, G. S. & Sazanov, L. A. Crystal structure of the entire respiratory complex I. *Nature* **494**, 443-448 (2013).

2 Zickermann, V. *et al.* Structural biology. Mechanistic insight from the crystal structure of mitochondrial complex I. *Science* **347**, 44-49 (2015).

3 Zhu, J., Vinothkumar, K. R. & Hirst, J. Structure of mammalian respiratory complex I. *Nature* **536**, 354-358 (2016).

4 Fiedorczuk, K. *et al.* Atomic structure of the entire mammalian mitochondrial complex I. *Nature* **538**, 406-410 (2016).

5 Guo, R., Zong, S., Wu, M., Gu, J. & Yang, M. Architecture of Human Mitochondrial Respiratory Megacomplex I2III2IV2. *Cell* **170**, 1247-1257 e1212 (2017).

6 Yu, H. *et al.* Structure of an ancient respiratory system. *Cell* **173**, 1636-1649 e1616 (2018).

7 Sazanov, L. A. A giant molecular proton pump: structure and mechanism of respiratory complex I. *Nat Rev Mol Cell Biol* **16**, 375-388 (2015).

8 Hirst, J. Mitochondrial complex I. *Annu Rev Biochem* **82**, 551-575 (2013).

9 Schut, G. J. *et al.* The role of geochemistry and energetics in the evolution of modern respiratory complexes from a proton-reducing ancestor. *Biochim Biophys Acta* **1857**, 958-970 (2016).

10 Letts, J. A. & Sazanov, L. A. Clarifying the supercomplex: the higher-order organization of the mitochondrial electron transport chain. *Nat Struct Mol Biol* **24**, 800-808 (2017).

11 Agip, A. A., Blaza, J. N., Fedor, J. G. & Hirst, J. Mammalian respiratory Complex I through the lens of cryo-EM. *Annual review of biophysics* (2019).

12 Sapra, R., Bagramyan, K. & Adams, M. W. A simple energy-conserving system: proton reduction coupled to proton translocation. *Proc Natl Acad Sci U S A* **100**, 7545-7550 (2003).

13 Mayer, F. & Muller, V. Adaptations of anaerobic archaea to life under extreme energy limitation. *FEMS Microbiol Rev* **38**, 449-472 (2014).

14 Kim, Y. J. *et al.* Formate-driven growth coupled with H(2) production. *Nature* **467**, 352-355 (2010).

15 Lim, J. K., Mayer, F., Kang, S. G. & Muller, V. Energy conservation by oxidation of formate to carbon dioxide and hydrogen via a sodium ion current in a hyperthermophilic archaeon. *Proc Natl Acad Sci U S A* **111**, 11497-11502 (2014).

16 Laughlin, T. G., Bayne, A. N., Trempe, J. F., Savage, D. F. & Davies, K. M. Structure of the complex I-like molecule NDH of oxygenic photosynthesis. *Nature* **566**, 411-414 (2019).

17 Nisbet, E. G. & Sleep, N. H. The habitat and nature of early life. *Nature* **409**, 1083-1091 (2001).

18 McTernan, P. M. *et al.* Intact functional fourteen-subunit respiratory membrane-bound [NiFe]-hydrogenase complex of the hyperthermophilic archaeon Pyrococcus furiosus. *J Biol Chem* **289**, 19364-19372 (2014).

19 Wu, C. H., Schut, G. J., Poole, F. L., 2nd, Haja, D. K. & Adams, M. W. W. Characterization of membrane-bound sulfane reductase: A missing link in the

evolution of modern day respiratory complexes. *J Biol Chem* **293**, 16687-16696 (2018).

20 Schut, G. J., Bridger, S. L. & Adams, M. W. Insights into the metabolism of elemental sulfur by the hyperthermophilic archaeon Pyrococcus furiosus: characterization of a coenzyme A- dependent NAD(P)H sulfur oxidoreductase. *J Bacteriol* **189**, 4431-4441 (2007).

21 Conover, R. C. *et al.* Spectroscopic characterization of the novel iron-sulfur cluster in Pyrococcus furiosus ferredoxin. *J Biol Chem* **265**, 8533-8541 (1990).

22 Schicho, R. N., Ma, K., Adams, M. W. & Kelly, R. M. Bioenergetics of sulfur reduction in the hyperthermophilic archaeon Pyrococcus furiosus. *J Bacteriol* **175**, 1823-1830 (1993).

23 Enemark, J. H. & Cosper, M. M. Molybdenum enzymes and sulfur metabolism. *Metal ions in biological systems* **39**, 621-654 (2002).

24 Jormakka, M. *et al.* Molecular mechanism of energy conservation in polysulfide respiration. *Nat Struct Mol Biol* **15**, 730-737 (2008).

25 Efremov, R. G. & Sazanov, L. A. The coupling mechanism of respiratory complex I - a structural and evolutionary perspective. *Biochim Biophys Acta* **1817**, 1785-1795 (2012).

26 Hedderich, R. Energy-converting [NiFe] hydrogenases from archaea and extremophiles: ancestors of complex I. *J Bioenerg Biomembr* **36**, 65-75 (2004).

27 Schut, G. J., Boyd, E. S., Peters, J. W. & Adams, M. W. The modular respiratory complexes involved in hydrogen and sulfur metabolism by heterotrophic

hyperthermophilic archaea and their evolutionary implications. *FEMS Microbiol Rev* **37**, 182-203 (2013).

28 Di Luca, A., Gamiz-Hernandez, A. P. & Kaila, V. R. I. Symmetry-related proton transfer pathways in respiratory complex I. *Proc Natl Acad Sci U S A* **114**, E6314-E6321 (2017).

29 Kaila, V. R. I. Long-range proton-coupled electron transfer in biological energy conversion: towards mechanistic understanding of respiratory complex I. *Journal of the Royal Society, Interface* **15** (2018).

30 Euro, L., Belevich, G., Verkhovsky, M. I., Wikstrom, M. & Verkhovskaya, M. Conserved lysine residues of the membrane subunit NuoM are involved in energy conversion by the proton-pumping NADH:ubiquinone oxidoreductase (Complex I). *Biochim Biophys Acta* **1777**, 1166-1172 (2008).

31 Brandt, U. Adaptations of an ancient modular machine. *Science* **363**, 230-231 (2019).

32 Agip, A. A. *et al.* Cryo-EM structures of complex I from mouse heart mitochondria in two biochemically defined states. *Nat Struct Mol Biol* **25**, 548-556 (2018).

33 Efremov, R. G. & Sazanov, L. A. Structure of the membrane domain of respiratory complex I. *Nature* **476**, 414-420 (2011).

34 Morino, M. *et al.* Single site mutations in the hetero-oligomeric Mrp antiporter from alkaliphilic Bacillus pseudofirmus OF4 that affect Na+/H+ antiport activity, sodium exclusion, individual Mrp protein levels, or Mrp complex formation. *J Biol Chem* **285**, 30942-30950 (2010).

35 Steiner, J. & Sazanov, L. Structure and mechanism of the Mrp complex, an ancient cation/proton antiporter. *Elife* **9** (2020).

36 Page, C. C., Moser, C. C., Chen, X. & Dutton, P. L. Natural engineering principles of electron tunnelling in biological oxidation-reduction. *Nature* **402**, 47-52, doi:10.1038/46972 (1999).

37 Volbeda, A. *et al.* Structure of the [NiFe] hydrogenase active site: Evidence for biologically uncommon Fe ligands. *Journal of the American Chemical Society* **118** (1996).

38 Schuller, J. M. *et al.* Structural adaptations of photosynthetic complex I enable ferredoxin-dependent electron transfer. *Science* **363**, 257-260 (2019).

39 Berrisford, J. M. & Sazanov, L. A. Structural basis for the mechanism of respiratory complex I. *J Biol Chem* **284**, 29773-29783 (2009).

40 Fontecilla-Camps, J. C., Volbeda, A., Cavazza, C. & Nicolet, Y. Structure/function relationships of [NiFe]- and [FeFe]-hydrogenases. *Chem Rev* **107**, 4273-4303 (2007).

41 Kashani-Poor, N., Zwicker, K., Kerscher, S. & Brandt, U. A central functional role for the 49-kDa subunit within the catalytic core of mitochondrial complex I. *J Biol Chem* **276**, 24082-24087 (2001).

42 Wagner, T., Koch, J., Ermler, U. & Shima, S. Methanogenic heterodisulfide reductase (HdrABC-MvhAGD) uses two noncubane [4Fe-4S] clusters for reduction. *Science* **357**, 699-703 (2017).

43 Watanabe, S. *et al.* Crystal structures of [NiFe] hydrogenase maturation proteins HypC, HypD, and HypE: Insights into cyanation reaction by thiol redox signaling. *Mol Cell* **27**, 29-40 (2007).

44 Walters, E. M. *et al.* Role of histidine-86 in the catalytic mechanism of ferredoxin:thioredoxin reductase. *Biochemistry* **48**, 1016-1024 (2009).

45 Torres-Bacete, J., Nakamaru-Ogiso, E., Matsuno-Yagi, A. & Yagi, T. Characterization of the NuoM (ND4) subunit in Escherichia coli NDH-1: conserved charged residues essential for energy-coupled activities. *J Biol Chem* **282**, 36914-36922 (2007).

46 Dey, A. *et al.* Solvent tuning of electrochemical potentials in the active sites of HiPIP versus ferredoxin. *Science* **318**, 1464-1468 (2007).

47 Galkin, A., Drose, S. & Brandt, U. The proton pumping stoichiometry of purified mitochondrial complex I reconstituted into proteoliposomes. *Biochim Biophys Acta* **1757** (2006).

48 Cabrera-Orefice, A. *et al.* Locking loop movement in the ubiquinone pocket of complex I disengages the proton pumps. *Nature communications* **9**, 4500 (2018).

49 Lipscomb, G. L. *et al.* Natural competence in the hyperthermophilic archaeon Pyrococcus furiosus facilitates genetic manipulation: construction of markerless deletions of genes encoding the two cytoplasmic hydrogenases. *Appl Environ Microbiol* **77**, 2232-2238 (2011).

50 Bryksin, A. V. & Matsumura, I. Overlap extension PCR cloning: a simple and reliable way to create recombinant plasmids. *Biotechniques* **48**, 463-465 (2010).

51 Grant, T. & Grigorieff, N. Measuring the optimal exposure for single particle cryo-EM using a 2.6 A reconstruction of rotavirus VP6. *Elife* **4**, e06980 (2015).

52 Zheng, S. Q. *et al.* MotionCor2: anisotropic correction of beam-induced motion for improved cryo-electron microscopy. *Nat Methods* **14**, 331-332 (2017).

53 Rohou, A. & Grigorieff, N. CTFFIND4: Fast and accurate defocus estimation from electron micrographs. *J Struct Biol* **192**, 216-221 (2015).

54 Kimanius, D., Forsberg, B. O., Scheres, S. H. & Lindahl, E. Accelerated cryo-EM structure determination with parallelisation using GPUs in RELION-2. *Elife* **5** (2016).

55 Punjani, A., Rubinstein, J. L., Fleet, D. J. & Brubaker, M. A. cryoSPARC: algorithms for rapid unsupervised cryo-EM structure determination. *Nat Methods* **14**, 290-296 (2017).

56 Rosenthal, P. B. & Henderson, R. Optimal determination of particle orientation, absolute hand, and contrast loss in single-particle electron cryomicroscopy. *J Mol Biol* **333**, 721-745 (2003).

57 Kucukelbir, A., Sigworth, F. J. & Tagare, H. D. Quantifying the local resolution of cryo-EM density maps. *Nat Methods* **11**, 63-65 (2014).

58 Arnold, K., Bordoli, L., Kopp, J. & Schwede, T. The SWISS-MODEL workspace: a web-based environment for protein structure homology modelling. *Bioinformatics* **22**, 195-201 (2006).

59 Pettersen, E. F. *et al.* UCSF Chimera--a visualization system for exploratory research and analysis. *J Comput Chem* **25**, 1605-1612 (2004).

60 Emsley, P., Lohkamp, B., Scott, W. G. & Cowtan, K. Features and development of Coot. *Acta Crystallogr D Biol Crystallogr* **66**, 486-501 (2010).

61 Adams, P. D. *et al.* PHENIX: a comprehensive Python-based system for macromolecular structure solution. *Acta Crystallogr D Biol Crystallogr* **66**, 213-221 (2010).

62 Chen, V. B. *et al.* MolProbity: all-atom structure validation for macromolecular crystallography. *Acta Crystallogr D Biol Crystallogr* **66**, 12-21 (2010).

Figure 3.1.

Overall structure of the *P. furiosus* MBS complex. **(A)** Schematic comparison of *P. furiosus* MBH and MBS complexes, both generating a Na^+ gradient for ATP synthesis. (**B)** Side (left) and top (right) views of the cryo-EM map of the dimeric MBS complex, segmented and colored by subunits. (**C)** The front (left) and back (right) view of the atomic model of an MBS monomeric complex. Individual subunits are colored as in (B). Inset in the right panel: a chain of three [4Fe-4S] clusters in the peripheral arm, with the center-to-center and edge-to-edge distances (in brackets) between metal sites indicated in Å.

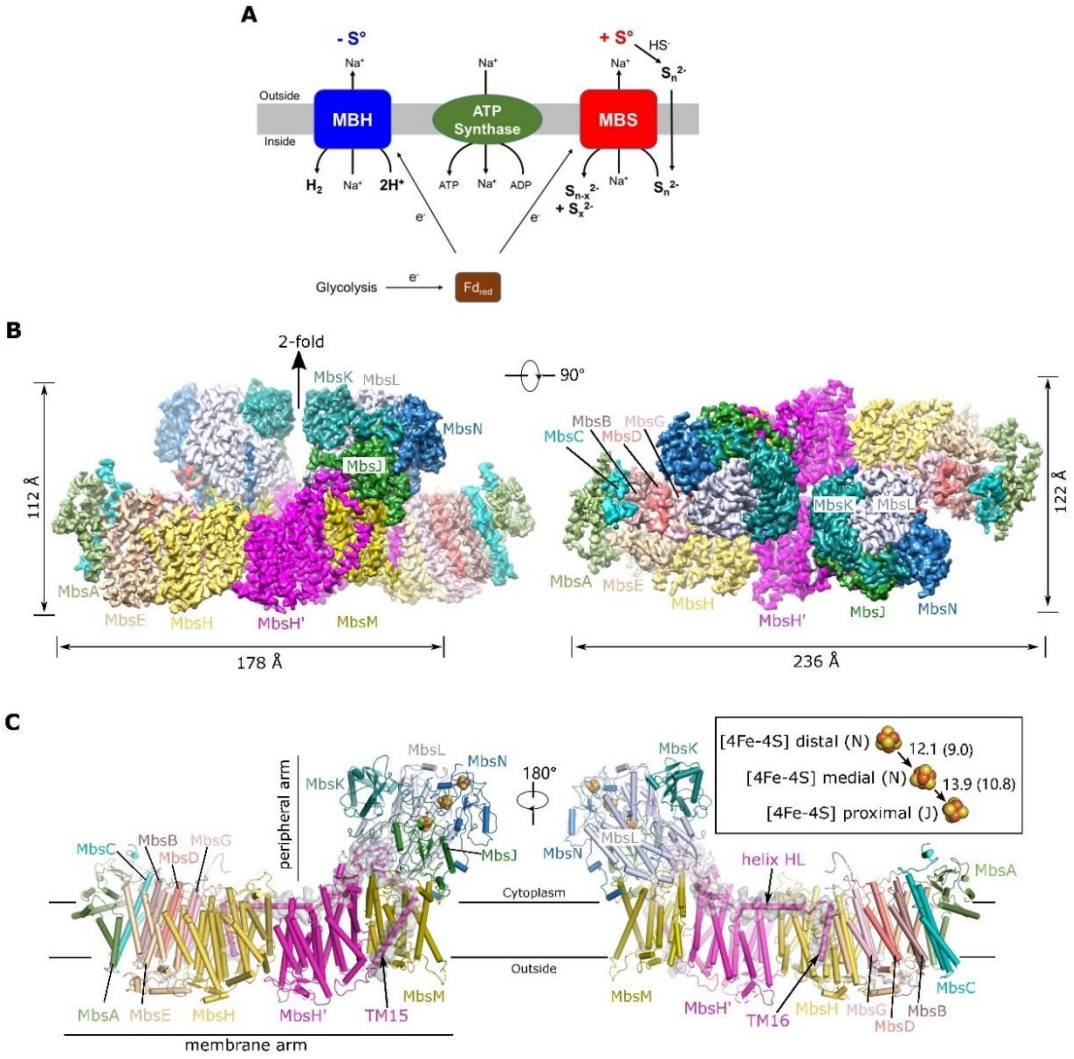
A
- S°
+ S°
HS⁻
Na⁺
Outside
Inside
MBH
ATP Synthase
MBS
H₂
2H⁺
ATP
ADP
e⁻
Glycolysis
Fd red
B
2-fold
90°
MbsK
MbsL
MbsN
MbsJ
MbsB
MbsG
MbsC
MbsD
MbsA
MbsE
MbsH
MbsH'
MbsM
112 Å
178 Å
122 Å
236 Å
C
180°
peripheral arm
membrane arm
[4Fe-4S] distal (N)
12.1 (9.0)
[4Fe-4S] medial (N)
13.9 (10.8)
[4Fe-4S] proximal (J)
Cytoplasm
Outside
helix HL
TM15
TM16

Figure 3.2.

The architecture of the dimeric MBS complex. **(A)** Side (left) and top cytoplasmic views (right) of an MBS monomer. The central proximal membrane module is flanked by distal membrane module and the membrane-anchored peripheral module, which are further highlighted by transparent surface views. (**B**) A top view showing the assembly of the dimeric MBS complex with the three different modules indicated as in **A**. (**C**) A zoomed view of the dashed rectangle in **B**. The dimer interface is composed of two regions, one involving the Helix HL of MbsH' (dashed blue box) and the other involving the elongated C-terminal tail of MbsD (dashed red box). (**D**) A close-up view of the dashed blue box in **C**. (**E**) A close-up view of the dashed red box in **C**. Residues contributing to the dimer interface are shown as sticks in **D** and **E**.

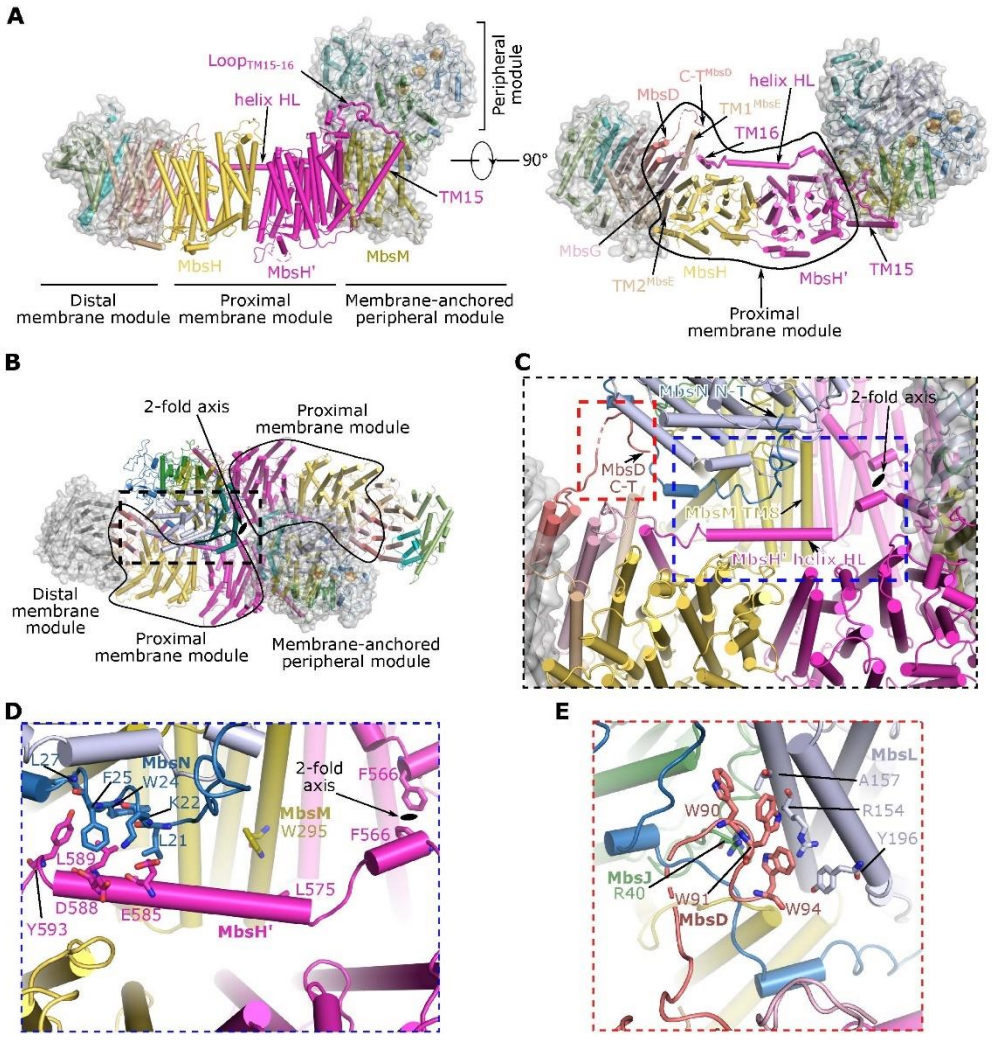
A
Loop$_{TM15-16}$
helix HL
Peripheral module
TM15
MbsH
MbsH'
MbsM
90°
C-T^{MbsD}
MbsD
TM1^{MbsE}
helix HL
TM16
MbsG
TM2^{MbsE}
MbsH
MbsH'
TM15
Distal membrane module
Proximal membrane module
Membrane-anchored peripheral module
Proximal membrane module
B
2-fold axis
Proximal membrane module
Distal membrane module
Proximal membrane module
Membrane-anchored peripheral module
C
MbsN N-T
2-fold axis
MbsD C-T
MbsM TM8
MbsH' helix HL
D
MbsN
F25
W24
K22
L21
2-fold axis
F566
MbsM
W295
F566
L589
L575
D588
E585
Y593
MbsH'
E
MbsL
A157
W90
R154
Y196
MbsJ
R40
W91
W94
MbsD

Figure 3.3

Assembly of the modular architecture of MBS and comparison with complex I and MBH. **(A)** Complex I (*T. thermophilus*; PDB ID 4HEA) is lined up with MBS and MBH (*P. furiosus*; PDB ID 6CFW) via their respective proton-pumping subunit Nqo14, MbsH and MbhH. The alignment detail is shown in Figure S3.4. The complexes are shown separately for clarity. All complexes have a similar peripheral arm (dashed outline) anchored either to the left end (complex I) or to the right end (MBS and MBH) of their respective membrane arm. Complex I has 3, MBS 2, and MBH 1 H^+-pumping subunits. MBS and MBH, but not complex I, have a Na^+ translocation module. (**B)** Superimposition of the two antiporter-like subunits of MBS (MbsH, MbsH') and complex I (Nqo14, Nqo13), by aligning MbsH with Nqo14 as in (**A**). Top, side view with complex I Nqo12 TMH1-14 hidden; bottom, top view with complex I Nqo12 TMH1-14 shown as cartoon and marked by the transparent surface. Note that the length of helix HL is evolved to match the number of antiporter-like subunits present in MBS and complex I. (**C)** The potential Na^+ and H^+ translocation paths in MBS. The Na^+ path and the adjacent H^+ path together form the potential Na^+/H^+ antiporter module in the distal end of membrane arm. The question mark above the proton path in the antiporter module indicates the tentative nature of the assignment. In the three H^+ paths, key residues conserved with complex I are shown as sticks. In the Na^+ path, key residues conserved with MBH and Mrp are shown as sticks. A series of charged and protonatable residues extend from MbsM to MbsH and MbsH' to form the charged axis across the membrane interior.

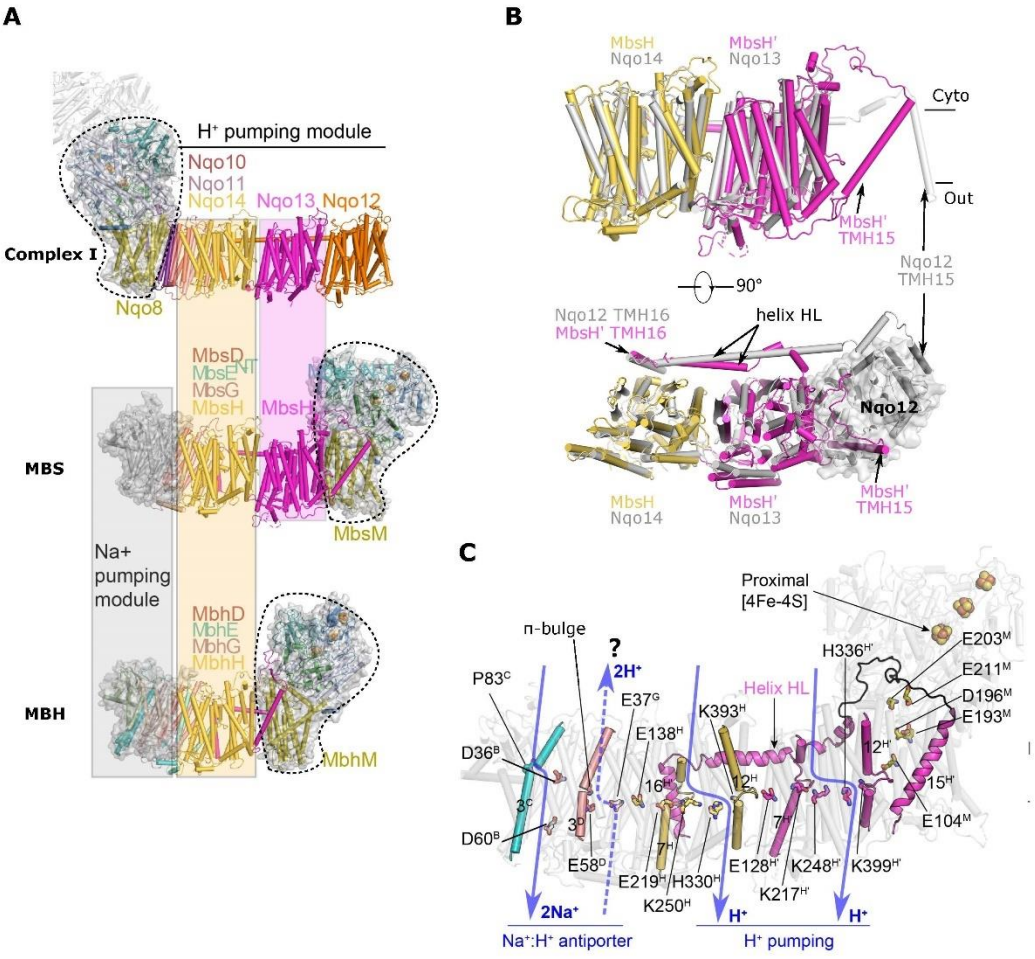
A
H⁺ pumping module
Nqo10
Nqo11
Nqo14
Nqo13
Nqo12
Complex I
Nqo8
MbsD
MbsE
MbsG
MbsH
MbsH'
MBS
MbsM
Na+
pumping
module
MbhD
MbhE
MbhG
MbhH
MBH
MbhM
B
MbsH
Nqo14
MbsH'
Nqo13
Cyto
Out
MbsH'
TMH15
Nqo12
TMH15
90°
Nqo12 TMH16
MbsH' TMH16
helix HL
Nqo12
MbsH
Nqo14
MbsH'
Nqo13
MbsH'
TMH15
C
Proximal
[4Fe-4S]
n-bulge
?
2H⁺
P83C
E37G
E138H
D36B
3C
3D
D60B
E58D
16H'
7H'
E219H'
H330H
K250H
12H
Helix HL
K393H
7H'
E128H'
K248H'
K217H'
K399H'
H336H'
E203M
E211M
D196M
E193M
12H'
15H'
E104M
2Na⁺
H⁺
H⁺
Na⁺:H⁺ antiporter
H⁺ pumping

Figure 3.4

Evolutionary relationship of Mrp, MBH, and MBS. (**A**) Comparison of the MBS membrane arm with the Mrp structure (PDB ID: 6Z16). The structures are aligned by superimposing MbsH and MrpD. The MBS subunits are colored as Fig. 3.1C and the Mrp is in cyan. Mrp structure is similar to MBS, with the conserved helix HL holds the two antiporter-like subunits in both complexes (MrpA and MrpD; MbsH and MbsH'). Notably, the MbsH' TMH15 immediately preceding helix HL moves a large distance, as compared to MrpA TMH15, to pack tightly against MbsM in order to accommodate MbsM in the MBS (see inset panel to the right). **B**) A possible evolutionary pathway from Mrp to MBH and to MBS. Mrp antiporter: PDB ID 6Z16; cytoplasmic [NiFe] hydrogenase: PDB ID 2FRV; MBH: PDB ID 6CFW. The question mark above the proton path in each antiporter module indicates the tentative nature of the assignment. Shown above the MBH and MBS structures are the reductive reactions that they catalyze and the associated free energy changes. Located around each complex is the respective modular architectures of the Mrp-derived respiratory complexes. These modules are: Na (green), sodium ion path; P (blue and purple), H^+ path(s) formed within a single subunit; Pc (cyan), composite H^+ path formed by multiple small subunits; A (orange), membrane anchor for the peripheral arm; H (turquoise), peripheral arm for proton reduction; S (turquoise), peripheral arm for polysulfide reduction.

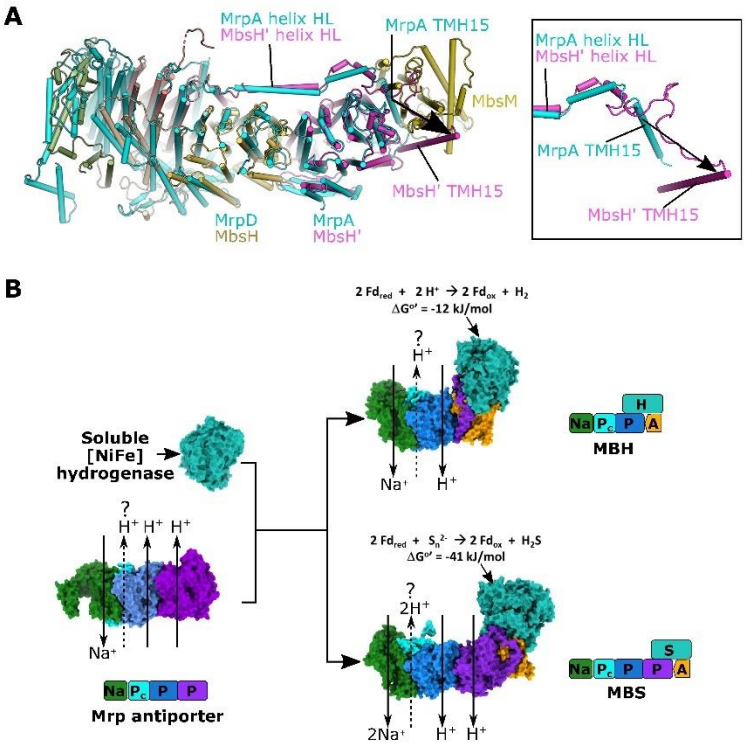
A
MrpA helix HL
MbsH' helix HL
MrpA TMH15
MbsM
MbsH' TMH15
MrpD
MbsH
MrpA
MbsH'
MrpA helix HL
MbsH' helix HL
MrpA TMH15
MbsH' TMH15
B
2 Fdred + 2 H+ → 2 Fdox + H2
ΔG°' = -12 kJ/mol
Soluble
[NiFe]
hydrogenase
MBH
2 Fdred + Sn2- → 2 Fdox + H2S
ΔG°' = -41 kJ/mol
MBS
Mrp antiporter

Figure 3.5

A comparison of the chamber at the active sites of MBS, MBH and complex I. The structures were overlaid based on MbsM, Nqo8 and MbhM and are shown individually. The chamber is similarly formed at the interface between the peripheral arm and its membrane anchor. The black arrow indicates the opening of the chamber proposed as the entrance of quinone in complex I studies. **(A)** MBS. (**B**) Complex I (PDB ID 4HEA). (**C**) MBH (PDB ID 6CFW). (**D**) A comparison of the chamber entry between MBS, MBH and complex I indicates wider opening in MBS and complex I than that in MBH. (**E**) Zoomed view of the end of the active site chamber, outlined as the boxed region in (**A**). The aligned Nqo4 of Tt complex I is shown as green cartoon where two residues (H38 and Y87) proposed for the binding of quinone headgroup are shown as sticks. (**F**) Sequence alignment of MbsL with its counterparts in different respiratory complexes (Nqo4 of Tt complex I, NdhH of NDH complex, MbhL of MBH complex I). Nqo4 H38 and Y87, proposed for quinone headgroup binding and protonation in complex I and MbhL E21, the key residue for proton reduction in MBH complex. These residues are all absent in MBS**.**

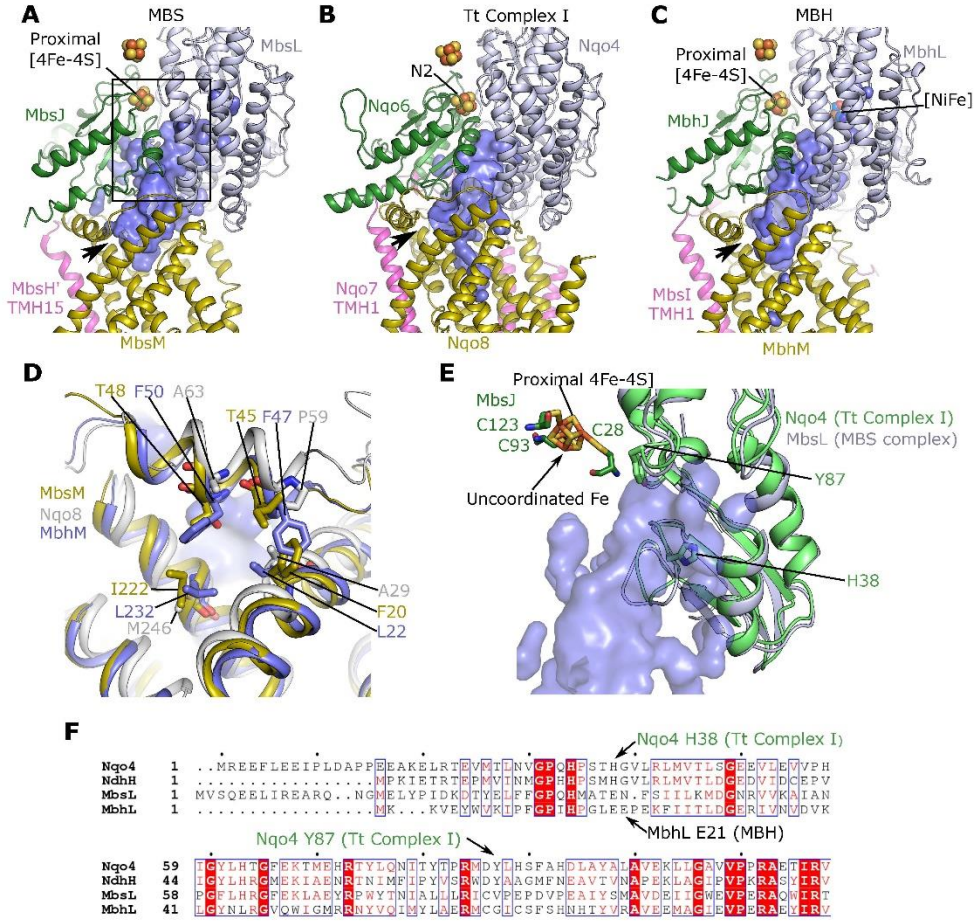
A
MBS
Proximal
[4Fe-4S]
MbsL
MbsJ
MbsH'
TMH15
MbsM
B
Tt Complex I
Nqo4
N2
Nqo6
Nqo7
TMH1
Nqo8
C
MBH
Proximal
[4Fe-4S]
MbhL
[NiFe]
MbhJ
MbsI
TMH1
MbhM
D
T48 F50 A63
T45 F47 P59
MbsM
Nqo8
MbhM
I222
L232
M246
A29
F20
L22
E
Proximal 4Fe-4S]
MbsJ
C123
C93
C28
Uncoordinated Fe
Nqo4 (Tt Complex I)
MbsL (MBS complex)
Y87
H38
F
Nqo4 H38 (Tt Complex I)
Nqo4 1 ..MREEFLEEIPLDAPPEEAKELRTEVMTLNVGPQHFSTHGVLRLMVTLSGEEVLEVVPH
NdhH 1 .....MPKIETRTEPMVTNMGPHHPSMHGVLRLMVTLDGEDVIDCEPV
MbsL 1 MVSQEELIREARQ..NGMELYPIDKDTYELFFGPQHMATEN.FSIILKMDGNRVVKAIAN
MbhL 1 .....MK...KVEYWVKIPFGPTHPGLEEPEKFIITLDGERIVNVDVK
MbhL E21 (MBH)
Nqo4 Y87 (Tt Complex I)
Nqo4 59 IGYLHTGFEKTMEHRTYLQNITYTPRMDYLHSFAHDLAYALAVEKLLGAVVPPRAETIRV
NdhH 44 IGYLHRGMEKIAENRTNIMFIPYVSRWDYAAGMFNEAVTVNAPEKLAGIPVPKRASYIRV
MbsL 58 PGFLHRGFEKLAEYRPWYTNIALLRICVPEPDVPEAIYSMAVDEIIGWEVPERAQWIRT
MbhL 41 IGYNLRGVQWIGMRRNYVQIMYLAERMCGICSFSHNHTYVRAVEEMAGIEVPERAEYIRV

Figure 3.6

Membrane-anchored peripheral module of MBS. **(A)** Superimposition of the membrane-anchored peripheral modules of MBS and complex I by aligning MbsL with Nqo4. The aligned regions are shown in cartoons and colored as the text labels. Structural elements that bridge the peripheral module to the H^+-pumping module (complex I Nqo7 and MBS MbsH' TMH15-16, more details in Fig. S3.4A) are shown as cylinders. **(B)** Between the peripheral arm and membrane arm are three interfacial loops, highlighted in gray shade, that are remarkably similar in MBH (red), MBS (magenta) and complex I (gray). The three loops are $Loop_{TMs}$ (Loop 1), $Loop_{\beta1\text{-}\beta2}$ (Loop 2) and $Loop_{TM5\text{-}6}$ (Loop 3) and are adjacent to the proximal [4Fe-4S] cluster. The C-terminal TMs following Loop 1 (boxed in the dashed blue square) are least similar among the three-loop systems of MBH, MBS, and complex I. **(C)** The three-loop system (gray shade) are linked to the membrane ion translocation module in semi-transparent surface through the C-terminal TMs following Loop 1. The dashed curve marks the central charge axis, a chain of red (negatively charged residues) and blue spheres (positively charged residues) spanning across the membrane arms. (**D**) Zoomed view of the area boxed with dashed blue square in (**A**) showing the coordination of the proximal [4Fe-4S]. MbsJ residues C28, C93 and C123 coordinate three irons of proximal [4Fe-4S] cluster, but MbsJ C25 is too far to coordinate the remaining iron. The semi-transparent orange surfaces show potential solvent-accessible chambers around the proximal cluster.

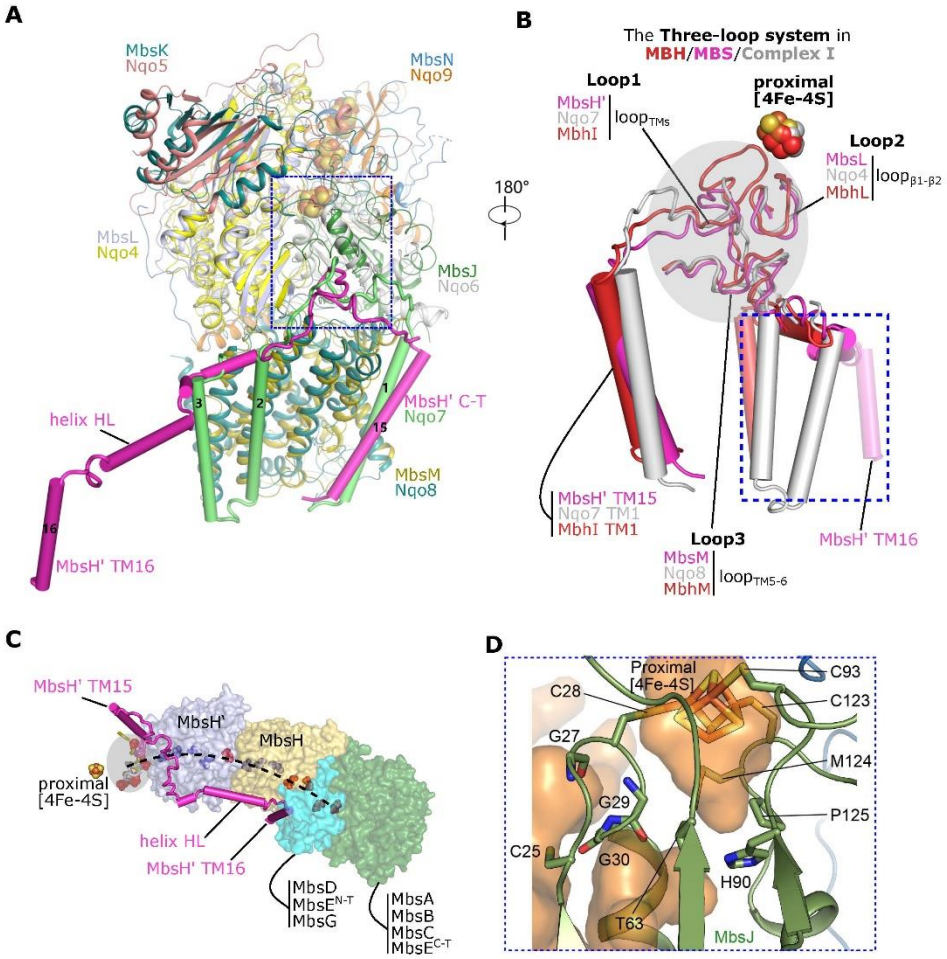
A
MbsK
Nqo5
MbsN
Nqo9
MbsL
Nqo4
MbsJ
Nqo6
MbsH' C-T
Nqo7
helix HL
MbsM
Nqo8
MbsH' TM16
B
The Three-loop system in
MBH/MBS/Complex I
Loop1
MbsH'
Nqo7
MbhI
loop TMs
proximal
[4Fe-4S]
Loop2
MbsL
Nqo4
MbhL
loop β1-β2
180°
MbsH' TM15
Nqo7 TM1
MbhI TM1
Loop3
MbsM
Nqo8
MbhM
loop TM5-6
MbsH' TM16
C
MbsH' TM15
MbsH'
MbsH
proximal
[4Fe-4S]
helix HL
MbsH' TM16
MbsD
MbsE N-T
MbsG
MbsA
MbsB
MbsC
MbsE C-T
D
Proximal
[4Fe-4S]
C93
C28
C123
G27
M124
G29
P125
C25
G30
H90
T63
MbsJ

Figure 3.7

MBS catalyzed polysulfide reduction mechanism. **(A)** Cysteines residues within electron tunneling distance of the proximal [4Fe-4S] cluster. (**B)** Polysulfide reduction activity assay of purified WT and mutant C-MBS subcomplexes, demonstrating that MbsJ C25 and MbsL C85 and C385 are not involved in catalysis. Error bars are centered from the average value and represent standard deviation obtained using technical triplicate samples. **(C)** Proposed catalytic mechanism of polysulfide reduction for the MBS complex. (**D)** A sketch summarizing energy transduction in complex I, MBH, and MBS.

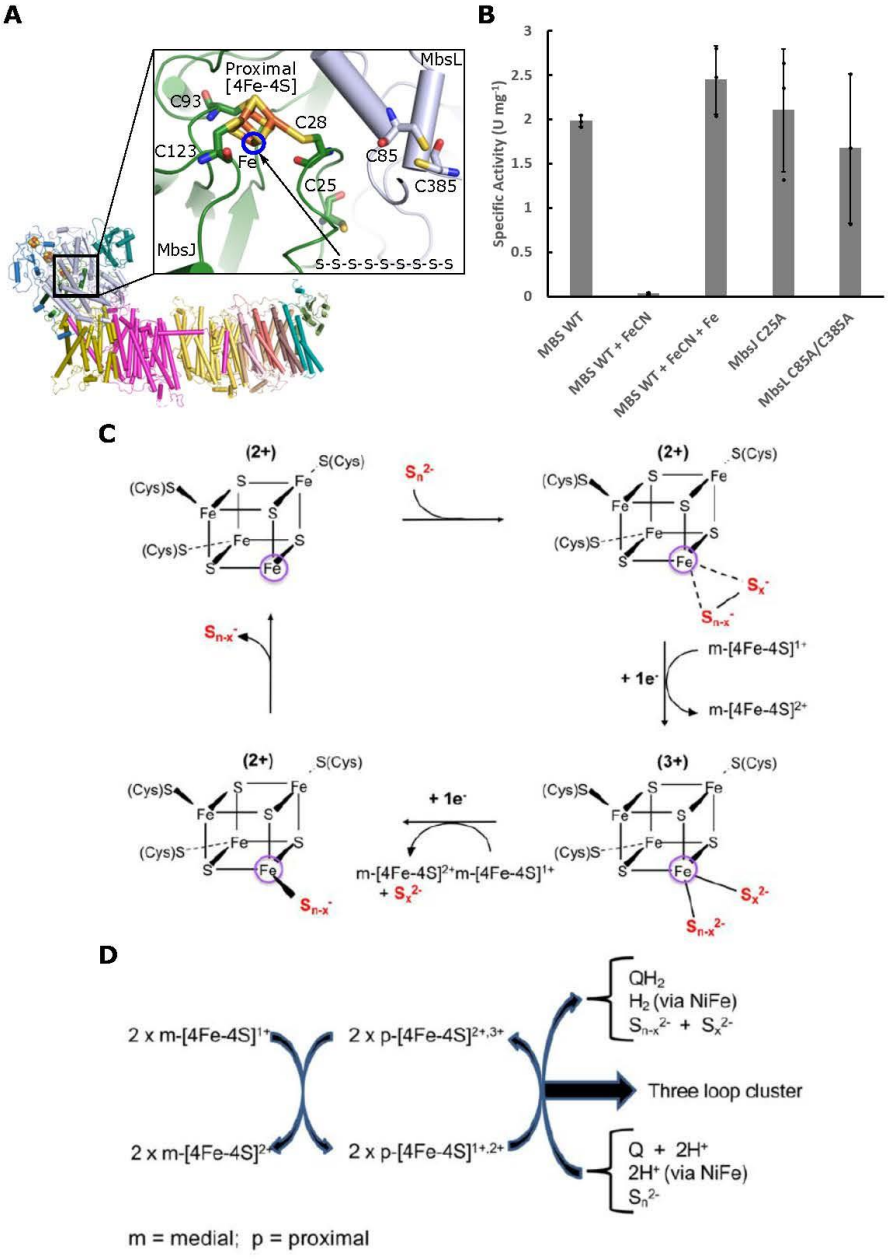
A
Proximal
[4Fe-4S]
MbsL
C93
C28
C123
Fe
C85
C25
C385
MbsJ
S-S-S-S-S-S-S-S-S
B
Specific Activity (U mg-1)
3
2.5
2
1.5
1
0.5
0
MBS WT
MBS WT + FeCN
MBS WT + FeCN + Fe
MbsJ C25A
MbsL C85A/C385A
C
(2+)
S(Cys)
(Cys)S
Fe
S
Sn2-
Sn-x-
Sx-
Sn-x-
+ 1e-
m-[4Fe-4S]1+
m-[4Fe-4S]2+
(3+)
m-[4Fe-4S]2+m-[4Fe-4S]1+
+ Sx2-
Sx2-
Sn-x2-
D
2 x m-[4Fe-4S]1+
2 x m-[4Fe-4S]2+
2 x p-[4Fe-4S]2+,3+
2 x p-[4Fe-4S]1+,2+
QH2
H2 (via NiFe)
Sn-x2- + Sx2-
Three loop cluster
Q + 2H+
2H+ (via NiFe)
Sn2-
m = medial; p = proximal

Supplementary Table 3.1. Cryo-EM data collection and refinement statistics

	MBS complex
Data collection	
Microscope	FEI Titan Krios
Voltage (kV)	300
Detector	Gatan K2 Summit
Electron dose ($e^-/Å^2$)	52
Pixel size (Å)	1.03
Defocus range (–μm)	1.1 – 3.0
Reconstruction	
Software	RELION 3.0
Particles for final refinement	203,673
Final Resolution (Å)	4.0
Map-sharpening B factor ($Å^2$)	–187.49
Model composition	
Peptide chains	26
Residues	6140
[4Fe-4S]	6
R.m.s. deviations	
Bond lengths (Å)	0.008
Bond angles (°)	1.205
Ramachandran plot	
Favored (%)	87.6
Outlier (%)	0.3
Validation	
Molprobity score	2.1
Rotamer outlier (%)	1.9
Clashscore	4.7

Supplementary Table 3.2. Homologous counterparts among respiratory Complex I (*T. thermophilus*), *B. subtilis* Mrp H^+/Na^+ antiporter, *P. furiosus* MBH, and *P. furiosus* MBS

Module proposed from MBH	*P. furiosus* MBH complex	*P. furiosus* Mbs complex	*B. subtilis* Mrp complex	*T. Thermophilus* Complex I	Module of Complex I
-	-	-	-	Nqo15/Nqo16	-
-	-	-	-	Nqo1/Nqo2/ Nqo3	N-module
Membrane-anchored hydrogenase module	MbhJ	MbsJ	-	Nqo6	Q-module
	MbhK	MbsK	-	Nqo5	
	MbhL	MbsL	-	Nqo4	
	MbhN	MbsN	-	Nqo9	
	MbhM	MbsM	-	Nqo8	P-module
Linker between hydrogenase module and ion-translocation modules	MbhI N-terminal	MbsH' TM15-16	MrpA TM15-16	Nqo7 N-terminal	
	MbhI C-terminal			Nqo12 C-terminal	
Proton translocation module	MbhD	MbsD	MrpA TM17-21	Nqo10	
	MbhE	MbsE TM1-2			
	MbhG	MbsG	MrpC	Nqo11	
	MbhH	MbsH	MrpD	Nqo14	
	-	MbsH' TM1-14	MrpA TM1-14	Nqo13	
	-	-	-	Nqo12	
Sodium translocation module	MbhF	MbsE TM3-6	MrpB	-	-
	MbhA	MbsA	MrpE	-	
	MbhB	MbsB	MrpF	-	
	MbhC	MbsC	MrpG	-	

Supplementary Table 3.3. Strains constructed and used in this study

Trivial Name	Strain Name	Description	Ref.
COM1	MW0002	Δ*pyrF*	52
MbsJ-His	MW0491	Δ*pyrF*::P_{gdh}*pyrF* P_{slp} 9x His *mbsJ*	5
ΔMbsL	MW0011	Δ*pyrF* Δ*mbsL*	21
MbsL^{WT}	MW0567	Δ*pyrF* Δ*mbsL*::P_{gdh}*pyrF* P_{slp} 9x His *mbsL-N*	5
MbsL$^{C85A/C385A}$	MW0572	Δ*pyrF* Δ*mbsL*::P_{gdh}*pyrF* P_{slp} 9x His *mbsL-N* (MbsL$^{C85A/C385A}$)	5
MbsJ^{C25A}	MW0584	Δ*pyrF* Δ*mbsL*::P_{gdh}*pyrF* P_{slp} 9x His *mbsL-N* (MbsJ^{C25A})	This study

Supplementary Table 4: Primers used in this study

Lab Name	**Target**	**Sequence (5' → 3')**
CH142	C-MBS UFR F	TCGAGGAGTACAACATCTTTGCCCAGGC
CH151	C-MBS DFR R	GTTTGGGTTGTGAGAGAAAGCCAAAAGC TTTCTCC
DH51	MbsJ C25A F	AAGAGTCTTTGGATTGTTGCATTTGCTACC GGATGTGGTGGAATAGAGAT
DH52	MbsJ C25A R	ATCTCTATTCCACCACATCCGGTAGCAAAT GCAACAATCCAAAGACTCTT

Supplementary Figure 3.1

Sample preparation and Cryo-EM of *P. furiosus* MBS. **(A)** A representative profile of gel filtration chromatography (Superose 6 10/300 GL column) of MBS purified with the detergent n-Dodecyl β-D-maltoside. The gel filtration were performed two times, for each sample used for data collection. Inset: SDS-PAGE of the purified MBS sample showing the presence of all thirteen MBS subunits as labeled to the right. Molecular weight markers in kDa are labeled to the left. (**B**) Representative cryo-EM micrograph of the MBS sample. We collected two datasets, one with 8352 and the other with 6355 micrographs. (**C**) Representative 2D class averages. A total of 203,673 particles were selected after 2D and 3D classifications. (**D**) The workflow of cryo-EM data processing. (**E**) Two views of the angular distribution of all particles used in the final 3D reconstruction (top panel). Shown below is the corresponding view of the 3D map. (**F**) The gold-standard Fourier shell correlation curve of the 3D map. (**G**) Local resolution of the cryo-EM 3D map calculated with ResMap. Inset: cut-open view showing the internal resolution range of the boxed area of the side view in the left most panel.

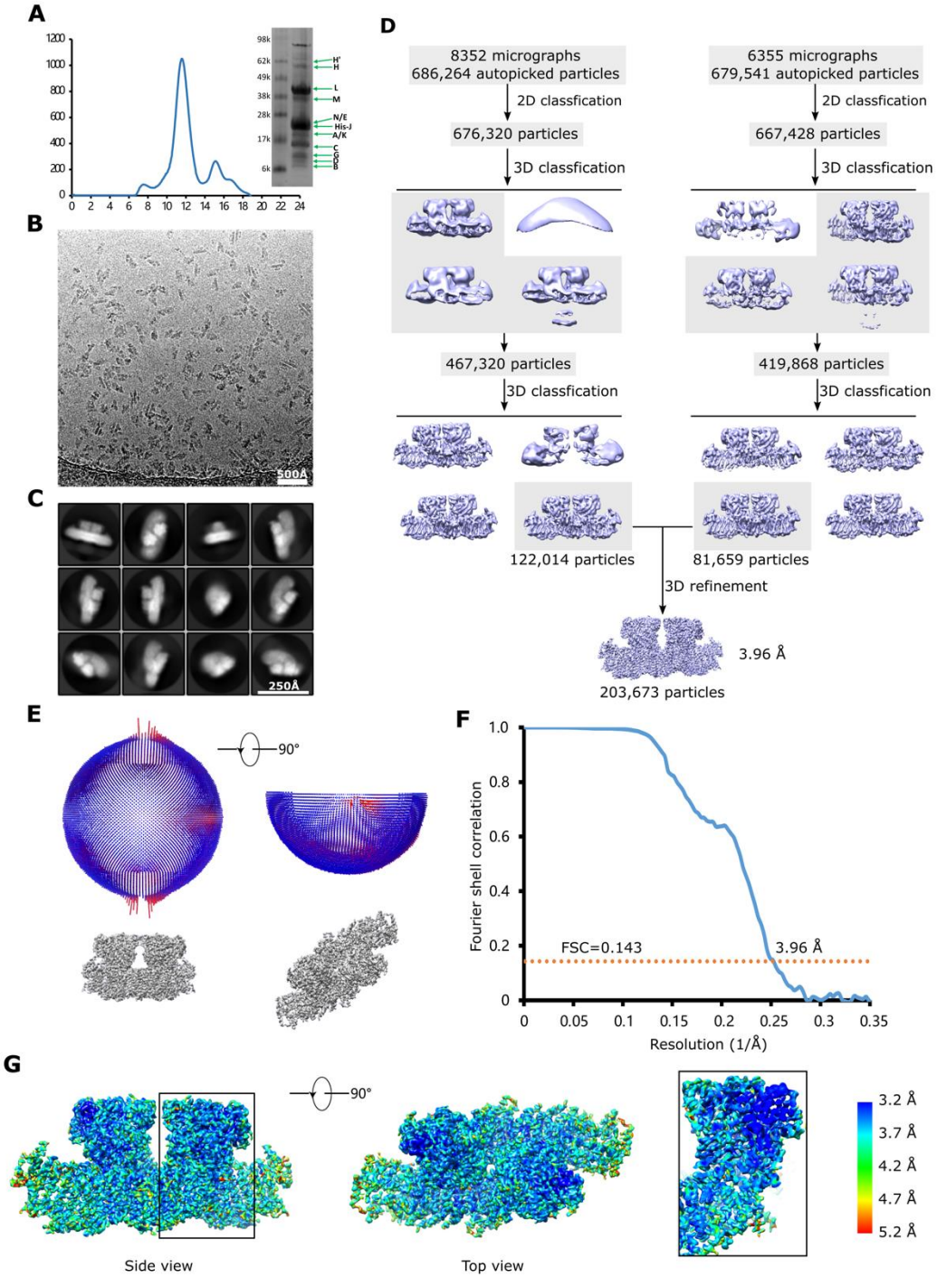
A
B
C
D
8352 micrographs
686,264 autopicked particles
2D classfication
676,320 particles
3D classfication
467,320 particles
3D classfication
122,014 particles
6355 micrographs
679,541 autopicked particles
2D classfication
667,428 particles
3D classfication
419,868 particles
3D classfication
81,659 particles
3D refinement
3.96 Å
203,673 particles
500Å
250Å
E
90°
F
Fourier shell correlation
FSC=0.143
3.96 Å
Resolution (1/Å)
G
90°
3.2 Å
3.7 Å
4.2 Å
4.7 Å
5.2 Å
Side view
Top view

Supplementary Figure 3.2.

A gallery of example regions of the EM density map and the atomic model fitted in the map. These regions include all 58 TMHs of all membrane subunits (**A-G**), $Loop_{TMH5-6}$ of MbsM (**D**), $Loop_{TMH15-16}$, helix HL of MbsH' (**G**), the N-terminal part of MbsJ containing C25 that unexpectedly does not coordinate the proximal [4Fe-4S] cluster (**H**), and the N-terminal β-sheets of MbsL connected by $Loop_{β1-β2}$ (**I**). (**J**) The EM densities around the three [4Fe-4S] clusters are rendered in surface view at the same display threshold.

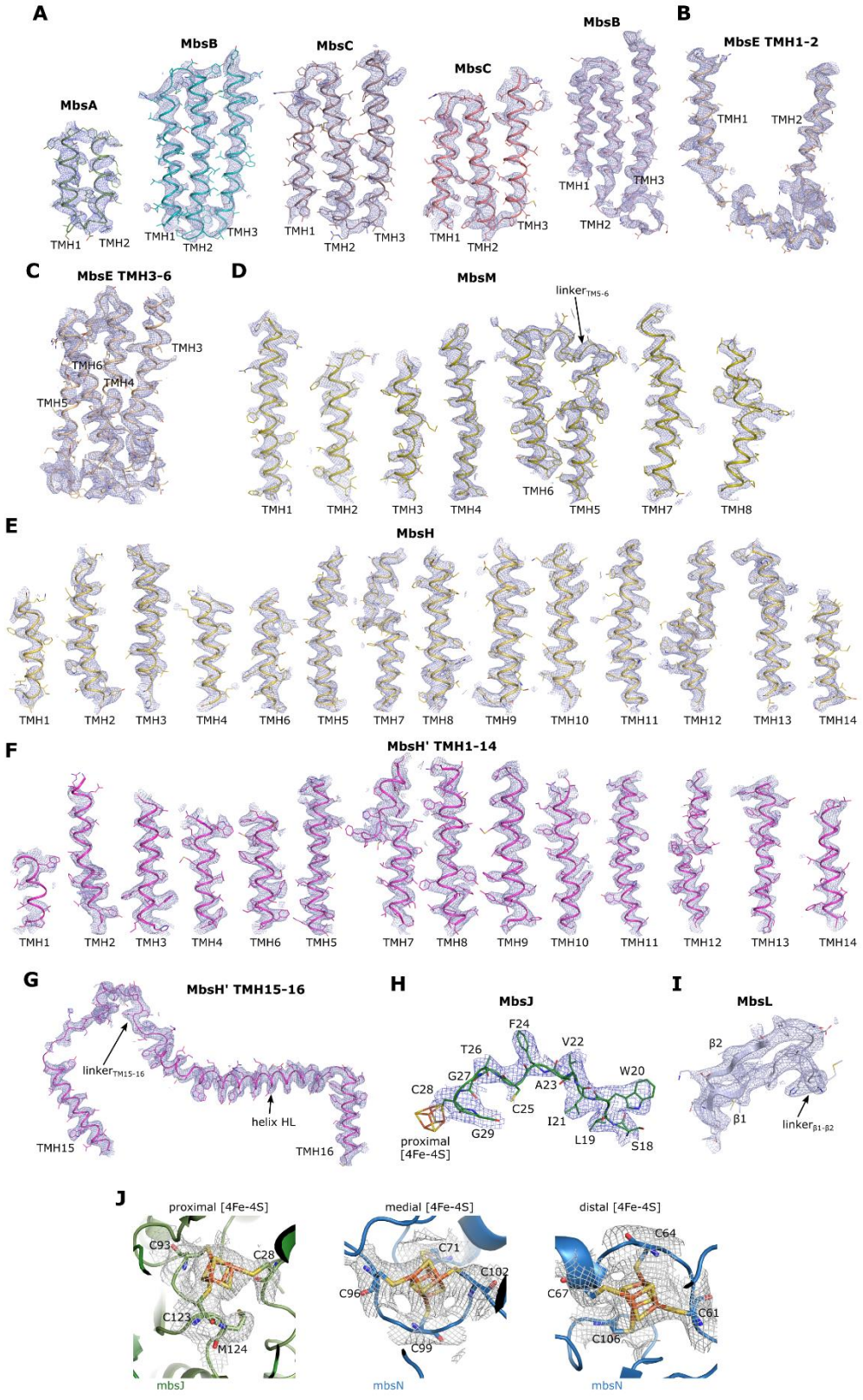
A
MbsA
MbsB
MbsC
MbsC
MbsB
TMH1
TMH2
TMH1
TMH2
TMH3
TMH1
TMH2
TMH3
TMH1
TMH2
TMH3
TMH1
TMH3
TMH2
B
MbsE TMH1-2
TMH1
TMH2
C
MbsE TMH3-6
TMH3
TMH6
TMH4
TMH5
D
MbsM
linker TM5-6
TMH1
TMH2
TMH3
TMH4
TMH6
TMH5
TMH7
TMH8
E
MbsH
TMH1
TMH2
TMH3
TMH4
TMH6
TMH5
TMH7
TMH8
TMH9
TMH10
TMH11
TMH12
TMH13
TMH14
F
MbsH' TMH1-14
TMH1
TMH2
TMH3
TMH4
TMH6
TMH5
TMH7
TMH8
TMH9
TMH10
TMH11
TMH12
TMH13
TMH14
G
MbsH' TMH15-16
linker TM15-16
helix HL
TMH15
TMH16
H
MbsJ
F24
T26
V22
G27
W20
A23
C28
C25
I21
G29
L19
S18
proximal [4Fe-4S]
I
MbsL
β2
β1
linker β1-β2
J
proximal [4Fe-4S]
C93
C28
C123
M124
mbsJ
medial [4Fe-4S]
C71
C102
C96
C99
mbsN
distal [4Fe-4S]
C64
C67
C61
C106
mbsN

Supplementary Figure 3.3

Assembly of the membrane arm of MBS. **(A)** A top view of the membrane arm of the MBS monomer showing the arrangement of membrane subunits. The outlined proximal membrane module is composed of MbsD, MbsE TMH1-2, MbsG, MbsH and MbsH'. **(B)** Structural alignment of the antiporter-like subunits MbsH (yellow) and MbsH' (magenta) of the proximal membrane module. TM helices are numbered. Left panel, top view of the alignment viewed from cytosol. The two putative proton-translocating five-helix folding units are outlined. They are superimposable when one unit is turned upside down with respect to the other. Right panel, side view of the alignment from the membrane side (MbsH' TMH15-16 is hidden for clarity). Two discontinuous α-helices (TMH7 and TMH12) are labeled with key charged residues shown as spheres.

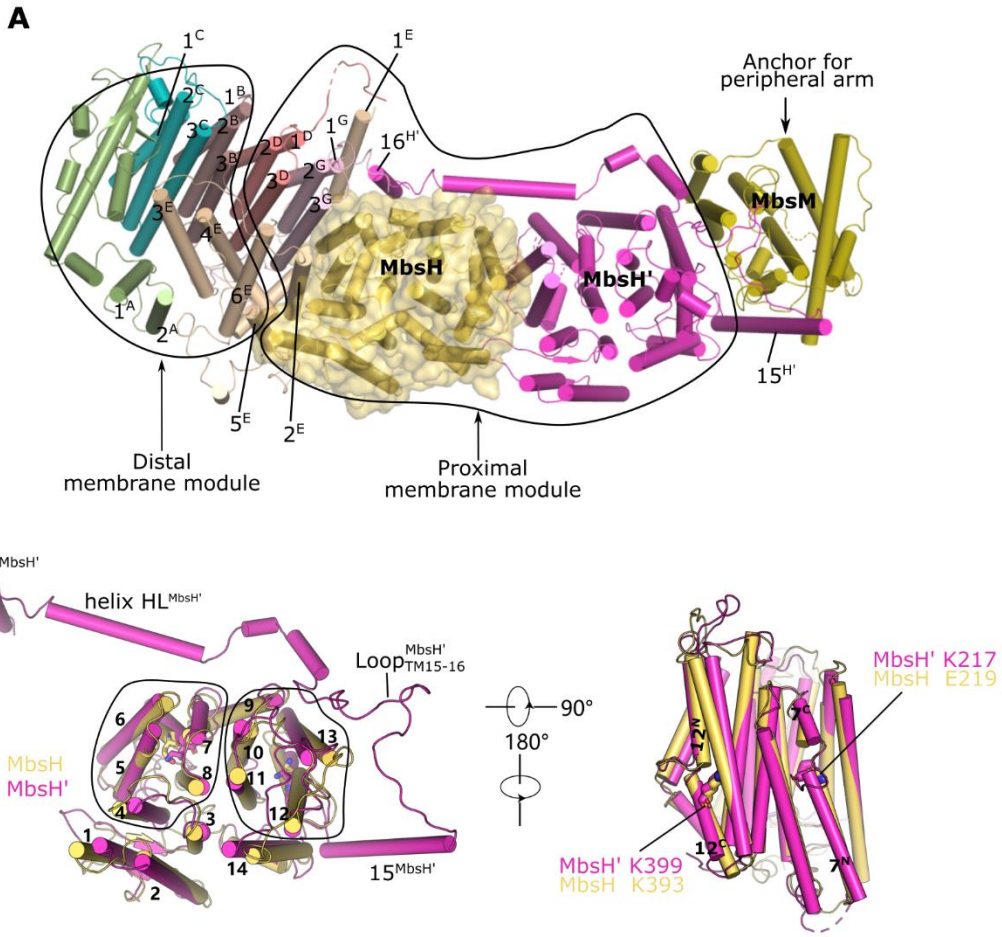
A
Anchor for peripheral arm
MbsM
MbsH
MbsH'
Distal membrane module
Proximal membrane module
B
helix HL MbsH'
Loop TM15-16 MbsH'
MbsH
MbsH'
90°
180°
MbsH' K217
MbsH E219
MbsH' K399
MbsH K393

Supplementary Figure 3.4

Comparison of three different respiratory machineries: Complex I, MBH and MBS**. (A)** A structural overlay of the MBS proximal membrane module with its counterparts in Complex I and MBH. The alignment (as done in Figure 3.3A) is based on the respective proton-pumping antiporter-like subunits Nqo14, MbsH and MbhH of Complex I (*T. thermophilus*; PDB ID 4HEA), MBS and MBH (*P. furiosus*; PDB ID 6CFW). Complex I has 3 proton-pumping antiporter-like subunits in the proximal membrane module, MBS has 2, and MBH has one. The different sizes of the proximal modules are accommodated by different lengths of their HL helices. Complex I Nqo8, MBS MbsM and MBH MbhM (shown as transparent cartoons) serve as the membrane anchors for their respective hydrogenase modules. The peripheral module in Complex I is located at the opposite end of the membrane arm as compared to that of MBH and MBS. **(B)** Different membrane interfaces adjacent to the membrane-anchored peripheral module revealed by the alignment of their antiporter-like subunits MbsH' (MBS) and MbhH (MBH). Note the tight interface between MbsH' and MbsM in MBS in contrast to the large gap between the two corresponding subunits in MBH. **(C)** A close-up view of the dashed box of the aligned structure in panel (**B**) shows the subunit-subunit correspondence between MBS and Complex I. **(D)** A close-up view of the shared Na^+-translocation module between MBH and MBS (as shown in Fig. 3.3A). (**E**) Putative Na^+-translocation path within the distal membrane module of MBS as outlined by the solid line red box in (**D**).

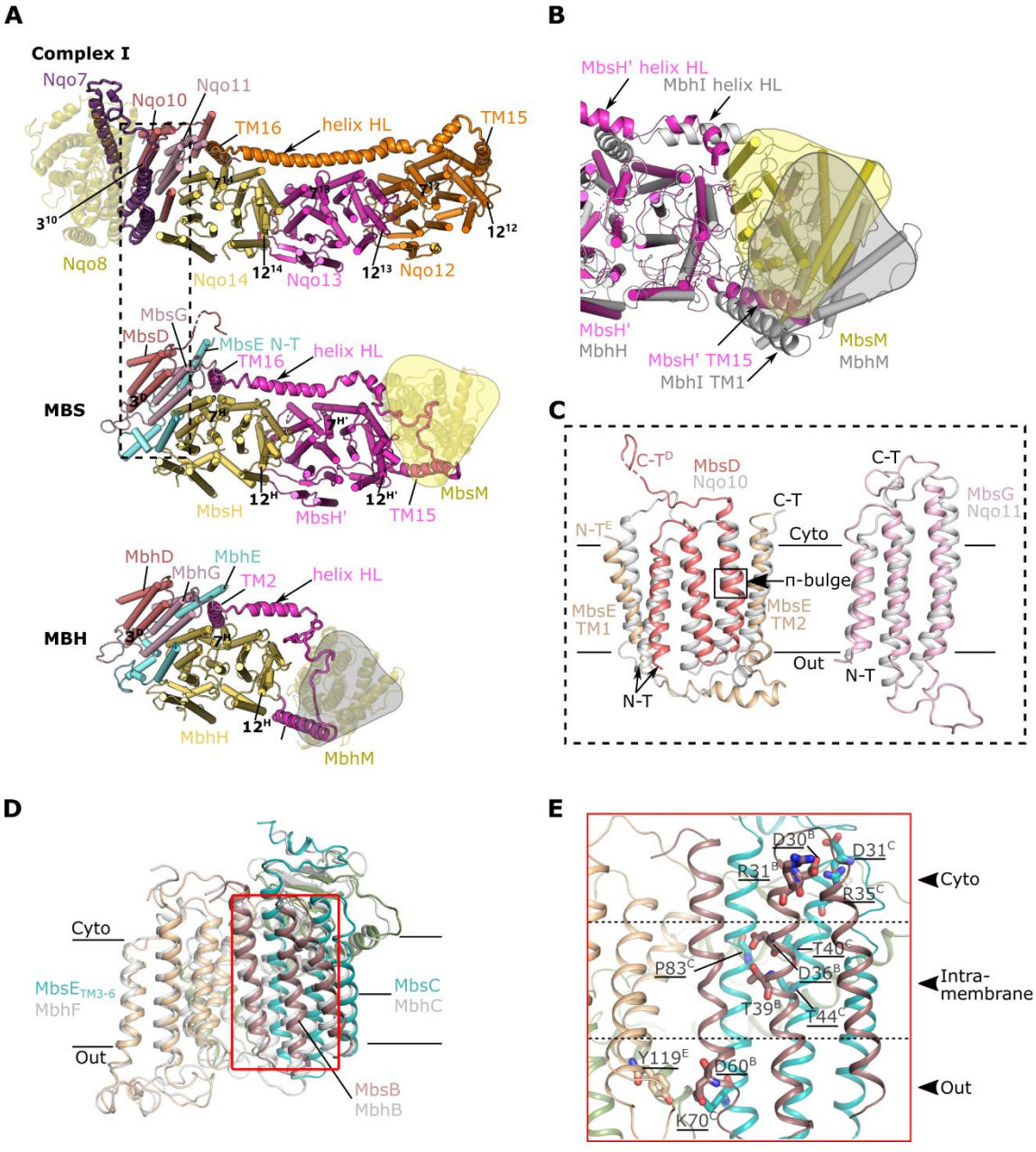
A
Complex I
Nqo7
Nqo10
Nqo11
TM16
helix HL
TM15
Nqo8
Nqo14
Nqo13
Nqo12
MBS
MbsG
MbsD
MbsE N-T
TM16
helix HL
MbsH
MbsH'
TM15
MbsM
MBH
MbhD
MbhE
MbhG
TM2
helix HL
MbhH
MbhM
B
MbsH' helix HL
MbhI helix HL
MbsH'
MbhH
MbsH' TM15
MbhI TM1
MbsM
MbhM
C
C-T
MbsD
Nqo10
C-T
Cyto
π-bulge
MbsE
TM1
MbsE
TM2
Out
N-T
N-T
MbsG
Nqo11
D
Cyto
MbsE
MbhF
Out
MbsC
MbhC
MbsB
MbhB
E
Cyto
Intra-
membrane
Out

Supplementary Figure 3.5

A comparison of the membrane-anchored peripheral modules of MBS, MBH and Complex I. **(A)** Side (left) and top (right) views of the aligned membrane-anchored peripheral modules of MBS (colored as in Figure 3.1C), MBH (salmon) and Complex I (grey). Structural alignment is based on MBS MbsL, MBH MbhL, and Complex I Nqo4. **(B-F)** Zoomed views of the subunit-subunit correspondences based on the structural alignment in **A**. Their respective N-terminal ends (N-T) are marked by semi-transparent grey disks and the C-terminal ends by the text label "C-T". (**B**) MbsM, MbhM and Nqo8. (**C**) MbsJ, MbhJ and Nqo6. (**D**) MbsK, MbhK and Nqo5. (**E**) MbsL, MbhL and Nqo4. (**F**) MbsN, MbhN and Nqo9.

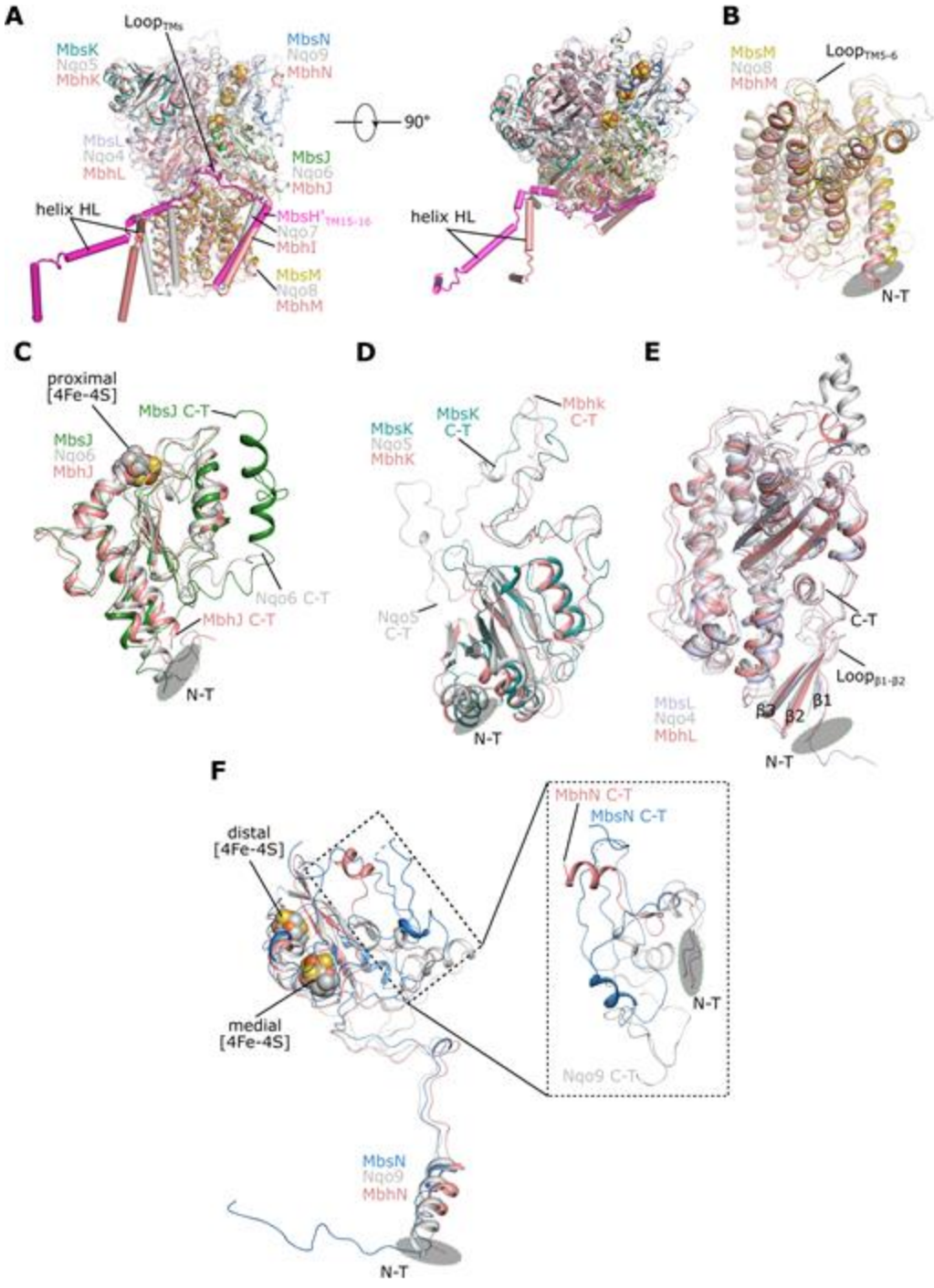
A
Loop$_{TMs}$
MbsK
Nqo5
MbhK
MbsN
Nqo9
MbhN
90°
MbsL
Nqo4
MbhL
MbsJ
Nqo6
MbhJ
helix HL
MbsH' $_{TM15-16}$
Nqo7
MbhI
MbsM
Nqo8
MbhM
helix HL
B
MbsM
Nqo8
MbhM
Loop$_{TM5-6}$
N-T
C
proximal
[4Fe-4S]
MbsJ C-T
MbsJ
Nqo6
MbhJ
Nqo6 C-T
MbhJ C-T
N-T
D
MbsK
C-T
Mbhk
C-T
MbsK
Nqo5
MbhK
Nqo5
C-T
N-T
E
C-T
Loop$_{β1-β2}$
β3
β2
β1
MbsL
Nqo4
MbhL
N-T
F
distal
[4Fe-4S]
medial
[4Fe-4S]
MbhN C-T
MbsN C-T
N-T
Nqo9 C-T
MbsN
Nqo9
MbhN
N-T

Supplementary Figure 3.6

Cysteine coordination of the [4Fe-4S] clusters in MBS. (A) Distribution of cysteine residues for the coordination of three [4Fe-4S] clusters. Note that MbsL C85 and C385 and MbsJ C25 near the proximal cluster don't participate in cluster interaction. **(B)** Near the proximal [4Fe-4S] cluster, a large chamber (shown as orange surface) is formed at the interface between the peripheral arm and membrane arm (as shown in Figure 3.5A), which defines the active site for the redox reaction. A possible substrate decylsulfide is shown in sticks and transparent spheres at the upper left corner, in the same scale as the proteins. MbsJ residues C28, C93 and C123 coordinate the proximal [4Fe-4S] cluster while a nearby free MbsJ C25 faces the chamber. Right below MbsJ C25, three interfacial loops (as highlighted in Figure 3.6B) define the boundaries of the chamber. **(C)** Sequence alignments of the structural motif (as shown in **B**) containing two variable cysteines (highlighted as yellow shade) for the coordination of proximal [4Fe-4S] cluster (C35 and C38 for MBH; C25 and C28 for MBS; C52 and C53 for NDH; C45 and C46 for Complex I). **(D)** MbsL C85 and C385 (as outlined by dashed box in panel **A**) correspond to two of the four [NiFe]-coordinating cysteines in MBH and its ancestor [NiFe] hydrogenase, as revealed by the structural comparison of MBS MbsL and MBH MbhL. The other two cysteines are lost, making a vestigial site unable for [NiFe] coordination in MBS.

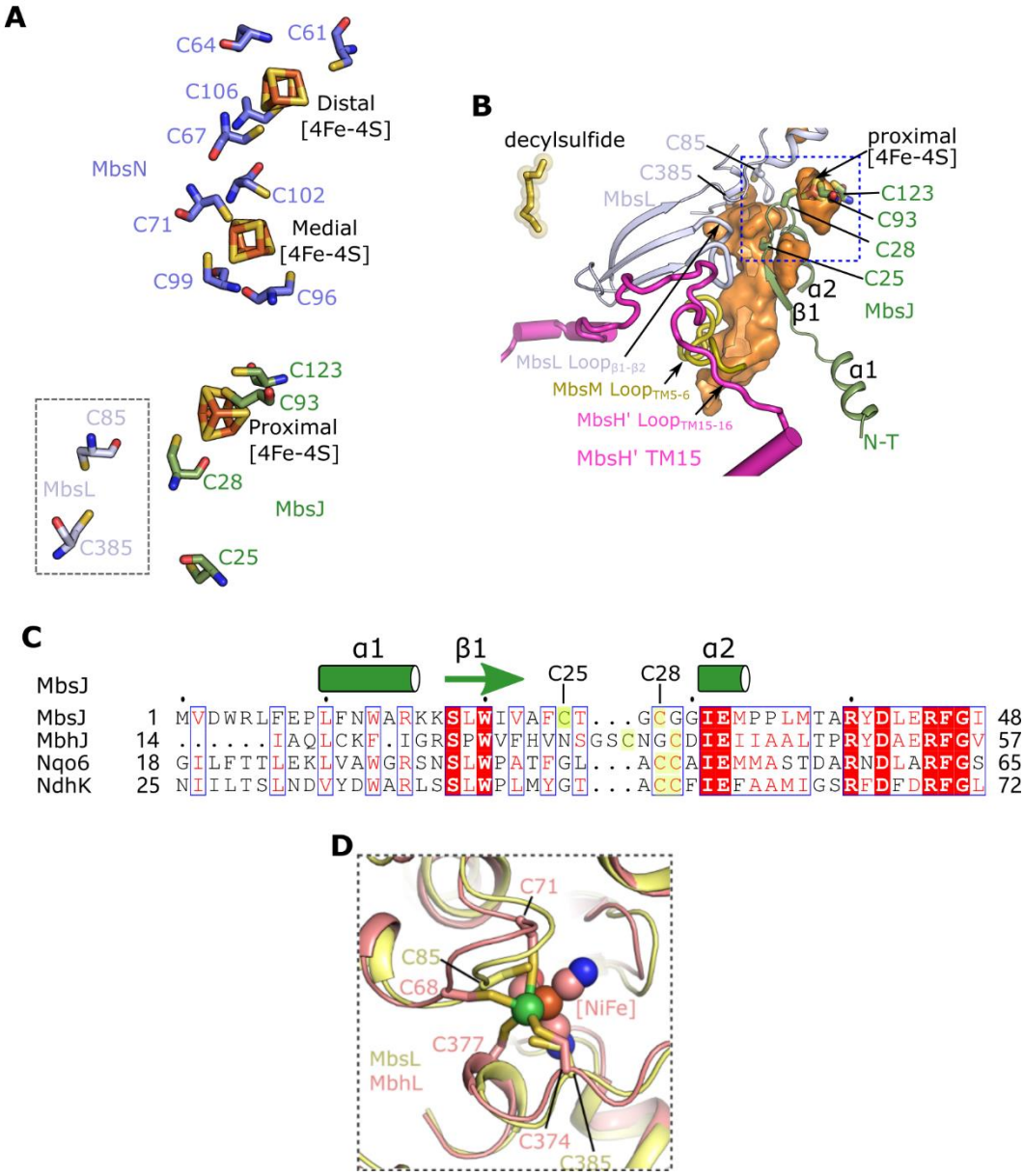
A
C64
C61
C106
Distal
[4Fe-4S]
C67
MbsN
C102
C71
Medial
[4Fe-4S]
C99
C96
C123
C93
Proximal
[4Fe-4S]
C85
C28
MbsL
MbsJ
C385
C25
B
decylsulfide
C85
proximal
[4Fe-4S]
C385
MbsL
C123
C93
C28
C25
α2
β1
MbsJ
MbsL Loop β1-β2
α1
MbsM Loop TM5-6
MbsH' Loop TM15-16
MbsH' TM15
N-T
C
α1
β1
C25
C28
α2
MbsJ
MbsJ 1 MVDWRLFEPLFNWARKKSLWIVAFCT...GCGGIEMPPLMTARYDLERFGI 48
MbhJ 14 .....IAQLCKF.IGRSPWVFHVNSGSCNGCDIEIIAALTPRYDAERFGV 57
Nqo6 18 GILFTTLEKLVAWGRSNSLWPATFGL...ACCAIEMMASTDARNDLARFGS 65
NdhK 25 NIILTSLNDVYDWARLSSLWPLMYGT...ACCFIEFAAMIGSRFDFDRFGL 72
D
C71
C85
C68
[NiFe]
C377
MbsL
MbhL
C374
C385

Supplementary Figure 3.7

EPR spectra of MBS and MBH. **(A)** EPR spectrum of dithionite -reduced MBS from S^0-grown cells showing a strong radical signal (g = 2.00). **(B)** EPR spectrum of dithionite-reduced MBS from non-S^0 grown cells. The g value (1.94) is characteristic of reduced [4Fe-4S] clusters. **(C)** EPR spectrum of FeCN-oxidized MBS from non-S^0 grown cells. The g value (2.09) is indicative of oxidized [3Fe-4S] clusters and corresponds to loss of the catalytic Fe atom upon oxidation. **(D)** EPR spectrum of dithionite-reduced MBH, indicating multiple reduced [4Fe-4S] clusters. **(E)** EPR spectrum of MBH after FeCN oxidation is silent, indicative of an oxidized [4Fe-4S] cluster. EPR parameters for each spectrum are temperature, 10K; microwave power, 20 mW; receiver gain, A: 75, B: 30, C: 300, D: 30, E: 30.

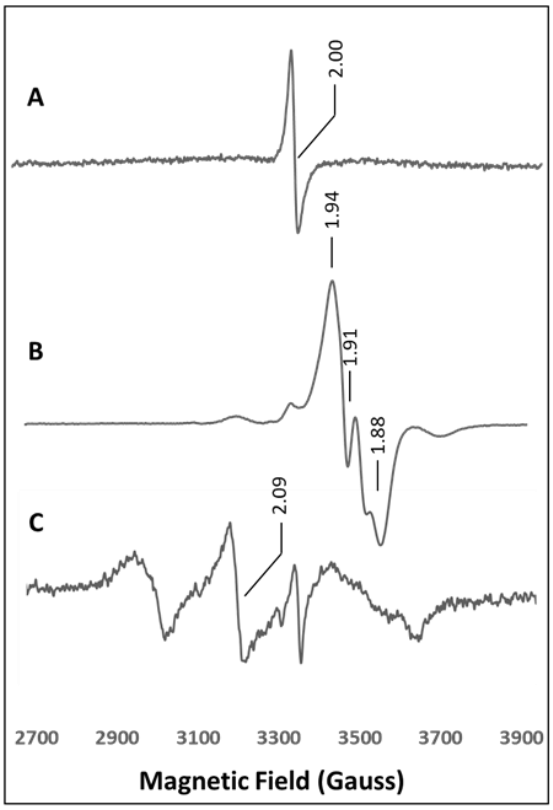
A
2.00
1.94
B
1.91
1.88
C
2.09
2700
2900
3100
3300
3500
3700
3900
Magnetic Field (Gauss)

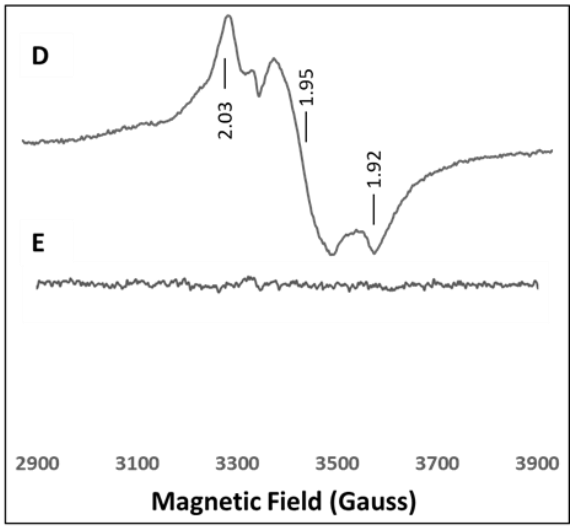
D
2.03
1.95
1.92
E
2900
3100
3300
3500
3700
3900
Magnetic Field (Gauss)

CHAPTER FOUR

CHARACTERIZATION OF THIOSULFATE REDUCTASE FROM *PYROBACULUM AEROPHILUM* HETEROLOGOUSLY PRODUCED BY *PYROCOCCUS FURIOSUS*[3]

[3] Haja, D.K.*, Wu, CH.*, Poole, F.L. *et al.* 2020. *Extremophiles.* 24, 53–62.

Reprinted here with permission from the publisher.

*The authors contributed equally to this work

Abstract

The genome of the archeaon *Pyrobaculum aerophilum* (T_{opt} ~ 100 ˚C) contains an operon (PAE2859-2861) encoding a putative pyranopterin-containing oxidoreductase of unknown function and metal content. These genes (with one gene modified to encode a His-affinity tag) were inserted into the fermentative anaerobic archaeon, *Pyrococcus furiosus* (T_{opt} ~ 100 ˚C). Dye-linked assays of cytoplasmic extracts from recombinant *P. furiosus* show that the *P. aerophilum* enzyme is a thiosulfate reductase (Tsr) and reduces thiosulfate but not polysulfide. The enzyme (Tsr-Mo) from molybdenum-grown cells contains Mo (Mo:W ~ 9:1) while the enzyme (Tsr-W) from tungsten-grown cells contains mainly W (Mo:W ~ 1:6). Purified Tsr-Mo has over ten times the activity (V_{max} = 1,580 vs. 141 μmoles min^{-1} mg^{-1}) and twice the affinity for thiosulfate (K_m = ~100 vs. ~200 μM) than Tsr-W and is reduced at a lower potential (E_{peak} = -402 mV vs -255 for Tsr-Mo). Tsr-Mo and Tsr-W proteins are heterodimers lacking the membrane anchor subunit (PAE2861). *P. furiosus* expressing *P. aerophilum* Tsr did not have the ability to reduce thiosulfate. *P. furiosus* contains five pyranopterin-containing enzymes, all of which utilize W. *P. aerophilum* Tsr-Mo is the first example of an active Mo-containing enzyme produced in *P. furiosus*.

Introduction

Pyrococcus furiosus is a hyperthermophilic euryarchaeon that grows optimally near 100 ˚C and is an attractive host for protein engineering studies because of the availability of an efficient genetic system (Lipscomb et al. 2011). Multiple studies have been conducted on homologously-expressed genes, proving the viability of *P. furiosus* for engineering and characterizing its native enzymes (Chandrayan et al. 2012; McTernan et al. 2015, Wu et al. 2018). In addition, two multi-subunit, energy-conserving complexes from the hyperthermophilic euryarchaeon *Thermococcus onnurineus*, the 18-subunit formate hydrogen lyase (Lipscomb et al. 2014) and the 16-subunit carbon monoxide dehydrogenase complex (Schut et al. 2016), were heterologously-expressed and were functional in *P. furiosus*. These complexes enabled *P. furiosus* to grow and produce hydrogen by the oxidation of formate or CO, respectively. Herein we expand the phylogenetic scope of heterologously-expressed genes in *P. furiosus* to those of *Pyrobaculum aerophilum*, a crenarchaeon that grows optimally near 100 ˚C.

P. aerophilum is a facultative chemoautotroph that grows with a wide range of respiratory electron acceptors, including oxygen, nitrate, arsenate, and ferric iron (Völkl et al. 1993). When *P. aerophilum* cultures are shifted from aerobic growth to anaerobic growth, transcriptional analyses show that genes PAE2859-2861 are up-regulated following the onset of anoxia (Cozen et al. 2009). PAE2859 contains a pyranopterin-thiosulfate-R domain conserved in thiosulfate, polysulfide and sulfur reductases, and PAE2861 contains an NrfD domain conserved in polysulfide reductases. *P. aerophilum* does not grow in the presence of elemental sulfur and grows only slowly with thiosulfate (Völkl et a. 1993; Cozen et al. 2009) so the physiological function of this complex is

unknown. PAE2859-2861 encode a member of the DMSOR subfamily of pyranopterin enzymes. These heterotrimeric enzymes consist of the catalytic subunit TsrA, containing a bis-pyranopterin guanine dinucleotide (bis-PGD) cofactor and a [4Fe-4S] cluster; the small subunit TsrB, containing an additional three [4Fe-4S] clusters; and the membrane anchor subunit TsrC that contains a quinone-binding site. In *P. aerophilum*, this complex is assumed to couple the oxidation of menaquinol from the quinone pool in the membrane to the reduction of thiosulfate, polysulfide or sulfur on the outside of the membrane and to be an important part of the sulfur cycle in marine environments (Jørgensen 1990). However, to date, neither a thiosulfate reductase nor a polysulfide reductase has been characterized from an archaeon or from a microbe that can grow near 100 °C. The first goal of this work is to express PAE2859-2861 in *P. furiosus* and determine its function.

While two respiratory enzymes have been purified from *P. aerophilum* biomass, namely, heme-containing NO reductase (de Vries et al. 2003) and pyranopterin-containing nitrate reductase (Afshar et al. 2001), it is not possible to improve enzyme yields by over-expressing target genes and/or using affinity tags to facilitate purification since *P. aerophilum* is not genetically-tractable. Heterologous expression of *P. aerophilum* PAE2859-2861 in *P. furiosus* is therefore an attractive option. However, a key issue is the nature of the metal that is inserted. The previous pyranopterin-containing enzyme purified from *P. aerophilum*, the respiratory nitrate reductase NarS, contained molybdenum in its active site. In contrast, *P. furiosus* contains five pyranopterin oxidoreductases but it only inserts the chemically-analogous element tungsten into their active sites, even when grown in a medium lacking tungsten and supplemented with molybdenum (Mukund and Adams 1996; Sevcenco et al. 2010). In this case there is sufficient tungsten present in the

"tungsten-free" medium as a contaminant. Consequently, it is not clear if *P. furiosus* can insert molybdenum into a pyranopterin-containing enzyme. Since all characterized thiosulfate reductases and polysulfide reductases from mesophilic bacteria contain molybdenum (Stoffels et al. 2012, Dietrich and Klimmek 2002), a second goal of this work is to determine whether the enzyme encoded by *P. aerophilum* PAE2859-2861 purified from *P. furiosus* contains molybdenum or tungsten.

P. furiosus grows by fermentation and produces hydrogen gas but it can also use elemental sulfur (S°) as a terminal electron acceptor and concomitantly produces hydrogen sulfide (Adams et al. 2001). A 13-subunit membrane-bound oxidoreductase is produced when cells are grown on elemental sulfur (Yang et al. 2010). It was recently shown that this enzyme is a sulfane sulfur reductase (MBS) and reduces polysulfide (Wu et al. 2018). MBS is not a member of the pyranopterin family of enzymes and is therefore distinctly different from the molybdenum-containing polysulfide reductases and thiosulfate reductases from mesophilic bacteria (Schut et al. 2007). While the heterologously-expressed enzyme encoded by *P. aerophilum* PAE2859-2861 is not likely to connect to electron transport in the membrane due to the lack of quinone-dependent respiratory system in *P. furiosus*, it should be able to dispose of excess reductant produced during fermentation to improve growth. Therefore, if PAE2859-PAE2861 encode a thiosulfate reductase, a third goal of this work is to determine whether the recombinant *P. furiosus* strain that is heterologously-expressing these genes can use thiosulfate as a terminal electron carrier in place of S°. Herein, we show that the genes PAE2859-PAE2861 do indeed encode a thiosulfate reductase, which we refer to as Tsr, rather than a polysulfide or sulfur reductase.

This is the first archaeal Tsr to be characterized and the first example of an active molybdenum-containing enzyme produced by *P. furiosus*.

Experimental Procedures

Strain construction

The genetically-tractable *P. furiosus* strain, COM1, was used for the heterologous expression of *P. aerophilum* genes in Pf (Lipscomb et al. 2011). A knock-in cassette was assembled by using overlapping PCR (Bryksin and Matsamura 2010), containing the fragments shown in Figure 4.1. UFR (Upstream Flanking Region), P_{slp} (S-Layer Protein Promoter) and DFR (Downstream Flanking Region) were amplified from *P. furiosus* genomic DNA, and the selection marker (*pyrF*-P_{gdh}) was amplified by using pGLW021 as the template (Lipscomb et al. 2011). PAE2859-PAE2861, PAE0022-PAE0023, and PAE3570-PAE3571 were amplified using *P. aerophilum* genomic DNA as the template. To facilitate purification, a 9x-histidine-tag was place at the N-terminus of PAE2860 and the ribosomal binding sites (RBS) of pyruvate ferredoxin oxidoreductase (POR) and the S-layer protein of *P. furiosus* were placed upstream of PAE2860 and PAE2861, respectively. The genomic DNA of *P. furiosus* and *P. aerophilum* were prepared using ZymoBead Genomic DNA Kit (Zymo Research). *P. aerophilum* (DSMZ-7523) was purchased from DSMZ, and it was grown using DSMZ medium 611.

P. furiosus COM1 transformants were grown as previous described (Lipscomb et al. 2011). The genomic DNA isolated by ZymoBead Genomic DNA Kit (Zymo Research) was used for PCR screening, which was carried out by using GXL polymerase (Takara, ClonTech). The PCR screening was performed by a pair of primers outside the intergenic

GR1 locus to confirm that the transformation cassette recombined into the correct locus. The PCR confirmed colony was further sequence confirmed using Genewiz Sanger Sequencing service (South Plainfield, NJ). A 5-FOA counterselection strategy was used to pop-out the selection marker from the Tsr-OE strain, and a second transformation step was performed for the co-expression of PAE2859-PAE2861 and either PAE0022-PAE0023 or PAE3570-PAE3571 (Lipscomb et al. 2011).

RNA Extraction and Quantitative RT-PCR

RNA was extracted from 50 mL samples of cultures using an RNA miniprep kit (Zymo Research). Synthesis of cDNA was performed with 1 μg of purified RNA using the Affinity Script QPCR cDNA synthesis kit (Agilent). The Brilliant II SYBR Green QPCR Master Mix (Agilent) was used for quantitative RT-PCR experiments with primers designed to amplify a ~150 bp gene product within the target gene: PF0971 (PORγ gene), PAE2859, PAE2861, PAE0022 and PAE3570).

Growth conditions and effect of Mo and W on the activity of Tsr

The *P. furiosus* strains constructed and used in this study are listed in Table 4.1. The growth medium was prepared as described previously (Lipscomb et al. 2011). For molybdenum- and tungsten-related experiments, Mo and W were omitted from the standard medium and this was then supplemented with either 10 μM sodium molybdate or 10 μM sodium tungstate. For the complex peptides-based medium, 0.05% (wt/vol) yeast extract and 0.5% (wt/vol) casein hydrolysate (enzymatic) were used as carbon sources. For defined sugar-based medium, 0.5% (wt/vol) maltose, 1x vitamin mix, and 1x 19-amino acid solution were added. Stock solutions of vitamin mix and 19 amino acid solution were made as described

previously (Lipscomb et al. 2011) For both complex and defined media, 2 g/L elemental sulfur or 10 mM sodium thiosulfate were added where indicated. Cells were grown in 50 mL cultures at 90 ℃ with shaking. For total cell protein determination, 1 mL of cell culture was removed using a syringe at desired timepoints and centrifuged in a Beckman Microfuge 18 centrifuge at 18,000 xg for 10 min to pellet cells. Cells were resuspended and lysed in 1 mL of distilled H_2O. The cell lysates were centrifuged at 18,000 xg for 1 min to remove cell debris, and the protein concentration was determined using the Bradford Protein Assay Dye (Bio-Rad). For sulfide determination, 1 mL of headspace was removed at desired timepoints and sulfide was determined using a standard methylene blue assay (Schut et al. 2007).

Purification of TsrAB

The Tsr over-expression (Tsr-OE) strain was subcultured 10 times in the appropriate Mo- or W-containing medium (Mukund and Adams 1996) before 20 L cultures were grown to generate biomass for enzyme purification as described previously (Chandrayan et al. 2012). The harvested cells were frozen in liquid nitrogen and stored at -80 °C. All purification procedures were performed under anaerobic conditions. 30 g cells (wet weight) were lysed in a 1:5 ratio of wet cell weight to buffer in 25 mM Tris-HCl, pH 8.0, containing 1 mM DTT, for 1 hr at room temperature in an anaerobic chamber (Coy, Grass Lake, MI). The cell-free extract was centrifuged in a Beckman-Coulter Optima L-90K ultracentrifuge at 110,000 xg for 1 hr. The supernatant was collected and loaded onto a 5 mL His-Trap FF column (GE Healthcare) equilibrated with 98% Buffer A (50 mM sodium phosphate, pH 7.5, 400 mM NaCL, 1 mM DTT) and 2 % Buffer B (Buffer A with 500 mM imidazole). The column was washed with 10 column volumes of 2% Buffer B and a stepwise elution

of 5 column volumes each of 15, 40, and 100% Buffer B was used to elute the bound protein. Active fractions were assayed by methyl-viologen-linked thiosulfate reduction (described below), were pooled and diluted 10-fold with 50 mM CHES buffer, pH 9.0 (Buffer A), and loaded directly onto a 5 mL HiTrap Q HP column (GE Healthcare). The column was washed with 5 column volumes of Buffer A and the bound protein was eluted with a 30-column volume gradient from 0 to 70% Buffer B (Buffer A with 1 M NaCL). Fractions from Ni-NTA and Q-HP were assayed for thiosulfate reduction activity and analyzed by SDS-PAGE using precast Miniprotean TGX Stain-Free gels (Bio-Rad). LC-MS/MS (PAMS Facility, UGA) was used to identify protein subunits, and the metal content of Tsr was measured using an octopole-based ICP-MS (7900 with x-lens; Agilent Technologies) as described previously (Vaccaro et al. 2009).

Enzyme assays

All the assays were carried out anaerobically at 80 °C. For thiosulfate reduction, assay cuvettes contained 100 mM 3-(N-morpholino)propanesulfonic acid (MOPS), pH 7.5, 150 mM NaCl, 5 mM sodium thiosulfate and 2 mM methyl viologen (MV). The mixture was reduced with concentrated titanium citrate to an OD of 2.5-3.0 units at 600 nm using a 100 Cary UV-Vis spectrophotometer with a peltier-based temperature controller from Agilent Technologies (Santa Clara, CA). The reaction was started by the addition of the enzyme. For the polysulfide reduction assay, thiosulfate was replaced with polysulfide (5 mM) and the activity was measured by the decrease of the absorbance of benzyl viologen (BV) at 580 nm. A stock of 0.5 M polysulfide was prepared by mixing 12 g Na_2S with 1.6 g elemental sulfur in 100 ml anoxic water (20). In the MV- and BV-linked assays, extinction coefficients of 8.25 mM^{-1} cm^{-1} and 8.8 mM^{-1} cm^{-1}, respectively, were used for calculations.

For *Pf* ferredoxin (Fd)-dependent activity, Fd was reduced using titanium citrate and the oxidation of Fd was monitored at 425 nm (ϵ = 13 mM^{-1} cm^{-1}). One unit of activity is defined as 1 μmol of MV, BV or Fd oxidized per minute. Temperature and pH dependence experiments were carried out in the same fashion except that different buffers were used for the pH dependence assays.

Electrochemistry

Electrochemical experiments were performed in a water-jacketed, temperature controlled electrochemical cell with a three-electrode setup using a PG-Stat 128N Autolab electrochemical analyzer (Metrohm) controlled by GPES software. The counter electrode was a platinum wire; the reference electrode was a saturated Ag/AgCl electrode (Basi, MF-2052); and a custom 25π μm^2 pyrolytic graphite edge (PGE) served as the working electrode. The working electrode was rotated by an AFMSRCE Series Rotator (Pine Instrument Co.) All potentials are adjusted to the standard hydrogen electrode (SHE) where SHE = Ag/AgCl + 0.197 V. Protein films were produced by pipetting 5-10 μL of protein solution (~ 0.1 mg/mL) onto the polished surface of a PGE electrode and dried with nitrogen gas. A 100 mM HEPES, MES, MOPS, TAPS buffer, with 100 mM potassium chloride as a secondary electrolyte, was utilized exclusively during electrochemical analysis. The electrode was rotated at 2.5-3 krpm to ensure mass transport did not influence voltammetry. Data was analyzed using QSOAS, a freely available data analysis software and an in-house Mathematica program (Fourmond et al. 2009). Other experimental details are outlined in the figure legends.

Results

PAE2859-PAE2861 can be successfully expressed in P. furiosus and encodes a thiosulfate reductase (Tsr)

Strains constructed and used in this study are listed in Table 4.1. The recombinant *P. furiosus* strain MW0484 containing PAE2859-PAE2861 was constructed using the parent strain COM1 by homologous recombination of the knock-in cassette into the intergenic space between PF0265 and PF0266, as shown in Figure 4.1. Based on our previous report on the purification procedure of a membrane bound hydrogenase, the N-terminus of the soluble small subunit of the complex is the best position for an affinity tag (McTernan et al. 2015). A 9x-histidine-tag was therefore placed at the N-terminus of PAE2860, annotated as the small iron-sulfur cluster subunit. *P. furiosus* ribosomal binding sites were placed upstream of each gene to optimize translation. The operon was placed under the control of promoter P_{slp} of the gene encoding the S-Layer Protein, one of the most highly expressed genes in the *P. furiosus* genome. Expression of PAE genes in Tsr-OE was confirmed by qPCR analysis, where the expression of PAE2859 (the catalytic subunit) and PAE2861 (the membrane bound subunit) were similar to the internal control, that of the γ subunit of pyruvate ferredoxin oxidoreductase (POR) (data not shown). *P. aerophilum* PAE2859-PAE2861 is annotated as encoding a membrane-bound polysulfide or thiosulfate reductase, although the physiological function of this complex is not known (Cozen et al. 2009). Cytoplasmic and membrane fractions of MW0484 cells grown with 10 μM Mo and 10 μM W, which should be sufficient to satisfy the metal requirement of the enzyme, were therefore assayed for both thiosulfate and polysulfide reductase activity. The results of these assays are summarized in Table S4.1. Only reduced MV to thiosulfate activity was measured, with no detectable reduced BV to polysulfide activity, indicating that PAE2859-

PAE2861 encodes a thiosulfate reductase (Tsr). Moreover, the majority of dye-linked enzyme activity is localized to the cytoplasm, suggesting that at least the catalytic subunit dissociates from the membrane upon cell lysis.

Thiosulfate reductase containing either molybdenum or tungsten can be purified from P. furiosus

To determine whether Tsr produced in *P. furiosus* contains Mo or W in its active site, the Tsr-OE strain was subcultured 10 times in media supplemented with either 10 μM Mo (to yield Tsr-Mo) or 10 μM W (to yield Tsr-W). *P. furiosus* is able to grow in a medium lacking added W by scavenging trace amounts W that contaminate other medium components for its native pyranopterin enzymes, potentially leaving the exogenous Mo for incorporation into Tsr if indeed Mo is the active site metal required for Tsr. Tsr-W and Tsr-Mo were purified from cells grown from media to which either W or Mo had been added, respectively, using thiosulfate reduction to monitor enzyme activity. The results are summarized in Tables S4.2 and S4.3. SDS-PAGE of pooled anion-exchange fractions shows TsrA and TsrB were present in the purified Tsr from both types of cells, but no TsrC was detected. This was confirmed by LC-MS/MS (Fig. 4.2A). We attempted a number of different purification methods to obtain a complex containing TsrC. These included solubilization of the whole cell extract in 10% Triton X-100 for 24 or 48 hrs (previously determined to be the most efficient method to solubilize *P. furiosus* membrane proteins, including the respiratory membrane-bound hydrogenase (McTernan et al. 2015)); solubilization using other detergents, including 1% n-dodecyl-β-D-maltopyranoside, 1% deoxycholate, and 1% n-octyl-β-D-glucopyranoside; and the addition of 5% glycerol and 0.5% aminocaproic acid to all buffers as “protective agents” to prevent dissociation (Guiral

et al. 2005). SDS-PAGE gel fragments, TCA precipitations, and gel-assisted digests of each attempt were analyzed by LC-MS/MS, but no TsrC was identified. We therefore conclude that a cytoplasmic form of heterodimeric Tsr was obtained from *P. furiosus* containing TsrA and TsrB but lacking TsrC.

Metal analysis using ICP-MS on purified Tsr-W and Tsr-Mo gave W:Mo ratios of approximately 9:1 and 1:6, respectively, indicating successful purification of enzymes that predominantly contain tungsten or molybdenum. Both Tsr-W and Tsr-Mo have an Fe:W/Mo ratio of approximately 20:1 consistent with the expected value of 16:1 and close to full occupancy (> 0.8 atoms/mole) of W/Mo in the active site (Fig. 4.2B). Kinetic analyses were carried out on Tsr-Mo and Tsr-W, and the results are summarized in Table 4.2. These show that the Mo-containing enzyme has greater than ten times the activity (V_{max} = 1,580 vs. 141 μmoles min^{-1} mg^{-1}) and has a two-fold higher affinity for thiosulfate (K_m = ~100 μM vs. ~200 μM) than the W-containing enzyme. Additionally, assays were conducted using *P. furiosus* ferredoxin (Fd) as an electron donor and the Mo-containing enzyme was found to couple the oxidation of Fd to the reduction of thiosulfate (V_{max} = ~4 μmoles min^{-1} mg^{-1} using 10 μM Fd). The optimal pH for both the Mo- and W-enzymes is between 7.5 and 8.0 (at 80 °C). Neither enzyme had detectable activity below 40 ˚C and, in both cases, activity increases with temperature up to 90 ˚C (the highest temperature used; data not shown). It is likely that the optimum temperature for Tsr activity is closer to or even above 100 ˚C.

Electrochemical analysis of Tsr-Mo and Tsr-W shows that Tsr-Mo becomes activated at a lower reduction potential

The ability to separately purify Mo- and W-containing enzymes from *P. furiosus* opens the door for comparative analyses to investigate the impact of active site metal on the enzyme's reduction potentials. Figure 4.3 shows square wave voltammograms obtained from Tsr-Mo and Tsr-W immobilized on a pyrolytic graphite electrode. Each voltammogram contains a strong peak that corresponds to oxidation/reduction of the enzyme. The peak is centered at -255 mV vs. SHE for Tsr-Mo and -402 mV vs. SHE for Tsr-W. In short, the W-containing Tsr is more difficult to reduce by approximately 150 mV. This is consistent with the known properties of these elements, as W is more difficult to reduce as a result of the Lanthanide contraction, and likely explains the dramatic difference in activity between Tsr-Mo and Tsr-W observed in solution assays. The reduction potentials of the electron donors MV and thiosulfate in the standard assay are -440 and -402 mV, respectively (Watanabe and Honda 1982; Thauer et al. 1977). Thus, based solely on thermodynamic considerations, the Tsr-Mo is expected to be more active in assays than Tsr-W.

The Tsr overexpression strain is not able to grow using thiosulfate as a terminal electron acceptor but does exhibit increased sulfide production

Wild type *P. furiosus* grows poorly on peptides in the absence of elemental sulfur (S°) as the cells are not able to dispose of excess reductant produced during peptide fermentation (Adams et al. 2001). In the parent strain, this growth phenotype can be overcome with the addition of S° leading to robust growth, while the addition of thiosulfate does not affect growth (Fig. S4.1a). The same was true with the recombinant Tsr-OE strain. Growth on peptides is not rescued when thiosulfate is added to the medium, even when grown with Mo to produce the more active Tsr-Mo (Fig. S4.1b). While there are a number of reasons that *P. furiosus* is not able to use thiosulfate as a terminal electron acceptor, it is possible

that *P. furiosus* can use Tsr to reduce thiosulfate to hydrogen sulfide *in vivo*. There is no significant difference in growth between the parent and Tsr-OE in the presence or absence of thiosulfate (Fig. 4.4a). However, Tsr-OE produced significantly more sulfide from thiosulfate and particularly at the early stages of growth compared to the parent strain (Fig. 4.4b), suggesting that heterologously-expressed Tsr has some *in vivo* activity in *P. furiosus*. The *P. furiosus* genome does not contain a homologue of Tsr and the sulfide produced by the parent strain is likely a product of non-soecufuc reduction of thiosulfate. Importantly, neither strain produced any sulfide in the absence of thiosulfate and no significant levels of sulfide were measured in the media (data not shown). The low sulfide production activity could be due to the lack of a thiosulfate-specific transporter in *P. furiosus*. The genome of *P. aerophilum* encodes for two putative (thio)sulfate transporters, PAE0022-0023 and PAE3570-3571. The two transporters were co-expressed with Tsr-OE generating strains MW0573 and MW0580, respectively. However, neither strain was able to grow on thiosulfate and both strains showed only a slight increase in sulfide production compared to the Tsr-OE strain alone (data not shown).

Discussion

Using heterologous expression in *P. furiosus*, we have shown here that PAE2859-2861 of *P. aerophilum* encodes a thiosulfate reductase that catalyzes the reaction (1).

$$S_2O_3^{2-} + 2H^+ + 2e^- \rightarrow HS^- + HSO_3^- \quad (1)$$

Interestingly, other characterized Tsr enzymes contain cytochrome b_{561}, but PAE2861 contains an NrfD domain that is characteristic of polysulfide reductase membrane subunits, where it functions as a membrane anchor and menaquinol binding site. Similarly, the previously characterized Tsr from the mesophilic bacterium *Salmonella typhimirium* also contains a PsrC homolog instead of the expected cytochrome-containing TsrC membrane

anchor. These examples illustrate the diversity of this class of pyranopterin-containing enzyme and indicate the difficulty in assigning function simply from gene sequences (Heinzinger et al. 1995).

P. aerophilum Tsr is the first archaeal thiosulfate reductase to be characterized and the first active Mo-containing enzyme to be produced in *P. furiosus*. Virtually all pyranopterin-containing enzymes that have been characterized contain molybdenum and either do not incorporate the chemically-analogous element tungsten, or become inactivated when tungsten replaces molybdenum in the catalytic site (Johnson and Rajagopalan 1976). Recently, however, a number of pyranopterin enzymes have been characterized that are active with either tungsten or molybdenum, depending on which element is present in the host organism's growth medium. These include *Rhodobacter capsulatus* DMSO Reductase (Hagedoorn et al. 2003), *Escherichia coli* TMAO Reductase (Buc et al. 1999), and *Desulfovibrio alaskensis* formate dehydrogenase (Brondino et al. 2004). *P. furiosus* is therefore extremely unusual in that it contains five tungsten-containing pyranopterin enzymes that are only active with tungsten and do not incorporate significant amounts of molybdenum, even when cells are grown with molybdenum in the absence of added tungsten (Sevcenco et al. 2010). Hence it is surprising to find that *P. furiosus* can insert molybdenum or tungsten into heterologously-expressed *P. aerophilum* Tsr, depending on the growth conditions, and apparently do so with great efficiency leading to almost full occupancy of the metal in the active site.

P. aerophilum Tsr is also the first reported example of a thiosulfate reductase that has been characterized in two forms that differ in having either molybdenum or tungsten in the active site. We assume that *P. aerophilum* can also generate both forms depending

on the growth conditions, just like *P. furiosus.* The nitrate reductase (Nar) of *P. aerophilum* has also been purified (from *P. aerophilum* biomass) in both Mo- and W-containing forms and in this case the Mo-form is twice as active as the W-form, but they have similar affinities for nitrate (de Vries et al. 2010). Hence *P. aerophilum* is unusual in being able to generate active Mo- and W-forms of two pyranopterin-containing enzymes, Tsr and Nar. This might be an adaptation to the high tungsten-containing marine environments that allows it to grow at concentrations that are inhibitory to other organisms (Kletzin and Adams 1996). However, *P. aerophilum* exhibits poor growth in the presence of thiosulfate, and the low catalytic activity and high K_m for thiosulfate for Tsr-W make it unlikely that the organism grows on thiosulfate under conditions where high concentrations of tungsten are present.

P. furiosus was previously shown to insert only W into the active site of its pyranopterin enzymes, (Mukund and Adams 1996) and, accordingly, it contains a transport protein, WtpA, that has a binding affinity for tungstate that is over three orders of magnitude stronger than that for molybdate. In addition, titration with tungstate of the molybdate-saturated WtpA shows that tungstate efficiently displaces molybdate from the binding site of the transporter (Bevers et al. 2006). While this novel transporter is beneficial for W-requiring *P. furiosus,* it explains why a high concentration of Mo (10 μM) is needed in the absence of added W in the growth medium to obtain an enzyme (Tsr) with predominately, although not exclusively, Mo in its catalytic site. The ability of *P. furiosus* to incorporate Mo into the active site of pyranopterin enzymes such as *P. aerophilum* Tsr, raises the issue of which element, Mo or W, has been incorporated into previous heterologously-expressed pyranopterin enzymes. For example, the preference of *T.*

onnurineus formate hydrogen lyase (FHL) for Mo or W is unknown and so both were added to the medium at equal concentrations for the heterologous production of this enzyme in *P. furiosus* (Schut et al. 2016). However, given the growth requirement of *T. onnurineus* for W and its close phylogenetic relationship to *P. furiosus* (Moon et al. 2012), it is likely that FHL is a W-enzyme, although that has yet to be demonstrated. This ability to insert the "correct" metal into the active site of pyranopterin enzymes, as well as the ability to facilitate purification using affinity tags and overexpression, makes *P. furiosus* an attractive option for future studies of various pyranopterin enzymes from hyperthermophilic species.

P. aerophilum uses a Twin-Arginine Translocation (TAT) system to export enzymes to the periplasmic side of the membrane. PAE2859 of the Tsr complex contains a TAT motif (Cozen et al. 2009), but *P. furiosus* does not have a TAT export system (Dilks et al. 2003). This is the likely reason why *P. aerophilum* thiosulfate reductase was produced in the cytoplasm of *P. furiosus* as a heterodimer lacking the membrane-anchoring TsrC subunit, even though all three genes encoding the enzyme are transcribed at comparable levels. The absence of the TAT system means that the heterotrimeric complex can not be properly inserted into the *P. furiosus* membrane. Tsr in *P. aerophilum* catalyzes the reduction of thiosulfate in the periplasm, but in *P. furiosus* the enzyme is located in the cytoplasm. Nevertheless, the *P. furiosus* Tsr-OE strain is able to reduce more thiosulfate to sulfide than the parent strain when grown in a defined medium. The likely electron donor for Tsr in *P. furiosus* is ferredoxin, the primary electron carrier in the cell capable of transferring electrons directly to the distal [4Fe-4S] cluster of TsrB in the heterodimeric TsrAB complex; indeed, we have shown that the Mo-containing TsrAB complex exhibits

ferredoxin-linked activity. The redox potential of ferredoxin is -454 mV, which compares with -402 mV for the thiosulfate/sulfide couple, making the ferredoxin-linked reduction of thiosulfate by Tsr an energetically-favorable reaction (Brereton et al. 1998). The question is how does thiosulfate enter the cytoplasm of *P. furiosus*? Interestingly, thiosulfate ($S_2O_3^{2-}$) is structurally very similar to tungstate (WO_4^{2-}) and molybdate (MoO_4^{2-}), and WtpA is known to bind the thiosulfate anion, although its affinity for thiosulfate has not been determined. Presumably it has low affinity for thiosulfate, which would explain the modest difference in sulfide production between Tsr-OE and the parent strain. The co-expression of Tsr and either PAE0022-PAE0023 or PAE3570-PAE3571, two putative (thio)sulfate transporters, did not have a significant effect on the growth or on sulfide production from thiosulfate. It is likely that both transporters are involved in either molybdate or tungstate transport in *P. aerophilum*, as the periplasmic orientation of Tsr in *P. aerophilum* membranes would not require the import of thiosulfate for activity. The co-expression of a thiosulfate-specific transporter might increase the sulfide production activity of the Tsr overexpression strain, but an appropriate transporter has yet to be identified in *P. aerophilum*.

Acknowledgements

This work was supported by grants (DE-FG05-95ER20175 to MWA and DE-SC0008074 to AKJ) from the Division of Chemical Sciences, Geosciences and Biosciences, Office of Basic Energy Sciences of the Department of Energy. We thank the Proteomics and Mass Spectrometry Core Facility at the University of Georgia for LC-MS/MS analysis.

Conflict of Interest

The authors declare that they have no conflicts of interest with the contents of this article.

Author Contributions

DKH, CHW, and MWA designed all experiments and wrote the paper. CHU and JS performed the genetic experiments, FLP performed metal analysis, DKH performed all enzymatic and physiological studies, and SW and AKJ designed and performed electrochemical experiments. All authors reviewed and edited the manuscript and approved the final version.

References

Adams, M. W. W., Holden, J. F., Menon, A. L., Schut, G. J., Grunden, A. M., Hou, C., Hutchins, A. M., Jenney, F. E., Kim, C., Ma, K., Pan, G., Roy, R., Sapra, R., Story, S. V., and Verhagen, M. F. J. M. (2001) Key role for sulfur in peptide metabolism and in regulation of three hydrogenases in the hyperthermophilic archaeon *Pyrococcus furiosus*. *J. Bacteriol.* **183**, 716–724

Afshar, S., Johnson, E., de Vries, S., and Schröder, I. (2001) Properties of a thermostable nitrate reductase from the hyperthermophilic archaeon *Pyrobaculum aerophilum*. *J. Bacteriol.* **183**, 5491–5495

Bevers, L. E., Hagedoorn, P.-L., Krijger, G. C., and Hagen, W. R. (2006) Tungsten transport protein A (WtpA) in *Pyrococcus furiosus*: the first member of a new class of tungstate and molybdate transporters. *J. Bacteriol.* **188**, 6498–6505

Brereton, P. S., Verhagen, M. F. J. M., Zhou, Z. H., and Adams, M. W. W (1998) Effect of iron- sulfur cluster environment in modulating the thermodynamic properties and biological function of ferredoxin from *Pyrococcus furiosus*. *Biochemistry* **37,** 7351-7362

Brondino, C. D., Passeggi, M. C. G., Caldeira, J., Almendra, M. J., Feio, M. J., Moura, J. J. G., and Moura, I. (2004) Incorporation of either molybdenum or tungsten into formate dehydrogenase from *Desulfovibrio alaskensis* NCIMB 13491; EPR assignment of the proximal iron-sulfur cluster to the pterin cofactor in formate dehydrogenases from sulfate-reducing bacteria. *JBIC J. Biol. Inorg. Chem.* **9**, 145–151

Bryksin, A. V., and Matsumura, I. (2010) Overlap extension PCR cloning: a simple and reliable way to create recombinant plasmids. *BioTechniques*. **48**, 463–465

Buc, J., Santini, C.-L., Giordani, R., Czjzek, M., Wu, L.-F., and Giordano, G. (1999) Enzymatic and physiological properties of the tungsten-substituted molybdenum TMAO reductase from *Escherichia coli*. *Mol. Microbiol.* **32**, 159–168

Chandrayan, S. K., McTernan, P. M., Hopkins, R. C., Sun, J., Jenney, F. E., and Adams, M. W. W. (2012) Engineering hyperthermophilic archaeon *Pyrococcus furiosus* to overproduce its cytoplasmic [NiFe]-hydrogenase. *J. Biol. Chem.* **287**, 3257–3264

Cozen, A. E., Weirauch, M. T., Pollard, K. S., Bernick, D. L., Stuart, J. M., and Lowe, T. M. (2009) Transcriptional map of respiratory versatility in the hyperthermophilic crenarchaeon *Pyrobaculum aerophilum*. *J. Bacteriol.* **191**, 782–794

de Vries, S., Momcilovic, M., Strampraad, M. J. F., Whitelegge, J. P., Baghai, A., and Schröder, I. (2010) Adaptation to a high-tungsten environment: *Pyrobaculum aerophilum* contains an active tungsten nitrate reductase. *Biochemistry (Mosc.)*. **49**, 9911–9921

de Vries, S., Strampraad, M. J. F., Lu, S., Moënne-Loccoz, P., and Schröder, I. (2003) Purification and characterization of the MQH_2:NO oxidoreductase from the hyperthermophilic Archaeon *Pyrobaculum aerophilum*. *J. Biol. Chem.* **278**, 35861–35868

Dietrich, W., and Klimmek, O. (2002) The function of methyl-menaquinone-6 and polysulfide reductase membrane anchor (PsrC) in polysulfide respiration of *Wolinella succinogenes*. *Eur. J. Biochem.* **269**, 1086–1095

Dilks, K., Rose, R. W., Hartmann, E., and Pohlschröder, M. (2003) Prokaryotic utilization of the twin-arginine translocation pathway: a genomic survey. *J. Bacteriol.* **185**, 1478–1483

Fourmond, V., Hoke, K. R., Heering, H. A., Baffert, C., Leroux, F., Bertrand, P., and Léger, C. (2009) SOAS: a free program to analyze electrochemical data and other one-dimensional signals. *Bioelectrochemistry* **76,** 141-147

Guiral, M., Tron, P., Aubert, C., Gloter, A., Iobbi-Nivol, C., and Giudici-Orticoni, M.-T. (2005) A membrane-bound multienzyme, hydrogen-oxidizing, and sulfur-reducing complex from the hyperthermophilic bacterium *Aquifex aeolicus*. *J. Biol. Chem.* **280**, 42004–42015

Hagedoorn, P.-L., Hagen, W. R., Stewart, L. J., Docrat, A., Bailey, S., and Garner, C. D. (2003) Redox characteristics of the tungsten DMSO reductase of *Rhodobacter capsulatus*. *FEBS Lett.* **555**, 606–610

Heinzinger, N. K., Fujimoto, S. Y., Clark, M. A., Moreno, M. S., and Barrett, E. L. (1995) Sequence analysis of the phs operon in *Salmonella typhimurium* and the contribution of thiosulfate reduction to anaerobic energy metabolism. *J. Bacteriol.* **177**, 2813–2820

Ikeda, S., Satake, H., Hisano, T., and Terazawa, T. (1972) Potentiometric argentimetric method for the successive titration of sulphide and dissolved sulphur in polysulphide solutions. *Talanta*. **19**, 1650–1654

Johnson, J. L., and Rajagopalan, K. V. (1976) Electron paramagnetic resonance of the tungsten derivative of rat liver sulfite oxidase. *J. Biol. Chem.* **251**, 5505–5511

Jørgensen, B. B. (1990) A thiosulfate shunt in the sulfur cycle of marine sediments. *Science*. **249**, 152–154

Kletzin, A., and Adams, M. W. W. (1996) Tungsten in biological systems. *FEMS Microbiol. Rev.* **18**, 5–63

Lipscomb, G. L., Schut, G. J., Thorgersen, M. P., Nixon, W. J., Kelly, R. M., and Adams, M. W. W. (2014) Engineering hydrogen gas production from formate in a hyperthermophile by heterologous production of an 18-subunit membrane-bound complex. *J. Biol. Chem.* **289**, 2873–2879

Lipscomb, G. L., Stirrett, K., Schut, G. J., Yang, F., Jenney, F. E., Scott, R. A., Adams, M. W. W., and Westpheling, J. (2011) Natural competence in the hyperthermophilic archaeon *Pyrococcus furiosus* facilitates genetic manipulation: construction of markerless deletions of genes encoding the two cytoplasmic hydrogenases. *Appl. Environ. Microbiol.* **77**, 2232–2238

McTernan, P. M., Chandrayan, S. K., Wu, C.-H., Vaccaro, B. J., Lancaster, W. A., and Adams, M. W. W. (2015) Engineering the respiratory membrane-bound hydrogenase of the hyperthermophilic archaeon *Pyrococcus furiosus* and characterization of the catalytically active cytoplasmic subcomplex. *Protein Eng. Des. Sel.* **28**, 1–8

Moon, Y.-J., Kwon, J., Yun, S.-H., Lim, H. L., Kim, M.-S., Kang, S. G., Lee, J.-H., Choi, J.-S., Kim, S. I., and Chung, Y.-H. (2012) Proteome analyses of hydrogen-producing hyperthermophilic archaeon *Thermococcus onnurineus* NA1 in different one-carbon substrate culture conditions. *Mol. Cell. Proteomics*.

Mukund, S., and Adams, M. W. (1996) Molybdenum and vanadium do not replace tungsten in the catalytically active forms of the three tungstoenzymes in the hyperthermophilic archaeon *Pyrococcus furiosus*. *J. Bacteriol.* **178**, 163–167

Schut, G. J., Bridger, S. L., and Adams, M. W. W. (2007) Insights into the metabolism of elemental sulfur by the hyperthermophilic archaeon *Pyrococcus furiosus*: characterization of a coenzyme A- dependent NAD(P)H sulfur oxidoreductase. *J. Bacteriol.* **189**, 4431–4441

Schut, G. J., Lipscomb, G. L., Nguyen, D. M. N., Kelly, R. M., and Adams, M. W. W. (2016) Heterologous production of an energy-conserving carbon monoxide dehydrogenase complex in the hyperthermophile P*yrococcus furiosus*. *Front. Microbiol.* **7**:29

Sevcenco, A.-M., Bevers, L. E., Pinkse, M. W. H., Krijger, G. C., Wolterbeek, H. T., Verhaert, P. D. E. M., Hagen, W. R., and Hagedoorn, P.-L. (2010) Molybdenum incorporation in tungsten aldehyde oxidoreductase enzymes from *Pyrococcus furiosus*. *J. Bacteriol.* **192**, 4143–4152

Stoffels, L., Krehenbrink, M., Berks, B. C., and Unden, G. (2012) Thiosulfate reduction in *Salmonella enterica* is driven by the proton motive force. *J. Bacteriol.* **194**, 475–485

Thauer, R. K., Jungermann, K., and Decker, K. (1977) Energy conservation in chemotrophic anaerobic bacteria. *Bacteriological Reviews* **41**, 100-180

Vaccaro, B. J., Menon, A. L., Lancaster, W. A., and Adams, M. W. W. (2009) Metallomics using inductively coupled plasma mass spectrometry. In *Current Protocols in Chemical Biology*, John Wiley & Sons, Inc., 10.1002/9780470559277.ch120031

Völkl, P., Huber, R., Drobner, E., Rachel, R., Burggraf, S., Trincone, A., and Stetter, K. O. (1993) *Pyrobaculum aerophilum* sp. nov., a novel nitrate-reducing hyperthermophilic archaeum. *Appl. Environ. Microbiol.* **59**, 2918–2926

Watanabe, T. and Honda, K. (1982) Measurement of the extinction coefficient of the methyl viologen cation radical and the efficiency of its formation by semiconductor photocatalysis. *J. Phys.Chem.* **1982**, 2617-2619

Wu, C.H., Schut, G. J., Poole, F. L., Haja, D. K., and Adams, M. W. W. (2018) Characterization of membrane-bound sulfane reductase: A missing link in the evolution of modern day respiratory complexes. *J Biol Chem* **293**, 16687-16696

Yang, H., Lipscomb, G. L., Keese, A. M., Schut, G. J., Thomm, M., Adams, M. W. W., Wang, B. C., and Scott, R. A. (2010) SurR regulates hydrogen production in *Pyrococcus furiosus* by a sulfur-dependent redox switch. *Mol. Microbiol.* **77**, 1111–1122

Table 4.1. Strains used and constructed in this study

Trivial Name	**Strain Name**	**Description**	**Ref.**
Parent	COM1	Δ*pyrF*	(1)
Tsr-OE	MW0484	Δ*pyrF*::P_{gdh} *pyrF*-P_{slp}(*PAE2859-61)*	This study
0022	MW0573	Δ*pyrF*::P_{gdh} *pyrF*-P_{slp}(*PAE2859-61);* P_{slp}(*PAE0022-3)*	This study
3570	MW0580	Δ*pyrF*::P_{gdh} *pyrF*-P_{slp}(*PAE2859-61);* P_{slp}(*PAE3570-1)*	This study

Table 4.2. Comparison of Tsr-W and Tsr-Mo

	Tsr-W	**Tsr-Mo**
V_{max} (U mg^{-1})	141	1,580
K_m (mM)	0.2 $\pm$ 0.02	0.1 $\pm$ 0.02
Metal content (W:Mo)	9:1	1:6
Metal content (Fe: W/Mo)	20:1	20:1
E_{peak} (mV)	-402	-255
Ferredoxin-linked activity (U mg^{-1})	N.D.	3.7 $\pm$ 0.4

N.D. Not determined

Figure 4.1

The genetic strategy used for construction of Tsr-OE. The knock-in cassette has homologous regions shown as the upstream flanking region (UFR) and downstream flanking region (DFR). The *pyrF* marker is under the control of the Pgdh promoter. The Tsr operon (PAE2859-61) is under the control of the Pslp promoter. *P. furiosus* Ribosome Binding Sites (RBS) were added upstream of genes as shown in black bars. The corresponding homologous loci of UFR and DFR are located in the GR1 intergenic region of COM1. Arrangement of the intergenic region after homologous recombination is also shown.

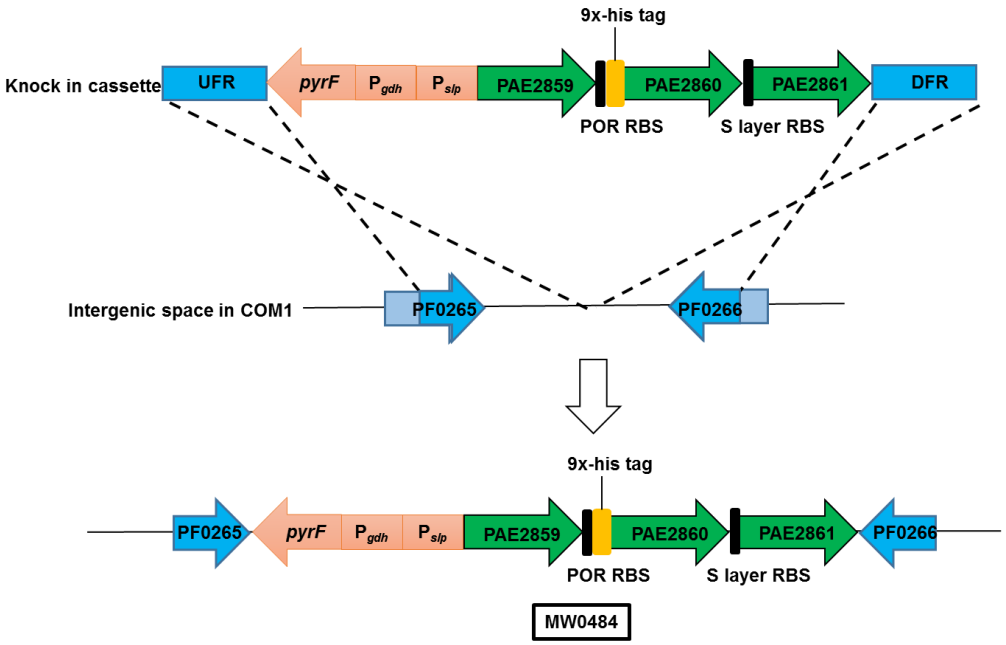
9x-his tag
Knock in cassette
UFR
pyrF
P gdh
P slp
PAE2859
PAE2860
PAE2861
DFR
POR RBS
S layer RBS
Intergenic space in COM1
PF0265
PF0266
9x-his tag
PF0265
pyrF
P gdh
P slp
PAE2859
PAE2860
PAE2861
PF0266
POR RBS
S layer RBS
MW0484

Figure 4.2

Purification of Tsr-W and Tsr-Mo. A: SDS PAGE gel of Q-HP fractions of Tsr-W and Tsr-Mo. B. Schematic representation of Tsr purified from *P. furiosus* cytoplasm.

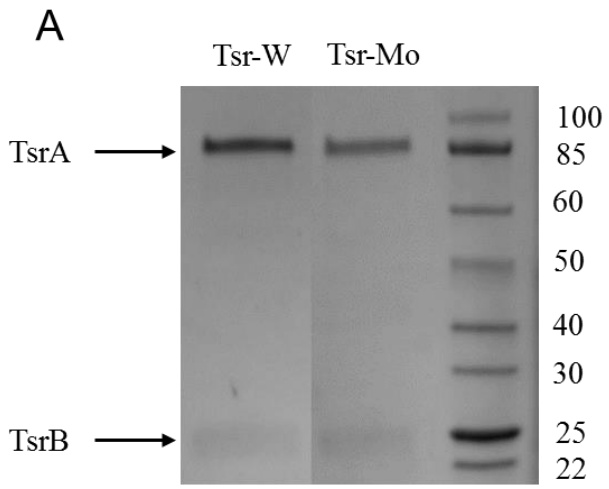
A
Tsr-W
Tsr-Mo
TsrA
TsrB
100
85
60
50
40
30
25
22

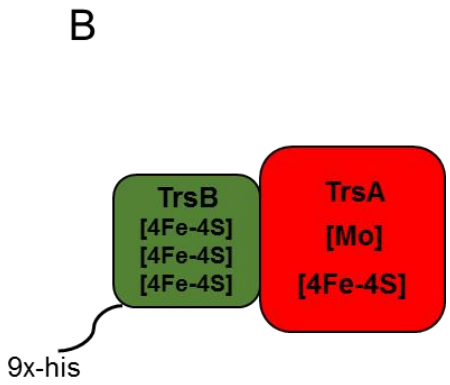
B
TrsB
[4Fe-4S]
[4Fe-4S]
[4Fe-4S]
TrsA
[Mo]
[4Fe-4S]
9x-his

Figure 4.3

Square wave voltammetry of Tsr-Mo (blue) and Tsr-W (red). SW current is normalized so that the maximum current is 1. The vertical dashed lines indicate the reduction potential of the peak for each enzyme's respective square wave. Other experimental conditions include: 60 °C, 2750 rpm electrode rotation rate, and pH 6.5.

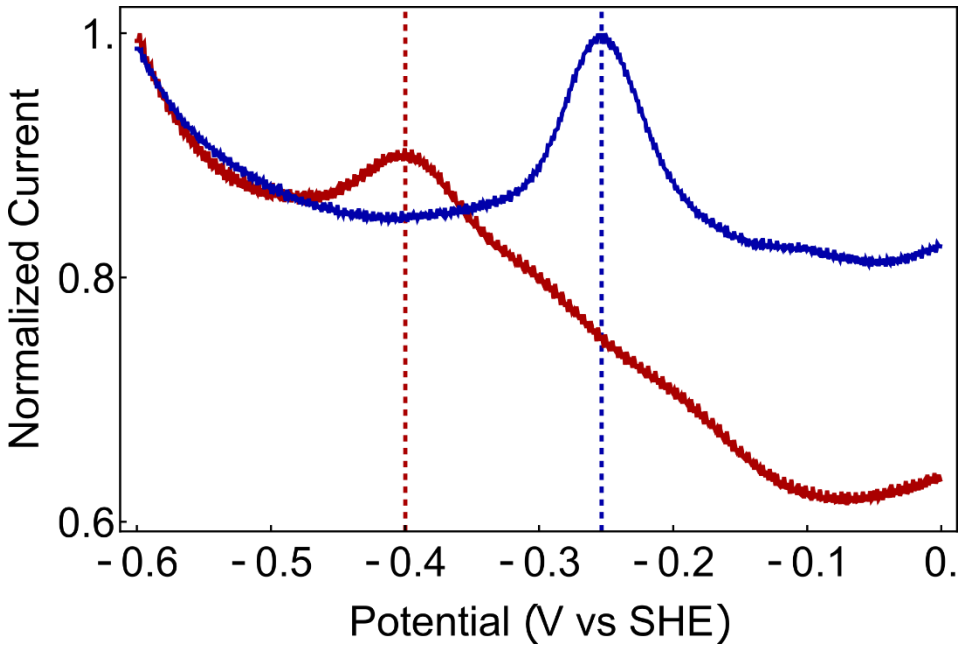
Normalized Current
1.
0.8
0.6
-0.6
-0.5
-0.4
-0.3
-0.2
-0.1
0.
Potential (V vs SHE)

Figure 4.4

Tsr shows *in vivo* activity when expressed in *P. furiosus*. A: Growth of the parent and Tsr-OE on maltose medium which does not require sulfur as a terminal electron acceptor. No difference in growth was observed ± thiosulfate between either strain. B: Hydrogen sulfide production in the headspace. Tsr-OE produced more hydrogen sulfide and at earlier time points than the parent. No sulfide was detected in either strain when thiosulfate was not added to the medium. Green lines: parent strain; Blue line: parent strain with addition of S_2O_3; purple lines: Tsr-OE strain; red lines: Tsr-OE strain with addition of S_2O_3. Error bars represent standard deviations obtained using biological triplicate samples.

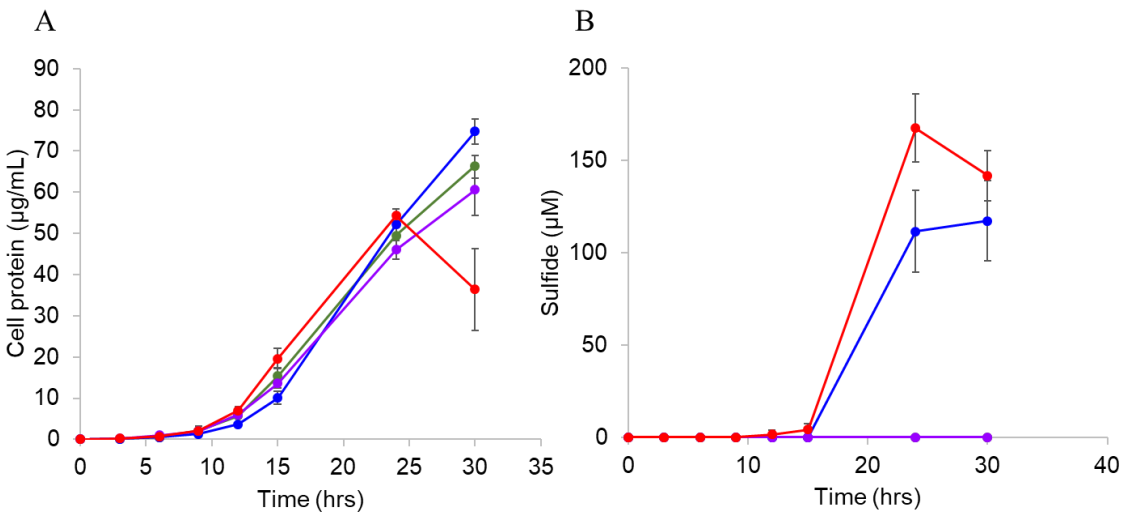
A
Cell protein (µg/mL)
90
80
70
60
50
40
30
20
10
0
0
5
10
15
20
25
30
35
Time (hrs)
B
Sulfide (µM)
200
150
100
50
0
0
10
20
30
40
Time (hrs)

Table S4.1. Localization of thiosulfate reductase activity

Fraction	Units (U)	Protein (mg)	Specific Activity (U/mg)
Cytoplasm	104.5	2464	0.04
Membrane	11.9	488	0.02

Table S4.2. Purification of Tsr-W

Step	Units (U)	Protein (mg)	Specific Activity (U/mg)	Yield (%)	Purification (fold)
WCE	135	3803	0.036	100	1
S100	241	2305	0.10	178	2.9
Ni-NTA	99	4	24.5	73	687
Q-HP	54	0.6	88.7	41	2494

Table S4.3. Purification of Tsr-Mo

Step	Units (U)	Protein (mg)	Specific Activity (U/mg)	Yield (%)	Purification (fold)
WCE	7729	3704	2.09	100	1
S100	7329	2544	2.88	94	1.4
Ni-NTA	1948	3.0	654	25	313
Q-HP	623	0.6	1015	8	486

Figure S4.1

Growth of the parent and Tsr-OE on peptides. A: The parent strain grows poorly on peptides in the absence of sulfur. Thiosulfate is not able to rescue this growth phenotype. B: Tsr-OE shows a similar phenotype to the parent, indicating that the reduction of thiosulfate is not able to support growth in *P. furiosus*. Blue line. no addition (of S^0 or thiosulfate (S2O3)); black line, addition of S^0; red line, addition of thiosulfate (S2O3). Error bars represent standard deviations obtained using biological triplicate samples.

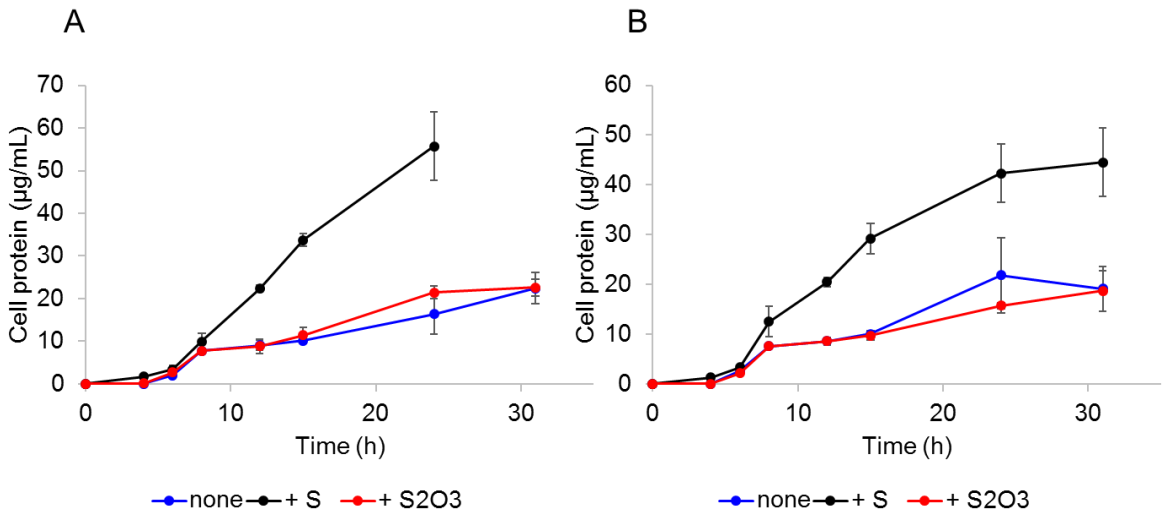
A
Cell protein (µg/mL)
70
60
50
40
30
20
10
0
0
10
20
30
Time (h)
none
+ S
+ S2O3
B
Cell protein (µg/mL)
60
50
40
30
20
10
0
0
10
20
30
Time (h)
none
+ S
+ S2O3

CHAPTER FIVE

IMPROVING ARSENIC TOLERANCE BY THE HETEROLOGOUS EXPRESSION OF A RESPIRATORY ARSENATE REDUCTASE IN *PYROCOCCUS FURIOSUS*[4]

[4] Haja DK*, Wu C-H*, Ponomarenko O, Poole FL, II, George GN, Adams MWW. 2020. *Applied and Environmental Microbiology*. 86.

*The authors contributed equally to this work

Abstract

Arsenate is a notorious toxicant that is known to disrupt multiple biochemical pathways. Many microorganisms have developed mechanisms to detoxify arsenate using the ArsC-type arsenate reductase and some even use arsenate as a terminal electron acceptor for respiration involving the arsenate respiratory reductase (Arr). ArsC-type reductases have been studied extensively but the phylogenetically-unrelated Arr system is less investigated and has not been characterized from Archaea. Herein, we heterologously-expressed the genes encoding Arr from the crenarchaeon *Pyrobaculum aerophilum* in the euryarchaeon *Pyrococcus furiosus*, both of which grow optimally near 100°C. Recombinant *P. furiosus* was grown on molybdenum (Mo)- or tungsten (W)-containing media and two types of recombinant Arr enzymes were purified, one containing Mo (Arr-Mo) and one containing W (Arr-W). Purified Arr-Mo had a 140-fold higher specific activity in arsenate (AsV) reduction than Arr-W and Arr-Mo also reduced arsenite (AsIII). The *P. furiosus* strain expressing Arr-Mo (the Arr strain) was able to use arsenate as a terminal electron acceptor during growth on peptides. In addition, the Arr strain had increased tolerance compared to the parent strain to arsenate and also, surprisingly, to arsenite. Compared to the parent, the Arr strain accumulated intracellularly almost an order of magnitude more arsenic when cells were grown in the presence of arsenite. XAS results suggest that the Arr strain of *P. furiosus* improves its tolerance to arsenite by increasing production of less toxic arsenate and non-toxic methylated arsenicals compared to the parent.

Importance

Arsenate respiratory reductases (Arr) are much less characterized than the detoxifying arsenate reductase system. The heterologous expression and characterization of an Arr from *Pyrobaculum aerophilum* in *Pyrococcus furiosus* provides new insights into the function of this enzyme. From *in vivo* studies, production of Arr not only enabled *P. furiosus* to use arsenate (AsV) as a terminal electron acceptor, it also provided the organism with a higher resistance to arsenate and also, surprisingly, to arsenite (AsIII). In contrast to the tungsten-containing oxidoreductase enzymes natively produced by *P. furiosus*, recombinant *Pb. aerophilum* Arr was much more active with molybdenum than it was with tungsten. It is also the first characterized Arr to be active with both molybdenum and tungsten in the active site.

Introduction

Arsenic is a well-known toxicant. The biologically-relevant oxidized pentavalent form, arsenate (AsV), replaces phosphate in many biochemical pathways due to the similarity in their structures and properties, while the reduced form, trivalent arsenite (AsIII), readily interacts with thiol-containing molecules such as cysteine (1). Microorganisms have developed systems to protect themselves against arsenic toxicity and to survive in natural environments where arsenic compounds are prevalent (2). Two distinct types of arsenate reductases are known, the cytoplasmic ArsC-type and the membrane-bound Arr-type, both of which reduce arsenate to arsenite (3).

The ArsC-type has been studied extensively in bacteria in which it functions in detoxification. The enzyme is encoded by an arsenic resistance (*ars*) operon that contains at minimum *arsR*, *arsB,* and *arsC.* Additionally, some genomes contain the accessory genes *arsD* and *arsA* (4). ArsR functions as a repressor of the operon (5, 6). ArsC is a small cytoplasmic protein that uses a redox active cysteine residue in the active site to reduces arsenate to arsenite using glutathione as the electron donor (7). Arsenite is then transported out of the cell by the arsenite transporter ArsB, which is energized by either a proton motive force or by the ArsA ATPase (4). ArsD is an arsenite chaperone that lowers the affinity of ArsA for arsenite (8). In contrast to ArsC, the Arr system enables arsenate to be used as a terminal electron acceptor of the respiratory chain. The enzyme consists of ArrA, the catalytic subunit that contains a pyranopterin cofactor and an iron sulfur cluster, and ArrB, which also contains iron-sulfur clusters. Compared to ArsC, the Arr-type arsenate reductase is much less studied. Three ArrAB have been purified from bacteria but none

have been characterized from archaea (9-11), which, as described below, appear to contain a different type of Arr.

The crenarchaeon *Pyrobaculum aerophilum* grows optimally at 100 °C using arsenate, as well as several other compounds, such as oxygen, nitrate and thiosulfate, as a terminal electron acceptor (12, 13). Based on transcriptional analyses in response to these respiratory substrates, the genes PAE1263-1265 were predicted to encode an arsenate respiratory reductase (Arr). Their expression increased up to eight-fold when arsenate was supplied in the growth medium (13, 14). Although the *P. aerophilum* Arr operon was not detected using degenerate PCR primers to bacterial Arr genes, the catalytic domain of bacterial Arr is conserved in *arrA* (PAE1265) (15). A model of *P. aerophilum* Arr based on the sequence analysis is shown in Figure 1. ArrA is the catalytic subunit containing a pyranopterin-binding site and a [4Fe-4S] cluster, while ArrB harbors three [4Fe-4S] clusters. In further contrast to characterized bacterial Arr, which are heterodimers, the enzyme from *P. aerophilum* contains a third subunit, ArrC, which is predicted to be a membrane bound anchor for ArrAB. ArrC is thought to oxidize quinol and transport the electrons to ArrA through the iron-sulfur clusters in ArrB (16). In contrast to this archaeal system, bacteria that respire arsenate, such as *Shewanella* species, do not have a gene encoding ArrC but contain the membrane-bound menaquinol-oxidizing protein CymA, which does not show any sequence similarity to ArrC. CymA has been shown by mutational studies to be crucial for arsenate reduction by *Shewanella* although it has not been biochemically characterized (17).

Since a genetic system is not available for *P. aerophilum,* we used the euryarchaeon *Pyrococcus furiosus* to heterologously produce its Arr with an affinity tag to facilitate

purification. *P. furiosus* is a strict anaerobe that also grows optimally near 100 °C (18) but unlike *P. aerophilum,* it grows only by fermenting carbohydrates or peptides. Elemental sulfur (S°) is essential as a terminal electron acceptor when cells are grown solely on peptides, while H_2 rather than H_2S is produced during growth on sugars in the absence of S° (19). The production of both H_2 and H_2S involves homologous respiratory complexes that use reduced ferredoxin (Fd) as the electron donor (20). *P. furiosus* has a well-developed genetic system and genes from other euryarcheota have been heterologously-expressed that enable the organism to oxidize formate and carbon monoxide and produce H_2 (21, 22).

The use of *P. furiosus* as an expression system also raises the issue of which metal it would insert into the recombinant Arr. The three bacterial ArrA enzymes contain molybdenum (Mo) (9-11); indeed, almost all life forms have one or more pyranopterin enzymes that all contain molybdenum (23). However, *P. furiosus* is very unusual in that it expresses five pyranopterin-containing oxidoreductases that instead contain tungsten (W) (24), a chemically-analogous metal (23). *P. furiosus* does not produce active native molybdoenzymes (25) and it has been proposed that in general hyperthermophilic microbes growing near the boiling point are predisposed to use tungsten rather than molybdenum as the metal in their pyranopterin enzymes (23). Previous work from our lab investigated the metal requirements of the closely related thiosulfate reductase (Tsr) complex from *P. aerophilum* heterologously purified from *P. furiosus*, and found that despite the fact that *P. aerophilum* requires tungsten for growth, the Tsr was more active with molybdenum than tungsten (26, 27). Hence, a key question was, does *P. furiosus* insert tungsten or

molybdenum into *P. aerophilum* Arr and, if both can be purified, which is the most active form?

To gain a deeper understanding of the biochemical properties of an archaeal Arr, we therefore heterologously expressed the *arr* operon (PAE1263-1265) from *P. aerophilum* in *P. furiosus*. The recombinant Arr enzyme was purified from *P. furiosus* cells grown on media with added molybdenum or tungsten and the recombinant enzymes were affinity purified and characterized. The response of *P. furiosus* with and without expressing the *P. aerophilum* Arr genes to growth in the presence of arsenate (AsV) and arsenite (AsIII) was also investigated.

Results

Recombinant P. aerophilum Arr produced in P. furiosus

The *P. furiosus* strain expressing the *P. aerophilum* Arr genes will be referred to as the Arr strain. It was constructed using the parent strain COM1 by homologous recombination of the knock-in cassette containing PAE1263-1265 into the intergenic space between PF0265 and PF0266, as shown in Figure S5.1. Initially a strain was constructed containing a sequence encoding a 9x-His-affinity tag at the N-terminus of ArrA, but we were unable to purify the Arr enzyme using a Ni-NTA column. A second strain was therefore constructed (MW0548) with the His-tag at the C-terminus of ArrA, and this enabled affinity purification of the recombinant Arr protein as described below. The expression of *arrA* (PAE1265), driven by the constitutive promoter P_{slp}, in the Arr strain was confirmed by qPCR analysis, where the level of expression was similar to that of pyruvate oxidoreductase (γ subunit, data not shown), an abundant enzyme involved in fermentation.

The *P. furiosus* Arr strain was initially grown in a medium containing both 10 μM W and 10 μM Mo, and the arsenate (AsV) reduction activity using reduced methyl viologen as the artificial electron donor was measured in the cell-free extract. As shown in Figure S5.2, no significant activity was observed in the parent strain (Par). To investigate if all three subunits were present as an intact complex in the Arr strain, the arsenate reduction assay was carried out using the cytoplasmic and membrane fractions, as shown in Figure S5.3. Unexpectedly, 80% of the activity was found in the cytoplasmic extract and ArrC could not be identified by LC-MS/MS in the active Arr-containing fractions purified from either the cytoplasmic or membrane fraction (see Figure 5.1). qPCR analysis indicated that its gene was transcribed at the expected level, suggesting that a stable ArrC subunit is not produced in the Arr strain.

Characterization of recombinant Arr containing Mo or W

The catalytic subunit ArrA is predicted to contain a pyranopterin cofactor. To investigate whether the active enzyme contained Mo or W bound to the pyranopterin site, the Arr strain was grown under two different conditions: 1) a so-called Mo condition in which 10 μM Mo but no W were added to the growth medium, and 2) a W condition, in which 10 μM W but no Mo were added. Cells (25 g wet wt.) grown under the Mo or W condition were used for the affinity purification of Arr and the results are summarized in Tables S5.1 and S5.2, respectively. With both cell types, after two chromatography steps (Ni-NTA and hydrophobic interaction), each enzyme was purified more than 1,400-fold with at least a 60% yield of activity. Surprisingly, we were able to purify active forms of the enzyme from

both cell types, but the Mo-containing enzyme (Arr-Mo) had more than a 140-fold higher arsenate reduction activity than the W-containing enzyme (Arr-W). Metal analysis revealed that the Fe to active-site metal ratio was 17:1 for both Arr-Mo and Arr-W, consistent with the presence of 4 [4Fe-4S] clusters. The Mo to W ratio in these enzymes was 9:1 and 1:86 for Arr-Mo and Arr-W, respectively, and kinetic analysis showed that Arr-W had a 20-fold higher affinity for arsenate compared to Arr-Mo (Table 5.1). The arsenite (AsIII) reduction activity and ferredoxin-linked arsenate (AsV) reduction activities (using the ferredoxin from *P. furiosus* in place of methyl viologen) were also measured for Arr-Mo and the activities were more than 100-fold lower than the arsenate (AsV) reduction activity using the artificial mediator (Table 5.1). Arr from *Alkalilimnicola ehrlichii* and *Shewanella* sp. strain ANA-3 were reported to exhibit arsenite (AsIII) oxidation activity (28). However, we were unable to measure arsenite oxidation activity with Arr-Mo using the high potential dye dichlorophenolindophenol as the electron acceptor. Because of the much higher arsenate reduction activity of Arr-Mo compared to Arr-W, the Mo growth condition was used to carry out the following *in vivo* experiments.

Arsenate (AsV) serves as a terminal electron acceptor for the Arr strain

P. furiosus shows significant growth on peptides only in the presence of S°, which is reduced to hydrogen sulfide. S° serves as a terminal electron acceptor with a reduction potential (E_0' ~ -280 mV) higher than hydrogen (E_0' = -420 mV) (19). The *P. furiosus* Arr strain (grown with Mo) was examined for the ability to use arsenate (E_0' = 60 mV) as a terminal acceptor to support peptide metabolism. The experiment was performed using a growth medium containing only peptides as the carbon source, and the Arr strain grew as well as the parent in the presence of S° (Figure 5.2a). However, the Arr strain showed

increased growth on peptides (by more than 50%, measured by cell protein) compared to the parent strain when 10 mM arsenate was present, although a long lag phase (30 hr) was observed before there was an effect. Stimulation of growth by arsenate was highly reproducible with the Arr strain, although under such conditions the strain did not reach the growth attained in the presence of S° (Figure 5.2a). These data suggested that the Arr strain was able to reduce arsenate (AsV) to arsenite (AsIII) to support growth. However, the parent strain also reduced arsenate to arsenite, as shown by the increase in the concentration of arsenite in growth medium, although the Arr strain produced slightly more arsenite than the parent (Figure 5.2b). Accordingly, as shown in Figure 5.2c, in the presence of arsenate, both the Par and Arr strains produced much less hydrogen gas during growth if arsenate was present. These results therefore suggest that *P. furiosus* can non-specifically reduce arsenate, and that the presence of Arr allows arsenate to stimulate growth, an effect not seen with the parent strain.

Arsenic toxicity

As shown in Figure 5.3a, the growth of *P. furiosus* by sugar (maltose) fermentation was strongly inhibited by the presence of 10 mM arsenate but the Arr strain was more resistant than the parent strain. Note that such inhibition of the parent strain was not observed during growth on peptides, presumably because there was minimal growth and the effect was not significant enough to be observed. As shown in Figure 5.3a, the maximum growth of the parent was about half that of the Arr strain in the presence of arsenate, although both strains exhibited a long lag phase compared to the control in the absence of arsenate (AsV). In addition, arsenite (AsIII) was detected in the growth medium of arsenate-inhibited cells. However, although the Arr strain generated slightly more (approximately 0.6 mM) than the

parent strain (approximately 0.5 mM), arsenite production was largely abiotic since a similar concentration was measured using the *P. furiosus* growth medium in the absence of cells (Figure 5.3b).

These data raised the issue of which species, arsenate or arsenite, was responsible for the growth inhibition. As shown in Figure 5.4, arsenite is a much more powerful inhibitor of growth than arsenate, and surprisingly, the Arr enzyme system once more confered high resistance. For example, in the presence of 1.0 mM arsenite, the growth of the parent was completely inhibited while that of the Arr strain decreased by about 30% (in terms of total cellular protein) although there was a significant lag phase. With 0.5 mM arsenite, the parent strain had a growth phenotype similar to that observed in the presence of 10 mM arsenate, and maximum growth was approximately half that of the Arr strain (Figure 5.4). These data therefore suggest that *P. furiosus* is inhibited not by arsenate (using 10 mM, Figure 5.3a) but by the arsenite (using 0.5 – 1.0 mM, Figure 5.4) that is generated abiotically (~ 0.5 mM, Figure 5.3b) and Arr confers resistance to arsenite rather than to arsenate.

Higher intracellular arsenic concentrations in the Arr strain

The intracellular arsenic concentration was determined in the parent and Arr strains when grown in the presence of 0.5 mM arsenite. As shown in Figure 5.5, the arsenic concentration in the cell-free extract of the Arr strain was almost an order of magnitude higher than that of the parent strain. A similar result was observed in the presence of 0.1 mM arsenite, where no lag phase was found before reaching stationary phase in the parent (data not shown). This suggests that the higher concentration of intracellular arsenic in the Arr strain might be due to the presence of the Arr enzyme. To investigate this, the

cytoplasmic extract of the Arr strain grown with 0.5 mM arsenite was applied to a desalting column and the distribution of arsenic was determined. As shown in Figure S5.4, most of arsenic was recovered in the low molecular weight fractions (< 5 kDa) suggesting that the majority of the arsenic in the cell is not associated with proteins.

In order to determine the identity of the arsenic species present in both the parent and Arr strains, cells grown in the presence of 0.5 mM arsenite were analyzed by X-ray Absorbption Spectroscopy (XAS). The results are shown in Figure 5.6. The major component contributing to both spectra is arsenite, with the rest of the fitting represented by pentavalent methylated arsenicals, including mono- and di-methyl arsenate (MMA and DMA), trimethylarsine oxide (TMAO), and trimethylarsine sulfide (TMAS) (Table S5.3-S5.4, Figure S5.5). However, the major difference between the samples was the distribution of these species, with methylated species representing only 27 $\pm$ 3% of the sample in the parent strain and 39 $\pm$ 7% in the Arr strain, indicating that the Arr strain was converting a larger percentage of arsenite to the methylated species. Because the Arr strain accumulates approximately 10x the intracellular arsenic compared to the parent (20 vs 2 nmol/mg cell protein), this corresponds to approximately 9 nmols/mg of methylated arsenicals, compared to ~0.5 nmols/mg in the parent. The implications of the increased production of methylated arsenicals by the Arr strain on arsenite toxicity in *P. furiosus* are discussed below.

Discussion

Herein we heterologously-expressed in *P. furiosus* an archaeal arsenate respiratory reductase (Arr) from *P. aerophilum.* The enzyme was affinity purified and is a heterodimer (ArrAB) although it is predicted to contain a third and membrane-bound subunit (ArrC).

Even though the *arrC* gene was transcribed as expected, most of the Arr activity was in the cytoplasmic extract rather than in the membranes (Figure S5.3) and ArrC was not detected by mass spectrometry in the purified enzyme. This is probably because *P. aerophilum* uses a Twin-Arginine Translocation (TAT) system for membrane transport and *arrC* has a TAT signal motif for translocation to the periplasmic side of the membrane (13). However, *P. furiosus* does not contain the TAT export system (29) and in its absence ArrC appears to be unstable and disassociates from ArrAB.

Although both Arr-Mo and Arr-W are active in reducing arsenate (AsV), the Mo form is about 100-fold more active, suggesting that the native enzyme contains molybdenum rather than tungsten. Nitrate reductase (Nar) and thiosulfate reductase (Tsr), both DMSO reductase-family enzymes, have been previously characterized from *P. aerophilum* and were both found to be more active with Mo than W (26, 30). However, a W-containing aldehyde ferredoxin oxidorectase (AOR) has also been characterized from *P. aerophilum*, and its growth has been shown to be dependent on tungstate and inhibited by molybdate (27, 31). While Arr-W has a lower catalytic activity than Arr-Mo, its affinity for arsenate is 20-fold higher, which is consistent with different metals in the catalytic site and could allow *P. aerophilum* to use arsenate as a terminal electron acceptor under tungsten growth conditions. This makes *P. aerophilum* Arr the first example of an active tungsten-containing arsenate reductase.

The Mo-form of Arr was extremely active *in vitro* in reducing arsenate with reduced methyl viologen and exhibited significant activity with reduced ferredoxin as the electron donor (Table 5.3). We assume that ferredoxin was also an electron donor *in vivo* and enabled *P. furiosus* to exhibit significant growth on peptides using arsenate as the electron

acceptor compared to the parent strain (Figure 5.2a). This is the first example of *P. furiosus* utilizing a Mo-enzyme to support growth. The decreased H_2 production also supported the diversion of reducing equivalents for arsenate reduction (Figure 5.2c). Interestingly, we also observed a similar result for the parent strain in H_2 production but, in contrast to the Arr strain, there was no stimulation of growth in the presence of arsenate. This lack of growth may be due to the toxicity of abiotically-generated arsenite (AsIII) to the parent strain but not the Arr strain. As discussed below, the physiological effects of heterologously-expressed Arr appear to be related to removing arsenite rather than arsenate.

Purified Arr-Mo had significant arsenite reduction activity (methyl viologen-linked, Table 5.3) and we hypothesize that this is responsible for the Arr strain of *P. furiosus* being much more resistant to arsenite compared to the parent strain, both from endogenous (growth on 10 mM AsV produces ~0.5 mM AsIII, Figure 5.3b) and exogenous (1.0 mM AsIII, Figure 5.4) sources. For example, in arsenate-resistant bacteria, arsenate (AsV) enters cells via phosphate transporters and is reduced by ArsC to arsenite (AsIII). The arsenite is then extruded to the outside of the cell either by an energy-dependent ArsB transporter or the acr3 efflux permease (32, 33). In arsenite resistance, arsenite enters cells through aquaglyceroporins (34) and an arsenite methyltransferase (ArsM) is involved in the process of detoxification, where arsenite is sequentuially reduced and oxidatively methylated to the volatile trimethylarsine (TMA) that leaves cells (35). Homologs of both ArsC and acr3 are annotated in the *P. furiosus* genome, but parent cells did not contain detectable arsenate reductase activity. While the genome of *P. furiosus* does not contain an annotated ArsM, it is possible that it used non-specific metal methylases or radical-SAM

enzymes to methylate reduced arsenic species. Best-fit calculations of the XAS spectra of both parent and Arr cells showed a mixture of methylated arsenicals, including MMA, DMA, and TMAS. MMA and DMA are both intermediates in the production of TMA, which readily reacts with sulfur species to produce the non-toxic TMAS (36). The overexpression of *P. aerophilum* Arr likely increased the pool of reduced arsenic species available for methylation, as the Arr strain showed a ~22% shift from AsIII to methylated species compared to the parent strain, corresponding to 9 nmols of methylated arsenicals per mg of protein in the Arr strain (compared to 0.5 nmols/mg in the parent) Because the Arr strain accumulates approximately 10x the intracellular arsenic compared to the parent, this corresponds to approximately 9 nmols of methylated arsenicals per 1 mg of cells, compared to ~0.5 nmols/mg in the parent. Hence, the over-expression of Arr likely explains the resistance of the *P. furiosus* Arr strain to both arsenate and to arsenite.

Materials and Methods

Strain construction

A genetically tractable *Pyrococcus furiosus* strain, COM1, was used for the heterologous expression of the arsenate respiratory reductase (Arr) from *Pyrobaculum aerophilum* (37). A knock-in cassette, containing the fragments shown in Figure S5.1, was assembled using overlapping PCR (38). The upstream flanking region (UFR), the promoter of the gene encoding the S-layer protein (P_{slp} of PF1399), and the downstream flanking region (DFR), were amplified from *P. furiosus* genomic DNA, and the selection marker (P_{gdh}-*pyrF*), was amplified from pGLW021 (37). PAE1263-PAE1265 were amplified using *P. aerophilum* genomic DNA as the template. A 9x-His-tag was placed at the C-terminus of PAE1265 and the ribosomal binding sites (RBS) of *P. furiosus* pyruvate oxidoreductase γ subunit

(PORγ, PF0971) and S-layer protein were placed upstream of *arrC* (PAE1264) and *arrA* (PAE1265), respectively. The genomic DNA of *P. furiosus* and *Pb. aerophilum* was isolated by ZymoBead Genomic DNA Kit (Zymo Research). The *P. aerophilum* strain was purchased from DSMZ (DSMZ-7523) and medium 611 was used for cultivation. The transformants were grown as previously described (37). Genomic DNA was also used for PCR screening using GXL polymerase (Takara, ClonTech). The PCR screening was performed using a pair of primers outside the UFR and DFR. The PCR confirmed colony was sequence verified using the Genewiz service.

Growth condition

The *P. furiosus* strains constructed and used in this study are listed in Table 5.2. The growth medium was used as previously described with some modifications (37). The inoculum was first transferred in the medium containing no exogenous Mo or W for ten generations before being used in the experiments. All media contained 1x base salt, 1x trace minerals without molybdenum, 2 g/L yeast extract, 5 g/L maltose, 0.17 g/L cysteine, 1 g/L sodium bicarbonate, 1 mM potassium phosphate (pH 6.8) and 1 mM MOPS buffer (pH 6.8). Molybdate or tungstate (to a final concentration of 10 μM) and sodium arsenate (10 mM) or sodium arsenite (0.5 and 1.0 mM) were added as indicated. For the growth study with peptides, the medium contained 1x base salt, 1x trace minerals without molybdenum, 0.1 g/L yeast extract, 5 g/L casein, 0.17 g/L cysteine, 1 g/L sodium bicarbonate, 1 mM potassium phosphate (pH 6.8), 1 mM MOPS buffer (pH 6.8), 10 μM molybdate and 10 mM sodium arsenate. The medium for the 20 L fermentations contained 1x base salt, 1 x trace minerals without molybdate 5 g/L yeast extract, 5 g/L maltose, 5 g/L casein, 1 g/L cysteine and 1 mM potassium phosphate (pH 6.8) with 10 μM molybdate or tungstate

supplied where indicated. The 20 L fermentations were carried out as previously described (39) and the harvested cells were frozen in liquid nitrogen and store at -80 °C. For growth studies, 1 mL cultures were harvested by centrifugation at 14,000 xg for 5 min. The cells were lysed osmotically using 1 mL distilled H_2O and cell debris was removed by centrifugation at 14,000 xg for 1 min. The supernatant was taken for protein estimation using Protein Assay Reagent (Bio-Rad).

Purification of Arr

All purification steps were performed under anaerobic conditions. Frozen cells were lysed osmotically in 25 mM sodium phosphate, pH 7.5, containing 1 mM DTT and 50 μg/mL DNase I (5 mL per gram of frozen cells) for 1 hour at room temperature in an anaerobic chamber (Coy, Grass Lake, MI). The cell-free extract was centrifuged at 100,000 xg for 1 hour using a Beckman-Coulter Optima L-90K ultracentrifuge. The supernatant was collected and applied to a 5 mL His-Trap FF Ni-NTA column (GE Healthcare) using a NGC Chromatography System (Bio-Rad). The column was equilibrated with 25 mM sodium phosphate, pH 7.5, containing 300 mM NaCl and 1 mM DTT (Buffer A) before loading the sample and 2% Buffer B (Buffer A containing 500 mM imidazole) was loaded with the cytoplasmic extract. The column was washed with Buffer A, and the bound protein was eluted with a 20-column volume gradient from 0 to 100% Buffer B. Active fractions containing MV-linked arsenate reduction were pooled and applied to an equilibrated 1 mL phenyl HP column (GE Healthcare) while diluting 5-fold with 50 mM sodium phosphate, pH 7.0, containing 1.5 M ammonium sulfate. A 30-column volume gradient from 20 to 100% 50 mM sodium phosphate, pH 7.0, was used to elute the bound protein.

Enzyme assays

All assays were carried out anaerobically at 80°C. The routine arsenate (AsV) reduction assay was carried out anaerobically using sealed cuvettes that contained 2 mL 100 mM 3-(N-morpholino) propanesulfonic acid (MOPS), pH 7.5, 150 mM NaCl, 5 mM sodium arsenate and 1 mM methyl viologen (MV). The assay cuvettes were pre-heated to 80°C. 0.1 mM Titanium citrate was added to reduce MV, and the activity was measured by monitoring the decrease in absorbance at 600 nm using a 100 Cary UV-Vis spectrophotometer with a peltier-based temperature controller from Agilent technologies (Santa Clara). The reaction was started with the addition of enyzme. An extinction coefficient of 8.25 mM^{-1} cm^{-1} was used for reduced MV. One unit of activity is defined as 1 µmol of substrate reduced per minute. The arsenite (AsIII) reduction assay was performed similarly with 5 mM sodium arsenite, which was purified using HPLC as described below, as the substrate. For arsenite oxidation activity, 1 mM dichlorophenolindophenol (DCPIP) was used to measure the activity in the presence of 5 mM sodium arsenite. For *Pf* ferredoxin (Fd)-dependent arsenate reduction activity, Fd was reduced using titanium citrate and the oxidation of Fd was monitored at 425 nm (ϵ = 13 mM^{-1} cm^{-1}).

Metal concentration determination

The concentrations of arsenic in spent media and the concentrations of Mo and W in purified proteins were measured using an octopole-based ICP-MS (7500ce; Agilent Technologies). Arsenite (AsIII) concentration was measured using HPLC for speciation followed by ICP-MS for concentration determination. A Zorbax SAX column (Agilent

Technologies) was used in the speciation with a mobile phase of 60 mM KH_2PO_4 and a flow rate of 1 mL/min.

Intracellular arsenic concentration determination

Cultures grown with 5g/L maltose, 2g/L yeast extract and 0.5 mM sodium arsenite were centrifuged at 5,000 xg for 1 min to remove insoluble materials. The cells were washed three times with 1x *P. furiosus* base salt medium. Washed cells were lysed osmotically with 50 mM Tris-HCl, pH 8.0, containing 50 μg/mL DNase I (5 mL per gram of wet cells) for 1 hour at room temperature in an anaerobic chamber. Cell debris was removed by centrifugation at 14,000 xg for 10 min. The supernatant was collected and the arsenic concentration was determined by ICP-MS. To estimate the size of the arsenic species in the cytoplasmic extract, the Arr strain was grown with 0.5 mM sodium arsenite ande prepared as described above. After a 1-hour lysis, the cell-free extract was centrifuged at 100,000 xg for 1 hour, and the supernatant was applied to a 5 mL HiTrap Desalting Column (GE Healthcare) that was equilibrated with 50 mM Tris-HCl, pH 8.0. ICP-MS was used to measure the arsenic concentration.

XAS Studies

Cultures grown with 5g/L maltose, 2g/L yeast extract and 0.5 mM sodium arsenite were centrifuged at 10,000 xg for 10 min to pellet cells. Cells were washed three times with 2x *P. furiosus* base salts medium and resuspended in the same medium. The Lucite cuvettes with 2 mm-wide window were insulated with a metal-free Mylar tape, filled with a syringe, frozen in liquid nitrogen, and sent on dry ice to the Canadian Light Source for XAS examination.

The XAS experiments were conducted at the BioXAS-Main Station of the Spectroscopy Sector of the newly commissioned BioXAS facility (07ID-2) at the Canadian Light Source. Spectra of standard compounds were collected at the Stanford Synchrotron Radiation Lightsource using beamline 7-3. In both cases a Si(220) double crystal monochromator was used and XAS data were measured as the primary fluorescence excitation spectrum using a 32-element germanium array detector (Canberra Indusries, Meriden CT, USA) (41) positioned at 90° to the incident X-ray beam, with the sample at 45°. Samples were maintained at a temperature of 10 K in a liquid helium flow cryostat (Oxford Instruments, Concord, MA, USA). The incident energy was calibrated with reference to the lowest energy As K-edge inflection point of elemental arsenic, which was assumed to be 11,867.0 eV. Primary data reduction and the least-square fitting of the samples' near-edge XAS spectra were conducted using the EXAFSPAK suite of programs (42). Selected As-K near-edge XAS spectra, used for the least-square fitting, are shown in supplemental Figure S5.

Other methods

Hydrogen was measured in the headspace for growth studies with the 6850 Network GC system from Agilent Technologies. Purified ArrAB was analyzed by SDS-PAGE using precast Criterion TGX (4-15%) gels (Bio-Rad). MALDI-TOF and LC-MS/MS were performed by the PAMS Facility at the University of Georgia.

Data Availability

All data are included here and in the supplemental material. All strains used are stored as glycerol stocks internally and are available upon request.

Acknowledgments

This work was supported by a grant (DE-FG05-95ER20175 to MWA) from the Division of Chemical Sciences, Geosciences and Biosciences, Office of Basic Energy Sciences of the Department of Energy. Research at the University of Saskatchewan was supported by a Canada Research Chair (GNG) and the Natural Sciences and Engineering Research Council of Canada (GNG). We thank the Proteomics and Mass Spectrometry Core Facility at the University of Georgia for MALDI-TOF and LC-MS/MS analyses. XAS was performed at the Spectroscopy Sector of the BioXAS facility (07ID-2) of the Canadian Light Source, a national research facility of the University of Saskatchewan, which is supported by the Canada Foundation for Innovation (CFI), the Natural Sciences and Engineering Research Council (NSERC), the National Research Council (NRC), the Canadian Institutes of Health Research (CIHR), the Government of Saskatchewan, and the University of Saskatchewan. We are thankful to Roman Chernikov, Emilio Heredia and Nataliya Dolgova for their assistance during XAS experiments. Use of the Stanford Synchrotron Radiation Lightsource (SSRL), SLAC National Accelerator Laboratory, is supported by the U.S. Department of Energy (DOE), Office of Science, Office of Basic Energy Sciences under Contract number DE-AC02-76SF00515, respectively. The SSRL Structural Molecular Biology Program is supported by the DOE Office of Biological and Environmental Research, and by the National Institutes of Health, National Institute of General Medical Sciences (including P41GM103393). The contents of this publication are solely the responsibility of the authors and do not necessarily represent the official views of NIGMS or NIH.

References

1. Hughes MF. 2002. Arsenic toxicity and potential mechanisms of action. Toxicol Lett 133:1-16.
2. Lebrun E, Brugna M, Baymann F, Muller D, Lievremont D, Lett MC, Nitschke W. 2003. Arsenite oxidase, an ancient bioenergetic enzyme. Mol Biol Evol 20:686-93.
3. Silver S, Phung LT. 2005. Genes and enzymes involved in bacterial oxidation and reduction of inorganic arsenic. Appl Environ Microbiol 71:599-608.
4. Rosen BP. 2002. Biochemistry of arsenic detoxification. FEBS Lett 529:86-92.
5. Silver S, Phung LT. 1996. Bacterial heavy metal resistance: new surprises. Annu Rev Microbiol 50:753-89.
6. Cai J, DuBow MS. 1996. Expression of the *Escherichia coli* chromosomal ars operon. Can J Microbiol 42:662-71.
7. Martin P, DeMel S, Shi J, Gladysheva T, Gatti DL, Rosen BP, Edwards BFP. 2001. Insights into the Structure, Solvation, and Mechanism of ArsC Arsenate Reductase, a Novel Arsenic Detoxification Enzyme. Structure 9:1071-1081.
8. Lin Y-F, Walmsley AR, Rosen BP. 2006. An arsenic metallochaperone for an arsenic detoxification pump. Proceedings of the National Academy of Sciences of the United States of America 103:15617-15622.
9. Afkar E, Lisak J, Saltikov C, Basu P, Oremland RS, Stolz JF. 2003. The respiratory arsenate reductase from *Bacillus selenitireducens* strain MLS10. FEMS Microbiol Lett 226:107-12.
10. Malasarn D, Keeffe JR, Newman DK. 2008. Characterization of the arsenate respiratory reductase from *Shewanella sp*. strain ANA-3. J Bacteriol 190:135-42.

11. Krafft T, Macy JM. 1998. Purification and characterization of the respiratory arsenate reductase of *Chrysiogenes arsenatis*. Eur J Biochem 255:647-53.

12. Volkl P, Huber R, Drobner E, Rachel R, Burggraf S, Trincone A, Stetter KO. 1993. *Pyrobaculum aerophilum* sp. nov., a novel nitrate-reducing hyperthermophilic archaeum. Appl Environ Microbiol 59:2918-26.

13. Cozen AE, Weirauch MT, Pollard KS, Bernick DL, Stuart JM, Lowe TM. 2009. Transcriptional map of respiratory versatility in the hyperthermophilic crenarchaeon *Pyrobaculum aerophilum*. J Bacteriol 191:782-94.

14. Fitz-Gibbon ST, Ladner H, Kim UJ, Stetter KO, Simon MI, Miller JH. 2002. Genome sequence of the hyperthermophilic crenarchaeon *Pyrobaculum aerophilum*. Proc Natl Acad Sci U S A 99:984-9.

15. Duval S, Ducluzeau AL, Nitschke W, Schoepp-Cothenet B. 2008. Enzyme phylogenies as markers for the oxidation state of the environment: the case of respiratory arsenate reductase and related enzymes. BMC Evol Biol 8:206.

16. van Lis R, Nitschke W, Duval S, Schoepp-Cothenet B. 2013. Arsenics as bioenergetic substrates. Biochim Biophys Acta, Bioenerg 1827:176-188.

17. Murphy JN, Saltikov CW. 2007. The cymA gene, encoding a tetraheme c-type cytochrome, is required for arsenate respiration in *Shewanella* species. J Bacteriol 189:2283-2290.

18. Fiala G, Stetter KO. 1986. *Pyrococcus furiosus* sp nov represents a novel genus of marine heterotrophic archaebacteria growing optimally at 100°C. Arch Microbiol 145:56-61.

19. Adams MW, Holden JF, Menon AL, Schut GJ, Grunden AM, Hou C, Hutchins AM, Jenney FE, Jr., Kim C, Ma K, Pan G, Roy R, Sapra R, Story SV, Verhagen MF. 2001. Key role for sulfur in peptide metabolism and in regulation of three hydrogenases in the hyperthermophilic archaeon *Pyrococcus furiosus*. J Bacteriol 183:716-24.

20. Schut GJ, Boyd ES, Peters JW, Adams MWW. 2013. The modular respiratory complexes involved in hydrogen and sulfur metabolism by heterotrophic hyperthermophilic archaea and their evolutionary implications. FEMS Microbiol Rev 37:182-203.

21. Lipscomb GL, Schut GJ, Thorgersen MP, Nixon WJ, Kelly RM, Adams MW. 2014. Engineering hydrogen gas production from formate in a hyperthermophile by heterologous production of an 18-subunit membrane-bound complex. J Biol Chem 289:2873-9.

22. Schut GJ, Lipscomb GL, Nguyen DM, Kelly RM, Adams MW. 2016. Heterologous production of an energy-conserving carbon monoxide dehydrogenase complex in the hyperthermophile *Pyrococcus furiosus*. Front Microbiol 7:29.

23. Johnson MK, Rees DC, Adams MW. 1996. Tungstoenzymes. Chem Rev 96:2817-2840.

24. Bevers LE, Bol E, Hagedoorn PL, Hagen WR. 2005. WOR5, a novel tungsten-containing aldehyde oxidoreductase from *Pyrococcus furiosus* with a broad substrate Specificity. J Bacteriol 187:7056-61.

25. Sevcenco AM, Bevers LE, Pinkse MW, Krijger GC, Wolterbeek HT, Verhaert PD, Hagen WR, Hagedoorn PL. 2010. Molybdenum incorporation in tungsten aldehyde oxidoreductase enzymes from *Pyrococcus furiosus*. J Bacteriol 192:4143-52.

26. Haja DK, Wu C-H, Poole FL, Sugar J, Williams SG, Jones AK, Adams MWW. 2020. Characterization of thiosulfate reductase from Pyrobaculum aerophilum heterologously produced in Pyrococcus furiosus. Extremophiles 24:53-62.

27. Hagedoorn PL, Chen T, Schröder I, Piersma SR, Vries Sd, Hagen WR. 2005. Purification and characterization of the tungsten enzyme aldehyde:ferredoxin oxidoreductase from the hyperthermophilic denitrifier Pyrobaculum aerophilum. JBIC Journal of Biological Inorganic Chemistry 10:259-269.

28. Richey C, Chovanec P, Hoeft SE, Oremland RS, Basu P, Stolz JF. 2009. Respiratory arsenate reductase as a bidirectional enzyme. Biochem Biophys Res Commun 382:298-302.

29. Dilks K, Rose RW, Hartmann E, Pohlschroder M. 2003. Prokaryotic utilization of the twin-arginine translocation pathway: a genomic survey. J Bacteriol 185:1478-83.

30. de Vries S, Momcilovic M, Strampraad MJ, Whitelegge JP, Baghai A, Schroder I. 2010. Adaptation to a high-tungsten environment: *Pyrobaculum aerophilum* contains an active tungsten nitrate reductase. Biochemistry 49:9911-21.

31. Afshar S, Kim C, Monbouquette HG, Schroder II. 1998. Effect of tungstate on nitrate reduction by the hyperthermophilic archaeon pyrobaculum aerophilum. Applied and environmental microbiology 64:3004-3008.

32. Bini E. 2010. Archaeal transformation of metals in the environment. FEMS Microbiol Ecol 73:1-16.

33. Fu H-L, Meng Y, Ordóñez E, Villadangos AF, Bhattacharjee H, Gil JA, Mateos LM, Rosen BP. 2009. Properties of Arsenite Efflux Permeases (Acr3) from Alkaliphilus metalliredigens and Corynebacterium glutamicum. Journal of Biological Chemistry 284:19887-19895.

34. Rosen BP, Tamas MJ. 2010. Arsenic transport in prokaryotes and eukaryotic microbes. Adv Exp Med Biol 679:47-55.

35. Qin J, Rosen BP, Zhang Y, Wang G, Franke S, Rensing C. 2006. Arsenic detoxification and evolution of trimethylarsine gas by a microbial arsenite S-adenosylmethionine methyltransferase. Proc Natl Acad Sci U S A 103:2075-80.

36. Rick Irvin T, Irgolic KJ. 1995. In-vitro prenatal toxicity of trimethylarsine, trimethylarsine oxide and trimethylarsine sulfide. Applied Organometallic Chemistry 9:315-321.

37. Lipscomb GL, Stirrett K, Schut GJ, Yang F, Jenney FE, Jr., Scott RA, Adams MW, Westpheling J. 2011. Natural competence in the hyperthermophilic archaeon *Pyrococcus furiosus* facilitates genetic manipulation: construction of markerless deletions of genes encoding the two cytoplasmic hydrogenases. Appl Environ Microbiol 77:2232-8.

38. Bryksin AV, Matsumura I. 2010. Overlap extension PCR cloning: a simple and reliable way to create recombinant plasmids. Biotechniques 48:463-5.

39. Chandrayan SK, McTernan PM, Hopkins RC, Sun J, Jenney FE, Jr., Adams MW. 2012. Engineering hyperthermophilic archaeon *Pyrococcus furiosus* to overproduce its cytoplasmic [NiFe]-hydrogenase. J Biol Chem 287:3257-64.

Table 5.1. Properties of Arr

Property	**Arr-Mo**	**Arr-W**
K_m (arsenate, µM)	340 ± 50	17.9 ± 2
V_{max} (U/mg)	1,800 ± 160	13.0 ± 2.0
Metal content (Mo:W)	9 : 1	1 : 86
Metal content (Fe:Mo/W)	17 : 1	17 : 1
Ferredoxin-linked arsenate (AsV) reduction (U/mg)	20.9 ± 1.7	N.D.
Arsenite (5 mM AsIII) reduction (U/mg)	6.79 ± 0.36	N.D.

N.D. Not determined

Table 5.2. Strains used and constructed in this study

Trivial Name	**Strain Name**	**Description**	**Ref.**
Par	COM1c	Δ*pyrF*::P_{gdh} *pyrF*	(40)
Arr	MW0548	Δ*pyrF*::P_{gdh} *pyrF* P_{slp} (PAE1263-PAE1265-9x His)	This study

Figure 5.1

SDS-PAGE of purified Arr and the proposed cofactor content of ArrABC based on sequence analysis. ArrA and ArrB were identified by MALDI-TOF from bands cut from the gel. ArrC was not identified in the purified protein and is shown with a dashed outline in the model.

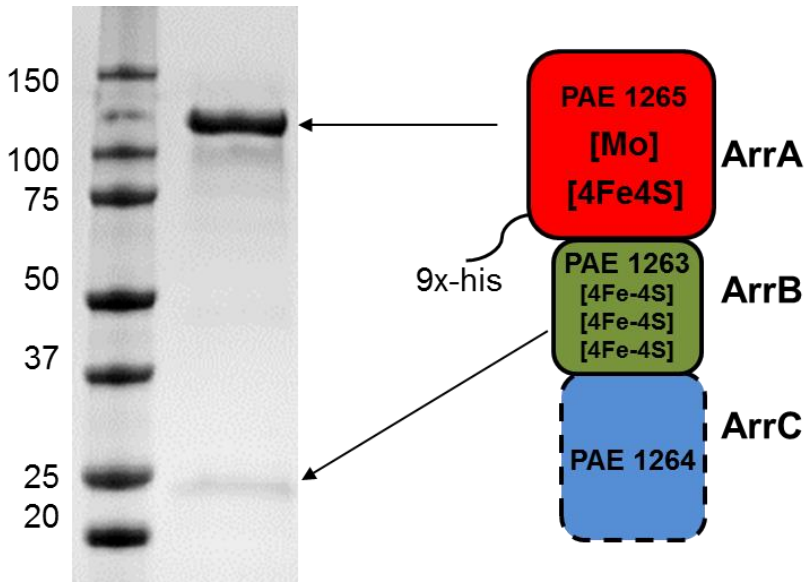
150
100
75
50
37
25
20
PAE 1265
[Mo]
[4Fe4S]
ArrA
9x-his
PAE 1263
[4Fe-4S]
[4Fe-4S]
[4Fe-4S]
ArrB
PAE 1264
ArrC

Figure 5.2

Growth of *P. furiosus* on peptides with and without arsenate (10 mM). a) The colors refer to: orange, the Arr strain with the addition of S° without arsenate; purple, Par with the addition of S° without arsenate; red, the Arr strain with the addition of arsenate; black, Par with the addition of arsenate; blue, Par without arsenate; green, the Arr strain without arsenate. b) Arsenite (AsIII) concentration in the spent media after the addition of 10 mM arsenate. Black line: Par; red line: the Arr strain. c) Hydrogen production normalized by protein concentration during growth. The colors refer to: blue, Par; green, the Arr strain; black, Par with the addition of arsenate; red, the Arr strain with the addition of arsenate. The error bars represent standard deviations obtained using biological triplicate samples.

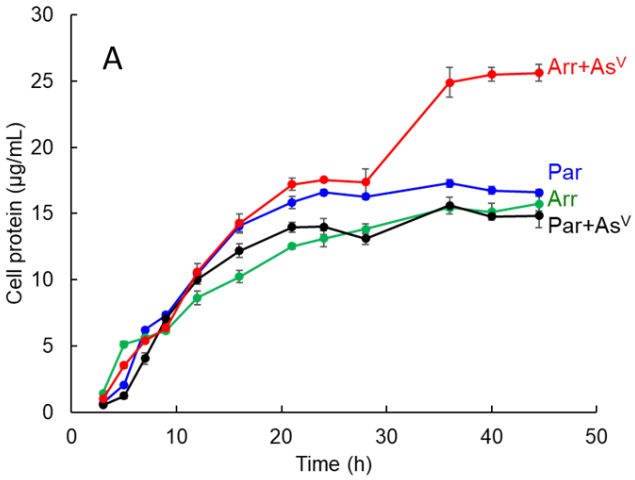
A
Cell protein (µg/mL)
Time (h)
Arr+As^V
Par
Arr
Par+As^V

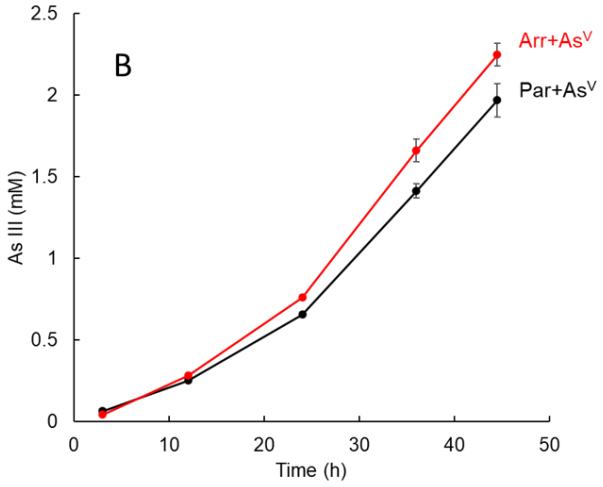
B
As III (mM)
Time (h)
Arr+As^V
Par+As^V

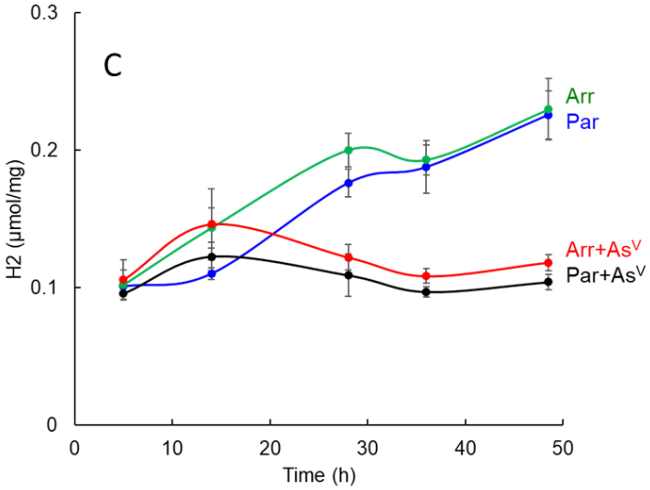
C
H2 (µmol/mg)
Time (h)
Arr
Par
Arr+As^V
Par+As^V

Figure 5.3

Inhibition of *P. furiosus* growing on maltose by arsenate. a) The colors refer to: blue, Par; green, the Arr strain; black, Par with the addition of 10 mM arsenate; red, the Arr strain with the addition of 10 mM arsenate. b) Arsenite (AsIII) concentration in the spent media with the addition of 10 mM arsenate. Black line: Par; red line: the Arr strain; purple line: abiotic control without addition of innoculumn. The error bars represent standard deviations obtained using biological triplicate samples.

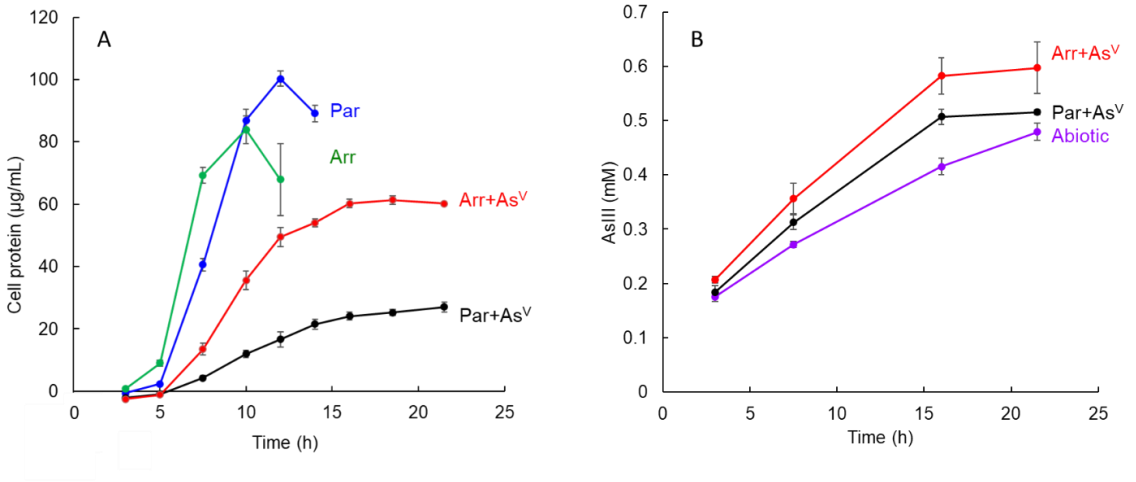
A
Cell protein (µg/mL)
Time (h)
Par
Arr
Arr+As^V
Par+As^V
B
AsIII (mM)
Time (h)
Arr+As^V
Par+As^V
Abiotic

Figure 5.4

Inhibition of *P. furiosus* grown on maltose by arsenite (AsIII). Par and the Arr strain were grown on 5 g/L maltose in the presence of 0.5 mM or 1 mM arsenite. The error bars represent standard deviations obtained using biological triplicate samples.

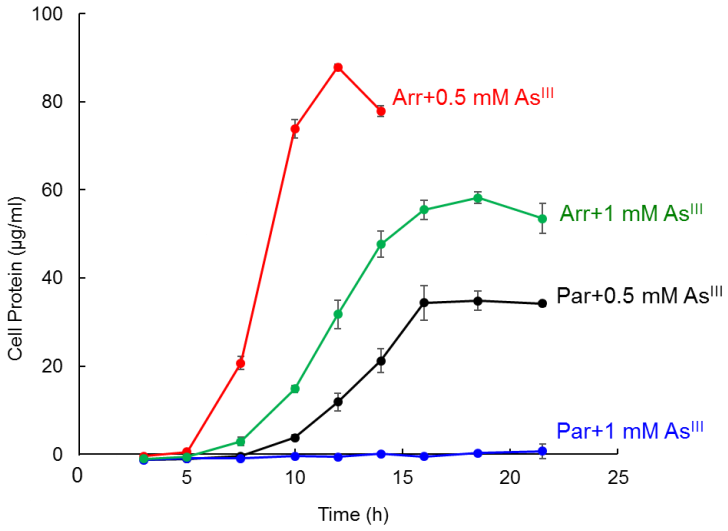
100
80
60
40
20
0
Cell Protein (µg/ml)
0
5
10
15
20
25
Time (h)
Arr+0.5 mM As^III
Arr+1 mM As^III
Par+0.5 mM As^III
Par+1 mM As^III

Figure 5.5

The intracellular arsenic concentrations in the parent and Arr strains grown on maltose with 0.5 mM arsenite (AsIII). The error bars represent standard deviations obtained using biological triplicate samples.

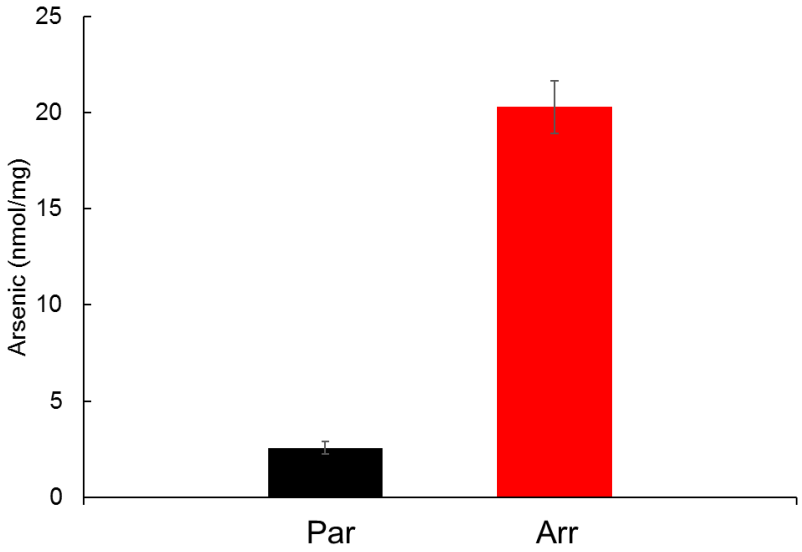
25
20
15
10
5
0
Arsenic (nmol/mg)
Par
Arr

Figure 5.6

X-ray absorption spectroscopy results. Normalized As-K near edge X-ray Absorption spectra collected in cell cultures exposed to 0.5 mM arsenite. Arr strain is denoted by red line with solid circles, the parent strain by black line with empty circles.

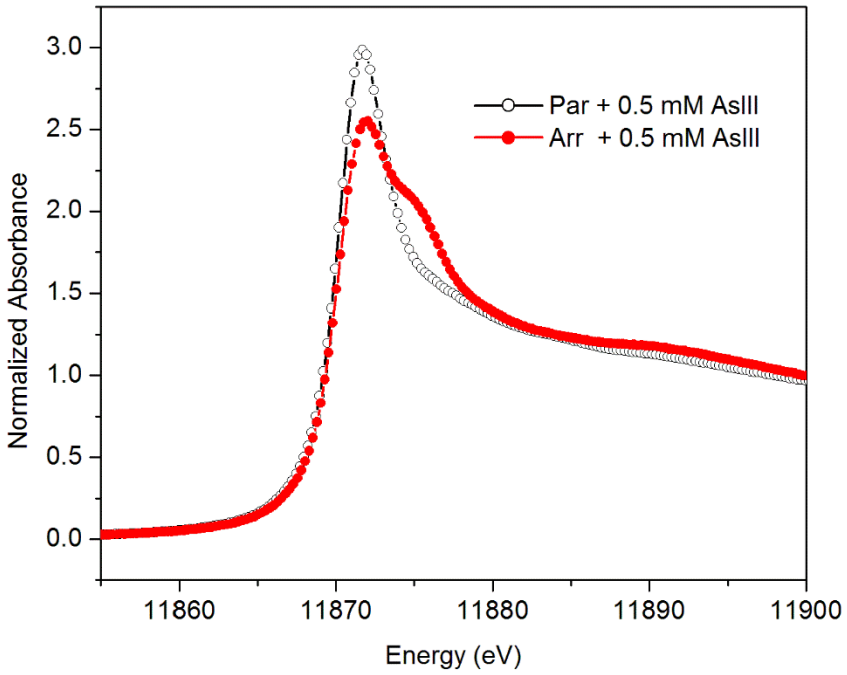
Par + 0.5 mM AsIII
Arr + 0.5 mM AsIII
Normalized Absorbance
Energy (eV)
3.0
2.5
2.0
1.5
1.0
0.5
0.0
11860
11870
11880
11890
11900

Table S5.1. Purification of Arr-Mo

Step	Total Units (μmol min^{-1})	Total Protein (mg)	Specific Activity (U/mg)	Yield (%)	Fold Purification
Cell-free extract	1,571	3,402	0.46	100	1
Cytoplasmic extract	1,236	2,319	0.53	79	1.1
Ni-NTA	1,221	4.45	274	78	596
Phenyl HP	1,027	1.07	960	65	2,087

Table S5.2. Purification of Arr-W

Step	Total Units (μmol min^{-1})	Total Protein (mg)	Specific Activity (U/mg)	Yield (%)	Fold Purification
Cell-free extract	20.9	3,465	0.006	100	1
Cytoplasmic extract	14.9	2,498	0.006	71	1
Ni-NTA	14.7	3.7	3.97	70	661
Phenyl HP	12.9	1.5	8.6	62	1,430

Table S5.3. The analysis of the As-K near-edge X-ray absorption spectrum of Arr sample exposed to 0.5 mM of arsenite via least–square fitting using linear combination of standard spectra. The numbers in brackets denote 3 x estimated standard deviations obtained from the diagonal elements of the covariance matrix. The fits 1 and 2 involve using the parent's spectrum as a major component, which shows that the majority (64-78%) of the Arr's spectrum is well represented by the parent's spectrum. The fits 3-8 demonstrate that Arr spectrum is a mixture of As (III) character (54-68%) and a mixture of As (V) character and, possibly, other oxidation state compounds, represented here by arsenobetaine (trimethylarsonioacetate, $(CH_3)_3As^+$ CH2COO$^-$). *)TMAS-trans denotes powdered trimethylarsine sulfide standard measured in XAS transmission mode. All other standards listed were prepared as described in the legend of supplemental Figure S5.5 and measured in the primary fluorescence mode.

Std / Fit	Par	AsO_4^-	$As(OH)_3$	MMAV	DMAV	TMAO	TMAS	TMAS-trans*)	AB	Res × 1000
1	64(7)	18(3)	11(6)	7(4)	-	-	-	-	-	0.28
2	78(1)	22(1)	-	-	-	-	-	-	-	0.33
3	-	17(2)	59(2)	-	24(3)	-	-	-	-	0.82
4	-	27(2)	54(3)	-	-	-	-	19(3)	-	1.43
5	-	22(2)	57(2)	-	-	21(3)	-	-	-	1.44
6	-	27(2)	57(2)	-	-	-	-	-	16(3)	1.56
7	-	26(2)	53(3)	-	-	-	21(4)	-	-	1.85
8	-	32(2)	68(3)	-	-	-	-	-	-	4.35

Table S5.4. The analysis of the As-K near-edge X-ray absorption spectrum of Par sample exposed to 0.5 mM of arsenite via least–square fitting using linear combination of standard spectra. The major component (70-76%) of all fits is represented by the arsenite in aqueous solution at pH ~7. The rest of the components are represented by combinations of methylated pentavalent arsenicals MMAV, DMAV, TMAO and TMAS with the addition of the compound which is fitted by arsenobetaine (AB). The numbers in brackets are 3 x estimated standard deviations obtained from the diagonal elements of the covariance matrix. The residual of the fit and the values of standard deviation serve as mathematical indicators of the goodness of the fit.

Std / Fit	AsO_4^-	$As(OH)_3$	MMAV	DMAV	TMAO	TMAS-trans	AB	Res × 1000
1	-	73(2)	-	18(3)	-	-	9(4)	1.08
2	-	72(2)	9(2)	-	-	-	19(3)	1.25
3	-	74(2)	-	16(8)	10(9)	-	-	1.35
4	-	76(2)	-	24(2)	-	-	-	1.39
5	-	70(3)	-	-	22(5)	7(7)	-	1.54
6	-	72(2)	-	-	28(2)	-	-	1.59
7	7(2)	70(2)	-	-	-	-	23(3)	1.66

Figure S5.1

Scheme for the construction of the Arr strain (MW0548). The knock-in cassette has homologous regions shown as the upstream flanking region (UFR) and downstream flanking region (DFR). The marker cassette is indicated as P_{gdh}-*pyrF*, and the promoter is indicated as P_{slp}. A 9x-his-tag was placed at the C-terminus of *arrA* (PAE1265). The ribosomal binding sites (RBS) of pyruvate oxidoreductase γ-subunit and the S-layer protein were placed upstream of *arrC* (PAE1264) and *arrA*, respectively. The corresponding homologous loci of the UFR and DFR in the parent strain COM1 are in the intergenic region between PF0265 and PF0266, which have minimal transcriptional activity (data not shown). The arrangement of the intergenic region after recombination is also shown.

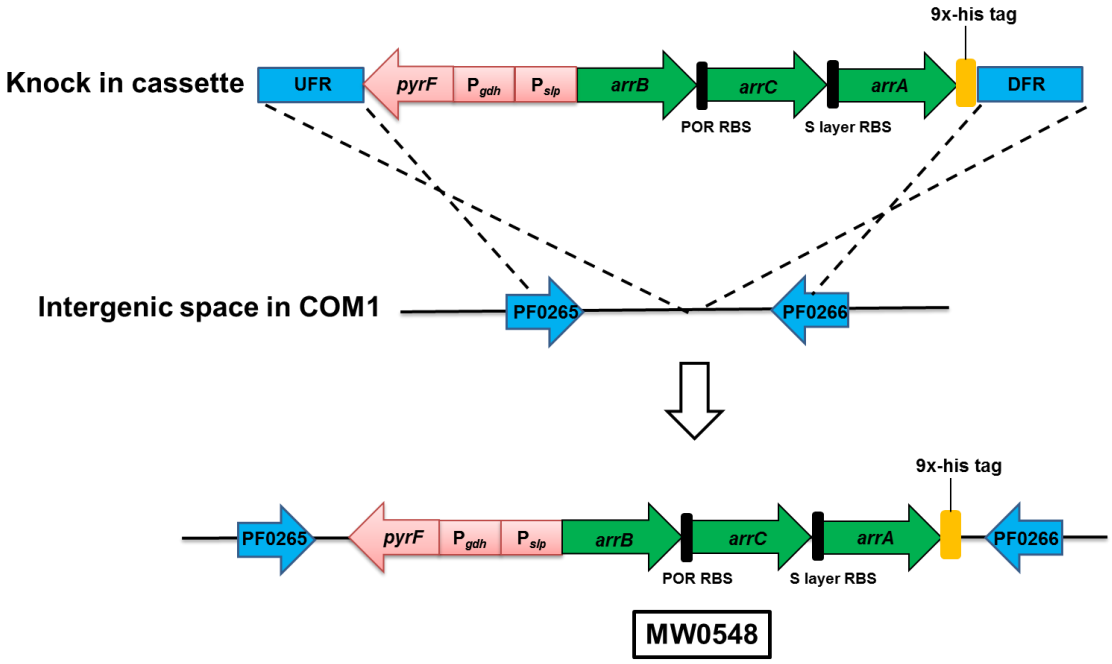
Knock in cassette
UFR
pyrF
P gdh
P slp
arrB
arrC
arrA
DFR
9x-his tag
POR RBS
S layer RBS
Intergenic space in COM1
PF0265
PF0266
PF0265
pyrF
P gdh
P slp
arrB
arrC
arrA
PF0266
9x-his tag
POR RBS
S layer RBS
MW0548

Figure S5.2

Arsenate reductase activity in the cell-free extracts of the Par and Arr strains grown in a medium containing 10 µM Mo and 10 µM W. The activity was measured by MV-linked arsenate (AsV) reduction. The activity measured for Par was below the detection limit (<0.001 U/mg).

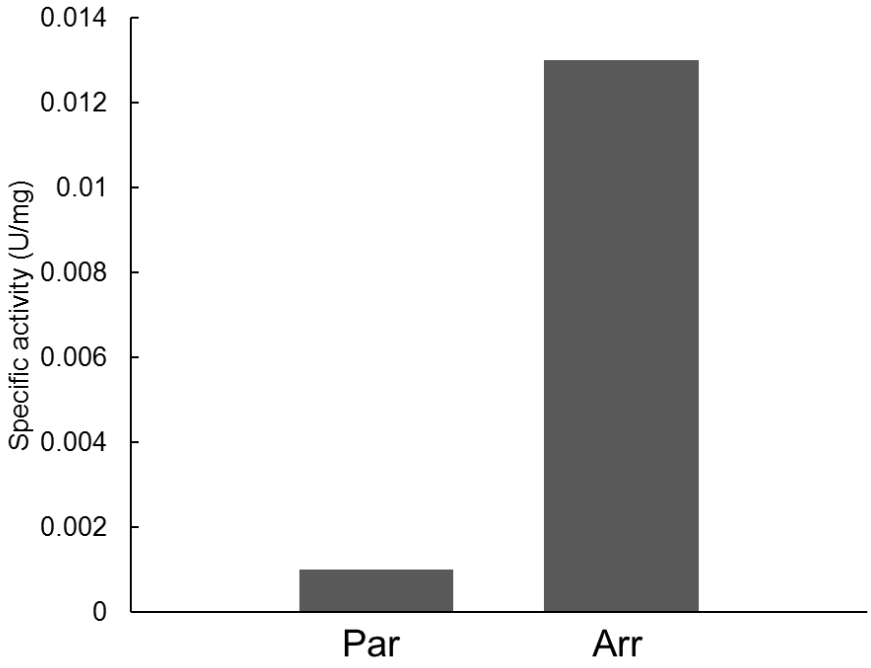
0.014
0.012
0.01
0.008
0.006
0.004
0.002
0
Specific activity (U/mg)
Par
Arr

Figure S5.3

Localization of arsenate reductase activity in the Arr strain. The activity was measured by MV-linked arsenate (As^{V}) reduction.

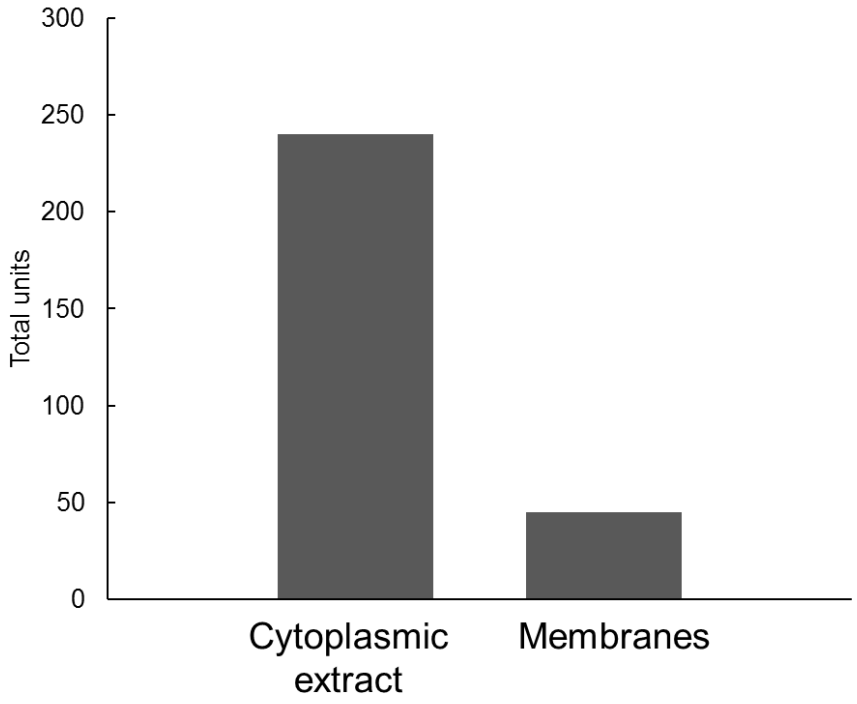
300
250
200
150
100
50
0
Total units
Cytoplasmic extract
Membranes

Figure S5.4

Molecular weight distribution of arsenic in the cytoplasmic extract of the Arr strain grown with 0.5 mM arsenite (AsIII). The elution from the desalting column was collected in fractions and the arsenic concentration was determined by ICP-MS (red line). The blue line represents the 280 nm absorbance.

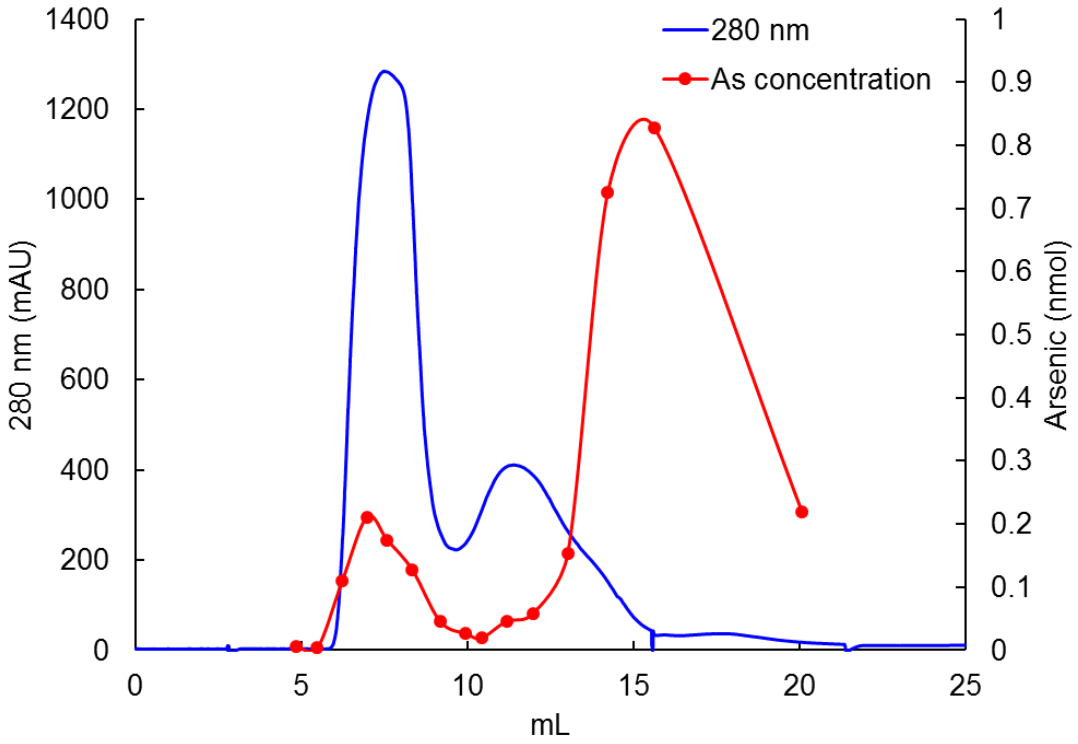
280 nm
As concentration
280 nm (mAU)
Arsenic (nmol)
mL
0
200
400
600
800
1000
1200
1400
0
0.1
0.2
0.3
0.4
0.5
0.6
0.7
0.8
0.9
1
0
5
10
15
20
25

Figure S5.5

X-ray absorption As-K near-edge spectra for Arr and Parent cultures exposed to 0.5 mM arsenite and relevant standard compounds. The standard compounds were prepared at 1 mM As in buffered aqueous solution (50 mM HEPES, pH 7.4) mixed with 30% v/v glycerol. Vertical lines are indicating the peak positions of $As(GS)_3$, arsenite [$As(OH)_3$], and arsenate [AsO_4]$^-$. Other displayed standard spectra include those of trivalent monomethylarsonous acid (MMAIII) and dimethylarsinous acid (DMAIII); pentavalent monomethylarsonic acid (mono-methyl arsenate, MMAV), dimethylarsenic acid (di-methyl arsenate, DMAV), trimethylarsine oxide (TMAO), and trimethylarsine sulfide (TMAS).

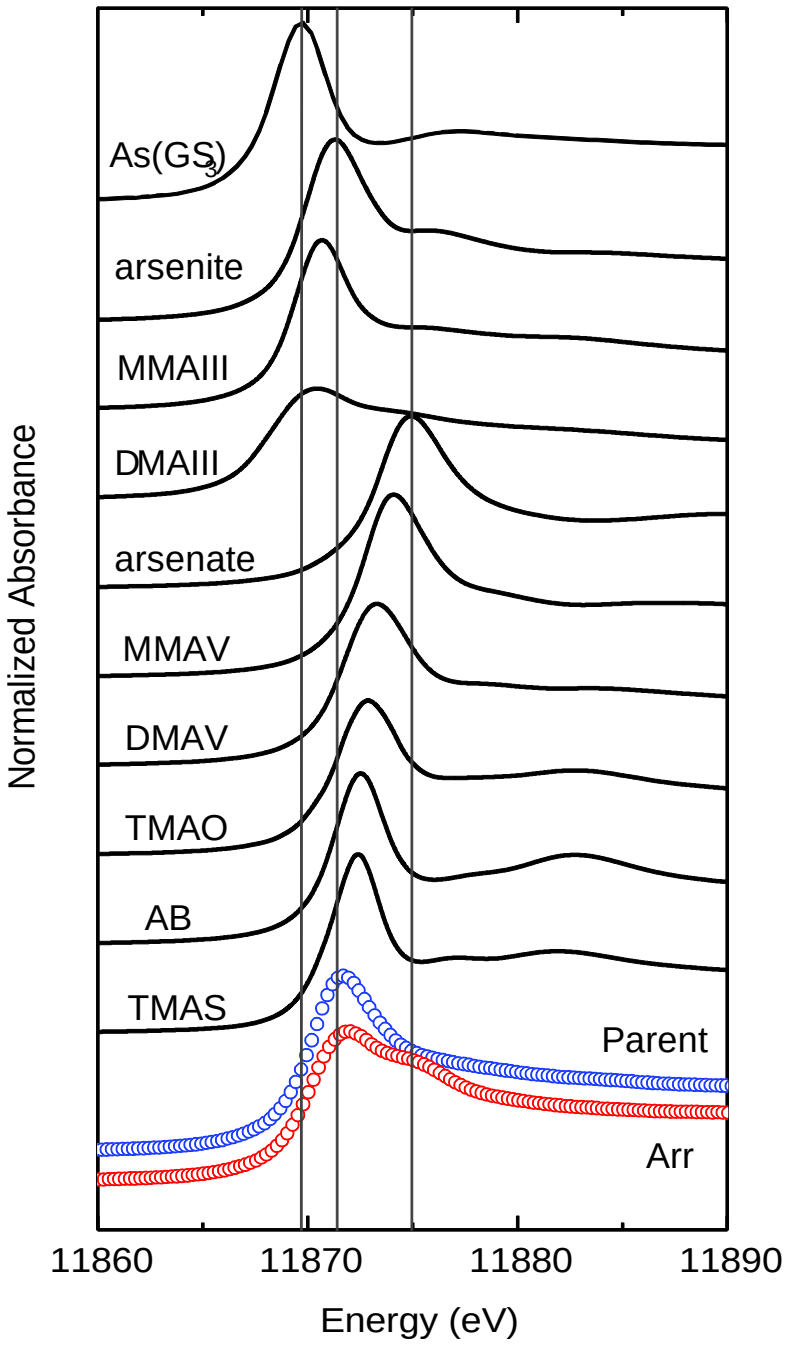
As(GS3)
arsenite
MMAIII
DMAIII
arsenate
MMAV
DMAV
TMAO
AB
TMAS
Parent
Arr
Normalized Absorbance
11860
11870
11880
11890
Energy (eV)

CHAPTER SIX

DISCUSSION AND CONCLUSIONS

The membrane-bound hydrogenase MBH in *Pyrococcus furiosus* couples the oxidation of ferredoxin and reduction of protons to hydrogen gas, and this redox activity is mechanically coupled to the pumping of sodium ions across the membrane (Appendix A)[84]. This sodium gradient is utilized by an Na^+-dependent ATP synthase in order to generate an additional 1.2 mol ATP per glucose consumed during glycolysis[86]. However, at the beginning of this research, the full details of the use of the Na^+ gradient by *P. furiosus* remained unknown. As a marine organism that grows in an environment containing ~500 mM NaCl, *P. furiosus* likely uses the Na^+ gradient for a number of different biological processes. MBH is predicted to have evolved from a soluble NiFe-hydrogenase joining with a multiple resistance and pH (Mrp) antiporter in an Ancestral Respiratory Complex (ARC) in order to take advantage of the additional ion gradient such a complex would produce in an energy-conserving mechanism[174]. In general, Mrp complexes utilize the proton motive force (pmf) to drive ion pumping across the membrane for a variety of physiological functions, including Na^+ and pH homeostasis[248]. Interestingly, in addition to the Mrp module of MBH (and the related membrane-bound sulfane sulfur reductase MBS) the genome of *P. furiosus* encodes a copy of a stand-alone Mrp operon with the structure *mrpEFGBB'CD*. The complex is missing a gene encoding a homologue of MrpA, which

has been shown to be essential for coupling the pmf to ion pumping in *Bacillus subtilis*[161]. Therefore, the function of this Mrp complex, in *P. furiosus* was unknown.

In chapter two, I used deletion strains of the sodium pumping module of MBH (ΔMbhABC) and of Mrp (ΔMrp) to determine the effects that the complexes have on flux of Na^+ throughout the cell. The negative growth phenotype of the ΔMbhABC strain compared to the parent represents the difference in growth rate between *P. furiosus* generating ATP through substrate level phosphorylation during glycolysis alone, as opposed to substrate level phosphorylation and additional ATP generated by electron transport phosphorylation by ATP synthase in the parent strain. There was no difference in H_2 production or maximum cell yield between ΔMbhABC and the parent, suggesting that hydrogenase activity is unaffected by the presence or absence of the Na^+ ion exchange. This is consistent with the proposed coupling mechanism of MBH, in which conformational changes brought about by the changing redox state of the active site during catalysis are propagated through the H^+-translocation module, driving H^+ outside the cell. This H^+-gradient is then passively exchanged by the Na^+-translocation module to pump Na^+ outside the cell to generate a gradient for ATP synthesis.

The ΔMrp strain, on the other hand, likely uses the Na^+ gradient to maintain cellular pH homeostasis, as it appears to be more sensitive to changes in pH than the parent strain. As the pH drops, Mrp uses Na^+ ions to expel H^+ from the cell; this comes at the cost of ATP synthesis, as the growth rate of the parent strain is slower than the ΔMrp strain. Mrp and ATP synthase essentially "compete" for Na^+ ions when the cell must maintain pH homeostasis. Interestingly, Mrp also appears to contribute to the Na^+ gradient under ideal pH conditions, with the parent strain exhibiting a faster growth rate than ΔMrp when

additional buffer is added to the growth medium to maintain the pH at physiological levels. Additionally, Na^+-dependent H_2 production assays conducted with cell suspensions show that Na^+-pumping is more affected in the absence of Mrp than the absence of the Na^+-translocation module of MBH, with ΔMrp producing less H_2 than ΔMbhABC. This suggests that Mrp may play a greater role than MBH in generating the Na^+ gradient for ATP synthesis.

P. furiosus is unique in that it encodes multiple copies of group 3 Mrp antiporters, making it a perfect organism in which to study their functions. Structures were recently solved of both a group 1 and group 2 Mrp antiporter, but a structure of a group 3 Mrp has yet to be reported[171,172]. The most striking difference between the various Mrp operons is the lack of a gene encoding a homologue of MrpA, which is proposed to contain a second H^+-translocation module and be essential for coupling the pmf to Na^+ pumping. In MBH (and MBS), MrpA has been replaced by the peripheral modules to utilize redox activity as an energy input instead. The *P. furiosus* Mrp appears to be unique in that it doesn't require an energy input in order to function. However, while Mrp antiporters enable growth in a wide range of pH levels or Na^+ concentrations, the ΔMrp strain did not show any differences in the range of pH or NaCl that enabled growth. In this manner, *P. furiosus* is similar to the anaerobic thermophile *Calaromater fervidus* (previously *Clostridium fervidus*), in which energy transduction is exclusively coupled to Na^+ ions[249,250]. Because *C. fervidus* lacks any H^+-pumping capabilities, it is unable to regulate its cytoplasmic pH and only grows in the narrow pH range of 6.3-7.7 that corresponds to optimum cytoplasmic pH levels. It is interesting to speculate that the coexpression of an appropriate *mrpA* homologue with the *P. furiosus mrp* operon could expand the range of pH or NaCl

concentrations suitable for growth. The *P. furiosus* Mrp represents an opportunity to study how a simple Na^+/H^+ antiporter evolved to utilize either a pmf (using MrpA) or redox activity (in MBH or MBS) in order to gain additional functionalities.

The initial goal of the MBH deletion strains was to generate negative controls for use in mutagenesis studies in order to elucidate H^+ and Na^+ transfer pathways in the membrane arm of the MBH complex. While the deletion of the Na^+-pumping module was easily achieved, deletion of the full membrane arm (ΔMbhABCDEFGH(I)) in order to create a negative control for the H^+-translocation module was unsuccessful (unpublished data). MbhL and the associated hydrogenase activity has been shown to be essential for growth in the absence of elemental sulfur, as demonstrated by a ΔMbhL deletion strain[187]. The cryo-EM structure of MBH reveals that a highly conserved series of three loops formed by MbhL, MbhM, and MbhI is situated directly near the NiFe active site in MbhL and has been proposed to be essential for the coupling of redox activity to ion pumping in the membrane (Appendix A). In fact, a recent study of the related respiratory complex I captured the complex in various states in the catalytic cycle, showing that movement of the three-loop system did in fact result in structural changes in the H^+-translocation module that allow for H^+-pumping to occur[156]. In MBH, the MbhI subunit containing loop 3 also contains the lateral helix HL (proposed to be involved in structural stability of the entire complex) as well as a transmembrane helix that forms part of the interface between the H^+-translocation and the Na^+-translocation module. It is easy to imagine that deletion of MbhH or MbhI could disrupt the structural stability of the complex, with changes to the conformation of the three loops likely being propagated to the active site in a reverse of the physiological function. Any disturbances that lead to a loss of catalytic activity are lethal

to the cell, as *P. furiosus* has no other way to recycle reduced Fd for glycolysis in the absence of S^0. These data together suggest that the primary role of MBH in *P. furiosus* is not energy generation but instead simply a mechanism to dispose of excess reductant during glycolysis. Future attempts to delete the H^+-translocation module from MBH will need be attempted under S^0 conditions (MBH function is not needed for growth on S^0) in order to provide the negative control for any mutagenesis studies of MBH activity.

In the presence of S^0, expression of MBH and NiFe-hydrogenase maturation genes decreases and expression of MBS increases[82]. MBS oxidizes reduced Fd in order to reduce the sulfane sulfur bond in both anionic and organic polysulfides, making smaller polysulfide chains that eventually spontaneously break down into hydrogen sulfide[88]. The characterization of MBS activity provided an answer to the almost 20-year old mystery of how *P. furiosus* produces H_2S during growth on S^0, and it represents a novel mechanism of sulfur reduction, but the details of the biochemical mechanism remained unknown. Unlike other well characterized sulfur and polysulfide reductase systems, which are all Mo-pterin enzymes, *P. furiosus* MBS does not contain any predicted pterin-binding sites[133,181]. Additionally, unlike MBH, which has a dedicated set of maturation genes that are co-regulated by SurR, MBS does not have any associated maturation genes that are also upregulated in the presence of S^0 [91]. The amino acid sequence doesn't have any predicted cofactor binding sites (other than FeS clusters) and metal analysis shows only iron is present in the enzyme, precluding the binding of any additional metal cofactors.

In chapter 3, we used an affinity-tagged MBS complex for structural determination using cryo-EM, providing valuable insights into the catalytic mechanism of MBS and into the evolutionary relationship between MBH, MBS, Mrp, and complex I (Figure 6.1). There

are a number of highly conserved cysteine residues that coordinate the metal centers in the three complexes. In MbhL, the NiFe active site is coordinated by four cysteine residues, similarly to all other NiFe hydrogenases (Appendix A)[136]. In MBS, only two of these cysteine residues are conserved, but experimental evidence suggests that they are not involved in catalysis; in complex I, none of these residues are conserved, suggesting an evolutionary transition from the NiFe metal center to FeS clusters as the final step in electron transfer in these respiratory complexes. Interestingly, it is the proximal FeS cluster to the hydrophobic substrate pocket that appears to be the key to modulating the catalytic properties in the respiratory enzymes. In MBH (and other NiFe-hydrogenases), the proximal cluster binding motif contains two cysteines that are separated by two residues, allowing for efficient electron transfer further into the NiFe active site. In complex I, the two cysteine residues are sequential, which has been proposed to enable sequential dissociation from the proximal cluster and facilitating electron and proton transfer to the substrate quinone[251]. In MBS, the binding motif is shortened by three residues, leaving one cysteine turned away from the active site and unable to coordinate the proximal cluster. Mutagenetic analyses showed that this cysteine residue is not essential for MBS activity. Instead, the non-cysteinal coordinated Fe of the proximal cluster directly reduces the sulfane bond in polysulfide. Treatment of the complex with potassium ferricyanide, which is known to remove non-cysteinal coordinated Fe from [4Fe-4S] clusters, resulted in conversion to a [3Fe-4S] cluster and a ~98% loss of activity, while incubating with ferrous iron under reducing conditions restored the [4Fe-4S] cluster. This cluster interconversion was confirmed using EPR spectroscopy. Based on this structural and biochemical data, a new mechanism was proposed for the reduction of internal disulfide bonds by MBS. This

is the first example of a biological system for reducing an inorganic disulfide bond that does not require protons or amino acid residues, and was clearly fundamentally important in the iron and sulfur rich hydrothermal vent environments of the early earth and in the development of early life[175].

The biochemical activity assays and site-directed mutagenesis of MBS took advantage of a unique split-operon system initially developed for studying MBH[193]. This allows for purification of an affinity-tagged subcomplex consisting of only the cytoplasmic (lacking transmembrane domains) MbhJKLN subunits (C-MBS) and eliminates the need for time-intensive solubilization and purification of the full membrane complex. Additionally, the operon-splitting strategy allows the C-MBS subcomplex to be placed under control of a constitutively expressed promoter and thus be purified from cells grown in the absence of S^0. This strategy was essential for EPR studies of MBS, as C-MBS purified from S^0-grown cells exhibits a large radical signal that is an artifact of purification; C-MBS purified from non-S^0 grown cells did not contain this signal. This also allowed for comparison of activities between C-MBS from both S^0- and non S^0-grown cells. If additional maturation genes were present that are co-upregulated with MBS in the presence of S^0, then the C-MBS purified from non-S^0 cells would be inactive. Activity assays using partially purified C-MBS from both S^0- and non S^0-grown cells showed similar dimethyl trisulfide reduction activity, further confirming that no additional maturation machinery is required for MBS as is the case for MBH.

The bioenergetics of the various electron transfer reactions catalyzed by respiratory complexes has been cited as a driving force for their evolution[174]. The standard free energy released by the reduction of protons and polysulfide by MBH and MBS is -12 and -41

kJ/mol, respectively. Accordingly, the total cell yield per glucose when *P. furiosus* is grown on maltose in the presence of S^0 is almost double that when it is grown in the absence of S^0 [83]. It is possible that this increase in free energy corresponds to an increasing number of H^+ pumped across the membrane, which could explain why MBS contains two H^+-translocating subunits where MBH only has one. The residues proposed to be involved in H^+-translocation are highly conserved between MBH, MBS, Mrp, and complex I, and many of these residues have already been studied extensively through mutagenesis of *Bacillus* Mrp complexes[168,169]. If increasing free energy released corresponds to increased H^+-pumping, then inactivating either of the H^+-translocation channels in MbsH or MbsH' should lead to a cell yield equivalent to that of cells grown in the absence of S^0. Additionally, these experiments could provide insights into the coupling of the H^+-translocating subunits to redox activity and to each other. For example, if conformational changes are first propagated through MbsH' then MbsH, it is possible that inactivating MbsH' will completely inactivate proton pumping activity in the complex. The results of these experiments could provide further insights into the evolution of complex I, which conserves more energy (-81 kJ/mol) and pumps more protons (4) than MBH and MBS.

The results of Chapters 4 and 5 are perhaps most interesting when interpreted in parallel. Two respiratory complexes, the thiosulfate reductase (Tsr) and respiratory arsenate reductase (Arr) from *Pyrobaculum aerophilum*, were each heterologously expressed in *P. furiosus* and each purified in two forms, one containing predominantly Mo and one predominantly W. In both cases, the Mo-enzyme was found to be more catalytically active than the W-enzyme, representing the first active Mo-enzymes purified from *P. furiosus*. The preference of DMSO reductase family enzymes for Mo is well

documented, with some organisms that use both metals containing separate cofactor maturation pathways and chaperone proteins to ensure that only the correct metal gets inserted into the correct active site[215,216]. This is not the case in *P. furiosus* as it only inserts W into its five W-containing enzymes. Hence the organism does have to be "tricked" into using Mo, as the heterologously-expressed Mo-enzymes could only be purified from cultures that had been adapted to grow in medium containing 1000 times more Mo than W for ten generations; these cells can scavenge enough W from the environment to satisfy the requirements of its native enzymes. Growing cultures in medium containing equal amounts of Mo and W resulted in W-containing enzymes. These findings drastically increase the potential for *P. furiosus* as an engineering platform for hyperthermophilic enzymes, as it is now known that it can be used to express both Mo- and - containing enzymes.

However, the results also demonstrated the limitations of *P. furiosus* as an expression system. Both Tsr and Arr are trimeric enzymes, with TsrA and ArrA containing the catalytic metallopterin binding site, TsrB and ArrB containing multiple FeS clusters to enable electron transfer, and TsrC and ArrC serving as membrane anchoring subunits. However, neither TsrC not ArrC were able to be copurified with the cytoplasmic subunits of either complex, and they were not able to be identified using mass spectrometry on any samples, suggesting that they are degraded before they can be inserted into the membrane. It is possible that this is a consequence of the physiological function of these respiratory enzymes in *P. aerophilum*, in which they are transported to the outer side of the membrane using a TAT export system[204]. *P. furiosus* does not utilize a TAT export system, which could explain why the TsrAB and ArrAB subcomplexes were purified from the cytoplasm while the membrane anchors were degraded[252]. Care must be taken in future studies to

identify the translocation pathways in native organisms in order to express the properly tagged systems in *P. furiosus*. Additionally, the Tsr and Arr enzymes were chosen from *P. aerophilum* as proof-of-concept enzymes for heterologous expression of genes from phylogenetically unrelated sources because they do not contain any additional cofactors. The respiratory nitrate reductase and aerobic cytochrome oxidase systems from *P. aerophilum*, on the other hand, contain cytochrome binding sites in their corresponding membrane-anchored subunits[206,208]. However, *P. furiosus* does not utilize hemes and does not encode any of the biosynthetic genes. Attempt to insert the heme biosynthesis pathway from *P. aerophilum* into *P. furiosus* were unsuccessful (unpublished data), so while this research expands the versatility of *P. furiosus* as an expression platform to include Mo-enzymes, it is not expanded as far as being able to express any DMSO reductase system, as a large number of these complexes utilize cytochromes in the quinone binding sites of their membrane anchored subunits.

A somewhat surprising result is that while the recombinant *P. furiosus* strain expressing Arr was able to utilize arsenate as a terminal electron acceptor for growth, the strain expressing Tsr was unable to utilize thiosulfate. Both enzyme complexes were found to have ferredoxin-linked activity, suggesting that the physiological electron donor in *P. furiosus* is able to donate electrons to heterologous systems *in vivo*. The difference lies in the structures of thiosulfate and arsenate and the ability of the compounds to utilize native transporters to enter the cell. The thiosulfate anion ($S_2O_3^{2-}$) is chemically analogous to tungstate (WO_4^{2-}) and molybdate (MoO_4^{2-}). *P. furiosus* utilizes the novel tungsten transport protein WtpA to selectively bring W inside the cell[253]. The binding affinity of WtpA for tungstate is almost three orders of magnitude higher than that for molybdate, and tungstate

ions will displace molybdate ions from the binding site of the transporter. WtpA is also known to bind thiosulfate, and although the affinity was not measured, it can be assumed to be lower than that for tungstate. *P. furiosus* is likely not able to import enough thiosulfate for it to make a difference in growth of the Tsr-expressing strain in the absence of S^0. On the other hand, arsenate (AsO_4^{3-}) is chemically analogous to phosphate (PO_4^{3-}), and arsenate readily replaces phosphate in many biochemical pathways; this is in fact the main mechanism of arsenic toxicity in most organisms[254]. Arsenate is likely imported into *P. furiosus* through its phosphate channels; in fact, the concentration of phosphate buffer in the medium had to be lowered before any growth benefits were seen in the presence of arsenate. The difference in the amount of thiosulfate and arsenate imported into the cytoplasm likely explains the results of the growth experiments in the Tsr- and Arr-expressing strains in *P. furiosus* and demonstrates the need to ensure that the substrate of any future heterologously-expressed systems has a means of entry into the cell.

In conclusion, the research described in this thesis have provided valuable insights into native H_2 and S^0 metabolism and Na^+ flux in *Pyrococcus furiosus*. A better understanding of native processes can improve the results of future genetic engineering experiments by making sure that any newly introduced pathways won't interfere with native metabolism, or vice versa. Deletion of native enzymes or controlling expression of respiratory enzymes using elemental sulfur can help direct electron flux towards desired products. Additionally, the results described here dramatically enhance the knowledge of what is and is not possible through heterologous expression of energy-conserving complexes, expanding the range of metal cofactors available for catalysis and showing that *P. furiosus* is able to utilize non-native substrates as terminal electron acceptors from

physiologically relevant donors. These lessons can and should be applied towards expressing novel energy conserving systems from anaerobic organisms that are difficult to cultivate or have limited genetic systems. Altogether, the results of this research have proven the robustness and effectiveness of *P. furiosus* as a genetic engineering platform.

Figure 6.1

Modular architecture of complex I-like respiratory complexes. (A)-(D) The structures and proposed working models of complex I-like family members: (A) complex I (*T. thermophiles*; PDB ID 4HEA); (B) MBH (PDB ID 6CFW); (C) MBS (PDB ID 6U8Y); (D) Mrp (PDB ID 6Z16). Outlined region is the membrane-anchored peripheral module conserved among these complexes.

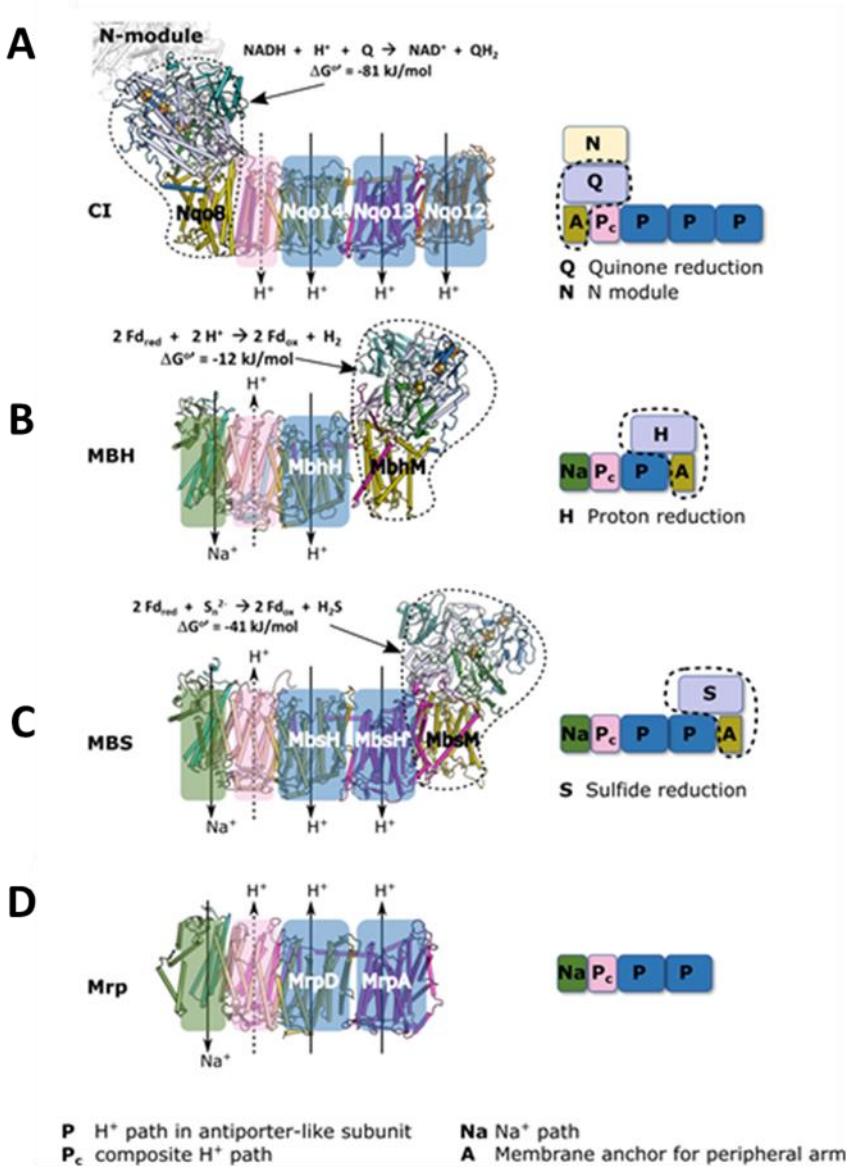
A
N-module
NADH + H+ + Q → NAD+ + QH2
ΔG°' = -81 kJ/mol
CI
Nqo8
Nqo14
Nqo13
Nqo12
H+
N
Q
A
Pc
P
Q Quinone reduction
N N module
B
2 Fdred + 2 H+ → 2 Fdox + H2
ΔG°' = -12 kJ/mol
MBH
MbhH
MbhM
Na+
H
Na
H Proton reduction
C
2 Fdred + Sn2- → 2 Fdox + H2S
ΔG°' = -41 kJ/mol
MBS
MbsH
MbsH'
MbsM
S
S Sulfide reduction
D
Mrp
MrpD
MrpA
P H+ path in antiporter-like subunit
Pc composite H+ path
Na Na+ path
A Membrane anchor for peripheral arm

References

1 Woese, C. R., Kandler, O. & Wheelis, M. L. Towards a natural system of organisms: proposal for the domains Archaea, Bacteria, and Eucarya. *Proc Natl Acad Sci USA* **87**, 4576-4579 (1990).

2 Woese, C. R. Bacterial evolution. *Microbiol Rev* **51**, 221-271 (1987).

3 Geiduschek, E. P. & Ouhammouch, M. Archaeal transcription and its regulators. *Mol Microbiol* **56**, 1397-1407 (2005).

4 Koonin, E. V., Mushegian, A. R., Galperin, M. Y. & Walker, D. R. Comparison of archaeal and bacterial genomes: computer analysis of protein sequences predicts novel functions and suggests a chimeric origin for the archaea. *Mol Microbiol* **25**, 619-637 (1997).

5 Benelli, D. & Londei, P. Translation initiation in archaea: conserved and domain-specific features. *Biochem Soc Trans* **39**, 89-93 (2011).

6 Beattie, T. R. & Bell, S. D. Molecular machines in archaeal DNA replication. *Curr Opin Chem Biol* **15**, 614-619 (2011).

7 Matsumi, R., Atomi, H., Driessen, A. J. M. & van der Oost, J. Isoprenoid biosynthesis in archaea – biochemical and evolutionary implications. *Res Microbiol* **162**, 39-52 (2011).

8 Brochier-Armanet, C., Forterre, P. & Gribaldo, S. Phylogeny and evolution of the archaea: one hundred genomes later. *Curr Opin Microbiol* **14**, 274-281 (2011).

9 Schleper, C. & Nicol, G. W. in *Advances in Microbial Physiology* Vol. 57 (ed Robert K. Poole) 1-41 (Academic Press, 2010).

10 Hua, Z.-S. *et al.* Genomic inference of the metabolism and evolution of the archaeal phylum Aigarchaeota. *Nat Commun* **9**, 2832 (2018).

11 Munson-McGee, J. H. *et al.* Nanoarchaeota, their sulfolobales host, and nanoarchaeota virus distribution across Yellowstone National Park hot springs. *Appl Environ Microbiol* **81**, 7860-7868 (2015).

12 Spang, A. *et al.* Complex archaea that bridge the gap between prokaryotes and eukaryotes. *Nature* **521**, 173-179 (2015).

13 Caceres, E. F. *et al.* Near-complete Lokiarchaeota genomes from complex environmental samples using long and short read metagenomic analyses. *bioRxiv* (2019).

14 Baker, B. J. *et al.* Diversity, ecology and evolution of archaea. *Nat Microbiol* **5**, 887-900 (2020).

15 Robertson, C. E., Harris, J. K., Spear, J. R. & Pace, N. R. Phylogenetic diversity and ecology of environmental archaea. *Curr Opin Microbiol* **8**, 638-642 (2005).

16 DeLong, E. F. Microbial community genomics in the ocean. *Nat Rev Microbiol* **3**, 459-469 (2005).

17 Keough, B. P., Schmidt, T. M. & Hicks, R. E. Archaeal nucleic acids in picoplankton from great lakes on three continents. *Microb Ecol* **46**, 238-248 (2003).

18 Ochsenreiter, T., Selezi, D., Quaiser, A., Bonch-Osmolovskaya, L. & Schleper, C. Diversity and abundance of crenarchaeota in terrestrial habitats studied by 16S RNA surveys and real time PCR. *Environ Microbiol* **5**, 787-797 (2003).

19 Simon, H. M., Dodsworth, J. A. & Goodman, R. M. Crenarchaeota colonize terrestrial plant roots. *Environ Microbiol* **2**, 495-505 (2000).

20 Kleikemper, J. *et al.* Activity and diversity of methanogens in a petroleum hydrocarbon-contaminated aquifer. *Appl Environ Microbiol* **71**, 149-158 (2005).

21 Lepp, P. W. *et al.* Methanogenic archaea and human periodontal disease. *Proc Natl Acad Sci USA* **101**, 6176-6181 (2004).

22 Blöchl, E. *et al. Pyrolobus fumarii*, gen. and sp. nov., represents a novel group of archaea, extending the upper temperature limit for life to 113 degrees C. *Extremophiles* **1**, 14-21 (1997).

23 Huber, R. & Stetter, K. O. in *Methods in Enzymology* Vol. 330 11-24 (Academic Press, 2001).

24 Takai, K. *et al.* Cell proliferation at 122°C and isotopically heavy CH4 production by a hyperthermophilic methanogen under high-pressure cultivation. *Proc Natl Acad Sci USA* **105**, 10949-10954 (2008).

25 Fuchs, T., Huber, H., Teiner, K., Burggraf, S. & Stetter, K. O. *Metallosphaera prunae*, sp. nov., a novel metal-mobilizing, thermoacidophilic archaeum, isolated from a uranium mine in Germany. *Syst Appl Microbiol* **18**, 560-566 (1995).

26 Stetter, K. O. *et al.* Hyperthermophilic archaea are thriving in deep North Sea and Alaskan oil reservoirs. *Nature* **365**, 743-745 (1993).

27 Stetter, K. O. Ultrathin mycelia-forming organisms from submarine volcanic areas having an optimum growth temperature of 105 °C. *Nature* **300**, 258-260 (1982).

28 Stetter, K. O. *et al. Methanothermus fervidus*, sp. nov., a novel extremely thermophilic methanogen isolated from an Icelandic hot spring. *Int J Med Microbiol* **2**, 166-178 (1981).

29 Jaeschke, A. *et al.* Microbial diversity of Loki's Castle black smokers at the Arctic Mid-Ocean Ridge. *Geobiology* **10**, 548-561 (2012).

30 Dahle, H., Garshol, F., Madsen, M. & Birkeland, N. K. Microbial community structure analysis of produced water from a high-temperature North Sea oil-field. *ANTON LEEUW INT J G* **93**, 37-49 (2008).

31 Stetter, K. O. Extremophiles and their adaptation to hot environments. *FEBS Lett* **452**, 22-25 (1999).

32 Stetter, K. O. Hyperthermophiles in the history of life. *Philos Trans R Soc Lond B Biol Sci* **361**, 1837-1843 (2006).

33 Schwartzman, D. W. & Lineweaver, C. H. The hyperthermophilic origin of life revisited. *Biochem Soc Trans* **32**, 168-171 (2004).

34 Giulio, M. D. The universal ancestor was a thermophile or a hyperthermophile: Tests and further evidence. *J Theor Biol* **221**, 425-436 (2003).

35 Abramov, O. & Mojzsis, S. J. Microbial habitability of the Hadean Earth during the late heavy bombardment. *Nature* **459**, 419-422 (2009).

36 Akanuma, S. *et al.* Experimental evidence for the thermophilicity of ancestral life. *Proc Natl Acad Sci USA* **110**, 11067-11072 (2013).

37 Bouthier de la Tour, C. *et al.* Reverse gyrase, a hallmark of the hyperthermophilic archaebacteria. *J Bacteriol* **172**, 6803-6808 (1990).

38 Kikuchi, A. & Asai, K. Reverse gyrase—a topoisomerase which introduces positive superhelical turns into DNA. *Nature* **309**, 677-681 (1984).

39 Lipscomb, G. L., Hahn, E. M., Crowley, A. T. & Adams, M. W. W. Reverse gyrase is essential for microbial growth at 95 °C. *Extremophiles* **21**, 603-608 (2017).

40 Huber, H. & Stetter, K. O. Hyperthermophiles and their possible potential in biotechnology. *J Biotechnol* **64**, 39-52 (1998).

41 Bertoldo, C. & Antranikian, G. The order thermococcales. (2006).

42 Zillig, W., Holz, I., Janekovic, D., Schäfer, W. & Reiter, W. D. The archaebacterium *Thermococcus celer* represents a novel genus within the thermophilic branch of the archaebacteria. *Syst Appl Microbiol* **4**, 88-94 (1983).

43 Takai, K., Sugai, A., Itoh, T. & Horikoshi, K. *Palaeococcus ferrophilus* gen. nov., sp. nov., a barophilic, hyperthermophilic archaeon from a deep-sea hydrothermal vent chimney. *Int J Syst Evol* **50**, 489-500 (2000).

44 Fiala, G. & Stetter, K. O. *Pyrococcus furiosus* sp. nov. represents a novel genus of marine heterotrophic archaebacteria growing optimally at 100°C. *Arch Microbiol* **145**, 56-61 (1986).

45 Kim, B. K. *et al.* Genome sequence of an oligohaline hyperthermophilic archaeon, *Thermococcus zilligii* AN1, isolated from a terrestrial geothermal freshwater spring. *J Bacteriol* **194**, 3765-3766 (2012).

46 González, J. M. *et al. Pyrococcus horikoshii* sp. nov., a hyperthermophilic archaeon isolated from a hydrothermal vent at the Okinawa Trough. *Extremophiles* **2**, 123-130 (1998).

47 Erauso, G. *et al. Pyrococcus abyssi* sp. nov., a new hyperthermophilic archaeon isolated from a deep-sea hydrothermal vent. *Arch Microbiol* **160**, 338-349 (1993).

48 Callac, N. *et al. Pyrococcus kukulkanii* sp. nov., a hyperthermophilic, piezophilic archaeon isolated from a deep-sea hydrothermal vent. *Int J Syst Evol Microbiol* **66**, 3142-3149 (2016).

49 Robb, F. T. *et al.* Genomic sequence of hyperthermophile, *Pyrococcus furiosus*: implications for physiology and enzymology. *Methods Enzymol* **330**, 134-157 (2001).

50 Daum, B. *et al.* Structure and in situ organisation of the *Pyrococcus furiosus* archaellum machinery. *eLife* **6**, e27470 (2017).

51 Albers, S.-V. & Jarrell, K. F. The archaellum: how Archaea swim. *Front Microbiol* **6** (2015).

52 Lee, H.-S. *et al.* Transcriptional and biochemical analysis of starch metabolism in the hyperthermophilic archaeon *Pyrococcus furiosus*. *J Bacteriol* **188**, 2115-2125 (2006).

53 Koch, R., Zablowski, P., Spreinat, A. & Antranikian, G. Extremely thermostable amylolytic enzyme from the archaebacterium *Pyrococcus furiosus*. *FEMS Microbiol Lett* **71**, 21-26 (1990).

54 Koning, S. M., Elferink, M. G., Konings, W. N. & Driessen, A. J. Cellobiose uptake in the hyperthermophilic archaeon *Pyrococcus furiosus* is mediated by an inducible, high-affinity ABC transporter. *J Bacteriol* **183**, 4979-4984 (2001).

55 Gueguen, Y., Voorhorst, W. G., van der Oost, J. & de Vos, W. M. Molecular and biochemical characterization of an endo-beta-1,3- glucanase of the hyperthermophilic archaeon *Pyrococcus furiosus*. *J Biol Chem* **272**, 31258-31264 (1997).

56 Gao, J., Bauer, M. W., Shockley, K. R., Pysz, M. A. & Kelly, R. M. Growth of hyperthermophilic archaeon *Pyrococcus furiosus* on chitin involves two family 18 chitinases. *Appl environ microbiol* **69**, 3119-3128 (2003).

57 Bauer, M. W., Bylina, E. J., Swanson, R. V. & Kelly, R. M. Comparison of a beta-glucosidase and a beta-mannosidase from the hyperthermophilic archaeon *Pyrococcus furiosus*. Purification, characterization, gene cloning, and sequence analysis. *J Biol Chem* **271**, 23749-23755 (1996).

58 Kengen, S. M., Stams, A. J. M. & de Vos, W. M. Sugar metabolism of hyperthermophiles. *FEMS Microbiol Rev* **18**, 119-137 (1996).

59 Kengen, S. M. & Stams, A. J. M. Growth and energy conservation in batch cultures of *Pyrococcus furiosus*. *FEMS Microbiol Lett* **117**, 305-309 (1994).

60 Kengen, S. W. M., Tuininga, J. E., de Bok, F. A. M., Stams, A. J. M. & de Vos, W. M. Purification and characterization of a novel ADP-dependent glucokinase from the hyperthermophilic archaeon *Pyrococcus furiosus*. *J Biol Chem* **270**, 30453-30457 (1995).

61 Hansen, T., Oehlmann, M. & Schönheit, P. Novel Type of glucose-6-phosphate isomerase in the hyperthermophilic archaeon *Pyrococcus furiosus*. *J Bacteriol* **183**, 3428-3435 (2001).

62 Tuininga, J. E. *et al.* Molecular and biochemical characterization of the ADP-dependent phosphofructokinase from the hyperthermophilic archaeon *Pyrococcus furiosus*. *J Biol Chem* **274**, 21023-21028 (1999).

63 Verhees, C. H. *et al.* The unique features of glycolytic pathways in Archaea. *Biochem J* **375**, 231-246 (2003).

64 Siebers, B. *et al.* Archaeal fructose-1,6-bisphosphate aldolases constitute a new family of archaeal type class I aldolase. *J Biol Chem* **276**, 28710-28718 (2001).

65 Sharma, P. & Guptasarma, P. Endoglucanase activity at a second site in *Pyrococcus furiosus* triosephosphate isomerase - Promiscuity or compensation for a metabolic handicap? *FEBS Open Bio* **7**, 1126-1143 (2017).

66 Kengen, S. W. *et al.* Evidence for the operation of a novel Embden-Meyerhof pathway that involves ADP-dependent kinases during sugar fermentation by *Pyrococcus furiosus*. *J Biol Chem* **269**, 17537-17541 (1994).

67 Mukund, S. & Adams, M. W. W. Glyceraldehyde-3-phosphate ferredoxin oxidoreductase, a novel tungsten-containing enzyme with a potential glycolytic role in the hyperthermophilic archaeon *Pyrococcus furiosus*. *J Biol Chem* **270**, 8389-8392 (1995).

68 Aono, S., Bryant, F. O. & Adams, M. W. A novel and remarkably thermostable ferredoxin from the hyperthermophilic archaebacterium *Pyrococcus furiosus*. *J Bacteriol* **171**, 3433-3439 (1989).

69 Schäfer, T. & Schönheit, P. Gluconeogenesis from pyruvate in the hyperthermophilic archaeon *Pyrococcus furiosus*: involvement of reactions of the Embden-Meyerhof pathway. *Arch Microbiol* **159**, 354-363 (1993).

70 Peak, M. J. *et al.* The hyperthermophilic glycolytic enzyme enolase in the archaeon, *Pyrococcus furiosus*: comparison with mesophilic enolases. *Arch Biochem Biophys* **313**, 280-286 (1994).

71 Sakuraba, H., Utsumi, E., Kujo, C. & Ohshima, T. An AMP-dependent (ATP-forming) kinase in the hyperthermophilic archaeon *Pyrococcus furiosus*: Characterization and novel physiological role. *Arch Biochem Biophys* **364**, 125-128 (1999).

72 Kengen, S. & Stams, A. Formation of l-alanine as a reduced end product in carbohydrate fermentation by the hyperthermophilic archaeon *Pyrococcus furiosus*. *Arch Microbiol* **161**, 168-175 (2004).

73 Blamey, J. M. & Adams, M. W. Purification and characterization of pyruvate ferredoxin oxidoreductase from the hyperthermophilic archaeon *Pyrococcus furiosus*. *Biochim Biophys Acta* **1161**, 19-27 (1993).

74 Mai, X. & Adams, M. W. Purification and characterization of two reversible and ADP-dependent acetyl coenzyme A synthetases from the hyperthermophilic archaeon *Pyrococcus furiosus*. *J Bacteriol* **178**, 5897-5903 (1996).

75 Adams, M. W. Enzymes and proteins from organisms that grow near and above 100 degrees C. *Annu Rev Microbiol* **47**, 627-658 (1993).

76 Andreotti, G. *et al.* An extremely thermostable aromatic aminotransferase from the hyperthermophilic archaeon *Pyrococcus furiosus*. *Biochim Biophys Acta* **1247**, 90-96 (1995).

77 Robb, F. T., Park, J. B. & Adams, M. W. Characterization of an extremely thermostable glutamate dehydrogenase: a key enzyme in the primary metabolism of the hyperthermophilic archaebacterium, *Pyrococcus furiosus*. *Biochim Biophys Acta* **1120**, 267-272 (1992).

78 Mai, X. & Adams, M. W. Indolepyruvate ferredoxin oxidoreductase from the hyperthermophilic archaeon *Pyrococcus furiosus*. A new enzyme involved in peptide fermentation. *J Biol Chem* **269**, 16726-16732 (1994).

79 Heider, J., Mai, X. & Adams, M. W. Characterization of 2-ketoisovalerate ferredoxin oxidoreductase, a new and reversible coenzyme A-dependent enzyme

involved in peptide fermentation by hyperthermophilic archaea. *J Bacteriol* **178**, 780-787 (1996).

80 Mai, X. & Adams, M. W. Characterization of a fourth type of 2-keto acid-oxidizing enzyme from a hyperthermophilic archaeon: 2-ketoglutarate ferredoxin oxidoreductase from *Thermococcus litoralis*. *J Bacteriol* **178**, 5890-5896 (1996).

81 Mukund, S. & Adams, M. W. The novel tungsten-iron-sulfur protein of the hyperthermophilic archaebacterium, *Pyrococcus furiosu*s, is an aldehyde ferredoxin oxidoreductase. Evidence for its participation in a unique glycolytic pathway. *J Biol Chem* **266**, 14208-14216 (1991).

82 Adams, M. W. *et al.* Key role for sulfur in peptide metabolism and in regulation of three hydrogenases in the hyperthermophilic archaeon *Pyrococcus furiosus*. *J Bacteriol* **183**, 716-724 (2001).

83 Schicho, R. N., Ma, K., Adams, M. W. & Kelly, R. M. Bioenergetics of sulfur reduction in the hyperthermophilic archaeon *Pyrococcus furiosus*. *J Bacteriol* **175**, 1823-1830 (1993).

84 Sapra, R., Verhagen, M. F. J. M. & Adams, M. W. W. Purification and characterization of a membrane-bound hydrogenase from the hyperthermophilic archaeon *Pyrococcus furiosus*. *J Bacteriol* **182**, 3423-3428 (2000).

85 Sapra, R., Bagramyan, K. & Adams, M. W. W. A simple energy-conserving system: Proton reduction coupled to proton translocation. *Proc Natl Acad Sci USA* **100**, 7545-7550 (2003).

86 Pisa, K. Y., Huber, H., Thomm, M. & Müller, V. A sodium ion-dependent A1AO ATP synthase from the hyperthermophilic archaeon *Pyrococcus furiosus*. *FEBS J* **274**, 3928-3938 (2007).

87 Schut, G. J., Zhou, J. & Adams, M. W. DNA microarray analysis of the hyperthermophilic archaeon *Pyrococcus furiosus*: evidence for a new type of sulfur-reducing enzyme complex. *J Bacteriol* **183**, 7027-7036 (2001).

88 Wu, C.-H., Schut, G. J., Poole, F. L., 2nd, Haja, D. K. & Adams, M. W. W. Characterization of membrane-bound sulfane reductase: A missing link in the evolution of modern day respiratory complexes. *J Biol Chem* **293**, 16687-16696 (2018).

89 Schut, G. J., Bridger, S. L. & Adams, M. W. W. Insights into the metabolism of elemental sulfur by the hyperthermophilic archaeon *Pyrococcus furiosus*: Characterization of a coenzyme A- dependent NAD(P)H sulfur oxidoreductase. *J Bacteriol* **189**, 4431-4441 (2007).

90 Vaccaro, B. J. *et al.* Biological iron-sulfur storage in a thioferrate-protein nanoparticle. *Nat Commun* **8**, 16110 (2017).

91 Bridger, S. L. *et al.* Deletion strains reveal metabolic roles for key elemental sulfur-responsive proteins in *Pyrococcus furiosus*. *J Bacteriol* **193**, 6498-6504 (2011).

92 Clarkson, S. M., Newcomer, E. C., Young, E. G. & Adams, M. W. The elemental sulfur-responsive protein (SipA) from the hyperthermophilic archaeon *Pyrococcus furiosus* is regulated by sulfide in an iron-dependent manner. *J Bacteriol* **192**, 5841-5843 (2010).

93 Lipscomb, G. L. *et al.* SurR: a transcriptional activator and repressor controlling hydrogen and elemental sulphur metabolism in *Pyrococcus furiosus*. *Mol Microbiol* **71**, 332-349 (2009).

94 Yang, H. *et al.* SurR regulates hydrogen production in *Pyrococcus furiosus* by a sulfur-dependent redox switch. *Mol Microbiol* **77**, 1111-1122 (2010).

95 Lipscomb, G. L., Schut, G. J., Scott, R. A. & Adams, M. W. W. SurR is a master regulator of the primary electron flow pathways in the order Thermococcales. *Mol Microbiol* **104**, 869-881 (2017).

96 Lubitz, W., Ogata, H., Rüdiger, O. & Reijerse, E. Hydrogenases. *Chem Rev* **114**, 4081-4148 (2014).

97 Thauer, R. K. *et al.* Hydrogenases from methanogenic archaea, nickel, a novel cofactor, and H2 Storage. *Annu Rev Biochem* **79**, 507-536 (2010).

98 Horner, D. S., Heil, B., Happe, T. & Embley, T. M. Iron hydrogenases; ancient enzymes in modern eukaryotes. *Trends Biochem Sci* **27**, 148-153 (2002).

99 Tamagnini, P. *et al.* Cyanobacterial hydrogenases: diversity, regulation and applications. *FEMS Microbiol Rev* **31**, 692-720 (2007).

100 Vignais, P. M. & Billoud, B. Occurrence, classification, and biological function of hydrogenases: An overview. *Chem Rev* **107**, 4206-4272 (2007).

101 Carrieri, D., Wawrousek, K., Eckert, C., Yu, J. & Maness, P. C. The role of the bidirectional hydrogenase in cyanobacteria. *Bioresour Technol* **102**, 8368-8377 (2011).

102 Buhrke, T. *et al.* Reduction of unusual iron-sulfur clusters in the H-sensing regulatory Ni-Fe hydrogenase from *Ralstonia eutropha*. *J Biol Chem* **280**, 19488-19495 (2005).

103 Kleihues, L., Lenz, O., Bernhard, M., Buhrke, T. & Friedrich, B. The H(2) sensor of Ralstonia eutropha is a member of the subclass of regulatory [NiFe] hydrogenases. *J Bacteriol* **182**, 2716-2724 (2000).

104 Greening, C. *et al.* Genomic and metagenomic surveys of hydrogenase distribution indicate H2 is a widely utilised energy source for microbial growth and survival. *ISME J* **10**, 761-777 (2016).

105 Afting, C., Kremmer, E., Brucker, C., Hochheimer, A. & Thauer, R. K. Regulation of the synthesis of H2-forming methylenetetrahydromethanopterin dehydrogenase (Hmd) and of HmdII and HmdIII in *Methanothermobacter marburgensis*. *Arch Microbiol* **174**, 225-232 (2000).

106 Afting, C., Hochheimer, A. & Thauer, R. K. Function of H2-forming methylenetetrahydromethanopterin dehydrogenase from *Methanobacterium thermoautotrophicum* in coenzyme F420 reduction with H2. *Arch Microbiol* **169**, 206-210 (1998).

107 Vogt, S., Lyon, E. J., Shima, S. & Thauer, R. K. The exchange activities of [Fe] hydrogenase (iron-sulfur-cluster-free hydrogenase) from methanogenic archaea in comparison with the exchange activities of [FeFe] and [NiFe] hydrogenases. *J Biol Inorg Chem* **13**, 97-106 (2008).

108 Schleucher, J., Griesinger, C., Schwörer, B. & Thauer, R. K. H2-forming N5, N10-methylenetetrahydromethanopterin dehydrogenase from *Methanobacterium*

thermoautotrophicum catalyzes a stereoselective hydride transfer as determined by two-dimensional NMR spectroscopy. *Biochemistry* **33**, 3986-3993 (1994).

109 Thauer, R. K., Klein, A. R. & Hartmann, G. C. Reactions with molecular hydrogen in microorganisms: Evidence for a purely organic hydrogenation catalyst. *Chem Rev* **96**, 3031-3042 (1996).

110 Shima, S. *et al.* The Crystal Structure of [Fe]-Hydrogenase Reveals the Geometry of the Active Site. *Science* **321**, 572-575 (2008).

111 Korbas, M. *et al.* The iron-sulfur cluster-free hydrogenase (Hmd) is a metalloenzyme with a novel iron binding motif. *J Biol Chem* **281**, 30804-30813 (2006).

112 Hiromoto, T., Warkentin, E., Moll, J., Ermler, U. & Shima, S. The crystal structure of an [Fe]-hydrogenase-substrate complex reveals the framework for H2 activation. *Angew Chem Int Ed Engl* **48**, 6457-6460 (2009).

113 Peters, J. W., Lanzilotta, W. N., Lemon, B. J. & Seefeldt, L. C. X-ray crystal structure of the Fe-only hydrogenase (CpI) from *Clostridium pasteurianum* to 1.8 angstrom resolution. *Science* **282**, 1853-1858 (1998).

114 Nicolet, Y., Piras, C., Legrand, P., Hatchikian, C. E. & Fontecilla-Camps, J. C. *Desulfovibrio desulfuricans* iron hydrogenase: the structure shows unusual coordination to an active site Fe binuclear center. *Structure* **7**, 13-23 (1999).

115 Happe, T. & Naber, J. D. Isolation, characterization and N-terminal amino acid sequence of hydrogenase from the green alga *Chlamydomonas reinhardtii*. *Eur J Biochem* **214**, 475-481 (1993).

116 Nicolet, Y., Lemon, B. J., Fontecilla-Camps, J. C. & Peters, J. W. A novel FeS cluster in Fe-only hydrogenases. *Trends Biochem Sci* **25**, 138-143 (2000).

117 Vignais, P. M., Billoud, B. & Meyer, J. Classification and phylogeny of hydrogenases. *FEMS Microbiol Rev* **25**, 455-501 (2001).

118 Kuchenreuther, J. M. *et al.* The HydG enzyme generates an Fe(CO)2(CN) synthon in assembly of the FeFe hydrogenase H-cluster. *Science* **343**, 424-427 (2014).

119 Kuchenreuther, J. M., Britt, R. D. & Swartz, J. R. New insights into [FeFe] hydrogenase activation and maturase function. *PLoS ONE* **7**, e45850 (2012).

120 King, P. W., Posewitz, M. C., Ghirardi, M. L. & Seibert, M. Functional studies of [FeFe] hydrogenase maturation in an *Escherichia coli* biosynthetic system. *J Bacteriol* **188**, 2163-2172 (2006).

121 Rubach, J. K., Brazzolotto, X., Gaillard, J. & Fontecave, M. Biochemical characterization of the HydE and HydG iron-only hydrogenase maturation enzymes from *Thermatoga maritima*. *FEBS Lett* **579**, 5055-5060 (2005).

122 Schut, G. J. & Adams, M. W. W. The iron-hydrogenase of *Thermotoga maritima* utilizes ferredoxin and NADH synergistically: a new perspective on anaerobic hydrogen production. *J Bacteriol* **191**, 4451-4457 (2009).

123 Wang, S. *et al.* NADP-specific electron-bifurcating [FeFe]-hydrogenase in a functional complex with formate dehydrogenase in *Clostridium autoethanogenum* grown on CO. *J Bacteriol* **195**, 4373-4386 (2013).

124 Zheng, Y., Kahnt, J., Kwon, I. H., Mackie, R. I. & Thauer, R. K. Hydrogen formation and its regulation in *Ruminococcus albus*: involvement of an electron-bifurcating [FeFe]-hydrogenase, of a non-electron-bifurcating [FeFe]-hydrogenase,

and of a putative hydrogen-sensing [FeFe]-hydrogenase. *J Bacteriol* **196**, 3840-3852 (2014).

125 Volbeda, A. *et al.* Crystal structure of the nickel-iron hydrogenase from *Desulfovibrio gigas*. *Nature* **373**, 580-587 (1995).

126 Lubitz, W., Reijerse, E. & van Gastel, M. [NiFe] and [FeFe] hydrogenases studied by advanced magnetic resonance techniques. *Chem Rev* **107**, 4331-4365 (2007).

127 Stuchebrukhov, A. A. Long-distance electron tunneling in proteins: A new challenge for time-resolved spectroscopy. *Laser Phys* **20**, 125-138 (2010).

128 Casalot, L. & Rousset, M. Maturation of the [NiFe] hydrogenases. *Trends Microbiol* **9**, 228-237 (2001).

129 Böck, A., King, P. W., Blokesch, M. & Posewitz, M. C. Maturation of hydrogenases. *Adv Microb Physiol* **51**, 1-71 (2006).

130 Forzi, L. & Sawers, R. G. Maturation of [NiFe]-hydrogenases in *Escherichia coli*. *Biometals* **20**, 565 (2007).

131 Watanabe, S., Sasaki, D., Tominaga, T. & Miki, K. Structural basis of [NiFe] hydrogenase maturation by Hyp proteins. *Biol Chem* **393**, 1089-1100 (2012).

132 Marques, M. C., Coelho, R., De Lacey, A. L., Pereira, I. A. & Matias, P. M. The three-dimensional structure of [NiFeSe] hydrogenase from *Desulfovibrio vulgaris* Hildenborough: a hydrogenase without a bridging ligand in the active site in its oxidised, "as-isolated" state. *J Mol Biol* **396**, 893-907 (2010).

133 Gross, R., Simon, J., Theis, F. & Kröger, A. Two membrane anchors of *Wolinella succinogenes* hydrogenase and their function in fumarate and polysulfide respiration. *Arch Microbiol* **170**, 50-58 (1998).

134 Maier, L. *et al.* Microbiota-derived hydrogen fuels *Salmonella typhimurium* invasion of the gut ecosystem. *Cell Host Microbe* **14**, 641-651 (2013).

135 Fritsch, J. *et al.* The crystal structure of an oxygen-tolerant hydrogenase uncovers a novel iron-sulphur centre. *Nature* **479**, 249-252 (2011).

136 Ogata, H., Kellers, P. & Lubitz, W. The crystal structure of the [NiFe] hydrogenase from the photosynthetic bacterium *Allochromatium vinosum*: Characterization of the oxidized enzyme (Ni-A state). *J Mol Biol* **402**, 428-444 (2010).

137 Tremblay, P.-L. & Lovley, D. R. Role of the NiFe hydrogenase Hya in oxidative stress defense in *Geobacter sulfurreducens*. *J Bacteriol* **194**, 2248-2253 (2012).

138 Laska, S., Lottspeich, F. & Kletzin, A. Membrane-bound hydrogenase and sulfur reductase of the hyperthermophilic and acidophilic archaeon *Acidianus ambivalens*. *Microbiology (Reading, Engl)* **149**, 2357-2371 (2003).

139 Greening, C., Berney, M., Hards, K., Cook, G. M. & Conrad, R. A soil actinobacterium scavenges atmospheric H2 using two membrane-associated, oxygen-dependent [NiFe] hydrogenases. *Proc Natl Acad Sci USA* **111**, 4257-4261 (2014).

140 Koch, H. *et al.* Growth of nitrite-oxidizing bacteria by aerobic hydrogen oxidation. *Science* **345**, 1052-1054 (2014).

141 Vignais, P. M., Elsen, S. & Colbeau, A. Transcriptional regulation of the uptake [NiFe] hydrogenase genes in *Rhodobacter capsulatus*. *Biochem Soc Trans* **33**, 28-32 (2005).

142 Mills, D. J., Vitt, S., Strauss, M., Shima, S. & Vonck, J. De novo modeling of the F420-reducing [NiFe]-hydrogenase from a methanogenic archaeon by cryo-electron microscopy. *eLife* **2**, e00218 (2013).

143 Ma, K., Schicho, R. N., Kelly, R. M. & Adams, M. W. Hydrogenase of the hyperthermophile *Pyrococcus furiosus* is an elemental sulfur reductase or sulfhydrogenase: Evidence for a sulfur-reducing hydrogenase ancestor. *Proc Natl Acad Sci USA* **90**, 5341-5344 (1993).

144 Kaster, A.-K., Moll, J., Parey, K. & Thauer, R. K. Coupling of ferredoxin and heterodisulfide reduction via electron bifurcation in hydrogenotrophic methanogenic archaea. *Proc Natl Acad Sci USA* **108**, 2981-2986 (2011).

145 McDowall, J. S. *et al.* Bacterial formate hydrogenlyase complex. *Proc Natl Acad Sci USA* **111**, E3948-E3956 (2014).

146 Lim, J. K., Mayer, F., Kang, S. G. & Müller, V. Energy conservation by oxidation of formate to carbon dioxide and hydrogen via a sodium ion current in a hyperthermophilic archaeon. *Proc Natl Acad Sci USA* **111**, 11497-11502 (2014).

147 Soboh, B., Linder, D. & Hedderich, R. Purification and catalytic properties of a CO-oxidizing:H2-evolving enzyme complex from *Carboxydothermus hydrogenoformans*. *Eur J Biochem* **269**, 5712-5721 (2002).

148 Porat, I. *et al.* Disruption of the operon encoding Ehb hydrogenase limits anabolic CO2 assimilation in the archaeon *Methanococcus maripaludis*. *J Bacteriol* **188**, 1373-1380 (2006).

149 Lie, T. J. *et al.* Essential anaplerotic role for the energy-converting hydrogenase Eha in hydrogenotrophic methanogenesis. *Proc Natl Acad Sci USA* **109**, 15473-15478 (2012).

150 Meuer, J., Kuettner, H. C., Zhang, J. K., Hedderich, R. & Metcalf, W. W. Genetic analysis of the archaeon Methanosarcina barkeri Fusaro reveals a central role for Ech hydrogenase and ferredoxin in methanogenesis and carbon fixation. *Proc Natl Acad Sci U S A* **99**, 5632-5637 (2002).

151 Sazanov, L. A. A giant molecular proton pump: structure and mechanism of respiratory complex I. *Nat Rev Mol* **16**, 375-388 (2015).

152 Hirst, J. Mitochondrial complex I. *Annu Rev Biochem* **82**, 551-575 (2013).

153 Berrisford, J. M., Baradaran, R. & Sazanov, L. A. Structure of bacterial respiratory complex I. *Biochim Biophys Acta* **1857**, 892-901 (2016).

154 Baradaran, R., Berrisford, J. M., Minhas, G. S. & Sazanov, L. A. Crystal structure of the entire respiratory complex I. *Nature* **494**, 443-448 (2013).

155 Zhu, J., Vinothkumar, K. R. & Hirst, J. Structure of mammalian respiratory complex I. *Nature* **536**, 354-358 (2016).

156 Kampjut, D. & Sazanov, L. A. The coupling mechanism of mammalian respiratory complex I. *Science* **370**, eabc4209 (2020).

157 Kudo, T., Hino, M., Kitada, M. & Horikoshi, K. DNA sequences required for the alkalophily of *Bacillus* sp. strain C-125 are located close together on its chromosomal DNA. *J Bacteriol* **172**, 7282-7283 (1990).

158 Swartz, T. H., Ikewada, S., Ishikawa, O., Ito, M. & Krulwich, T. A. The Mrp system: a giant among monovalent cation/proton antiporters? *Extremophiles* **9**, 345-354 (2005).

159 Krulwich, T. A., Hicks, D. B. & Ito, M. Cation/proton antiporter complements of bacteria: why so large and diverse? *Mol microbiol* **74**, 257-260 (2009).

160 Ito, M., Guffanti, A. A., Wang, W. & Krulwich, T. A. Effects of nonpolar mutations in each of the seven *Bacillus subtilis* mrp genes suggest complex interactions among the gene products in support of Na+ and alkali but not cholate resistance. *J Bacteriol* **182**, 5663-5670 (2000).

161 Ito, M., Guffanti, A. A., Oudega, B. & Krulwich, T. A. Mrp, a multigene, multifunctional locus in *Bacillus subtilis* with roles in resistance to cholate and to Na+ and in pH homeostasis. *J Bacteriol* **181**, 2394-2402 (1999).

162 Dzioba-Winogrodzki, J., Winogrodzki, O., Krulwich, T. A., Boin, M. A. & Dibrov, P. The *Vibrio cholerae* Mrp system: cation/proton antiport properties and enhancement of bile salt resistance in a heterologous host. *J Microbiol Biotechnol* **16**, 176-186 (2009).

163 Kosono, S., Morotomi, S., Kitada, M. & Kudo, T. Analyses of a *Bacillus subtilis* homologue of the Na+/H+ antiporter gene which is important for pH homeostasis of alkaliphilic *Bacillus* sp. C-125. *Biochim Biophys Acta Bioenerg* **1409**, 171-175 (1999).

164 Kosono, S. *et al.* Characterization of a multigene-encoded sodium/hydrogen antiporter (Sha) from *Pseudomonas aeruginosa*: its involvement in pathogenesis. *J Bacteriol* **187**, 5242-5248 (2005).

165 Kosono, S., Ohashi, Y., Kawamura, F., Kitada, M. & Kudo, T. Function of a principal Na+/H+ antiporter, ShaA, is required for initiation of sporulation in *Bacillus subtilis*. *J Bacteriol* **182**, 898-904 (2000).

166 Putnoky, P. *et al.* The pha gene cluster of *Rhizobium meliloti* involved in pH adaptation and symbiosis encodes a novel type of K+ efflux system. *Mol Microbiol* **28**, 1091-1101 (1998).

167 Kashyap, D. R., Botero, L. M., Lehr, C., Hassett, D. J. & McDermott, T. R. A Na+: H+ antiporter and a molybdate transporter are essential for arsenite oxidation in *Agrobacterium tumefaciens*. *J Bacteriol* **188**, 1577-1584 (2006).

168 Morino, M., Natsui, S., Swartz, T. H., Krulwich, T. A. & Ito, M. Single gene deletions of mrpA to mrpG and mrpE point mutations affect activity of the Mrp Na+/H+ antiporter of alkaliphilic *Bacillus* and formation of hetero-oligomeric Mrp complexes. *J Bacteriol* **190**, 4162-4172 (2008).

169 Morino, M., Ogoda, S., Krulwich, T. A. & Ito, M. Differences in the phenotypic effects of mutations in homologous MrpA and MrpD subunits of the multi-subunit Mrp-type Na+/H+ antiporter. *Extremophiles* **21**, 51-64 (2017).

170 Morino, M. *et al.* Single site mutations in the hetero-oligomeric Mrp antiporter from alkaliphilic *Bacillus pseudofirmus* OF4 that affect Na+/H+ antiport activity, sodium exclusion, individual Mrp protein levels, or Mrp complex formation. *J Biol Chem* **285**, 30942-30950 (2010).

171 Steiner, J. & Sazanov, L. Structure and mechanism of the Mrp complex, an ancient cation/proton antiporter. *eLife* **9**, e59407 (2020).

172 Li, B. *et al.* Structure of the *Dietzia* Mrp complex reveals molecular mechanism of this giant bacterial sodium proton pump. *Proc Natl Acad Sci USA* **117**, 31166-31176 (2020).

173 Boyd, E. S., Schut, G. J., Adams, M. W. & Peters, J. W. Hydrogen metabolism and the evolution of biological respiration. *Microbe* **9**, 361-367 (2014).

174 Schut, G. J. *et al.* The role of geochemistry and energetics in the evolution of modern respiratory complexes from a proton-reducing ancestor. *Biochim Biophys ACTA Bioenerg* **1857**, 958-970 (2016).

175 Philippot, P. *et al.* Early Archaean microorganisms preferred elemental sulfur, not sulfate. *Science* **317**, 1534-1537 (2007).

176 Kletzin, A., Urich, T., Müller, F., Bandeiras, T. M. & Gomes, C. M. Dissimilatory oxidation and reduction of elemental sulfur in thermophilic archaea. *J Bioenerg Biomembr* **36**, 77-91 (2004).

177 Meyer, B. Elemental sulfur. *Chem Rev* **76**, 367-388 (1976).

178 Hedderich, R. *et al.* Anaerobic respiration with elemental sulfur and with disulfides. *FEMS Microbiol Rev* **22**, 353-381 (1998).

179 Blank, C. E. Phylogenomic dating—the relative antiquity of archaeal metabolic and physiological traits. *Astrobiology* **9**, 193-219 (2009).

180 Laska, S., Lottspeich, F. & Kletzin, A. Membrane-bound hydrogenase and sulfur reductase of the hyperthermophilic and acidophilic archaeon *Acidianus ambivalens*. *Microbiology* **149**, 2357-2371 (2003).

181 Jormakka, M. *et al.* Molecular mechanism of energy conservation in polysulfide respiration. *Nat Struct Mol Biol* **15**, 730-737 (2008).

182 Leigh, J. A., Albers, S.-V., Atomi, H. & Allers, T. Model organisms for genetics in the domain Archaea: methanogens, halophiles, Thermococcales and Sulfolobales. *FEMS Microbiol Rev* **35**, 577-608 (2011).

183 Lipscomb, G. L. *et al.* Natural competence in the hyperthermophilic archaeon *Pyrococcus furiosus* facilitates genetic manipulation: construction of markerless deletions of genes encoding the two cytoplasmic hydrogenases. *Appl Environ Microbiol* **77**, 2232-2238 (2011).

184 Bridger, S. L., Lancaster, W. A., Poole, F. L., Schut, G. J. & Adams, M. W. W. Genome sequencing of a genetically tractable *Pyrococcus furiosus* strain reveals a highly dynamic genome. *J Bacteriol* **194**, 4097-4106 (2012).

185 Yoon, S. H. *et al.* Parallel evolution of transcriptome architecture during genome reorganization. *Genome Res* **21**, 1892-1904 (2011).

186 Schut, G. J., Boyd, E. S., Peters, J. W. & Adams, M. W. The modular respiratory complexes involved in hydrogen and sulfur metabolism by heterotrophic hyperthermophilic archaea and their evolutionary implications. *FEMS Microbiol Rev* **37**, 182-203 (2013).

187 Schut, G. J., Nixon, W. J., Lipscomb, G. L., Scott, R. A. & Adams, M. W. W. Mutational analyses of the enzymes involved in the metabolism of hydrogen by the hyperthermophilic archaeon *Pyrococcus furiosus*. *Front Microbiol* **3**, 163-163 (2012).

188 Thorgersen, M. P., Stirrett, K., Scott, R. A. & Adams, M. W. W. Mechanism of oxygen detoxification by the surprisingly oxygen-tolerant hyperthermophilic archaeon, *Pyrococcus furiosus*. *Proc Natl Acad Sci USA* **109**, 18547-18552 (2012).

189 Thorgersen, M. P., Lipscomb, G. L., Schut, G. J., Kelly, R. M. & Adams, M. W. Deletion of acetyl-CoA synthetases I and II increases production of 3-hydroxypropionate by the metabolically-engineered hyperthermophile Pyrococcus furiosus. *Metab Eng* **22**, 83-88 (2014).

190 de la Tour, C. B., Portemer, C., Kaltoum, H. & Duguet, M. Reverse gyrase from the hyperthermophilic bacterium *Thermotoga maritima*: Properties and gene structure. *J Bacteriol* **180**, 274-281 (1998).

191 Chandrayan, S. K. *et al.* Engineering hyperthermophilic archaeon *Pyrococcus furiosus* to overproduce its cytoplasmic [NiFe]-hydrogenase. *J Biol Chem* **287**, 3257-3264 (2012).

192 McTernan, P. M. *et al.* Intact functional fourteen-subunit respiratory membrane-bound [NiFe]-hydrogenase complex of the hyperthermophilic archaeon *Pyrococcus furiosus*. *J Biol Chem* **289**, 19364-19372 (2014).

193 McTernan, P. M. *et al.* Engineering the respiratory membrane-bound hydrogenase of the hyperthermophilic archaeon *Pyrococcus furiosus* and characterization of the catalytically active cytoplasmic subcomplex. *Protein Eng Des Sel* **28**, 1-8 (2015).

194 Wu, C.-H., Ponir, C. A., Haja, D. K. & Adams, M. W. W. Improved production of the NiFe-hydrogenase from *Pyrococcus furiosus* by increased expression of maturation genes. *Protein Eng Des Sel* **31**, 337-344 (2018).

195 Nguyen, D. M. N. *et al.* Two functionally distinct NADP(+)-dependent ferredoxin oxidoreductases maintain the primary redox balance of *Pyrococcus furiosus*. *J Biol Chem* **292**, 14603-14616 (2017).

196 Keller, M. W. *et al.* Exploiting microbial hyperthermophilicity to produce an industrial chemical, using hydrogen and carbon dioxide. *Proc Natl Acad Sci USA* **110**, 5840-5845 (2013).

197 Keller, M. W. *et al.* Ethanol production by the hyperthermophilic archaeon *Pyrococcus furiosus* by expression of bacterial bifunctional alcohol dehydrogenases. *Microb Biotechnol* **10**, 1535-1545 (2017).

198 Keller, M. W. *et al.* A hybrid synthetic pathway for butanol production by a hyperthermophilic microbe. *Metab Eng* **27**, 101-106 (2015).

199 Nguyen, D. M. N. *et al.* Temperature-dependent acetoin production by *Pyrococcus furiosus* is catalyzed by a biosynthetic acetolactate synthase and its deletion improves ethanol production. *Metab Eng* **34**, 71-79 (2016).

200 Lipscomb, G. L. *et al.* Engineering hydrogen gas production from formate in a hyperthermophile by heterologous production of an 18-subunit membrane-bound complex. *J Biol Chem* **289**, 2873-2879 (2014).

201 Schut, G. J., Lipscomb, G. L., Nguyen, D. M., Kelly, R. M. & Adams, M. W. Heterologous production of an energy-conserving carbon monoxide dehydrogenase complex in the hyperthermophile *Pyrococcus furiosus*. *Front Microbiol* **7**, 29 (2016).

202 Völkl, P. *et al. Pyrobaculum aerophilum* sp. nov., a novel nitrate-reducing hyperthermophilic archaeum. *Appl Environ Microbiol* **59**, 2918-2926 (1993).

203 Fitz-Gibbon, S. T. *et al.* Genome sequence of the hyperthermophilic crenarchaeon *Pyrobaculum aerophilum*. *Proc Natl Acad Sci USA* **99**, 984-989 (2002).

204 Cozen, A. E. *et al.* Transcriptional map of respiratory versatility in the hyperthermophilic crenarchaeon *Pyrobaculum aerophilum*. *J Bacteriol* **191**, 782-794 (2009).

205 Afshar, S., Kim, C., Monbouquette, H. G. & Schröder, I. Effect of tungstate on nitrate reduction by the hyperthermophilic archaeon *Pyrobaculum aerophilum*. *Appl Environ Microbiol* **64**, 3004-3008 (1998).

206 De Vries, S. & Schröder, I. Comparison between the nitric oxide reductase family and its aerobic relatives, the cytochrome oxidases. *Biochem Soc Trans* **30**, 662-667 (2002).

207 De Vries, S., Strampraad, M. J., Lu, S., Moënne-Loccoz, P. & Schröder, I. Purification and characterization of the MQH2: NO oxidoreductase from the hyperthermophilic archaeon *Pyrobaculum aerophilum*. *J Biol Chem* **278**, 35861-35868 (2003).

208 de Vries, S. *et al.* Adaptation to a high-tungsten environment: *Pyrobaculum aerophilum* contains an active tungsten nitrate reductase. *Biochemistry* **49**, 9911-9921 (2010).

209 Stoffels, L., Krehenbrink, M., Berks, B. C. & Unden, G. Thiosulfate reduction in *Salmonella enterica* is driven by the proton motive force. *J Bacteriol* **194**, 475-485 (2012).

210 Mukund, S. & Adams, M. W. Molybdenum and vanadium do not replace tungsten in the catalytically active forms of the three tungstoenzymes in the hyperthermophilic archaeon *Pyrococcus furiosus*. *J Bacteriol* **178**, 163-167 (1996).

211 Holm, R. H., Solomon, E. I., Majumdar, A. & Tenderholt, A. Comparative molecular chemistry of molybdenum and tungsten and its relation to hydroxylase and oxotransferase enzymes. *Coord Chem Rev* **255**, 993-1015 (2011).

212 Schoepp-Cothenet, B. *et al*. The ineluctable requirement for the trans-iron elements molybdenum and/or tungsten in the origin of life. *Sci Rep* **2**, 263 (2012).

213 Kishida, K., Sohrin, Y., Okamura, K. & Ishibashi, J.-i. Tungsten enriched in submarine hydrothermal fluids. *Earth Planet Sci Lett* **222**, 819-827 (2004).

214 Hille, R., Hall, J. & Basu, P. The mononuclear molybdenum enzymes. *Chem Rev* **114**, 3963-4038 (2014).

215 Seelmann, C. S., Willistein, M., Heider, J. & Boll, M. Tungstoenzymes: occurrence, catalytic diversity and cofactor synthesis. *Inorganics* **8**, 44 (2020).

216 Miralles-Robledillo, J. M., Torregrosa-Crespo, J., Martínez-Espinosa, R. M. & Pire, C. DMSO reductase family: phylogenetics and applications of extremophiles. *Int J Mol Sci* **20**, 3349 (2019).

217 Leimkühler, S. The biosynthesis of the molybdenum cofactors in *Escherichia coli*. *Environ Microbiol* **22**, 2007-2026 (2020).

218 Reschke, S. *et al.* Identification of a bis-molybdopterin intermediate in molybdenum cofactor biosynthesis in *Escherichia coli*. *J Biol Chem* **288**, 29736-29745 (2013).

219 Feng, C., Tollin, G. & Enemark, J. H. Sulfite oxidizing enzymes. *Biochim Biophys ACTA* **1774**, 527-539 (2007).

220 Brondino, C. D., Romão, M. J., Moura, I. & Moura, J. J. G. Molybdenum and tungsten enzymes: the xanthine oxidase family. *Curr Opin Chem Biol* **10**, 109-114 (2006).

221 Roy, R. *et al.* Purification and molecular characterization of the tungsten-containing formaldehyde ferredoxin oxidoreductase from the hyperthermophilic archaeon *Pyrococcus furiosus*: the third of a putative five-member tungstoenzyme family. *J Bacteriol* **181**, 1171-1180 (1999).

222 Roy, R. & Adams, M. W. Characterization of a fourth tungsten-containing enzyme from the hyperthermophilic archaeon *Pyrococcus furiosus*. *J Bacteriol* **184**, 6952-6956 (2002).

223 Bevers, L. E., Bol, E., Hagedoorn, P.-L. & Hagen, W. R. WOR5, a novel tungsten-containing aldehyde oxidoreductase from *Pyrococcus furiosus* with a broad substrate specificity. *J Bacteriol* **187**, 7056-7061 (2005).

224 Scott, I. M. *et al.* The thermophilic biomass-degrading bacterium *Caldicellulosiruptor bescii* utilizes two enzymes to oxidize glyceraldehyde 3-phosphate during glycolysis. *J Biol Chem* **294**, 9995-10005 (2019).

225 Chan, M., Mukund, S., Kletzin, A., Adams, M. & Rees, D. Structure of a hyperthermophilic tungstopterin enzyme, aldehyde ferredoxin oxidoreductase. *Science* **267**, 1463-1469 (1995).

226 Arndt, F. *et al.* Characterization of an aldehyde oxidoreductase from the mesophilic bacterium *Aromatoleum aromaticum* EbN1, a member of a new subfamily of tungsten-containing enzymes. *Front Microbiol* **10**, 71 (2019).

227 Fuchs, G., Boll, M. & Heider, J. Microbial degradation of aromatic compounds—from one strategy to four. *Nat Rev Microbiol* **9**, 803-816 (2011).

228 Boll, M. & Fuchs, G. Benzoyl-coenzyme A reductase (dearomatizing), a key enzyme of anaerobic aromatic metabolism. *Eur J Biochem* **234**, 921-933 (1995).

229 Huwiler, S. G. *et al.* One-megadalton metalloenzyme complex in *Geobacter metallireducens* involved in benzene ring reduction beyond the biological redox window. *Proc Natl Acad Sci USA* **116**, 2259-2264 (2019).

230 Anselmann, S. E. *et al.* The class II benzoyl-coenzyme A reductase complex from the sulfate-reducing *Desulfosarcina cetonica*. *Environ Microbiol* **21**, 4241-4252 (2019).

231 Moura, J. J., Brondino, C. D., Trincão, J. & Romao, M. J. Mo and W bis-MGD enzymes: nitrate reductases and formate dehydrogenases. *J Biol Inorg Chem* **9**, 791-799 (2004).

232 Maia, L. B., Moura, J. J. & Moura, I. Molybdenum and tungsten-dependent formate dehydrogenases. *J Biol Inorg Chem* **20**, 287-309 (2015).

233 Vorholt, J. A. & Thauer, R. K. Molybdenum and tungsten enzymes in C1 metabolism. *Biometals* **39**, 571-619 (2002).

234 Enoch, H. G. & Lester, R. L. Effects of molybdate, tungstate, and selenium compounds on formate dehydrogenase and other enzyme systems in *Escherichia coli*. *J Bacteriol* **110**, 1032-1040 (1972).

235 May, H. D., Patel, P. S. & Ferry, J. G. Effect of molybdenum and tungsten on synthesis and composition of formate dehydrogenase in *Methanobacterium formicicum*. *J Bacteriol* **170**, 3384-3389 (1988).

236 Ljungdahl, L. G. & Andreesen, J. R. in *Methods in enzymology* Vol. 53 360-372 (Elsevier, 1978).

237 Strobl, G., Feicht, R., White, H., Lottspeich, F. & Simon, H. The tungsten-containing aldehyde oxidoreductase from *Clostridium thermoaceticum* and its complex with a viologen-accepting NADPH oxidoreductase. *Biol Chem* **373**, 123-132 (1992).

238 Mota, C. S. *et al.* Effects of molybdate and tungstate on expression levels and biochemical characteristics of formate dehydrogenases produced by *Desulfovibrio alaskensis* NCIMB 13491. *J Bacteriol* **193**, 2917-2923 (2011).

239 da Silva, S. M., Pimentel, C., Valente, F. M., Rodrigues-Pousada, C. & Pereira, I. A. Tungsten and molybdenum regulation of formate dehydrogenase expression in *Desulfovibrio vulgaris* Hildenborough. *J Bacteriol* **193**, 2909-2916 (2011).

240 Matschiavelli, N. & Rother, M. Role of a putative tungsten-dependent formylmethanofuran dehydrogenase in *Methanosarcina acetivorans*. *Arch Microbiol* **197**, 379-388 (2015).

241 Stewart, L. J. *et al.* Dimethylsulfoxide reductase: an enzyme capable of catalysis with either molybdenum or tungsten at the active site. *J Mol Biol* **299**, 593-600 (2000).

242 Johnson, M. K., Rees, D. C. & Adams, M. W. Tungstoenzymes. *Chem Rev* **96**, 2817-2840 (1996).

243 Wolterink, A. F. *et al.* Characterization of the chlorate reductase from *Pseudomonas chloritidismutans*. *J Bacteriol* **185**, 3210-3213 (2003).

244 Kengen, S. W., Rikken, G. B., Hagen, W. R., van Ginkel, C. G. & Stams, A. J. Purification and characterization of (per)chlorate reductase from the chlorate-respiring strain GR-1. *J Bacteriol* **181**, 6706-6711 (1999).

245 Del Giudice, I., Limauro, D., Pedone, E., Bartolucci, S. & Fiorentino, G. A novel arsenate reductase from the bacterium *Thermus thermophilus* HB27: its role in arsenic detoxification. *Biochim Biophys Acta* **1834**, 2071-2079 (2013).

246 Mukhopadhyay, R. & Rosen, B. P. Arsenate reductases in prokaryotes and eukaryotes. *Environ Health Perspect* **110 Suppl 5**, 745-748 (2002).

247 Hinojosa-Leon, M., Dubourdieu, M., Sanchez-Crispin, J. A. & Chippaux, M. Tetrathionate reductase of *Salmonella thyphimurium*: a molybdenum containing enzyme. *Biochem Biophys Res Commun* **136**, 577-581 (1986).

248 Ito, M., Morino, M. & Krulwich, T. A. Mrp antiporters have important roles in diverse bacteria and archaea. *Front Microbiol* **8** (2017).

249 Collins, M. D. *et al.* The phylogeny of the genus *Clostridium*: proposal of five new genera and eleven new species combinations. *Int J Syst Evol* **44**, 812-826 (1994).

250 Speelmans, G., Poolman, B., Abee, T. & Konings, W. N. Energy transduction in the thermophilic anaerobic bacterium *Clostridium fervidus* is exclusively coupled to sodium ions. *Proc Natl Acad Sci USA* **90**, 7975-7979 (1993).

251 Berrisford, J. M. & Sazanov, L. A. Structural basis for the mechanism of respiratory complex I. *J Biol Chem* **284**, 29773-29783 (2009).

252 Dilks, K., Rose, R. W., Hartmann, E. & Pohlschröder, M. Prokaryotic utilization of the twin-arginine translocation pathway: a genomic survey. *J Bacteriol* **185**, 1478-1483 (2003).

253 Bevers, L. E., Hagedoorn, P.-L., Krijger, G. C. & Hagen, W. R. Tungsten transport protein A (WtpA) in *Pyrococcus furiosus*: the first member of a new class of tungstate and molybdate transporters. *J Bacteriol* **188**, 6498-6505 (2006).

254 Hughes, M. F. Arsenic toxicity and potential mechanisms of action. *Toxicol Lett* **133**, 1-16 (2002).

APPENDIX A

STRUCTURE OF AN ANCIENT RESPIRATORY SYSTEM[5]

[5] Hongjun Yu, Chang-Hao Wu, Gerrit J. Schut, Dominik K. Haja, Gongpu Zhao, John W. Peters, Michael W. W. Adams and Huilin Li. *Cell.* 173.

Reprinted here with permission from the publisher.

Summary

Hydrogen gas-evolving membrane-bound hydrogenase (MBH) and quinone-reducing Complex I are homologous respiratory complexes with a common ancestor but a structural basis for their evolutionary relationship is lacking. Herein we report the cryo-EM structure of a 14-subunit MBH from the hyperthermophilie *Pyrococcus furiosus*. MBH contains a membrane-anchored hydrogenase module that is highly similar structurally to the quinone-binding Q-module of Complex I while its membrane-embedded ion-translocation module can be divided into a H^+- and a Na^+-translocating unit. The H^+-translocating unit is turned around with respect to its counterpart in Complex I, leading to distinctive architectures for the two respiratory systems despite their largely conserved proton-pumping mechanisms. The Na^+-translocating unit, absent in Complex I, resembles that found in the Mrp H^+/Na^+ antiporter and enables hydrogen gas evolution by MBH to establish a Na^+ gradient for ATP synthesis near 100 °C. MBH also provides insights into Mrp structure and evolution of MBH-based respiratory enzymes.

Highlights

• Atomic model of an ancient 14-protein respiratory system

• A potential structure-based mechanism for coupling H^+ and Na^+ ion translocation

• Insights into evolutionary relationship with Mrp antiporter and formate- and CO-oxidizing respiratory systems.

• MBH and Complex I are closely related evolutionarily but with some unexpected structural variations

Introduction

The evolution of complex life from anaerobic ancestors on this planet was driven in part by the high energy yield of aerobic respiration wherein membrane-bound electron transfer from NADH to molecular oxygen is coupled in a highly efficient manner to conserve energy in the form of a proton motive force. NADH oxidation is catalyzed by proton-pumping Complex I (or NADH quinone oxidoreductase) (Hirst, 2013; Letts and Sazanov, 2017; Sazanov, 2015). Some anaerobic archaea lacking Complex I instead use a sodium-pumping mechanism to provide chemical potential for ATP synthesis (Mayer and Muller, 2014). Typical examples are the 14-subunit membrane bound hydrogenase (MBH) (Sapra et al., 2003) of the hyperthermophile *Pyrococcus furiosus* and the closely related 18-subunit formate hydrogen lyase (FHL) (Lim et al., 2014) and 16-subunit carbon monoxide dehydrogenase (CODH) (Schut et al., 2016a) of *Thermococcus onnurineus*. CODH and FHL enable *T. onnurineus* to grow using only formate or CO as its sole energy (ATP) source. MBH, FHL, and CODH all evolve H_2 gas and contain group 4 [NiFe]-hydrogenase modules. They differ mainly in that FHL and CODH have additional subunits that enable

formate or CO, respectively, to serve as electron donors (Lipscomb et al., 2014; Schut et al., 2016a; Schut et al., 2016b). Hence MBH oxidizes reduced ferredoxin generated by sugar fermentation and evolves H_2 gas whereas FHL and CODH oxidize formate or CO to evolve H_2. In all cases, the redox reaction leads to H_2 production and generates a sodium ion gradient across the cell membrane (Kim et al., 2010; Lim et al., 2014; Mayer and Muller, 2014; Sapra et al., 2003). The membrane potential established by these membrane complexes is subsequently utilized by a Na^+-driven ATP synthase (Mayer and Muller, 2014; Pisa et al., 2007). Consistent with the similar mechanism of energy conservation among these complexes, both FHL (Lipscomb et al., 2014) and CODH (Schut et al., 2016a) have been heterologously-expressed in *P. furiosus* and the organism is then able to evolve H_2 by oxidizing formate or CO and also uses CO as a source of energy for growth. Indeed, stimulation of H_2 evolution by Na^+ ions has been experimentally demonstrated both with FHL (Lim et al., 2014) and with MBH (**Figure SA.1A**).

Complex I and these MBH-type respiratory complexes are evolutionarily related and share an ancestral root, which is generally considered to be the Mrp antiporter (**Figure A.1A**) (Efremov and Sazanov, 2012; Hedderich, 2004; Sazanov, 2015). Many of the membrane-embedded ion-translocating subunits of these complexes clearly have a common ancestor (**Table A.1**). For example, the MBH subunits D and E together, G, and H correspond to the *Thermus thermophilus* Complex I subunits Nqo10, Nqo11 and Nqo14, and the C-terminal region of MrpA, MrpC, and MrpD of the *Bacillus subtilis* Mrp antiporter, respectively. Interestingly, Complex I lack subunits corresponding to the MBH subunits A, B, C and F and Mrp subunits E, F, G and B (**Table A.1**) (Schut et al., 2013; Schut et al., 2016b). The Mrp antiporter system belongs to cation:proton antiporter-3

(CPA3) family. It provides resistance to high Na^+ stress through a H^+/Na^+ exchange mechanism and plays an essential role in numerous bacteria, including pathogens, although its molecular mechanism remains a mystery due to lack of a Mrp structure (Kosono et al., 2005; Krulwich et al., 2011; Morino et al., 2010; Morino et al., 2008; Swartz et al., 2005). Notably, except for MrpA, six out of the seven Mrp subunits have homologs in MBH (**Table A.1**), suggesting a shared Na^+ translocation core module between these complexes (Schut et al., 2013; Schut et al., 2016b).

Herein we have used the MBH from the anaerobic hyperthermophilic microorganism *Pyrococcus furiosus.* This grows optimally near 100°C in marine volcanic vents and has been proposed to represent an ancestral life form (Nisbet and Sleep, 2001). MBH conserves much less energy (ΔE=60mV; 12 kJ/mol/2e^-) than Complex I (ΔE=320mV; 41 kJ/mol/2e^-) because its electron acceptor, the proton (H^+/H_2 -420 mV), is of much lower potential than that of quinone (Q/QH_2, 0 mV) (Mayer and Muller, 2014; McTernan et al., 2014; Sapra et al., 2003). The fourteen MBH subunits are named alphabetically (Mbh A-N) and together they make up a molecular mass of ~300 kDa (McTernan et al., 2014). Like Complex I, MBH has peripheral and membrane arms. Four subunits (MbhJ, K, L and N) are predicted to be exposed to the cytoplasm and form the peripheral arm while the remaining ten (Mbh A-I, M) are predicted to be integral membrane proteins forming the membrane arm (Schut et al., 2013; Schut et al., 2016b). The peripheral arm contains the catalytic [NiFe] site (in MbhL) together with three iron-sulfur clusters (in Mbh N and J). MbhL and MbhJ show surprisingly low sequence homology to the corresponding subunits in the other three types of [NiFe] hydrogenase but they are homologous to the quinone-reducing Q-module of Complex I (Schut et al., 2013; Schut et

al., 2016b). These peripheral arms are involved in coupling electron transfer to hydrogen gas production and ubiquinone reduction, respectively (Schut et al., 2013; Schut et al., 2016b). Structural knowledge of an ancient respiratory complex such as the MBH would be invaluable to understanding the functional relationships among the anaerobic H_2-evolving membrane complexes (MBH, FHL and CODH) and the path that led to the evolution of Complex I of the aerobic respiratory chain. Therefore, we determined the structure of the MBH by cryo-EM single particle reconstruction and derived a 3.7-Å resolution atomic model.

Results

Structure determination.

We modified the 14-gene operon encoding MBH with an insert at the N-terminus of *mbhJ* encoding an affinity tag (His_9) (**Figure A.1B**). The affinity-tagged MBH complex was natively expressed in and purified from *P. furiosus* (see methods and **Figure SA.2**). Cryo-EM of the MBH resulted in a 3D density map at an average resolution of 3.7 Å; however, the transmembrane region has a better resolution of ~3.3 Å (**Figure A.1C**, **Figures SA.3-4 and Table SA.1**). Most loops and many side-chain densities were well resolved in the experimental electron density map allowing *de novo* model building for 2470 out of the total 2502 residues of the complex (**Figures SA.5-6**). A 32-residue flexible loop region of MbhI (residues 42-73) was not as well resolved and only allowed for main chain tracing (**Figure SA.5I**). Like Complex I, MBH adopts an L-shaped structure with dimensions of 120 Å *130 Å *60 Å with a peripheral arm and a membrane arm (**Figure A.1C-D).** The MBH atomic model represents the first structure of a group 4 [NiFe]-hydrogenase.

Membrane arm

The membrane arm of MBH contains 44 transmembrane helices (TMH) from 10 membrane-embedded subunits, Mbh A-I and M (**Figure A.2A**). The largest membrane subunit is MbhH and this features 14 TMH. Its TMH4-8 and TMH9-13 form two inverted folding units (**Figure SA.7A-B**) and each of these two 5-TMH units features a discontinuous 4th helix, TMH7 and TMH12, respectively. This fold with two discontinuous helices and internal symmetry is typically found in antiporter-like subunits of Complex I (Baradaran et al., 2013; Zhu et al., 2016; Zickermann et al., 2015). Indeed, subunit H is homologous to the antiporter-like subunits *T. thermophilus* Nqo14, Nqo13 and Nqo12 and mammalian ND2, ND4 and ND5 (**Figure SA.7A**), which are proposed to translocate protons (Baradaran et al., 2013; Hirst, 2013; Sazanov, 2015; Zhu et al., 2016; Zickermann et al., 2015). Therefore, we suggest a similar role for subunit H in MBH. Loosely packed against the H subunit is the M subunit and this has eight TMH and anchors the peripheral arm. The M subunit also contains a 5-TMH fold: TMH2-6 with a discontinuous 4th α-helix (TMH5). This is similar to subunit Nqo8 of Complex I (**Figure SA.7C-D**), consistent with their predicted homology (Schut et al., 2013). However, it is unclear if subunit M contributes to ion translocation because it is largely separated from the main ion-translocating module by a sizable gap that appears filled by two phospholipid molecules (**Figure SA.8**). Unexpectedly, a bridging subunit I ties together the otherwise separated main ion-translocating module and the subunit M-anchored peripheral module (**Figure A.2A**).

Located at the distal region of the membrane arm of MBH are seven smaller subunits, A-G, that are homologous to Mrp antiporter subunits (**Figure A.2A, Table A.1**)

(Schut et al., 2016b). Remarkably, MBH subunits B, C, D and G each fold into a three-helix sheet-like structure and they pack sequentially to form four contiguous layers (**Figure SA.7E**). Subunit G is sandwiched between TMH1 and TMH2 of subunit E. Subunit F contains four TMHs; two (TMH3-4) are exposed to the lipids and the other two (TMH1-2) are internal, tilted, and contact the four TMH3 of subunits B, C, D and G. At the distal end of the complex, subunit A starts with two short TMH that pack against TMH3 of subunit C and TMH1 of subunit F, followed by a long lateral helix (LH) (V60-I88), and ends with a cytosolic ferredoxin-like domain that wraps around the three TMHs of subunit C. The subunit F ferredoxin-like domain lacks the Cys residues necessary to coordinate an iron-sulfur cluster and indeed no such cluster was founded in our structure. The function of this domain is currently unknown.

The potential proton translocation subunits in the MBH membrane module

By aligning the homologous antiporter-like MBH subunit H with Nqo14 of Complex I, we identified a common core between these two respiratory complexes (**Figure A.2A-D**): subunit H corresponds to Nqo14, G to Nqo11, and D and E combined together correspond to Nqo10 (**Figure SA.9A-D**). Notably, the MBH core is turned around with respect to that of Complex I (**Figure A.2A-B**), giving rise to the apparently distinct architectures of the two complexes: the membrane-bound peripheral module is located to the left of the core in MBH, whereas the peripheral module in Complex I is at the right side of the core (**Figure A.2C**). Except for this 180° in-membrane relative rotation, the two commons cores are highly similar and share several important structural details: (1) MBH subunit D contains a π-bulge in the middle of TMH3 (**Figure SA.9D**); this is a structural feature observed in the corresponding TMH3 of Nqo10 of Complex I from various origins (Efremov and

Sazanov, 2011; Zhu et al., 2016; Zickermann et al., 2015); (2) MBH subunit I anchors the discontinuous TMH7 of subunit H via its middle lateral helix and the C-terminal region of TMH2 (**Figure A.2A**); this resembles another important feature observed in the Complex I structures, - the anchoring of Nqo12 onto Nqo14 (**Figure A.2D**, **Figure SA.9E**) (Baradaran et al., 2013; Zhu et al., 2016; Zickermann et al., 2015). (3) Two chains of polar and charged residues form two putative hydrophilic channels across the membrane arm: one within the antiporter-like subunit MbhH and the other within the small subunits D, E and G (**Figure A.2E**). They contribute two possible proton translocation pathways, which are connected via a hydrophilic central axis across the interior of this membrane core. Although there is controversy over the proton path across the small subunits in Complex I (the counterparts of MbhD, E and G) (Baradaran et al., 2013; Efremov and Sazanov, 2011; Kaila et al., 2014; Sazanov, 2015; Zickermann et al., 2015), the proposed proton paths and the central hydrophilic axis within this core MBH module are generally consistent with what has been proposed in Complex I (Baradaran et al., 2013; Efremov and Sazanov, 2011; Fiedorczuk et al., 2016; Zhu et al., 2016; Zickermann et al., 2015). In summary, given the structural correspondence described above, we suggest that this core (subunits D, E, G and H) identified in MBH is a module shared with Complex I and likely functions in proton translocation.

Peripheral arm and evolutionary relationship with Complex I

The MBH peripheral arm transfers electrons from ferredoxin to reduce protons to form H_2 gas (Sapra et al., 2003). This arm contains cytosolic subunits J, K, L, and N that are associated with the membrane by docking on integral membrane subunit M. The five subunits together are referred to as the membrane-anchored hydrogenase module (**Figures**

A.1D and **A.3A**). The MBH subunits L and J are equivalent to the large and small subunits, respectively, of the heterodimeric core present in all known [NiFe]-hydrogenases, but their structural (and sequence) similarity are limited only to the regions that coordinate the [NiFe]-catalytic site and its proximal [4Fe-4S] cluster (**Figure SA.10A**) (Hedderich, 2004). Indeed, the MBH hydrogenase module is much more similar in both sequence and structure to the hydrophilic Q-module and the associated membrane Nqo8 subunit of Complex I (**Figure SA.10B**). These observations support the concept of modular evolution of Complex I from an H_2-evolving ancestor (Efremov and Sazanov, 2012; Schut et al., 2013; Schut et al., 2016b).

As described above, the hydrogenase module and the proton-translocating membrane module are bridged by MBH subunit I, which is equivalent to a combination of the N-terminal region of Nqo7 and the C-terminal region of Nqo12 of Complex I (**Figure A.2D, Figure SA.10B**). The TMH1 of subunit I and Nqo7 are superimposable, but their second and third α-helices are configured differently: in Nqo7 they are both TMHs whereas in MBH subunit I the second α-helix is amphipathic and horizontal and only the third helix is a TMH. Both MbhI and Nqo7 feature a long loop adjacent to their respective redox active sites. The MBH subunits L, J, M, and I enclose a chamber that is equivalent to the quinone-binding chamber In Complex I (**Figure SA.10B**) (Baradaran et al., 2013; Zickermann et al., 2015). The entry to the chamber is open in Complex I for quinone diffusion, but is sealed off in MBH by bulky several residues, such as F47 and F50 of subunit M (**Figure SA.10C**).

The MBH peripheral arm lacks the equivalent of the so-called N-module of Complex I, which are the three additional subunits (Nqo1-3) that oxidize NADH and, via

flavin and multiple iron-sulfur clusters, channel electrons to the Q-module (**Figure SA.11A**). The four Q-module subunits of Complex I each contains an insertion loop that interacts with the N-module but these loops are not found in the homologous MBH subunits (J, K, L, and N; **Figure SA.11B-E**). These structural features confirm the evolutionary relationship between the MBH and Complex I and support the proposal that the N-module is the latest addition in the evolution of Complex I from a ferredoxin-oxidizing, hydrogen-gas evolving respiratory complex (Efremov and Sazanov, 2012; Moparthi and Hagerhall, 2011; Schut et al., 2013; Schut et al., 2016b).

A possible proton reduction mechanism of the hydrogenase module

In the MBH peripheral arm, the three [4Fe-4S] clusters form a chain and extend from the proposed ferredoxin-binding site by ~40 Å towards the interior [NiFe] site that catalyzes proton reduction to generate H_2 gas (**Figure A.1D inset**). The edge-to-edge distances between the neighboring clusters are smaller than 12 Å thereby allowing efficient electron tunneling (Page et al., 1999). The distal and medial [4Fe-4S] clusters are each coordinated by four Cys in subunit N, in a manner similar to the coordination of N6a and N6b [4Fe-4S] clusters in Complex I Nqo9 (**Figure SA.12A**). The [NiFe]-site and its proximal [4Fe-4S] cluster are also individually coordinated by four Cys in subunit L and J, respectively. This coordination scheme resembles the distantly-related dimeric hydrogenase core but it is different from that in Complex I Nqo4 as this lacks all four of the Cys that coordinate the NiFe cluster in MbhL (Sazanov and Hinchliffe, 2006) (**Figure SA.12B-C**). In the core of dimeric [NiFe]-hydrogenases, the proton is proposed to be transferred between a Cys and a nearby Glu (Dementin et al., 2004; Fontecilla-Camps et al., 2007). In MBH, E21 of subunit L likely plays the role of the Glu and donates a proton to the nearby C374 (**Figure**

A.3B). These two residues are invariably conserved among known members of group 4 hydrogenases (**Figure A.3C**). Upstream of E21, the proton is probably taken up from the bulk solvent and transferred via β2 and β3 strands of subunit L, involving residues E23, K24, D38, K40, and Y43 (**Figure A.3B**). Hence, although the overall sequence similarity between the dimeric cores of group 4 MBH and the other three groups of NiFe-hydrogenases is extremely low, their proton pathways may be conserved (Ogata et al., 2015; Shomura et al., 2011).

Two potential sodium-binding sites in MBH and their evolutionary relationship with the Mrp antiporter

The overall sequence identities between the Mrp subunits of the mesophilic bacterium *Bacilus subtilis* and their MBH counterparts range from 22-28% but there are highly conserved regions are between MrpB, C, D, E, F and G and the MBH subunits F, G, H, A, B and C, respectively (**Figure SA.13 and Table A.1**). Interestingly, MBH subunits D and E together appear to correspond to the C-terminal region of MrpA (**Figure SA.13F**). Mrp can be separated into two stable sub-complexes, MrpA-D and MrpE-G (Morino et al., 2008). This organization is consistent with the structure of MBH in which the corresponding MBH subunits D-H and A-C are packed together, respectively (**Figure A.2A**). Notably, we identified two negatively-charged cavities in MBH subunits A-C and F (**Figure A.4A**) and these four subunits are equivalent to MrpE-G and MrpB, homologs of which are not present in Complex I (**Table A.1**). Moreover, we have experimental evidence that MBH subunits A-C are involved in Na^+ pumping as the deletion strain of *P. furiosus* lacking these three subunits (Δ*mbhabc*) showed diminished Na^+-dependent H_2 evolution (**Figure SA.1B**).

Analyses of the negatively-charged cavities in MbhA-C suggest that they likely constitute a sodium ion translocation pathway. The first cavity reaches halfway into the membrane and is lined by the carboxyl group of the invariably-conserved D35 of MBH subunit B and by hydroxyl groups of five highly conserved residues: T36 and T72 of B and T39, T42 and T43 of C (**Figure A.4B, Figure SA.13B-C**). Together these residues could form a six coordinate site within this cavity, consistent with the binding of a single sodium ion (Kuppuraj et al., 2009). Another structural feature that supports of sodium ion binding is the presence of the conserved P88 of subunit C. It is located adjacent to conserved D35 of subunit B and breaks TMH3 of subunit C into two half-helices (TMH3i and TMH3ii) (**Figure A.4A-B**). Such a feature (an aspartate residue near the break in the TMH in the middle of membrane) is often found H+/Na+ antiporters (Coincon et al., 2016; Hunte et al., 2005; Lee et al., 2013; Wohlert et al., 2014). Indeed, MBH subunit C P88 is equivalent to P81 in MrpG and in a previous study it was demonstrated that the H^+/Na^+ antiporter activity of Mrp was abolished when P81 is substituted by an alanine or a glycine (Morino et al., 2010). Adjacent to and directly interacting with the potential sodium ion-binding cavity in MbhABC is a conserved loop (119-TPGT/S-122) in the subunit A ferredoxin-like domain. Mutations of MrpE T113Y and P114G, equivalent to T119 and P120 of MBH subunit A, were found previously to significantly reduce the Mrp H^+/Na^+ antiporter activity (Morino et al., 2010). Interestingly, this first potential Na^+-binding site in MBH faces the cytoplasm and is closed by a conserved salt bridge between D29 of subunit B and R34 of subunit C (**Figure A.4B**). If the first cavity is truly a Na^+-binding site, one might further speculate that two adjacent aspartate residues, D29 of subunit B and D30 of subunit C, may function to concentrate Na^+ ions. Adjacent to the potential Na^+ concentrator D29 is the

conserved R30 of subunit B that stabilizes a loop around the cavity entrance. Mutations D32A and R33A in MrpF, equivalent to D29 and R30 of MBH subunit B, either abolished (D32A) or reduced (R33A) the H^+/Na^+ antiporter activity (Morino et al., 2010).

The second negatively-charged cavity in MBH is enclosed by TMH1 of subunit A, TMH3 of subunit B, TMH3 of subunit C, and a loop of subunit F containing the GHxxPGGGF motif that is highly conserved in Mrp antiporters (**Figure A.4A, C, E**). Several positively charged residues line the cavity and because this cavity faces the outside of the cell we propose that these residues may facilitate the release of Na^+ ions (**Figure A.4C-D**). The conserved and potentially Na^+-coordinating D59 of subunit B in the cavity is 15 Å above the exit face and 18 Å below the potential Na^+-coordinating D35 of subunit B in the first cavity. The two Na^+-binding cavities are separated by several hydrophobic residues. Therefore, if the two cavities are indeed the Na^+ binding sites, a conformational change would be required during a H^+/Na^+ translocation cycle. Interestingly, subunit F contains a pair of tilted helices (TMH1-2) that bridge the potential Na^+-translocating module with the proton-translocation subunit G via hydrophobic interactions, and may just play such a role (**Figure A.4C, E**). Consistent with this scenario, mutations that disrupt the interactions in the Mrp system, such as MrpB F41A and MrpC T75A, equivalent to F39 of MBH subunit F and T81 of MBH subunit G, resulted in a reduced tolerance of the microbes to Na^+ (Morino et al., 2010).

As noted above, MrpA is the only Mrp subunit that does not have a homolog in MBH (**Table A.1**). MrpA and MrpD are both homologous to the antiporter-like Nqo12-14 subunits of Complex I (Sazanov, 2015), where the latter are proposed to pump protons in Complex I (Baradaran et al., 2013; Fiedorczuk et al., 2016; Zhu et al., 2016; Zickermann

et al., 2015). Furthermore, MrpA-D was previously shown to form a stable sub-complex (Morino et al., 2008). On the basis of these analyses, we suggest that the Mrp antiporter has an extra proton path within MrpA, in addition to those within the H^+ translocation module shared with MBH (**Table A.1**, **Figure A.5C**). Therefore, from an evolutionary perspective, MrpA appears to have been replaced by the membrane-anchored hydrogenase module - the peripheral arm attached to subunit M in MBH - converting the secondary antiporter system into a system that couples a redox reaction with ion pumping activity, as now found in MBH.

Discussion

How modern-day Complex I evolved is a fundamental yet not well understood question. The cryo-EM structure of MBH as we have described above shows that (1) Complex I and MBH share a closely-related substrate-reducing (either protons or quinone) module in their respective peripheral arm, which is similarly anchored to one membrane subunit (**Figure SA.10B**); (2) MBH shares a potential proton-translocation module with Complex I, despite the fact that the proton translocating module within each of these complexes is turned around with respect to their respective peripheral module (**Figure A.2A-B**); (3) Both respiratory systems show bimodular architecture and the two modules are tied together by a similar linking structure at the peripheral arm involving MBH subunit I and Complex I Nqo7 (**Figure A.2A-B**, **Figure SA.10B**). However, the linking mechanism is different at the membrane arm: two TMHs of Complex Nqo7 and a lateral helix and one TMH of MBH subunit I (**Figure SA.10B**), possibly arising from the different orientation of the proton-translocation module between MBH and Complex I (**Figure A.2A-B**). A major distinction between the two complexes is a proposed sodium ion translocation unit that is absent in

Complex I but resides in subunit A-C and F in MBH and is shared with the Mrp antiporter (**Figure A.5A-C**). Therefore, it appears that MBH evolved from the Mrp antiporter by acquiring the membrane-bound hydrogenase module with the concomitant loss of MrpA (**Figure A.5B-C**). One could imagine that Complex I may have evolved from Mrp by acquiring a second proton translocation unit with an additional proton path at the expense of the sodium translocation unit, as well as acquiring the ability to reduce quinone in the peripheral arm rather than reducing protons to hydrogen gas (**Figure A.5A, C**). These insights structurally confirm the long-recognized evolutional relationship among MBH, Complex I and the Mrp antiporter, and supports the hypothesis that they may have evolved by the assembly of prebuilt modules (Efremov and Sazanov, 2012; Hedderich, 2004; Sazanov, 2015).

Because the potential proton-translocation module of MBH is turned around when compared to Complex I and is proximal to the redox-reaction site (**Figure A.2A-B**), it is likely that the released redox energy of ferredoxin oxidation by the hydrogenase module is coupled to pumping out a proton through the first proton path in the adjacent subunit H. Subsequently, the outside proton may flow back in via the second proton path, driving the outward pumping of a sodium ion through the proposed sodium translocation path (**Figures A.4, 5B**). Such a scheme is consistent with the Na^+-dependent energy conservation mechanism proposed for certain anaerobic archaea, particularly involving the MBH-family member and closely-related FHL of *T. onnurineus* (Kim et al., 2010; Lim et al., 2014; Mayer and Muller, 2014).

The structural conservation between MBH and Complex I in the redox site is somewhat unexpected, given they utilize very different electron donors and acceptors. We

highlight the following three conserved features: (1) Three loops near the catalytic [NiFe] center in MBH ($Linker_{\beta1\text{-}\beta2}{}^{L}$, $Linker_{TM1\text{-}2}{}^{I}$ and $Linker_{TM5\text{-}6}{}^{M}$, **Figure A.3A**) show good agreement with their counterparts in Complex I ($Linker_{\beta1\text{-}\beta2}{}^{Nqo4}$, $Linker_{TM1\text{-}2}{}^{Nqo7}$ and $Linker_{TM5\text{-}6}{}^{Nqo8}$; *T. thermophilus*) (**Figure SA.14**); (2) The hydrogen gas-evolving catalytic [NiFe]-site of MBH (MbhL E21-C374-[NiFe]) is close to the proposed binding site of the quinone head-group in Complex I (**Figure SA.14A**) (Baradaran et al., 2013); (3) The long $Linker_{TM1\text{-}2}{}^{I}$ is partially disordered (**Figure SA.5I**), comparable to its counterpart (TMH1-2 loop of ND3) in a structure of the *B. taurus* Complex I (Zhu et al., 2016). These conserved structural features may suggest a similar energy transduction mechanism between the peripheral and membrane arms in the two complexes (Baradaran et al., 2013; Zhu et al., 2016; Zickermann et al., 2015). However, the exact molecular mechanism is currently unknown in either system (Berrisford et al., 2016; Brandt, 2011; Hirst, 2013; Hirst and Roessler, 2016; Letts and Sazanov, 2017; Sazanov, 2015; Wirth et al., 2016). Indeed, the lateral helix linking unit conserved between MBH (helix HL) and Complex I is a remarkable feature (**Figure A.2D**). Some have suggested that this helix in Complex I may function as a coupling rod to transduce the redox potential to proton translocation (Baradaran et al., 2013; Hunte et al., 2010; Sazanov, 2015; Steimle et al., 2011). However, such a role is debatable based on recent biochemical studies (Belevich et al., 2011; Hirst, 2013; Zhu and Vik, 2015). It is possible that the required energy transduction in MBH is coupled via the lateral helix of subunit I but it may simply play a structural role by cementing the two MBH subcomplexes into a stable molecular machine.

To summarize, the cryo-EM derived atomic model of MBH represents a first structure of any respiratory complex directly related to Complex I. The MBH structure has

illuminated several aspects of the evolutionary relationship between Mrp antiporter and Complex I, and will serve as a starting point for mechanistic understanding of these fundamental energy-transducing systems that are ubiquitous in biology.

Supplementary Information is available in the online version of the paper.

Author Contributions

M.W.W.A. and H.L. conceived and designed experiments**.** H.Y., C.H.W., G.J.S., G.Z. and D.K.H. performed experiments. H.Y, G.J.S., M.W.W.A, J.W.P., and H.L. analyzed the data. H.Y., G.J.S, M.W.W.A., and H.L. wrote the manuscript.

Acknowledgements

Cryo-EM images were collected at the David Van Andel Advanced Cryo-Electron Microscopy Suite in the Van Andel Research Institute. This work was funded by grants from the Division of Chemical Sciences, Geosciences and Biosciences, Office of Basic Energy Sciences of the U.S. Department of Energy (DOE; DE-FG05-95ER20175 to M.W.W.A.), the Van Andel Research Institute (to H.L.), and the US National Institutes of Health (AI070285 to H.L.). J.W.P. was supported for contribution to the structural analysis as part of the Biological and Electron Transfer and Catalysis (BETCy) EFRC, an Energy Frontier Research Center funded by the U.S. Department of Energy, Office of Science (DE-SC0012518).

Accession Codes

The cryo-EM 3D map of the MBH complex has been deposited at the EMDB database with accession code EMD-7468. The corresponding atomic model was deposited at the RCSB PDB with accession code 6CFW.

References

Adams, P.D., Afonine, P.V., Bunkoczi, G., Chen, V.B., Davis, I.W., Echols, N., Headd, J.J., Hung, L.W., Kapral, G.J., Grosse-Kunstleve, R.W., *et al.* (2010). PHENIX: a comprehensive Python-based system for macromolecular structure solution. Acta Crystallogr D Biol Crystallogr *66*, 213-221.

Arnold, K., Bordoli, L., Kopp, J., and Schwede, T. (2006). The SWISS-MODEL workspace: a web-based environment for protein structure homology modelling. Bioinformatics *22*, 195-201.

Baradaran, R., Berrisford, J.M., Minhas, G.S., and Sazanov, L.A. (2013). Crystal structure of the entire respiratory complex I. Nature *494*, 443-448.

Belevich, G., Knuuti, J., Verkhovsky, M.I., Wikstrom, M., and Verkhovskaya, M. (2011). Probing the mechanistic role of the long alpha-helix in subunit L of respiratory Complex I from Escherichia coli by site-directed mutagenesis. Mol Microbiol *82*, 1086-1095.

Berrisford, J.M., Baradaran, R., and Sazanov, L.A. (2016). Structure of bacterial respiratory complex I. Biochim Biophys Acta *1857*, 892-901.

Brandt, U. (2011). A two-state stabilization-change mechanism for proton-pumping complex I. Biochim Biophys Acta *1807*, 1364-1369.

Bryksin, A.V., and Matsumura, I. (2010). Overlap extension PCR cloning: a simple and reliable way to create recombinant plasmids. Biotechniques *48*, 463-465.

Chen, S., McMullan, G., Faruqi, A.R., Murshudov, G.N., Short, J.M., Scheres, S.H., and Henderson, R. (2013). High-resolution noise substitution to measure overfitting and validate resolution in 3D structure determination by single particle electron cryomicroscopy. Ultramicroscopy *135*, 24-35.

Chen, V.B., Arendall, W.B., 3rd, Headd, J.J., Keedy, D.A., Immormino, R.M., Kapral, G.J., Murray, L.W., Richardson, J.S., and Richardson, D.C. (2010). MolProbity: all-atom structure validation for macromolecular crystallography. Acta Crystallogr D Biol Crystallogr *66*, 12-21.

Coincon, M., Uzdavinys, P., Nji, E., Dotson, D.L., Winkelmann, I., Abdul-Hussein, S., Cameron, A.D., Beckstein, O., and Drew, D. (2016). Crystal structures reveal the molecular basis of ion translocation in sodium/proton antiporters. Nat Struct Mol Biol *23*, 248-255.

Dementin, S., Burlat, B., De Lacey, A.L., Pardo, A., Adryanczyk-Perrier, G., Guigliarelli, B., Fernandez, V.M., and Rousset, M. (2004). A glutamate is the essential proton transfer gate during the catalytic cycle of the [NiFe] hydrogenase. J Biol Chem *279*, 10508-10513.

Efremov, R.G., and Sazanov, L.A. (2011). Structure of the membrane domain of respiratory complex I. Nature *476*, 414-420.

Efremov, R.G., and Sazanov, L.A. (2012). The coupling mechanism of respiratory complex I - a structural and evolutionary perspective. Biochim Biophys Acta *1817*, 1785-1795.

Emsley, P., Lohkamp, B., Scott, W.G., and Cowtan, K. (2010). Features and development of Coot. Acta Crystallogr D Biol Crystallogr *66*, 486-501.

Fiedorczuk, K., Letts, J.A., Degliesposti, G., Kaszuba, K., Skehel, M., and Sazanov, L.A. (2016). Atomic structure of the entire mammalian mitochondrial complex I. Nature *538*, 406-410.

Fontecilla-Camps, J.C., Volbeda, A., Cavazza, C., and Nicolet, Y. (2007). Structure/function relationships of [NiFe]- and [FeFe]-hydrogenases. Chem Rev *107*, 4273-4303.

Grant, T., and Grigorieff, N. (2015). Measuring the optimal exposure for single particle cryo-EM using a 2.6 A reconstruction of rotavirus VP6. Elife *4*, e06980.

Hedderich, R. (2004). Energy-converting [NiFe] hydrogenases from archaea and extremophiles: ancestors of complex I. J Bioenerg Biomembr *36*, 65-75.

Hirst, J. (2013). Mitochondrial complex I. Annu Rev Biochem *82*, 551-575.

Hirst, J., and Roessler, M.M. (2016). Energy conversion, redox catalysis and generation of reactive oxygen species by respiratory complex I. Biochim Biophys Acta *1857*, 872-883.

Hunte, C., Screpanti, E., Venturi, M., Rimon, A., Padan, E., and Michel, H. (2005). Structure of a Na+/H+ antiporter and insights into mechanism of action and regulation by pH. Nature *435*, 1197-1202.

Hunte, C., Zickermann, V., and Brandt, U. (2010). Functional modules and structural basis of conformational coupling in mitochondrial complex I. Science *329*, 448-451.

Kaila, V.R., Wikstrom, M., and Hummer, G. (2014). Electrostatics, hydration, and proton transfer dynamics in the membrane domain of respiratory complex I. Proc Natl Acad Sci U S A *111*, 6988-6993.

Kim, Y.J., Lee, H.S., Kim, E.S., Bae, S.S., Lim, J.K., Matsumi, R., Lebedinsky, A.V., Sokolova, T.G., Kozhevnikova, D.A., Cha, S.S., *et al.* (2010). Formate-driven growth coupled with H(2) production. Nature *467*, 352-355.

Kimanius, D., Forsberg, B.O., Scheres, S.H., and Lindahl, E. (2016). Accelerated cryo-EM structure determination with parallelisation using GPUs in RELION-2. Elife *5*.

Kosono, S., Haga, K., Tomizawa, R., Kajiyama, Y., Hatano, K., Takeda, S., Wakai, Y., Hino, M., and Kudo, T. (2005). Characterization of a multigene-encoded sodium/hydrogen antiporter (sha) from Pseudomonas aeruginosa: its involvement in pathogenesis. J Bacteriol *187*, 5242-5248.

Krulwich, T.A., Sachs, G., and Padan, E. (2011). Molecular aspects of bacterial pH sensing and homeostasis. Nat Rev Microbiol *9*, 330-343.

Kucukelbir, A., Sigworth, F.J., and Tagare, H.D. (2014). Quantifying the local resolution of cryo-EM density maps. Nat Methods *11*, 63-65.

Kuppuraj, G., Dudev, M., and Lim, C. (2009). Factors governing metal-ligand distances and coordination geometries of metal complexes. J Phys Chem B *113*, 2952-2960.

Lee, C., Kang, H.J., von Ballmoos, C., Newstead, S., Uzdavinys, P., Dotson, D.L., Iwata, S., Beckstein, O., Cameron, A.D., and Drew, D. (2013). A two-domain elevator mechanism for sodium/proton antiport. Nature *501*, 573-577.

Letts, J.A., and Sazanov, L.A. (2017). Clarifying the supercomplex: the higher-order organization of the mitochondrial electron transport chain. Nat Struct Mol Biol *24*, 800-808.

Lim, J.K., Mayer, F., Kang, S.G., and Muller, V. (2014). Energy conservation by oxidation of formate to carbon dioxide and hydrogen via a sodium ion current in a hyperthermophilic archaeon. Proc Natl Acad Sci U S A *111*, 11497-11502.

Lipscomb, G.L., Schut, G.J., Thorgersen, M.P., Nixon, W.J., Kelly, R.M., and Adams, M.W. (2014). Engineering hydrogen gas production from formate in a hyperthermophile by heterologous production of an 18-subunit membrane-bound complex. J Biol Chem *289*, 2873-2879.

Lipscomb, G.L., Stirrett, K., Schut, G.J., Yang, F., Jenney, F.E., Jr., Scott, R.A., Adams, M.W., and Westpheling, J. (2011). Natural competence in the hyperthermophilic archaeon Pyrococcus furiosus facilitates genetic manipulation: construction of markerless deletions of genes encoding the two cytoplasmic hydrogenases. Appl Environ Microbiol *77*, 2232-2238.

Mastronarde, D.N. (2005). Automated electron microscope tomography using robust prediction of specimen movements. Journal of Structural Biology *152*, 36-51.

Mayer, F., and Muller, V. (2014). Adaptations of anaerobic archaea to life under extreme energy limitation. FEMS Microbiol Rev *38*, 449-472.

McTernan, P.M., Chandrayan, S.K., Wu, C.H., Vaccaro, B.J., Lancaster, W.A., Yang, Q., Fu, D., Hura, G.L., Tainer, J.A., and Adams, M.W. (2014). Intact functional

fourteen-subunit respiratory membrane-bound [NiFe]-hydrogenase complex of the hyperthermophilic archaeon Pyrococcus furiosus. J Biol Chem *289*, 19364-19372.

Moparthi, V.K., and Hagerhall, C. (2011). The evolution of respiratory chain complex I from a smaller last common ancestor consisting of 11 protein subunits. J Mol Evol *72*, 484-497.

Morino, M., Natsui, S., Ono, T., Swartz, T.H., Krulwich, T.A., and Ito, M. (2010). Single site mutations in the hetero-oligomeric Mrp antiporter from alkaliphilic Bacillus pseudofirmus OF4 that affect Na+/H+ antiport activity, sodium exclusion, individual Mrp protein levels, or Mrp complex formation. J Biol Chem *285*, 30942-30950.

Morino, M., Natsui, S., Swartz, T.H., Krulwich, T.A., and Ito, M. (2008). Single gene deletions of mrpA to mrpG and mrpE point mutations affect activity of the Mrp Na+/H+ antiporter of alkaliphilic Bacillus and formation of hetero-oligomeric Mrp complexes. J Bacteriol *190*, 4162-4172.

Nisbet, E.G., and Sleep, N.H. (2001). The habitat and nature of early life. Nature *409*, 1083-1091.

Ogata, H., Nishikawa, K., and Lubitz, W. (2015). Hydrogens detected by subatomic resolution protein crystallography in a [NiFe] hydrogenase. Nature *520*, 571-574.

Page, C.C., Moser, C.C., Chen, X., and Dutton, P.L. (1999). Natural engineering principles of electron tunnelling in biological oxidation-reduction. Nature *402*, 47-52.

Pettersen, E.F., Goddard, T.D., Huang, C.C., Couch, G.S., Greenblatt, D.M., Meng, E.C., and Ferrin, T.E. (2004). UCSF Chimera--a visualization system for exploratory research and analysis. J Comput Chem *25*, 1605-1612.

Pisa, K.Y., Huber, H., Thomm, M., and Muller, V. (2007). A sodium ion-dependent A1AO ATP synthase from the hyperthermophilic archaeon Pyrococcus furiosus. FEBS J *274*, 3928-3938.

Rohou, A., and Grigorieff, N. (2015). CTFFIND4: Fast and accurate defocus estimation from electron micrographs. J Struct Biol *192*, 216-221.

Rosenthal, P.B., and Henderson, R. (2003). Optimal determination of particle orientation, absolute hand, and contrast loss in single-particle electron cryomicroscopy. J Mol Biol *333*, 721-745.

Sapra, R., Bagramyan, K., and Adams, M.W. (2003). A simple energy-conserving system: proton reduction coupled to proton translocation. Proc Natl Acad Sci U S A *100*, 7545-7550.

Sazanov, L.A. (2015). A giant molecular proton pump: structure and mechanism of respiratory complex I. Nat Rev Mol Cell Biol *16*, 375-388.

Sazanov, L.A., and Hinchliffe, P. (2006). Structure of the hydrophilic domain of respiratory complex I from Thermus thermophilus. Science *311*, 1430-1436.

Schut, G.J., Boyd, E.S., Peters, J.W., and Adams, M.W. (2013). The modular respiratory complexes involved in hydrogen and sulfur metabolism by heterotrophic

hyperthermophilic archaea and their evolutionary implications. FEMS Microbiol Rev *37*, 182-203.

Schut, G.J., Lipscomb, G.L., Nguyen, D.M., Kelly, R.M., and Adams, M.W. (2016a). Heterologous Production of an Energy-Conserving Carbon Monoxide Dehydrogenase Complex in the Hyperthermophile Pyrococcus furiosus. Front Microbiol *7*, 29.

Schut, G.J., Zadvornyy, O., Wu, C.H., Peters, J.W., Boyd, E.S., and Adams, M.W. (2016b). The role of geochemistry and energetics in the evolution of modern respiratory complexes from a proton-reducing ancestor. Biochim Biophys Acta *1857*, 958-970.

Shomura, Y., Yoon, K.S., Nishihara, H., and Higuchi, Y. (2011). Structural basis for a [4Fe-3S] cluster in the oxygen-tolerant membrane-bound [NiFe]-hydrogenase. Nature *479*, 253-256.

Steimle, S., Bajzath, C., Dorner, K., Schulte, M., Bothe, V., and Friedrich, T. (2011). Role of subunit NuoL for proton translocation by respiratory complex I. Biochemistry *50*, 3386-3393.

Swartz, T.H., Ikewada, S., Ishikawa, O., Ito, M., and Krulwich, T.A. (2005). The Mrp system: a giant among monovalent cation/proton antiporters? Extremophiles *9*, 345-354.

Tang, G., Peng, L., Baldwin, P.R., Mann, D.S., Jiang, W., Rees, I., and Ludtke, S.J. (2007). EMAN2: an extensible image processing suite for electron microscopy. J Struct Biol *157*, 38-46.

Volbeda, A., Garcin, E., Piras, C., deLacey, A.L., Fernandez, V.M., Hatchikian, E.C., Frey, M., and FontecillaCamps, J.C. (1996). Structure of the [NiFe] hydrogenase active site: Evidence for biologically uncommon Fe ligands. Journal of the American Chemical Society *118*, 12989-12996.

Wirth, C., Brandt, U., Hunte, C., and Zickermann, V. (2016). Structure and function of mitochondrial complex I. Biochim Biophys Acta *1857*, 902-914.

Wohlert, D., Kuhlbrandt, W., and Yildiz, O. (2014). Structure and substrate ion binding in the sodium/proton antiporter PaNhaP. Elife *3*, e03579.

Yang, J., Yan, R., Roy, A., Xu, D., Poisson, J., and Zhang, Y. (2015). The I-TASSER Suite: protein structure and function prediction. Nat Methods *12*, 7-8.

Zheng, S.Q., Palovcak, E., Armache, J.P., Verba, K.A., Cheng, Y., and Agard, D.A. (2017). MotionCor2: anisotropic correction of beam-induced motion for improved cryo-electron microscopy. Nat Methods *14*, 331-332.

Zhu, J., Vinothkumar, K.R., and Hirst, J. (2016). Structure of mammalian respiratory complex I. Nature *536*, 354-358.

Zhu, S., and Vik, S.B. (2015). Constraining the Lateral Helix of Respiratory Complex I by Cross-linking Does Not Impair Enzyme Activity or Proton Translocation. J Biol Chem *290*, 20761-20773.

Zickermann, V., Wirth, C., Nasiri, H., Siegmund, K., Schwalbe, H., Hunte, C., and Brandt, U. (2015). Structural biology. Mechanistic insight from the crystal structure of mitochondrial complex I. Science *347*, 44-49.

Table A.1. Homologous counterparts among respiratory Complex I (*Thermus thermophilus*), *Bacillus subtilis* Mrp H^+/Na^+ antiporter and *Pyrococcus furiosus* MBH

Proposed MBH module	***P. furiosus*** **MBH complex**	***B. subtilis*** **Mrp complex**	***T. thermophilus*** **Complex I**	**Module of Complex I**
-	-	-	Nqo15/Nqo16	-
-	-	-	Nqo1/Nqo2/ Nqo3	N-module
Membrane-anchored hydrogenase module	MbhJ	-	Nqo6	Q-module
	MbhK	-	Nqo5	
	MbhL	-	Nqo4	
	MbhN	-	Nqo9	
	MbhM	-	Nqo8	P-module
-	-	MrpA TM1-16	Nqo12/Nqo13	
-	MbhI N-terminal[a]	-	Nqo7 N-terminal	
-	MbhI C-terminal[b]	-	Nqo12 C-terminal	
Proton translocation module	MbhD[c]	MrpA TM17-21	Nqo10	
	MbhE[c]			
	MbhG	MrpC	Nqo11	
	MbhH	MrpD	Nqo14	
Sodium translocation module	MbhF	MrpB	-	-
	MbhA	MrpE	-	
	MbhB	MrpF	-	
	MbhC	MrpG	-	

[a]MbhI N-terminal TMH1 and its following loop are homologous to Nqo7 N-terminal TMH1 and its following loop (Figure S10B).

[b]MbhI C-terminal lateral helix and TMH2 is homologous to Nqo12 C-terminal lateral helix and TMH16 (Figure 2D and Figure S9E).

[c]MbhD and MbhE together are homologous to Nqo10 (Figure 2D and Figure S9D).

Figure A.1

Overall structure of the *Pyrococcus furiosus* MBH.

A. The respiratory MBH complex and Complex I are evolutionarily and functionally related to the Mrp H^+/Na^+ antiporter system. Fd_{ox} and Fd_{red} represent oxidized and reduced ferredoxin, respectively.

B. Operon encoding 14 subunits (MbhA-N) of *P. furiosus* MBH are coloured as labeled. Three modules based on the MBH structure are indicated. The operon was genetically modified for complex preparation: a Hisx9 tag was inserted to the N terminus of *mbhJ* with preceding promoters (*Pgdh* and *Pslp*) and selectable marker (pyrF). See Methods for more details.

C. Cryo-EM map of MBH complex segmented by subunits and viewed from the membrane side (left) and cytoplasmic side (right). Subunits are coloured as those in panel (**B**).

D. Two orthogonal views of the MBH structure in cartoon display. Subunits are coloured the same as in panel (**B**). **D** inset, Arrangement of three [4Fe-4S] clusters and one [NiFe]-center in the peripheral arm, viewed in an orientation as in the right panel. The distance between metal sites, including center-to-center and edge-to-edge distances (in brackets) are indicated in Å.

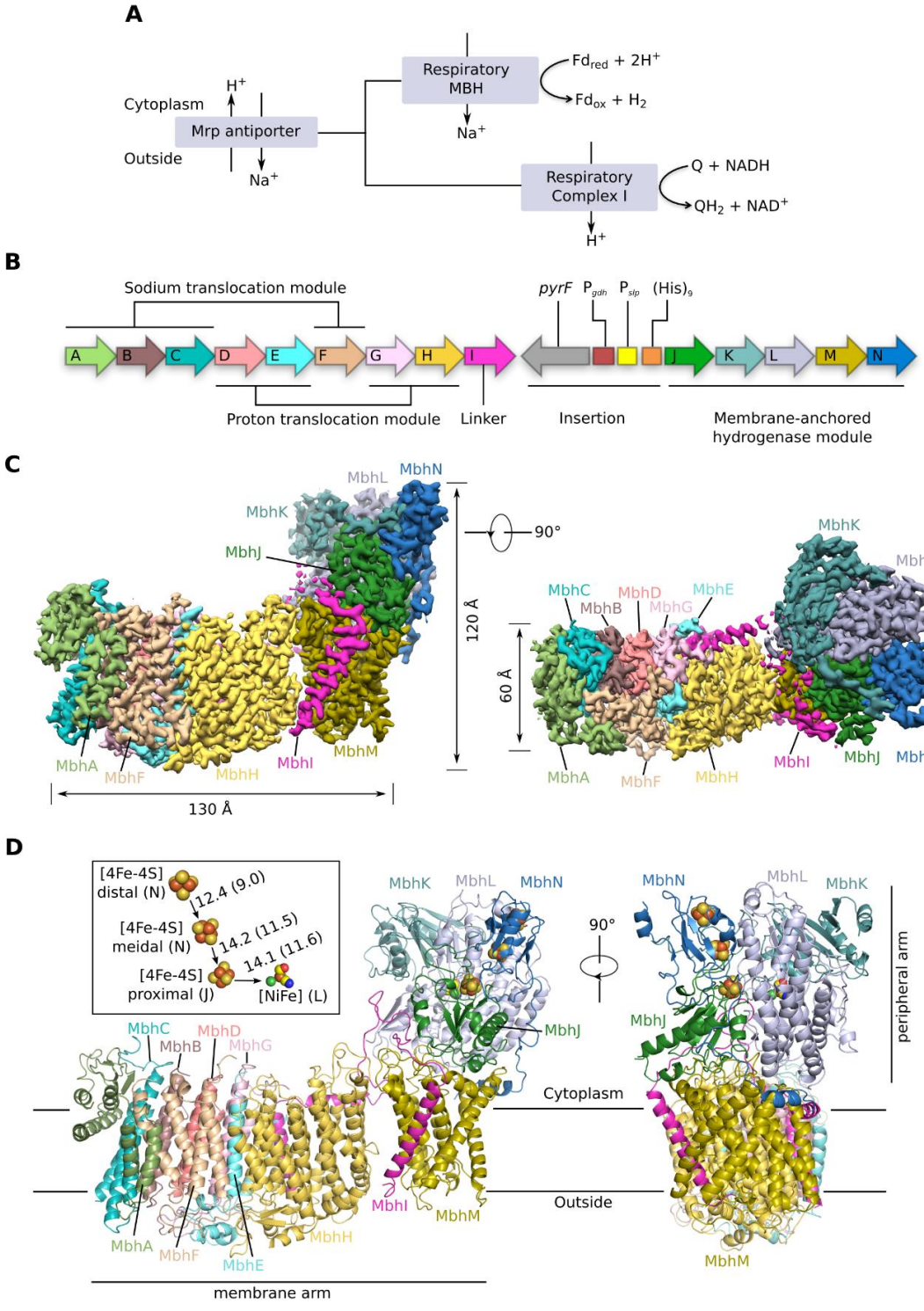
A
Respiratory MBH
Fdred + 2H+
Fdox + H2
H+
Cytoplasm
Mrp antiporter
Outside
Na+
Na+
Respiratory Complex I
Q + NADH
QH2 + NAD+
H+
B
Sodium translocation module
pyrF
Pgdh
Pslp
(His)9
A
B
C
D
E
F
G
H
I
J
K
L
M
N
Proton translocation module
Linker
Insertion
Membrane-anchored hydrogenase module
C
MbhL
MbhN
MbhK
MbhJ
90°
120 Å
60 Å
MbhA
MbhF
MbhH
MbhI
MbhM
130 Å
MbhC
MbhB
MbhD
MbhG
MbhE
D
[4Fe-4S] distal (N)
12.4 (9,0)
[4Fe-4S] meidal (N)
14.2 (11.5)
14.1 (11.6)
[4Fe-4S] proximal (J)
[NiFe] (L)
Cytoplasm
Outside
membrane arm
peripheral arm

Figure A.2

Membrane arm.

A. Top view of the MBH membrane arm from the cytoplasm. Subunits are coloured as in **Figure A.1D**. Outlined region is the proton-translocation module containing two potential proton pathways.

B. Complex I (*T. thermophiles*; PDB ID 4hea) membrane arm is lined up with MBH in (**A**) through the alignment of their homologous subunits on the proximal end of the membrane domain: Nqo8 (Complex I) and MbhM (MBH complex). Subunits are coloured as labelled where homologous subunits between Complex I and MBH are coloured the same. Outlined region is the proton-translocation module shared with MBH but its orientation is reversed compared to that in MBH.

C. Complex I (*T. thermophiles*; PDB ID 4hea) is lined up with MBH via their respective antiporter-like subunits Nqo14 and MbhH. They are shown separately for clarity. The well-aligned proton-translocation modules (as outlined in panel **A** and **B**) are shown as transparent surfaces. MBH subunits are coloured as in **A**. Complex I Nqo12 is in orange, Nqo13 green, Nqo10, Nqo11 and Nqo14 light grey, and all the other subunits dark grey.

D. Zoomed view of the alignment as in (**C**). Subunits within the shared proton-translocation module are shown. Complex I Nqo8 and MBH MbhM are shown as transparent cartoon. Prominent shared features are labeled, including: (1) the discontinuous TMH7 and TMH12 of MbhH/Nqo14; (2) the lateral helix HL and the following TMH of MbhI/Nqo12 anchored to the discontinuous TMH7; (3) TMH3 of MbhD/Nqo10 with a π-bulge.

E. Two potential proton translocation paths in the MBH. The discontinuous helices of MbhH (TMH7 and TMH12; featured in antiporter-like subunits of Complex I) and the π-bulge helix (TMH3 of MbhD) are shown as cylinders. Polar residues lining the proton path are shown as sticks. Protonatable residues along the horizontal central hydrophilic axis are underlined. A hydrophilic axis across MbhM membrane interior is also identified but it is separated from that in MbhH due to a gap between the two subunits.

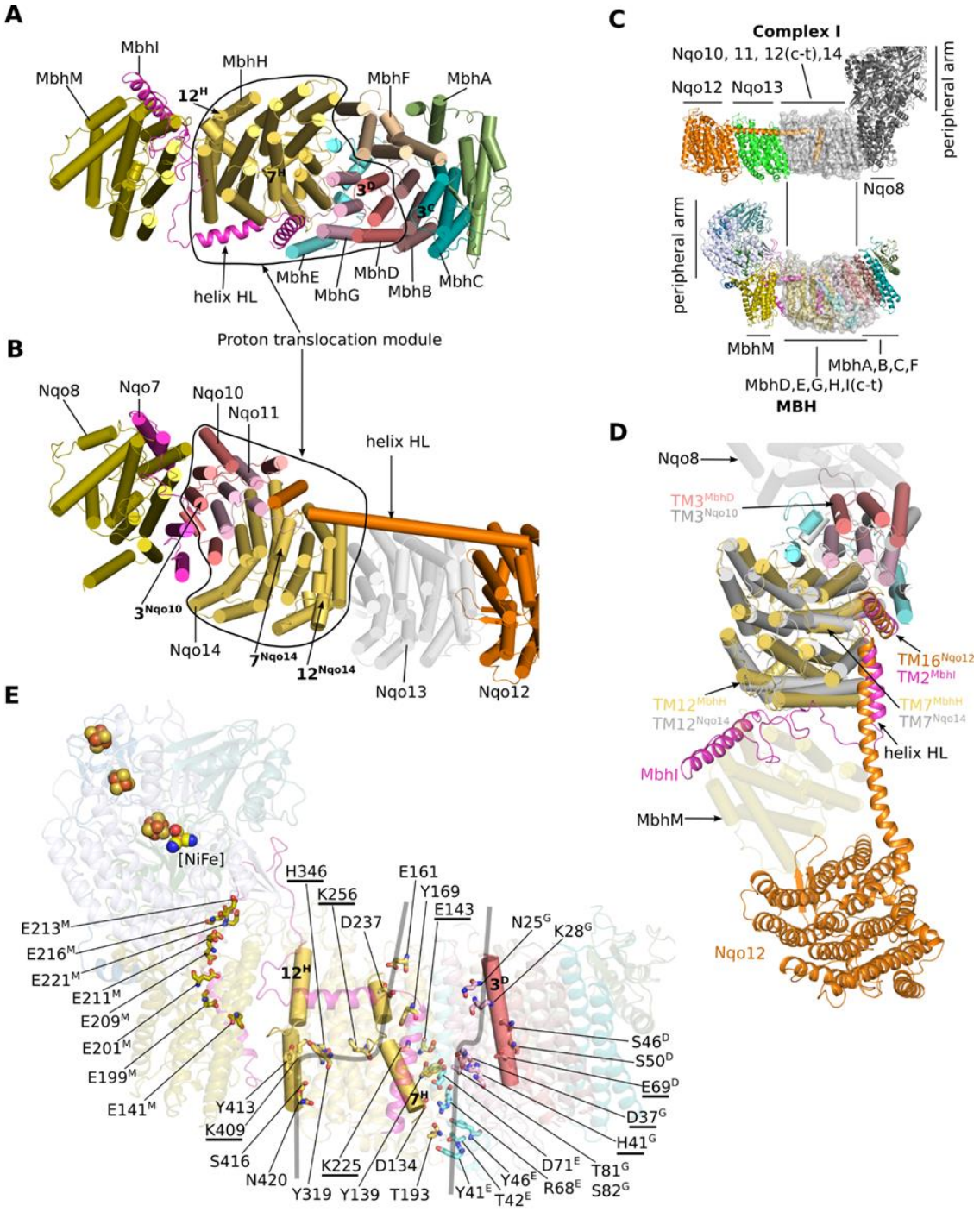
A
MbhI
MbhM
MbhH
MbhF
MbhA
12H
7H
3D
3C
MbhE
MbhG
MbhD
MbhB
MbhC
helix HL
Proton translocation module
B
Nqo8
Nqo7
Nqo10
Nqo11
helix HL
3Nqo10
Nqo14
7Nqo14
12Nqo14
Nqo13
Nqo12
C
Complex I
Nqo10, 11, 12(c-t),14
Nqo12
Nqo13
peripheral arm
Nqo8
peripheral arm
MbhM
MbhA,B,C,F
MbhD,E,G,H,I(c-t)
MBH
D
Nqo8
TM3MbhD
TM3Nqo10
TM16Nqo12
TM2MbhI
TM12MbhH
TM12Nqo14
TM7MbhH
TM7Nqo14
helix HL
MbhI
MbhM
Nqo12
E
[NiFe]
H346
K256
E161
Y169
E143
D237
N25G
K28G
E213M
E216M
E221M
E211M
E209M
E201M
E199M
E141M
12H
3D
S46D
S50D
E69D
D37G
H41G
7H
Y413
K409
S416
N420
K225
D134
Y319
Y139
T193
D71E
T81G
Y46E
R68E
S82G
Y41E
T42E

Figure A.3

Peripheral arm.

A. Architecture of the peripheral arm of the MBH complex anchored to the membrane by MbhM, viewed parallel to the membrane. Three loops that link the first two N-terminal β-strands (β1-β2) of MbhL, TMH1 and TMH2 of MbhI, and TMH5 and TMH6 of MbhM are at the interface between peripheral and membrane arms. The hydrogen-evolving [NiFe]-center is located right above the three interfacial loops. The MBH subunits are coloured as in **Figure A.1D**. **B,** Zoomed view of the structure around the hydrogenase catalytic center. The curved black arrow marks a possible proton pathway from the bulk solvent to the catalytic [NiFe] center. **C**, Sequence alignment of MbhL with its counterparts in selected members of group 4 energy-converting hydrogenases. EcoHycE: *Escherichia coli* hydrogenase-3 subunit HycE; EcoHyfG: *Escherichia coli* hydrogenase-4 subunit HyfG; MbaEchE: *Methanosarcina barkeri* hydrogenase subunit EchE.

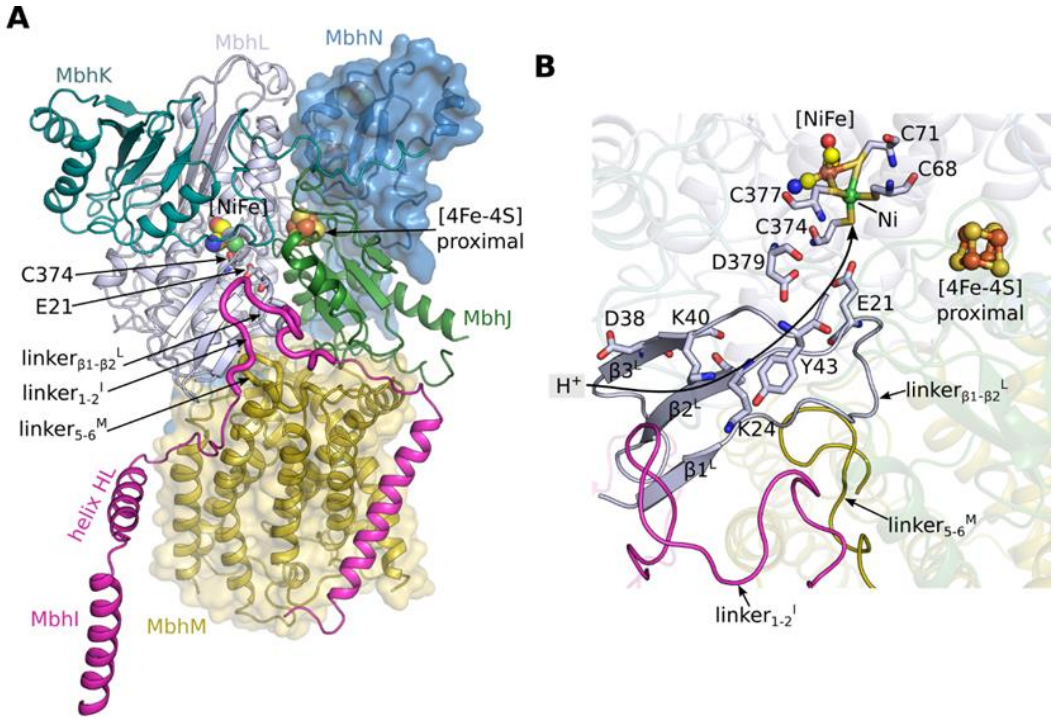

C

```
PfuMbhL      1  MKKVEYWVKIPFGPIHPGLEEPEKFIITLDGERIVNVDVKLGYNLRGVQWIGMR.
EcoHycE    173  ELGDKKNNVVPIGPLHVTSDEPGHFRLFVDGENIIDADYRLFYVHRGMEKLAETR
EcoHyfG    176  E.GNSDARVIPVGPLHITSDEPGHFRLFVDGEQIVDADYRLFYVHRGMEKLAETR
MbaEchE      1  .....MTTVIPFGPQHPVLPEPVSLKLEIDDNVVVGVLPSLGYVHRGLETFINT.

PfuMbhL     55  RNYVQIMYLAERMCGICSFSHNHTYV
EcoHycE    228  MGYNEVTFLSDRVCGICGFAHSTAYT
EcoHyfG    230  MGYNEVTFLSDRVCGICGFAHSVAYT
MbaEchE     50  KDFNQTTYVCERICGICSALHGITYT

365  VVAIASIDPCLSCTDR
522  PLIIGSLDPCYSCTDR
508  PLIIGSLDPCYSCTDR
343  PIVVLTIDPCVSCTER
```

Figure A.4

Putative sodium translocation path in MBH.

A. Two negatively-charged cavities are identified as potential sodium-binding sites in MbhA-C and F and are shown as red surfaces. Subunits are coloured as in **Figure A.1D**. TMHs are shown as cylinders and the MbhA ferredoxin-like domain is shown as cartoon. **B.** The first cavity is halfway through the membrane where the highly conserved D35 of MbhB resides.

C. The second cavity is at the extracellular side where the highly conserved MbhB D59 is located. The extracellular linker$_{TMH1\text{-}TMH2}$ of MbhF packs against MbhG via hydrophobic interactions, shown by the shaded area, and constricts the size of the cavity opening to the solvent. For B and C, residues highly conserved between MBH and Mrp system are underlined. Detailed sequence alignment is shown in **Figure A.S13**.

D. A cutaway electrostatic surface potential of the second cavity showing that MbhB D59 is located at the tip of a funnel-like opening.

E. Sequences of the interacting structural elements of MbhF and MbhG (shaded in C) are highly conserved in the Mrp system.

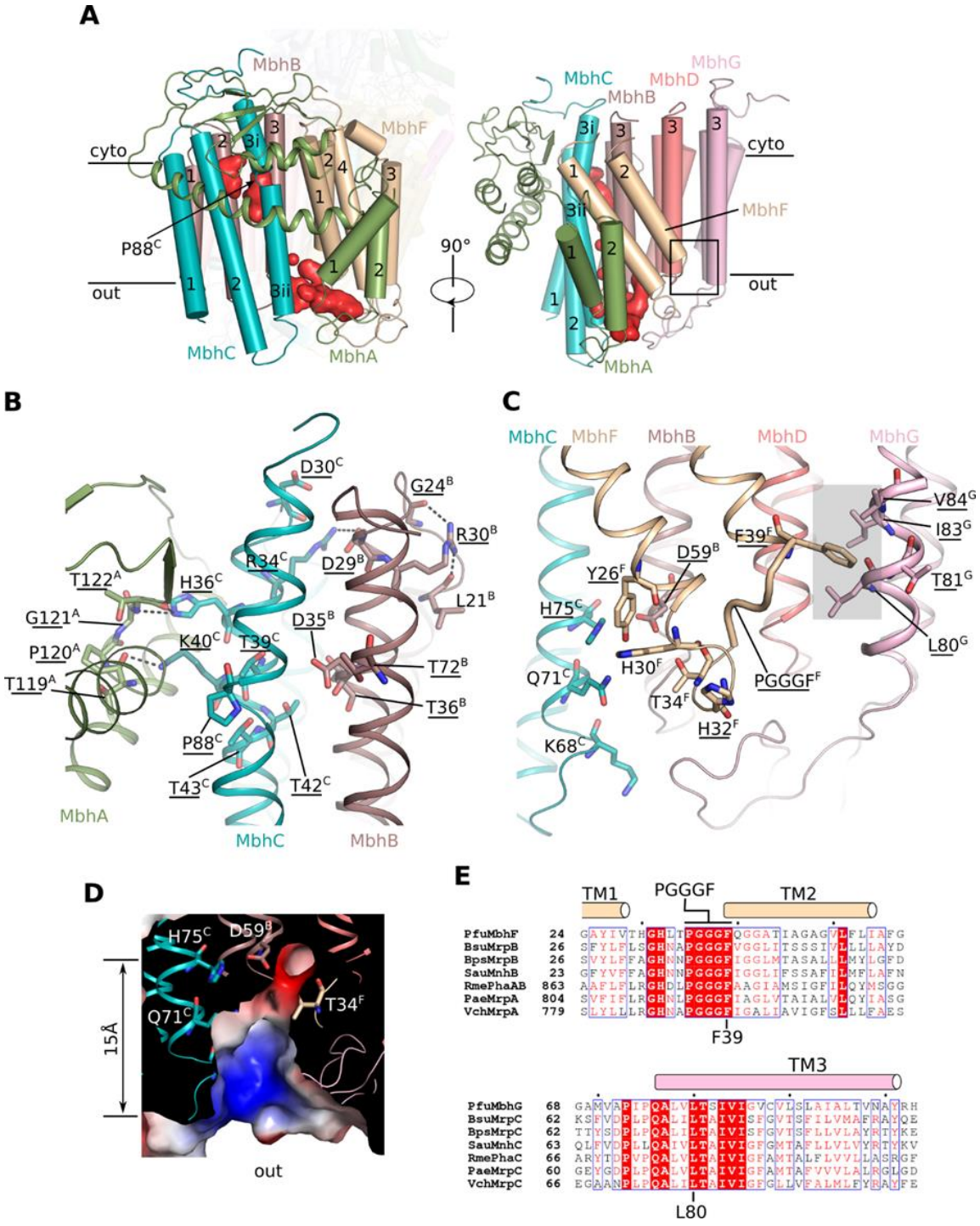
A
MbhB
MbhF
cyto
P88C
out
MbhC
MbhA
90°
MbhG
MbhD
MbhC
MbhB
cyto
MbhF
out
MbhA
B
D30C
G24B
R30B
R34C
D29B
T122A
H36C
L21B
G121A
D35B
K40C
T39C
P120A
T72B
T119A
T36B
P88C
T43C
T42C
MbhA
MbhC
MbhB
C
MbhC
MbhF
MbhB
MbhD
MbhG
V84G
I83G
F39F
D59B
Y26F
T81G
H75C
L80G
H30F
PGGGF
Q71C
T34F
H32F
K68C
D
H75C
D59B
15Å
Q71C
T34F
out
E
TM1
PGGGF
TM2
PfuMbhF 24 GAYIVTHGHLTPGGGFQGGATIAGAGVLFLIAFG
BsuMrpB 26 SFYLFLSGHNAPGGGFVGGLITSSSIVLLLLAYD
BpsMrpB 26 SVYLFFAGHNNPGGGFIGGLMTASALLLMYLGFD
SauMnhB 23 GFYVFFAGHNNPGGGFIGGLIFSSAFILMFLAFN
RmePhaAB 863 AAFLFLRGHDLPGGGFAAGIAMSIGFILQYMSGG
PaeMrpA 804 SVFIFLRGHNLPGGGFIAGLVTAIALVLQYIASG
VchMrpA 779 SLYLLLRGHNAPGGGFIGALIAVIGFSLLLFAES
F39
TM3
PfuMbhG 68 GAMVAPIPQALVLTSIVIGVCVLSLAIALTVNAYRH
BsuMrpC 62 KSFVDPLPQALILTAIVISFGVTSFILVMAFRAYQE
BpsMrpC 62 TTYSDPLPQALILTAIVISFGVTSFLLVLAYRTYKE
SauMnhC 63 QLFVDPLLQAIVLTAIVIGFGMTAFLLVLVYRTYKV
RmePhaC 66 ARYTDPVPQALVLTAIVIGFAMTALFLVVLLASRGF
PaeMrpC 60 GEYGDPLPQALVLTAIVIGFAMTAFVVVLALRGLGD
VchMrpC 66 EGAANPLPQALILTAIVIGFGLLVFALMLFYRAYFE
L80

Figure A.5

Comparison of the working models of Complex I, MBH and the homologous Mrp H^+/Na^+ antiporter.

A. A putative redox-driven proton pumping mechanism of Complex I. Sketched are the prominent features highlighted in previous studies of Complex I: three-loop cluster, lateral helix HL and the four potential proton translocation pathways (gray arrows). Note that the left three antiporter-like subunits are the primary candidates for proton translocation while the fourth proton path within the small subunits is controversial.

B. A working model of MBH. The MBH modules shared with Complex I - the membrane-anchored hydrogenase module and H^+ translocation module - are differently arranged, suggesting a mechanism related to Complex I but with some variations: the redox reaction may drive the outward flow of proton through antiporter-like subunit MbhH and then the expelled proton may flow inward through the second proton path to drive the export of the sodium ion via the tentatively-identified sodium path.

C. The proposed proton- and sodium-translocation paths in MBH may be conserved in the Mrp H^+/Na^+ antiporter. See sequence alignment in **Figure A.S13** and a list of subunit correspondence among MBH, Mrp, and Complex I in **Table A.1**. MrpA, the predicted antiporter-like subunit, may contribute an extra proton path to the antiporter, as illustrated by the left dashed arrow.

For **A-C**, A dashed line within a proton-translocation module separate the antiporter-like subunits from the other small subunits within the same module. The curved arrows mark

the potential proton- or sodium-translocation paths: the solid arrows indicate paths with stronger evidence, and the dashed arrows mark those with less certainty.

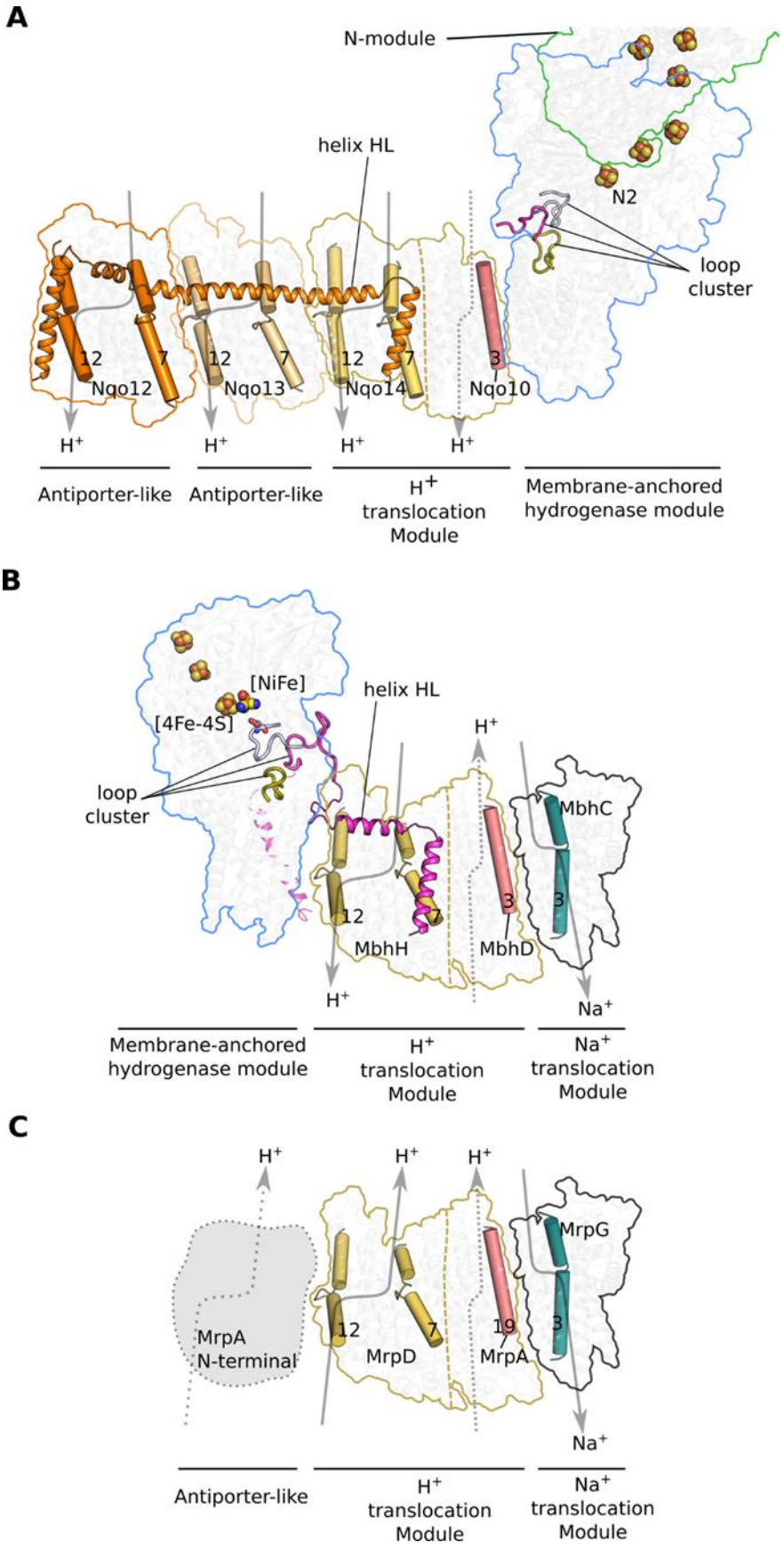
A
N-module
helix HL
N2
loop cluster
12
7
Nqo12
12
7
Nqo13
12
7
Nqo14
3
Nqo10
H+
H+
H+
H+
Antiporter-like
Antiporter-like
H+ translocation Module
Membrane-anchored hydrogenase module
B
[NiFe]
[4Fe-4S]
helix HL
H+
loop cluster
MbhC
12
7
MbhH
3
MbhD
3
H+
Na+
Membrane-anchored hydrogenase module
H+ translocation Module
Na+ translocation Module
C
H+
H+
H+
MrpG
MrpA N-terminal
12
7
MrpD
19
MrpA
3
Na+
Antiporter-like
H+ translocation Module
Na+ translocation Module

Star Methods

Key Resources Table

REAGENT or RESOURCE	SOURCE	IDENTIFIER
Bacterial and Virus Strains		
Pyrococcus furiosus strain MW0414	(McTernan et al., 2014)	MW0414
Chemicals, Peptides, and Recombinant Proteins		
EPPS	Sigma	E9502
n-dodecyl-β-D-maltoside	Inalco	1758-1350
Critical Commercial Assays		
His-Trap crude FF Ni-NTA	GE Healthcare	17-5286-01
His-Trap HP Ni-NTA	GE Healthcare	17-5247-01
Superose 6, 10/300 GL	GE Healthcare	17517201
Deposited Data		
Coordinates of MBH complex	This study	PDB: 6CFW
Cryo-EM map of MBH complex	This study	EMDB: EMD-7468
Coordinates of *Thermus thermophilus* Complex I	(Baradaran et al., 2013)	PDB: 4hea
Coordinates of *D. gigas* [NiFe] hydrogenase	(Volbeda et al., 1996)	PDB: 2frv
Software and Algorithms		
SerialEM	(Mastronarde, 2005)	http://bio3d.colorado.edu/SerialEM
FEI EPU	FEI	https://www.fei.com/software/epu/
MotionCor2 with dose weighting	(Zheng et al., 2017)	http://msg.ucsf.edu/em/software/motioncor2.html
CTFFIND4	(Rohou and Grigorieff, 2015)	http://grigoriefflab.janelia.org/ctffind4
RELION-2.0	(Kimanius et al., 2016)	http://www2.mrc-lmb.cam.ac.uk/relion
EMAN2	(Tang et al., 2007)	http://blake.bcm.edu/emanwiki/EMAN2

ResMap	(Kucukelbir et al., 2014)	http://resmap.sourceforge.net/
SWISS-MODEL server	(Arnold et al., 2006)	https://swissmodel.expasy.org/
CHIMERA	(Pettersen et al., 2004)	https://www.cgl.ucsf.edu/chimera
Coot	(Emsley et al., 2010)	https://www2.mrc-lmb.cam.ac.uk/personal/pemsley/coot
PHENIX	(Adams et al., 2010)	https://www.phenix-online.org/
MOLPROBITY	(Chen et al., 2010)	http://molprobity.biochem.duke.edu/
PyMOL	Schrödinger, LLC.	http://www.pymol.org/2/
Other		
C-Flat Cu CF-1.2/1.3, 400 mesh grid	ELECTRON MICROSCOPY SCIENCES	CF-1.2/1.3-4C-T

Contact For Reagent And Resource Sharing

Further information and requests for resources and reagents should be directed to and will be fulfilled by the Lead Contact, Huilin Li (huilin.li@vai.org)

Experimental model and subject details

Cell lines

Pyrococcus furiosus strain MW0414 was used for expression. Cells were cultured as described in the Method Details section.

Methods Details

Expression and purification of MBH

The MBH holoenzyme (S-MBH) was solubilized and purified anaerobically from *Pyrococcus furiosus* strain MW0414, in which a His_9-tag had been engineered at the N-terminus of the MbhJ subunit. The procedure was as previously described with some modifications (McTernan et al., 2014). Frozen cells were lysed in 25 mM sodium phosphate, pH 7.5, containing 1 mM DTT and 50 μg/ml DNase I (5 ml per gram of frozen cells). After stirring for one hour, the cell-free extract was centrifuged at 100,000 x g for one hour. The supernatant was removed and the membranes were washed twice using 50 mM EPPS buffer, pH 8.0, containing 5 mM $MgCl_2$, 50 mM NaCl, 10% (v/v) glycerol, 1 mM DTT and 0.1 mM PMSF. The membrane pellet was collected by ultracentrifugation at 100,000 x g for one hour after each wash step. The washed membranes were resuspended in 50 mM Tris-HCl, pH 8.0, containing 5 mM MgCl2, 50 mM NaCl, 5% (v/v) glycerol, 1 mM DTT, and 0.1 mM PMSF. MBH was solubilized by adding n-dodecyl-β-D-maltoside (DDM, Inalco) to 3% (w/v) followed by incubation at 4 °C for 16 hours. The solubilized membranes were centrifuged at 100,000 x g for 1 hour. The supernatant was applied to a 5-ml His-Trap crude FF Ni-NTA column (GE Healthcare) while diluting it 10-fold with buffer A (25 mM sodium phosphate, 300 mM NaCl, pH 7.5, containing 1 mM DTT and 0.03 % DDM). The column was washed with 10 column volumes of buffer A and the bound protein was eluted with a 20-column volume gradient from 0 to 100 % buffer B (buffer A containing 500 mM imidazole). The eluted protein was further purified by applying it to a 1-mL His-Trap HP Ni-NTA column (GE Healthcare) while diluting it 5-fold with buffer A. A 30-column volume gradient from 0 to 100 % buffer B was used to elute the bound protein. The MBH sample was concentrated and further purified using a Superose 6 10/300

GL column (GE Healthcare) equilibrated with 50 mM Tris-HCl, pH 8.2, containing 300 mM NaCl, 2 mM sodium dithionite, and 0.03 % DDM.

Deletion of MbhABC

The genetically-tractable *P. furiosus* strain COM1 was used to delete the genes (PF1423-1425) encoding MbhABC from the MBH holoenzyme. Flanking regions (500 bp) were amplified from *P. furiosus* genomic DNA for the UFR and DFR, and the selection marker (*pyrF*-P_{gdh}) was amplified by using pGL021 as the template (Lipscomb et al., 2011). The knock-in cassette was assembled using overlapping PCR (Bryksin and Matsumura, 2010). The genomic DNA was prepared using ZYmobead Genomic DNA Kit (Zymo Research). *P. furiosus* transformants were grown as previously described (Lipscomb et al., 2011). The genomic DNA isolated by Zymobead Genomic DNA Kit (Zymo Research) was used for PCR screening, which was carried out by using GXL polymerase (Takara, ClonTech). PCR screening was performed using a pair of primers outside the Mbh locus in order to confirm that the transformation cassette recombined into the correct locus.

Preparation of cell suspensions and assays

Defined maltose growth medium was prepared as described previously (Lipscomb et al., 2011). The parent (COM1) and mutant (Δ*mbhABC*) were grown in 1L culture bottles at 90 °C with shaking. Cells were harvested by centrifugation at 18,000 xg for 10 min in a Beckman-Coutler Avanti J-30i centrifuge. Cell suspensions were created by washing harvested cells with an anaerobic resuspension buffer containing 20 mM imidazole, 30 mM $MgCl_2 \cdot 6H_2O$, 0.5 M KCl, 2 mM cysteine-HCl, pH 6.5 and resuspending them in the same buffer at cell densities of OD_{600} = 0.6. H_2 production assays of the cell suspensions are

modified from that reported previously (Lim et al., 2014). For H_2 production assays, cell suspensions (2.0 ml) were added to rubber-sealed glass vials and the headspace was flushed with argon. Samples were incubated at 80 °C for 3 min and the reaction was initiated by the addition of the desired concentration of NaCl from an anaerobic 2.0 M stock solution. At various time intervals, gas samples were taken and analyzed in a 6850 Network Gas Chromatograph (Agilent Technologies).

Cryo-EM data acquisition

For cryo-EM analysis, 3 µl aliquots of the purified MBH complex at 2-3 mg/ml was applied to a glow-discharged holey carbon grids (C-Flat Cu CF-1.2/1.3, 400 mesh). The grids were blotted for 3-4 s at 10 °C with 95% humidity and flash-frozen in liquid ethane using an FEI Vitrobot IV. Cryo-EM data collection was performed on a 300 kV FEI Titan Krios electron microscopy with a K2 camera positioned post a GIF quantum energy filter. Automated data acquisition was performed with SerialEM (Mastronarde, 2005) and FEI EPU package. Micrographs were recorded in super-resolution counting mode at a nominal magnification of 130,000×, resulting in a physical pixel size of 1.09 Å per pixel. Defocus values varied from 1.2 µm to 3 µm. The dose rate was 10.2 electron per pixel per second. Exposures of 6 s were dose-fractionated into 30 sub-frames, leading to a total accumulated dose of 51.7 electrons per $Å^2$.

Image processing and 3D reconstruction

Two batches of data were collected. Dose fractionated movie frames were motion corrected (globally and locally), dose weighted and binned by 2 fold with MotionCor2 (Grant and Grigorieff, 2015; Zheng et al., 2017), resulting in summed micrographs in a pixel size of

1.09 Å per pixel. Contrast transfer function (CTF) parameters for each micrograph were estimated by CTFFIND4 (Rohou and Grigorieff, 2015). RELION-2.0 was used for further processing steps (Kimanius et al., 2016). Bad micrographs revealed by manual inspection were excluded from further analysis, yielding 2804 and 2155 good micrographs for each dataset. For each dataset, a manually picked sets of particles were subject to 2D classification. This generated templates for reference-based particle picking, which yielded 674,607 and 574,955 automatically picked particles, respectively. Particle sorting and reference-free 2D classification was performed to remove contaminants and noisy particles, resulting in two datasets with 636,689 and 548,230 particles, respectively. Then 3D classification was performed using an *ab initio* map generated by EMAN2 (Tang et al., 2007) as the initial reference model. For each dataset, one out of 4 classes with high-resolution features was obtained. The two identified good classes were combined as a new set of 301,300 particles, which was subjected to another round of 3D classification. The most populated 3D class (131,679 particles) was subsequently selected for the final 3D auto-refinement with a soft mask including the protein and detergent regions. This generated a map with an overall resolution of 3.7 Å. The resolution was estimated based on the gold-standard Fourier shell correlation 0.143 criterion (Rosenthal and Henderson, 2003). The final map was corrected for the modulation transfer function (MTF) of the detector and sharpened by applying a negative B-factor, estimated by the post-processing procedure in RELION-2.0. Local resolution distribution was estimated using ResMap (Kucukelbir et al., 2014).

Atomic model building

Most regions of the map, especially the transmembrane helices of membrane subunits, exhibit sufficient features for *de novo* model building of MBH, which started from the global assignment of its 14 subunits. Homology models for six subunits (hydrophilic MbhJ-MbhN and membrane MbhH and MbhM) were generated with the SWISS-MODEL server (Arnold et al., 2006) using the structure of *T. thermophilus* Complex I as a template (PDB ID 4hea) (Baradaran et al., 2013). They were fitted into the EM map as rigid bodies with CHIMERA (Pettersen et al., 2004). The assignments of remaining 8 membrane subunits were assisted by their predicted secondary structural features and the excellent main chain connectivity of the map. MbhF, the only membrane subunit with 4 TMHs, was assigned first. Although they all contain 2 TMH, the specific structural features of MbhA, MbhE and MbhI helped to individually locate them to the map. MbhA TM2 is followed by a ferredoxin-like fold, which was predicted by I-TASSER (Yang et al., 2015). For MbhI and MbhE, their TM1-TM2 linkers were predicted to be quite different: a long loop and a following long amphipathic helix for MbhI; a loop with a short helix in the middle for MbhE. Lastly, MbhB, MbhC, MbhD and MbhG all contain 3 transmembrane helices and they form 4 layers of three-helix bundle together. Among them, MbhC has the longest predicted helices and MbhG TM2-TM3 has the longest loop linker, which helped to locate them on the map. The positioning of last two subunits MbhB and MbhD was assisted by their sequence information.

After the subunit assignment, for the six subunits MbhJ-MbhN, MbhH and MbhM, the fitted homology models were improved by manual adjustments and rebuilding using Coot (Emsley et al., 2010). For each of the remaining 8 membrane subunits MbhA-MbhG and MbhI, a polyalanine model was first built with Coot and subsequent sequence

assignment was mainly guided by bulky residues such as Arg, Tyr, Phe and Trp. In the final MBH model, 2470 of 2502 residues was assigned with side chains. MbhI loop Aa42-73 only allows the tracing of its main chain, which were built as polyalanine.

The refinement of the MBH complex model against the cryo-EM map in real space was performed using the phenix.real_space_refine in PHENIX(Adams et al., 2010). The final model was assessed using MOLPROBITY (Chen et al., 2010). All figures were prepared using PyMOL (Schrödinger, LLC.) and CHIMERA. Statistics of the 3D reconstruction and model refinement were provided in **Table A.S1**.

Quantification And Statistical Analysis

Resolution estimations of cryo-EM density maps are based on the 0.143 Fourier Shell Correlation (FSC) criterion (Chen et al., 2013; Rosenthal and Henderson, 2003).

Data And Software Availability

Data Resources

The accession number for the atomic coordinates reported in this paper is PDB: 6CFW. The accession number for the EM density maps reported in this paper is EMDB: EMD-7468.

Table SA.1. Cryo-EM data collection and refinement statistics

	MBH complex
Data collection	
Microscope	FEI Titan Krios
Voltage (kV)	300
Detector	Gatan K2 Summit
Electron dose ($e^- Å^2$)	52
Pixel size (Å)	1.09
Defocus range (μm)	1.2-3
Reconstruction	
Software	RELION 2.0
Particles for final refinement	131,679
Final Resolution (Å)	3.7
Map-sharpening B factor ($Å^2$)	-142.4
Model composition	
Peptide chains	14
Residues	2500
[4Fe-4S]	3
[NiFe]	1
R.m.s. deviations	
Bond lengths (Å)	0.010
Bond angles (°)	1.532
Ramachandran plot	
Favored (%)	89.0
Outlier (%)	0.3
Validation	
Molprobity score	1.9
Rotamer outlier (%)	1.4
Clashscore	4.3

Figure SA.1.

Na^+-dependent H_2 production activity of *P. furiosus.*

Effect of NaCl concentration (0, 50 or 150 mM) on the H_2 production activity of cell suspensions of the parent (COM1, panel **A**) or Δ*mbhABC* (**B**) strains.

C. Hydrogenase specific activities in the membranes of the parent and Δ*mbhABC* strains.

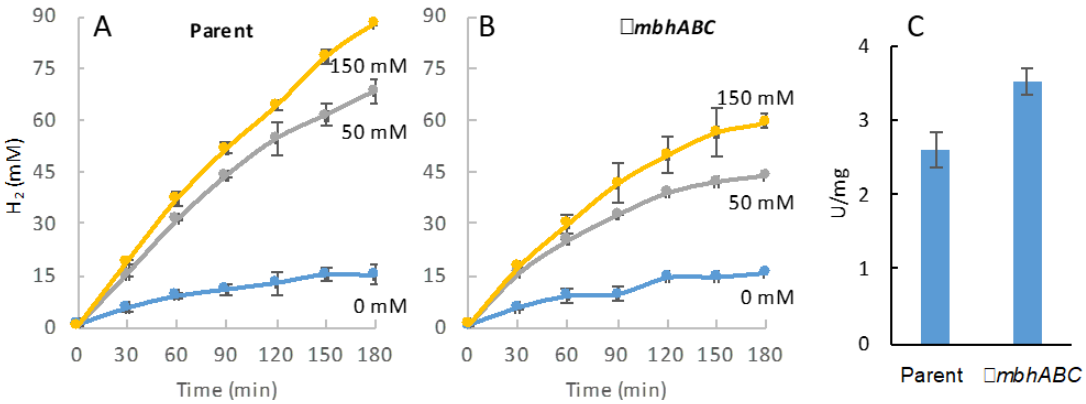
A
Parent
150 mM
50 mM
0 mM
H2 (mM)
Time (min)
B
□mbhABC
150 mM
50 mM
0 mM
Time (min)
C
U/mg
Parent
□mbhABC

Figure SA.2

Preparation of MBH for single-particle cryo-EM analysis.

A. The predicted molecular weight (kDa) of each of the fourteen MBH subunits.

B. A representative profile of size-exclusion chromatography (Superose 6 10/300 GL column) of the purified MBH complex solubilized in the detergent n-Dodecyl β-D-maltoside.

C. SDS-PAGE of the pooled gel filtration peak fractions shows the presence of all fourteen MBH subunits as labeled to the right. Molecular weight markers in kDa are labeled to the left.

a

MBH Subunit	MW (KDa)
H	54.9
L	47.9
M	35.4
K	20.2
A	18.7
J	18.3
N	15.7
F	15.5
C	13.5
I	13.0
G	12.8
E	11.1
D	10.4
B	9.1

b

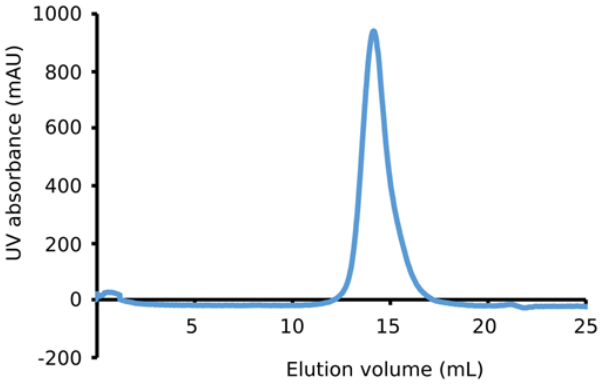

c

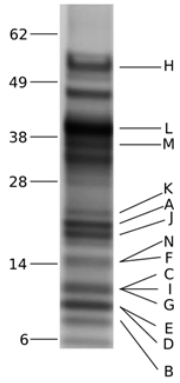

Figure SA.3

Cryo-EM analysis of the archaeon *Pyrococcus furiosus* MBH complex.

A. Representative cryo-EM micrograph of the MBH particles.

B. Representative 2D class averages of the MBH particles.

C. The workflow of cryo-EM data processing. Two datasets, each contains 2804 and 2155 micrographs, respectively, were collected and processed separately during 2D classification and the first round of 3D classification. The best 3D class from these two datasets were combined for the second round of 3D classification. Then the most populated 3D class (131,679 particles, ~44% of total particles) was subjected to the final refinement, which resulted in a 3D density map with an estimated resolution of 3.7 Å. See Methods for more details.

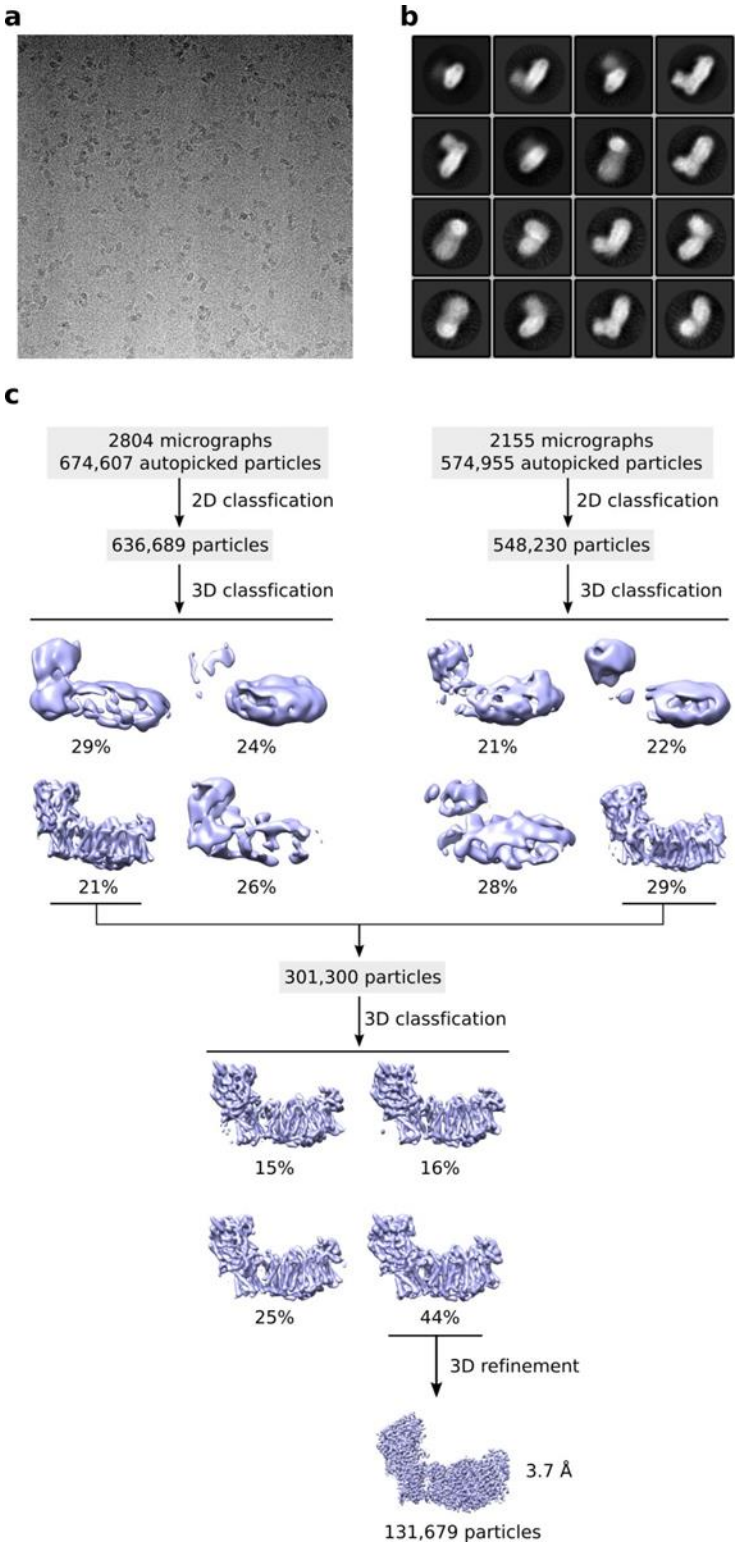
a
b
c
2804 micrographs
674,607 autopicked particles
2D classfication
636,689 particles
3D classfication
29%
24%
21%
26%
2155 micrographs
574,955 autopicked particles
2D classfication
548,230 particles
3D classfication
21%
22%
28%
29%
301,300 particles
3D classfication
15%
16%
25%
44%
3D refinement
3.7 Å
131,679 particles

Figure SA.4

Statistics of the cryo-EM 3D map.

A. Angular distribution of all particles used in the final 3D reconstruction (top panel) is shown with the corresponding view of the 3D map (bottom panel). The number of particles in each orientation is indicated by bar length and color (blue, low; red, high).

B. The gold-standard Fourier shell correlation (FSC) curve of the 3D map.

C. Local resolution for of the 3D density map, calculated with ResMap. The range of resolution is color-coded from blue high resolution to red low resolution.

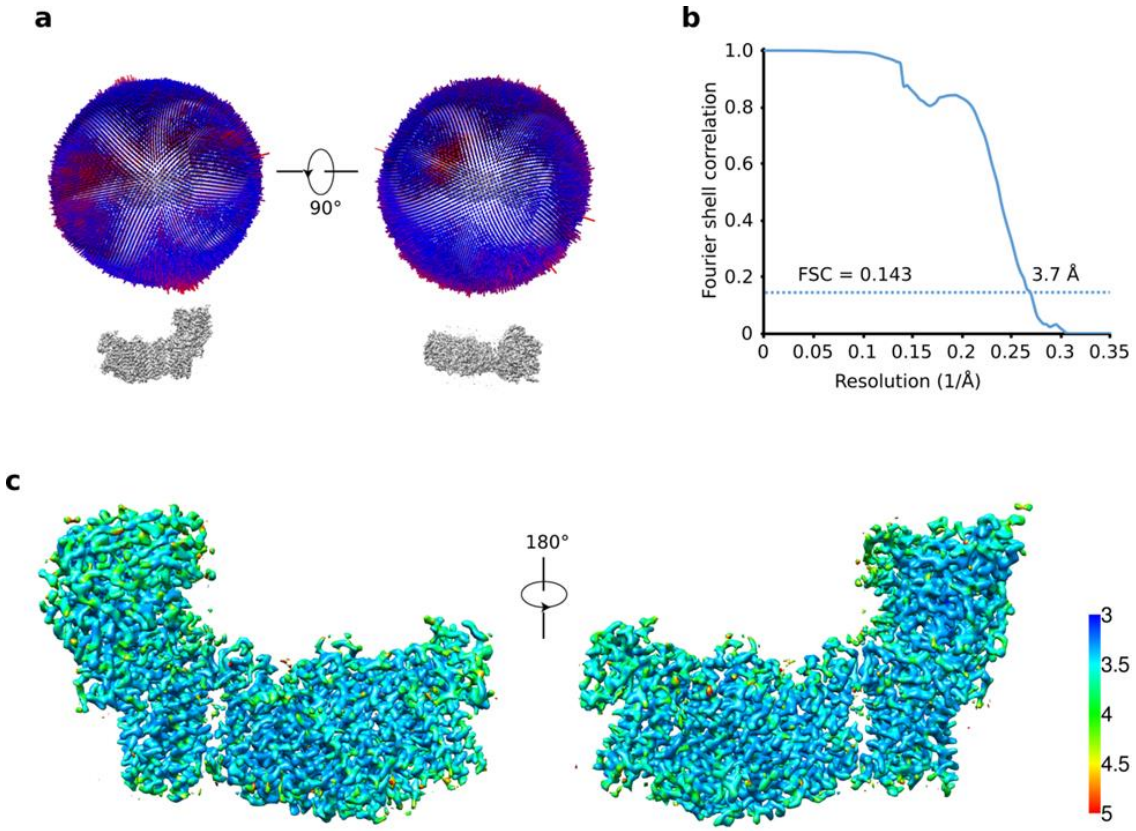
a
90°
b
Fourier shell correlation
1.0
0.8
0.6
0.4
0.2
0
FSC = 0.143
3.7 Å
0 0.05 0.1 0.15 0.2 0.25 0.3 0.35
Resolution (1/Å)
c
180°
3
3.5
4
4.5
5

Figure SA.5

A gallery of EM density maps of each of the 10 membrane subunits, superimposed with their corresponding atomic models in cartoon and stick views. **A.** MbhA. **B.** MbhB. **C.** MbhC. **D.** MbhD. **E.** MbhE. **F.** MbhG. **G.** MbhH. **H.** MbhI. **I.** MbhI. Densities for Aa4273 were weak and allowed the tracing of only their main-chain atoms. **J**. MbhM.

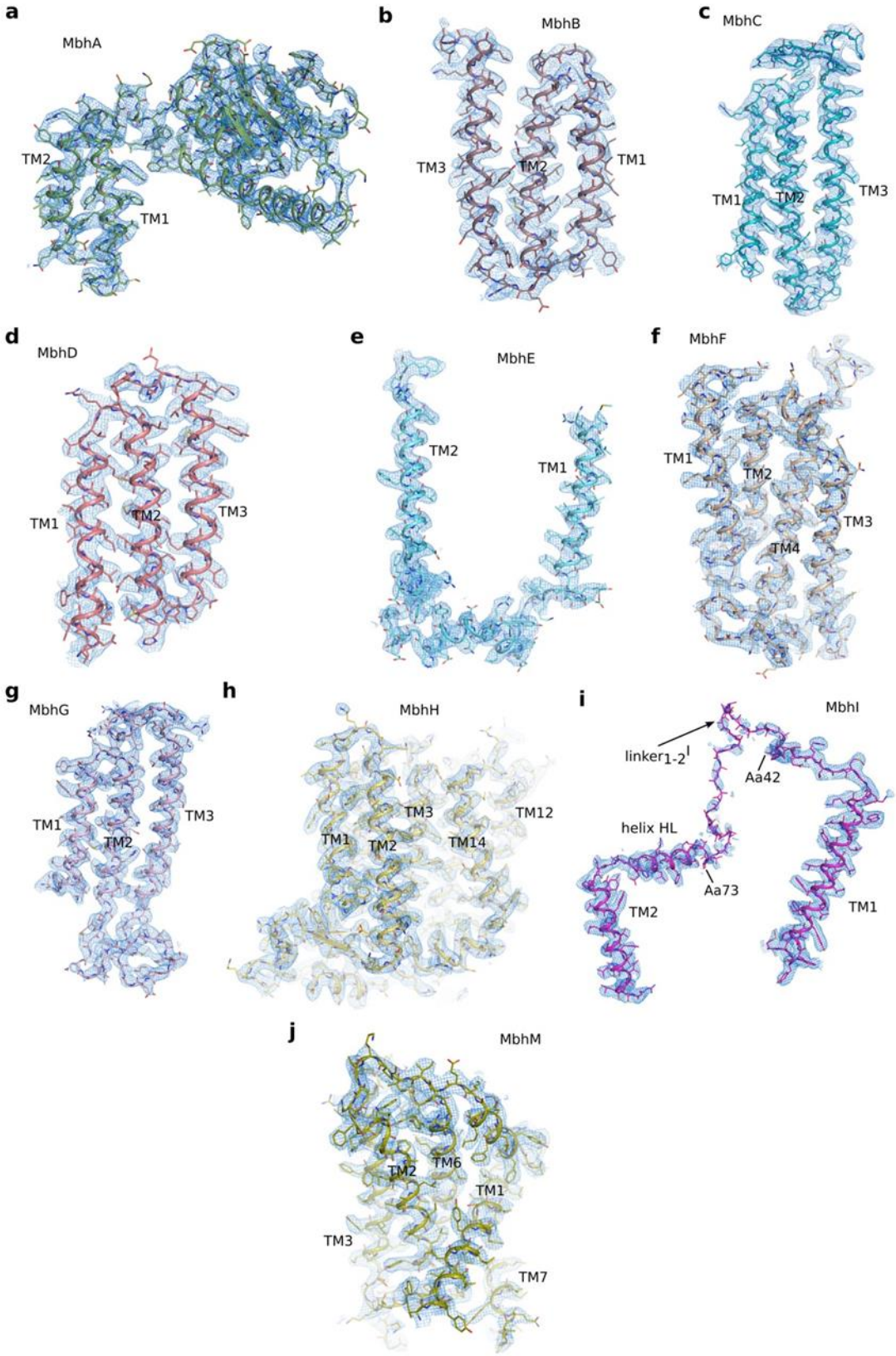
a
MbhA
TM2
TM1
b
MbhB
TM3
TM2
TM1
c
MbhC
TM1
TM2
TM3
d
MbhD
TM1
TM2
TM3
e
MbhE
TM2
TM1
f
MbhF
TM1
TM2
TM3
TM4
g
MbhG
TM1
TM2
TM3
h
MbhH
TM3
TM12
TM1
TM2
TM14
i
MbhI
linker1-2
Aa42
helix HL
Aa73
TM2
TM1
j
MbhM
TM2
TM6
TM1
TM3
TM7

Figure SA.6

A gallery of EM density maps of each of the 4 cytoplasmic MBH subunits, superimposed with their corresponding atomic models in cartoon and stick views. **A.** MbhJ. **B.** MbhK. **C.** MbhL. **D.** MbhN.

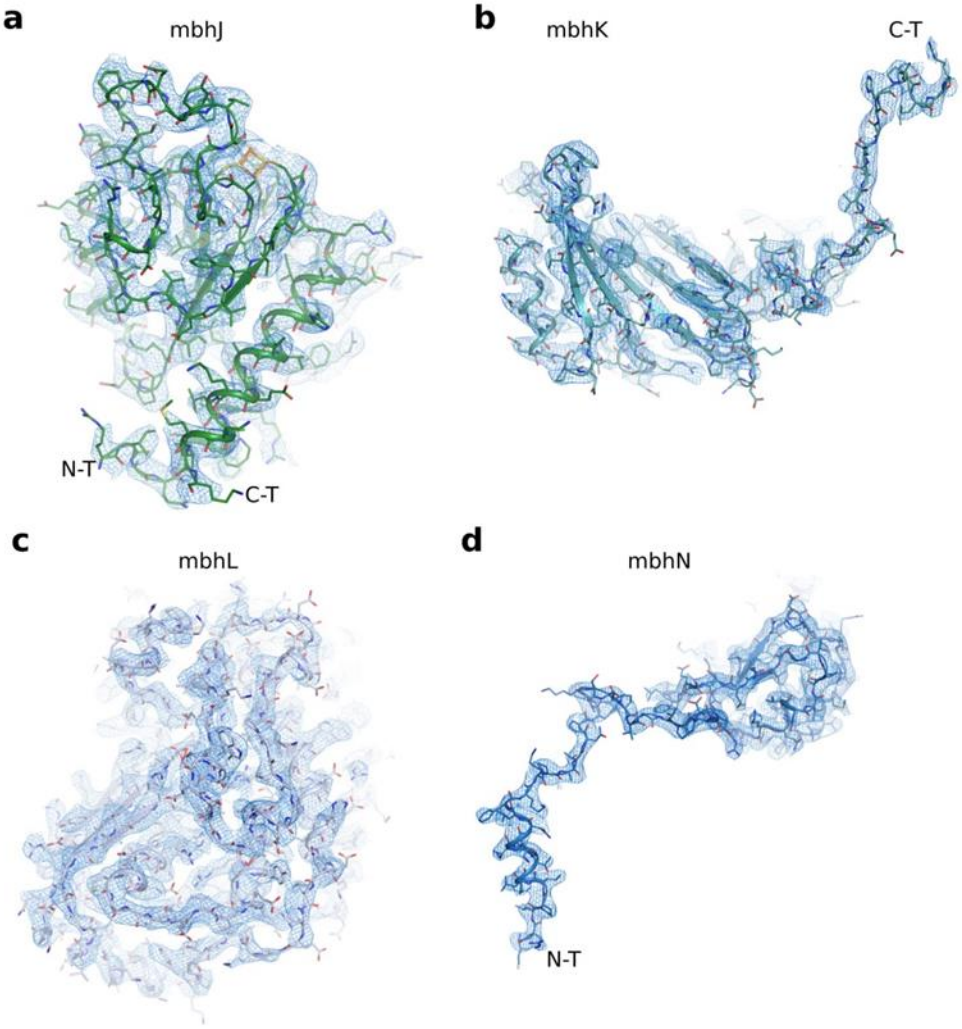
a
mbhJ
N-T
C-T
b
mbhK
C-T
c
mbhL
d
mbhN
N-T

Figure SA.7

Structures of the membrane subunits in the MBH complex.

A. Overlay of MbhH (yellow) with Nqo14 (magenta) of *T. thermophiless* Complex I (PDB ID 4hea) with the TMH numbered illustrates the common fold of the antiporter-like subunits. TMH7 and TMH12 are discontinuous, a hallmark of the proton-translocating antiporter-like subunits observed previously in the respiratory complex I.

B. Left, top view from the cytoplasmic side showing the detailed fold of the antiporter-like subunit MbhH with the TMHs numbered. The putative proton-translocating five-helix folding units TMH4-8 and TMH9-13 are coloured in blue and light grey, respectively. The rotation label under folding unit TMH9-13 indicates its operation for overlay shown in the right panel. Right**,** the internal symmetry between the two folding units: the MbhH TMH9-13 unit can be superimposed with the TMH4-8 unit when the former is flipped upside down, indicating the inverted arrangement of the two proton-translocating units.

C. Structure of the membrane subunit MbhM in cartoon presentation as viewed from cytoplasmic side.

D. Overlay of MbhM with the Nqo8 of *T. thermophiless* Complex I (PDB ID 4hea) shows a conserved fold of the two proteins. The Nqo8 has a cytoplasmic TMH9 (shaded area) that is absent in MbhM.

E. Architecture of the seven small MBH subunits. Left panel, top view from cytoplasmic side with all TMH numbered. Right view, a side view from membrane.

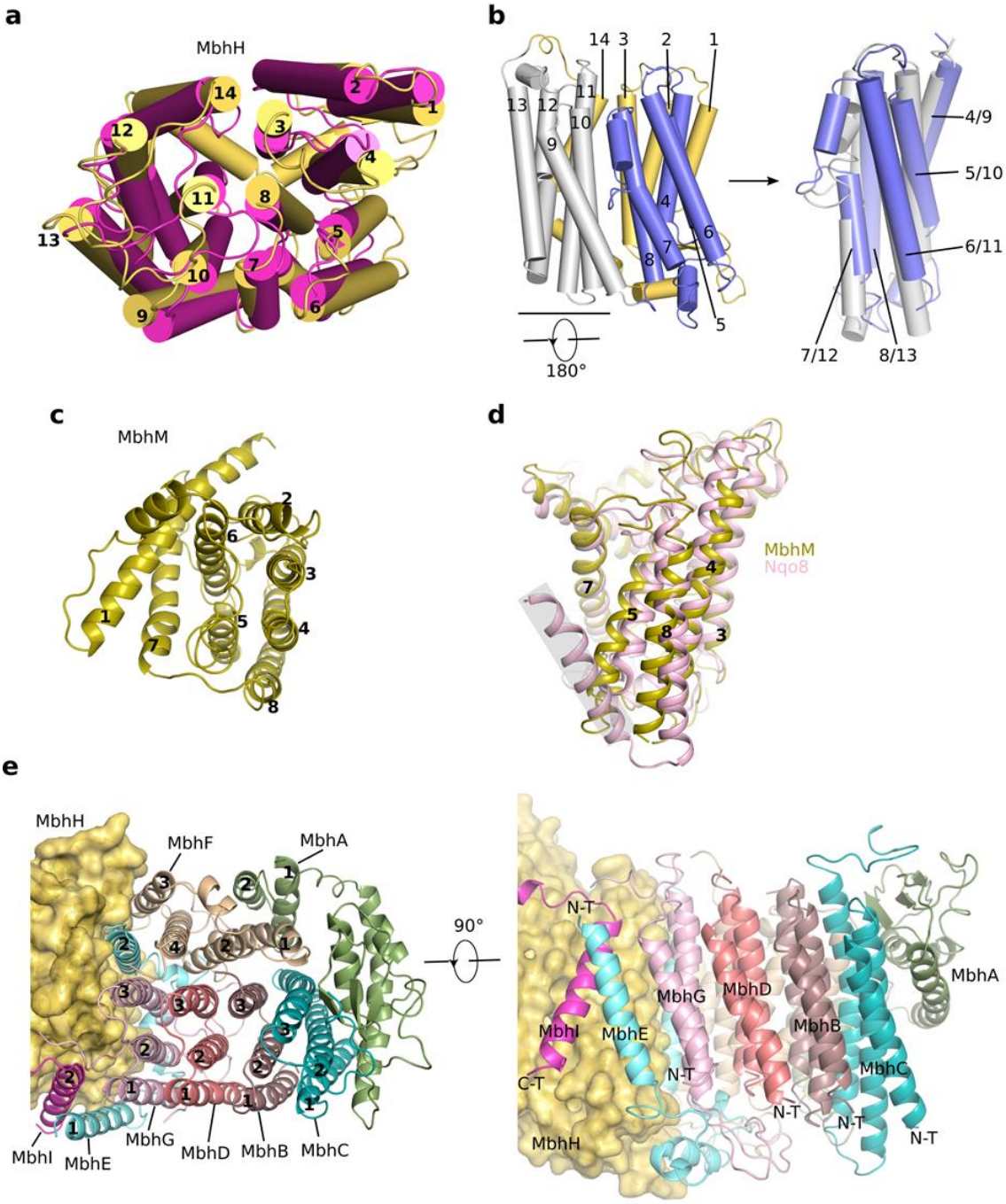
a
MbhH
b
180°
4/9
5/10
6/11
7/12
8/13
c
MbhM
d
MbhM
Nqo8
e
MbhH
MbhF
MbhA
90°
MbhI
MbhE
MbhG
MbhD
MbhB
MbhC
N-T
C-T

Figure SA.8

MbhM and MbhH interface in MBH complex.

A-D. MBH complex (**A, C**) and Complex I (**B, D**; *T. thermophiles*; PDB ID 4hea) were aligned by their membrane subunits Nqo8 (Complex I) vs MbhM in MBH. Complex I Nqo8 and MBH MbhM are right below their respective peripheral arms. Side views of this comparison are shown separately in panel **A** (MBH) and **B** (Complex I). The top views are shown separately in panes **C** (MBH) and **D** (Complex I), respectively. Note the large gap between M and H in MBH (**A**). There are four elongated densities located to the lower region of the gap (**A** inset), which stack against several hydrophobic residues of M and H. These densities are probably from two phospholipid molecules that stabilize the structure and prevent ion leakage across the membrane bilayer. Please also note the contiguous chain of hydrophilic residues found in complex I (**C**) is discontinuous in MBH (**D**).

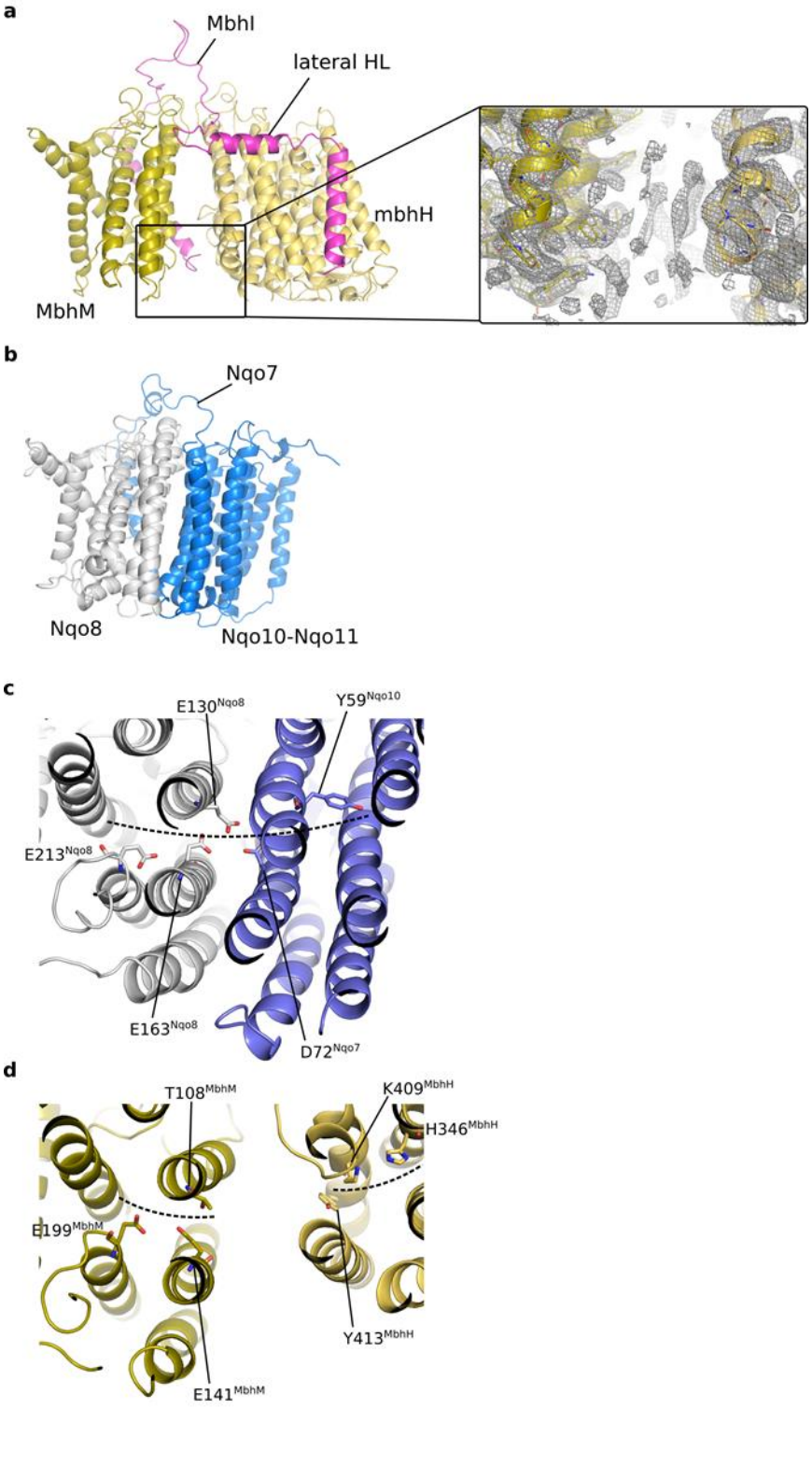
a
MbhI
lateral HL
mbhH
MbhM
b
Nqo7
Nqo8
Nqo10-Nqo11
c
E130Nqo8
Y59Nqo10
E213Nqo8
E163Nqo8
D72Nqo7
d
T108MbhM
K409MbhH
H346MbhH
E199MbhM
Y413MbhH
E141MbhM

Figure SA.9

The proton translocation module shared between the MBH complex and Complex I.

A. The MBH complex and *T. thermophilus* complex I (PDB ID 4hea) aligned (as **Fig. 2C**) based solely on their respective antiporter-like subunit MbhH and Nqo14. The peripheral arm is docked to the right in complex I, and to the left in the MBH complex, of the membrane arm.

B-E. Structural alignment shown in (**A**) revealed a module shared between the MBH complex and Complex I. The corresponding subunits are superimposed and shown in **B-E**: **B**, MbhH and Nqo14. **C**, MbhG and Nqo11. **D**, MbhD and MbhE together are equivalent to Nqo10. Notably, MbhD TMH3 contains a π-bulge similar to that found in Nqo10. **E**, Similarity between the MbhI C-terminal region (lateral helix HL and TMH2) with the Nqo12 C-terminal region (lateral helix HL and TMH16).

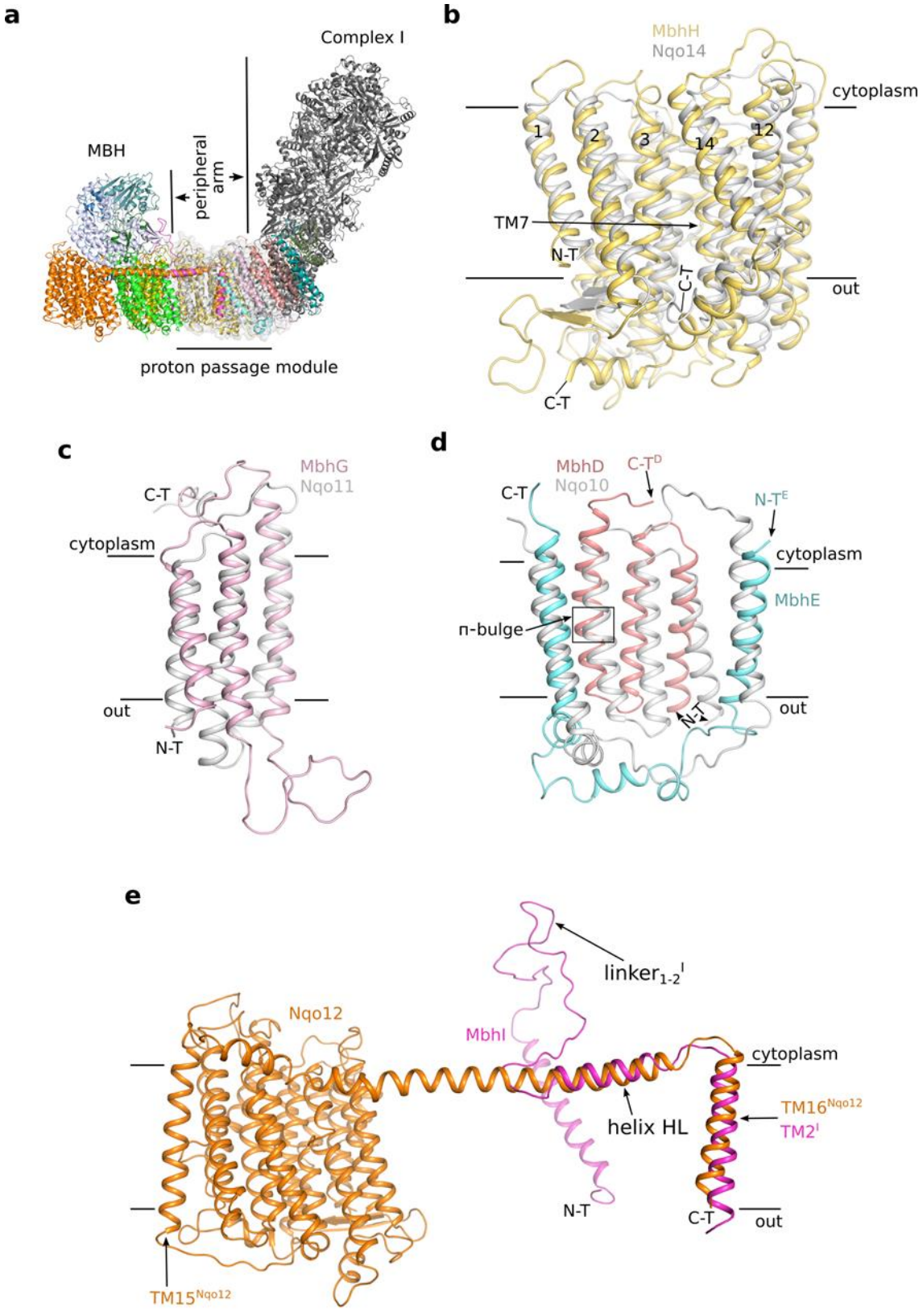
a
Complex I
MBH
peripheral arm
proton passage module
b
MbhH
Nqo14
cytoplasm
1
2
3
14
12
TM7
N-T
C-T
out
C-T
c
MbhG
Nqo11
C-T
cytoplasm
out
N-T
d
MbhD
Nqo10
C-T^D
C-T
N-T^E
cytoplasm
MbhE
π-bulge
out
N-T
e
linker1-2^I
Nqo12
MbhI
cytoplasm
TM16^Nqo12
TM2^I
helix HL
N-T
C-T
out
TM15^Nqo12

Figure SA.10

The membrane-anchored hydrogenase module shared between the MBH complex and Complex I.

A. Overlay of MBH peripheral arm with the classic dimeric [NiFe] hydrogenase from *D. gigas* (PDB ID 2frv) by aligning MbhL with the large subunit of the two-subunit classic hydrogenase. Only MbhL and MbhJ are visible here. The membrane subunit MbhM of MBH is also shown, although it is absent in the dimeric [NiFe] hydrogenase.

B. Overlay of MBH peripheral arm plus the membrane Mbh M and I with the corresponding *T. thermophilus* complex I subunits – the Q-module and the membrane Nqo8, Nqo7. The alignment is based on MbhL and Nqo4. The two systems share a similar architecture except for the C-terminal regions of MbhI and Nqo7, suggesting that this sub-complex is well conserved between the MBH complex and Complex I.

C. Like in complex I, there is also a chamber at the interface between the peripheral arm and the membrane subunit MbhM in the MBH complex. The internal cavity is shown as a red surface. The entry to the chamber in the MBH complex, which is equivalent to the quinone entry site in Complex I, is closed due to the presence of several bulky residues there. Structural alignment was based on MbhM and Nqo8.

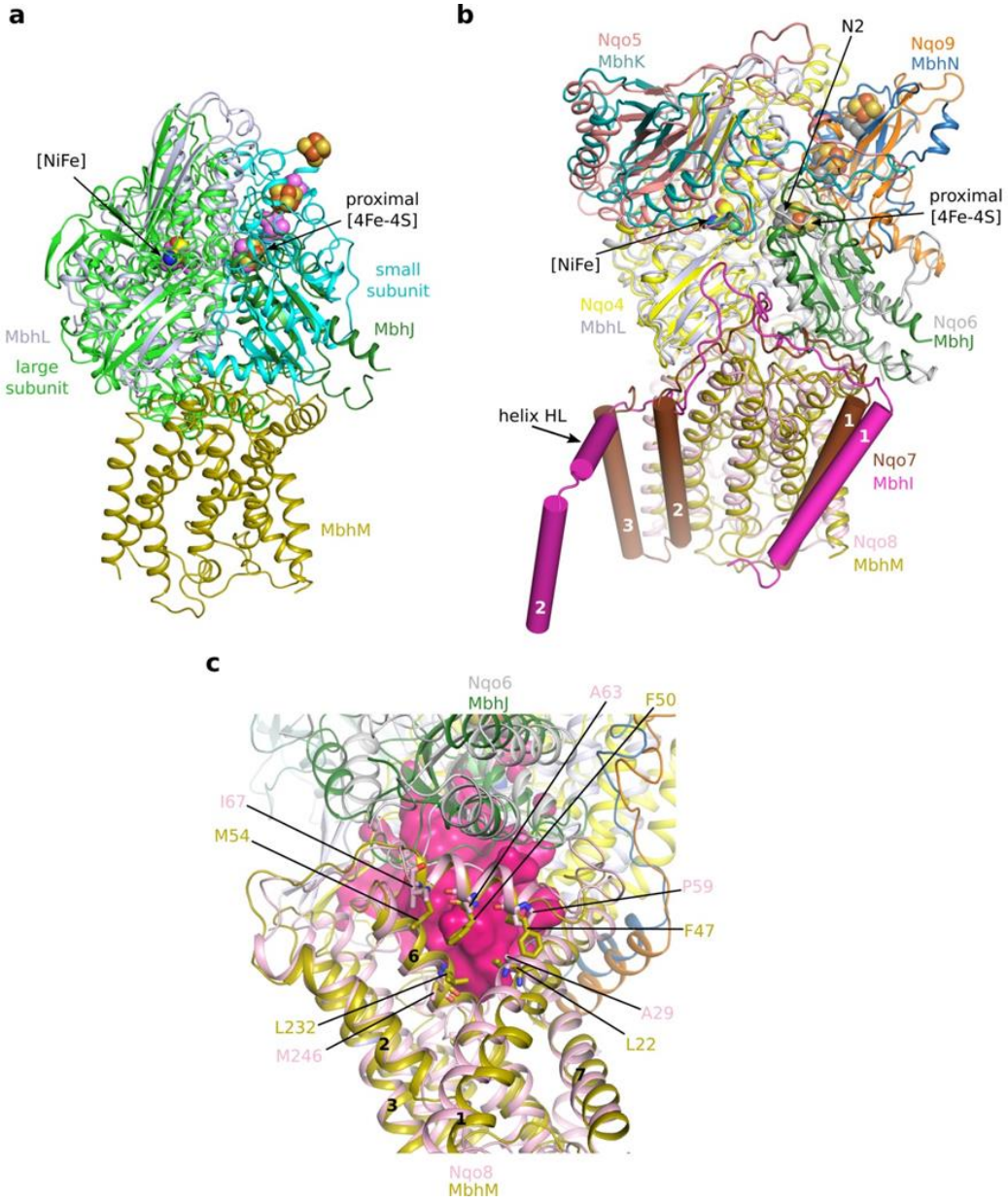
a
[NiFe]
proximal
[4Fe-4S]
small
subunit
MbhJ
MbhL
large
subunit
MbhM
b
Nqo5
MbhK
N2
Nqo9
MbhN
proximal
[4Fe-4S]
[NiFe]
Nqo4
MbhL
Nqo6
MbhJ
helix HL
Nqo7
MbhI
Nqo8
MbhM
c
Nqo6
MbhJ
A63
F50
I67
M54
P59
F47
A29
L22
L232
M246
Nqo8
MbhM

Figure SA.11

Structure and sequence comparison of the peripheral arms of the MBH complex with Complex I revealed several insertions in Complex I evolved for anchoring its N-module.

A. Overlay of MBH peripheral arm and the membrane MbhM with the *T. thermophilus* Complex I N-module, Q-module, and the membrane Nqo8. Alignment was based on MbhL and Nqo4. Individual subunits are coloured as in **Figure A.S9B**. The later-evolved N-module of Complex I is shown in cartoon as well as in transparent surface view.

B-E. Structural overlay (top panel) and sequence alignment (bottom panel) of individual subunits between Complex I and the MBH complex**: B**, MbhL and Nqo4; **C**, MbhN and Nqo9; **D**, MbhJ and Nqo6; **E**, MbhK and Nqo5. Protein sequence sources are Pfu, *Pyrococcus furiosus;* Tth, *Thermus thermophilus;* Ova, *Ovis aries*. The sequence differences and their locations are highlighted in the bottom panel as shaded boxes and in top panel as shaded ovals.

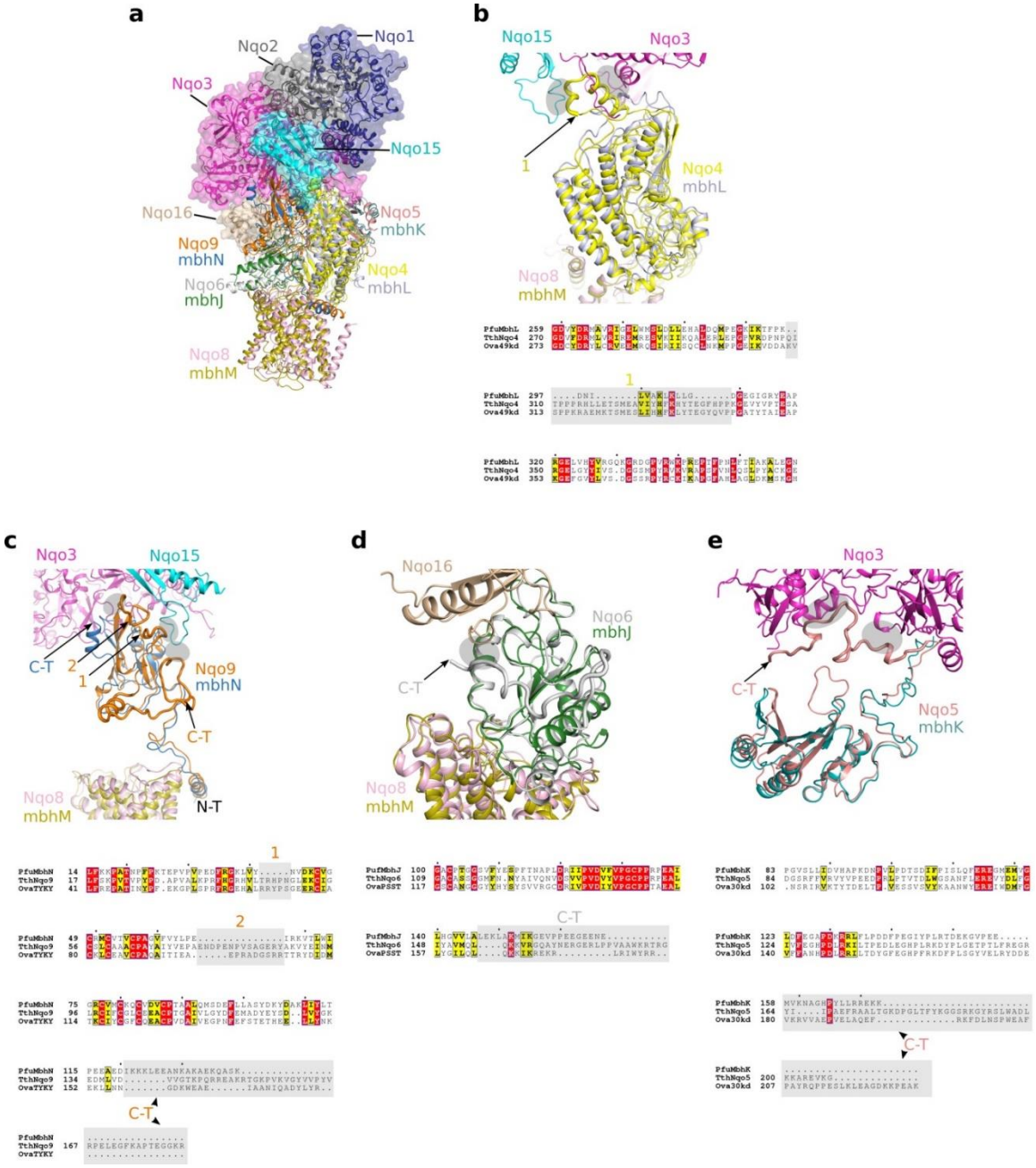
a
Nqo1
Nqo2
Nqo3
Nqo15
Nqo16
Nqo5
mbhK
Nqo9
mbhN
Nqo6
mbhJ
Nqo4
mbhL
Nqo8
mbhM
b
Nqo15
Nqo3
1
Nqo4
mbhL
Nqo8
mbhM
c
Nqo3
Nqo15
C-T
2
1
Nqo9
mbhN
C-T
Nqo8
mbhM
N-T
d
Nqo16
Nqo6
mbhJ
C-T
Nqo8
mbhM
e
Nqo3
C-T
Nqo5
mbhK

Figure SA.12

A comparison of coordinations of the [4Fe-4S] and [Ni-Fe] clusters in the peripheral arm of the MBH complex with those in *D. gigas* hydrogenase and Complex I.

The structures are coloured as in **Figure SA.9A-B**.

A. The coordination of the distal and medial [4Fe-4S] clusters in MBH MbhN is highly similar to that in Nqo9 of Complex I.

B. The coordination of the proximal [4Fe-4S] cluster is similar between the MBH and *D. gigas* hydrogenase. In Complex I, coordination of the N2 cluster involves an unusual pair of tandem Cys residues (C45 and C46).

C. The side chains coordinating the [NiFe] cluster in MBH are similar to those in the *D. gigas* hydrogenase. The structural elements for coordinating [Ni-Fe] cluster are not present in Complex I.

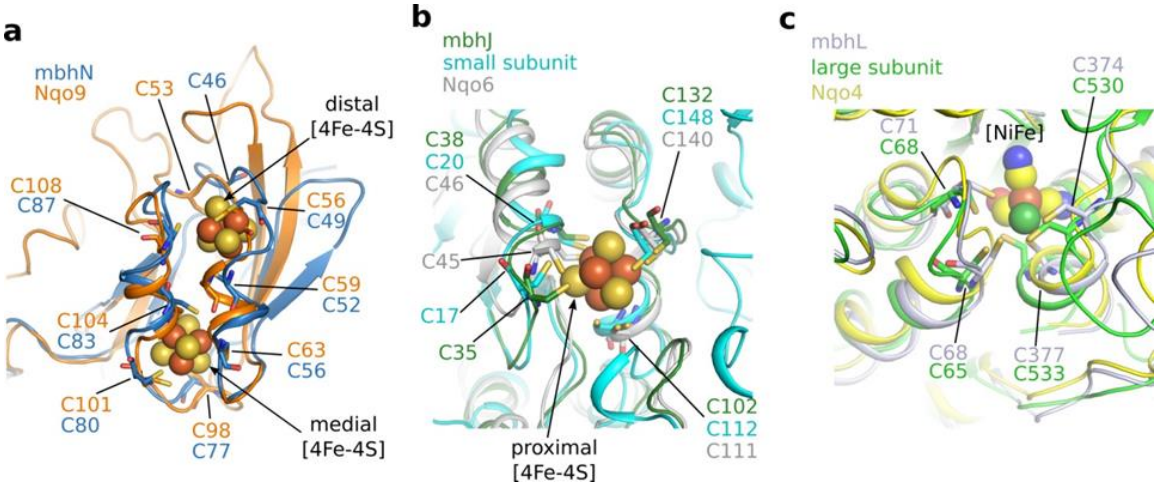
a
mbhN
Nqo9
C53
C46
distal
[4Fe-4S]
C108
C87
C56
C49
C59
C52
C104
C83
C63
C56
C101
C80
C98
C77
medial
[4Fe-4S]
b
mbhJ
small subunit
Nqo6
C132
C148
C140
C38
C20
C46
C45
C17
C35
C102
C112
C111
proximal
[4Fe-4S]
c
mbhL
large subunit
Nqo4
C374
C530
C71
C68
[NiFe]
C68
C65
C377
C533

Figure SA.13

Sequence alignments of individual MBH membrane subunits with their counterparts in the Mrp H^+/Na^+ antiporter.

The TMH numbers shown above the primary sequences are based on the MBH structure. The predicted secondary structural elements of *Bacillus subtilis* Mrp subunits are shown below the sequences. Protein sequence sources are Pfu, *Pyrococcus furiosus*; Bsu, *Bacillus subtilis*; Bps, *Bacillus pseudofirmus*; Sau, *Staphylococcus aureus*; Rme, *Rhizobium meliloti*; Pae, *Pseudomonas aeruginosa*; Vch, *Vibrio cholera*. The filled black triangles mark residues shown in **Fig. A.2C**, and the filled black squares mark residues shown in **Fig. A.4B-C**.

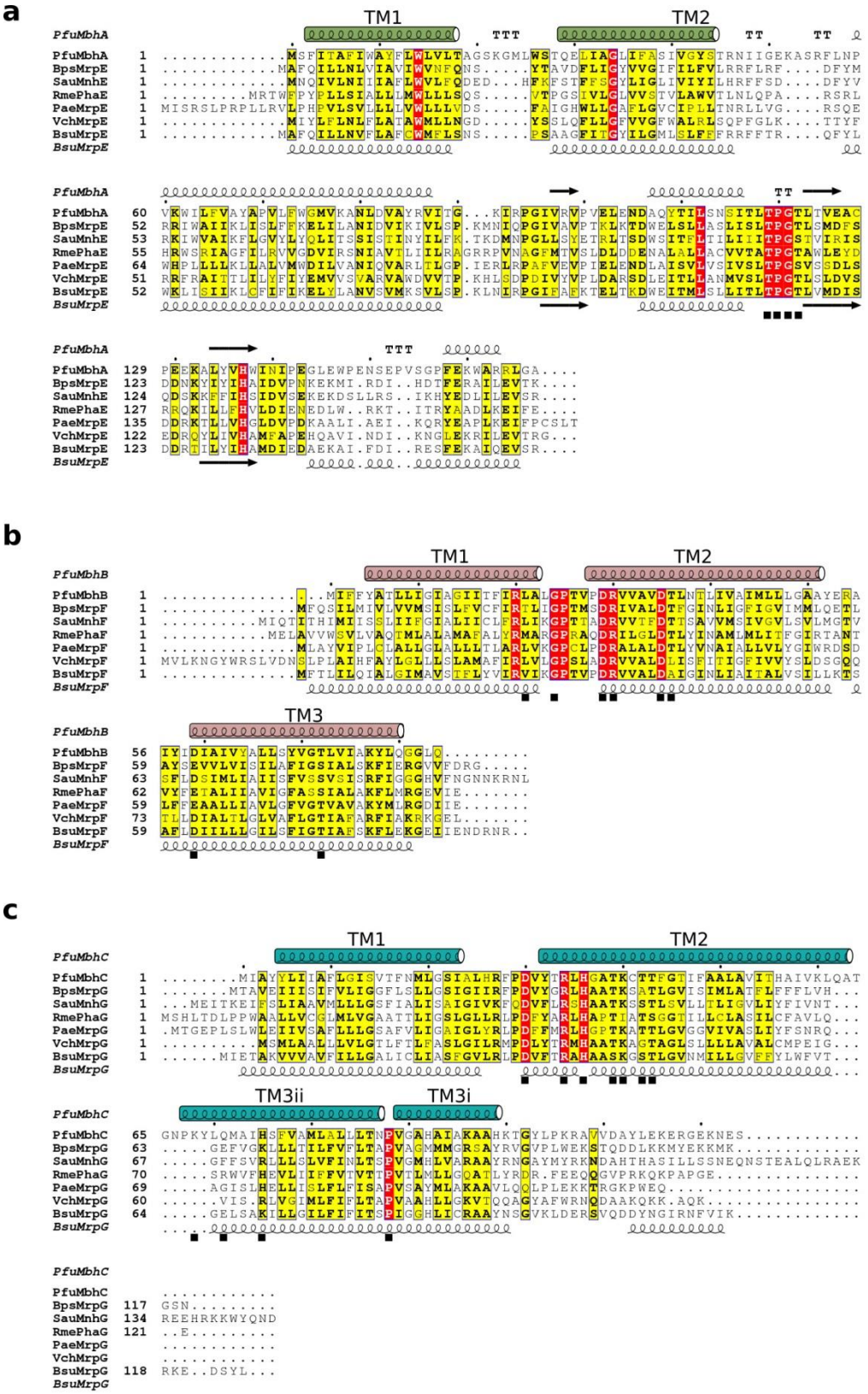
a
TM1
TM2
PfuMbhA
PfuMbhA 1 ...MSFITAFIWAYFLWLVLTAGSKGMLWSTQELIAGLIFASIVGYSTRNIIGEKASRFLNP
BpsMrpE 1 ...MAFQILLNLVIAVIWVNFQNS.....YTAVDFLIGYVVGIFILFVLRRFLRF....DFYM
SauMnhE 1 ...MNQIVLNIIIAFLWVLFQDED...HFKFSTFFSGYLIGLIVIYILHRFFSD....DFYV
RmePhaE 1 .....MRTWFPYPLLSIALLLMWLLLSQS.....VTPGSIVLGLVVSTVLAWVTLNLQPA....RSRL
PaeMrpE 1 MISRSLPRPLLRVLPHPVLSVLLLLVWLLLVDS.....FAIGHWLLGAFLGVCIPLLTNRLLVG....RSQE
VchMrpE 1 ...MIYLFLNLFLATAWMLLNGD.....YSSLQFLLGFVVGFWALRLSQPFGLK....TTYF
BsuMrpE 1 ...MAFQILLNVFLAFCWMFLSNS.....PSAAGFITGYILGMLSLFFFRRFFTR....QFYL
BsuMrpE
PfuMbhA
PfuMbhA 60 VKWILFVAYAPVLFWGMVKANLDVAYRVITG...KIRPGIVRVPVELENDAQYTILSNSITLTPGTLTVEAC
BpsMrpE 52 RRIWAIIKLISLFFKELILANIDVIKIVLSP.KMNIQPGIVAVPTKLKTDWELSLLASLISLTPGTLSMDFS
SauMnhE 53 RKIWVAIKFLGVYLYQLITSSISTINYILFK.TKDMNPGLLSYETRLTSDWSITFLTILIITPGSTVIRIS
RmePhaE 55 HRWSRIAGFILRVVGDVIRSNIAVTLIILRAGRRPVNAGFMTVSLDLDDENALALLACVVTATPGTAWLEYD
PaeMrpE 64 WHPLLLKLLALVMWDILVANIQVARLTLGP.IERLRPAFVEVPIELENDLAISVLVSIVSLTPGSVSSDLS
VchMrpE 51 RRFRAITTLILYFIYEMVVSVARVAWDVVTP.KHLSDPDIVYVPLDARSDLEITLLANMVSLTPGTLSLDVS
BsuMrpE 52 WKLISIIKLCFIFIKELYLANVSVMKSVLSP.KLNIRPGIFAFKTELTKDWEITMLSLLITLTPGTLVMDIS
BsuMrpE
PfuMbhA
TM3
PfuMbhA 129 PEEKALYVHWINIPEGLEWPENSEPVSGPFEKWARRLGA....
BpsMrpE 123 DDNKYIYIHAIDVPNKEKMI.RDI..HDTFERAILEVTK....
SauMnhE 124 QDSKKFFIHSIDVSEKEKDSLLRS..IKHYEDLILEVSR....
RmePhaE 127 RRQKILLFHVLDIENEDLW..RKT..ITRYAADLKEIFE....
PaeMrpE 135 DDRKTLLVHGLDVPDKAALI.AEI..KQRYEAPLKEIFPCSLT
VchMrpE 122 EDRQYLIVHAMFAPEHQAVI.NDI..KNGLEKRILEVTRG...
BsuMrpE 123 DDRTILYIHAMDIEDAEKAI.FDI..RESFEKAIQEVSR....
BsuMrpE
b
TM1
TM2
PfuMbhB
PfuMbhB 1 ...MIFFYATLLIGIAGIIIFIRLALGPTVPDRVVAVDTLNTLIVAIMLLLGAAYEFA
BpsMrpF 1 ...MFQSILMIVLVVMSISLFVCFIRTLIGPTMSDRIVALDTFGINLIGFIGVIMMLQETL
SauMnhF 1 ...MIQTITHIMIISSLIIFGIALIICLFRLIKGPTTADRVVTFDTTSAVVMSIVGVLSVLMGTV
RmePhaF 1 ...MELAVVWSVLVAQTMLALAMAFALYRMARGPRAQDRILGLDTLYINAMLMLITFGIRTANT
PaeMrpF 1 ...MLAYVIPLCLALLGLALLLTLARLVKGPCLPDRALALDTLYVNAIALLVLYGIWRDSD
VchMrpF 1 MVLKNGYWRSLVDNSLPLAIHFAYLGLLLSLAMAFIRLVLGPSLADRVVALDLISFITIGFIVVYSLDSGQQ
BsuMrpF 1 ...MFTLILQIALGIMAVSTFLYVIRVIKGPTVPDRVVALDAIGINLIAITALVSILLKTS
BsuMrpF
TM3
PfuMbhB
PfuMbhB 56 IYIDIAIVYALLSYVGTLVIAKYLQGGLQ.....
BpsMrpF 59 AYSEVVLVISILAFIGSIALSKFIERGVVFDRG.....
SauMnhF 63 SFLDSIMLIAIISFVSSVSISRFIGGGHVFNGNNKRNL
RmePhaF 62 VYFETALIIAVIGFASSIALAKFLMRGEVIE.....
PaeMrpG 59 LFFEAALLIAVLGFVGTVAVAKYMLRGDIIE.....
VchMrpF 73 TLLDIALTLGLVAFLGTIAFARFIAKRKGEL.....
BsuMrpF 59 AFLDIILLLGILSFIGTIAFSKFLEKGEIIENDRNR..
BsuMrpF
c
TM1
TM2
PfuMbhC
PfuMbhC 1 .....MIAYYLIIAFLGISVTFNMLGSIALHRFPDVYTRLHGATKCTTFGTIFAALAVITHAIVKLQAT
BpsMrpG 1 .....MTAVFIIISIFVLIGGFLSLLGSIGIIRFPDVYGRLHAATKSATLGVISIMLATFLFFFLVH...
SauMnhG 1 ...MEITKEIFSLIAAVMLLLGSFIALISAIGIVKFQDVFLRSHAATKSSTLSVLLTLIGVLIYFIVNT...
RmePhaG 1 MSHLTDLPPWAALLVCGLMLVGAATTLIGSLGLLRLPDFYARLHAPTIATSGGTILLCLASILCFAVLQ...
PaeMrpG 1 .MTGEPLSLWLEIIVSAFLLLGSAFVLIGAIGLYRLPDFFMRLHGPTKATTLGVGGVIVASLIYFSNRQ...
VchMrpG 1 .....MSMLAALLLVLGTLFTLFASLGILRMPDLYTRMHAATKAGTAGLSLLLLAVALCMPEIG...
BsuMrpG 1 .....MIETAKVVVAVFILLGALICLIASFGVLRLPDVFTRAHAASKGSTLGVNMILLGVFFYLWFVT...
BsuMrpG
TM3ii
TM3i
PfuMbhC
PfuMbhC 65 GNPKYLQMAIHSFVAMLALLLTNPVGAHAIAKAAHKTGYLPKRAVDAYLEKERGEKNES.....
BpsMrpG 63 .....GEFVGKLLLTILFVFLTAPVAGMMMGRSAYRVGVPLWEKSTQDDLKKMYEKKMK.....
SauMnhG 67 .....GFFSVRLLLSLVFINLTSPVGMHLVARAAYRNGAYMYRKNDAHTHASILLSSNEQNSTEALQLRAEK
RmePhaG 70 .....SRWVFHEVLIIFFVTVTTPVTLMLLGQATLYRDR.FEEQQGVPRKQKPAPGE.....
PaeMrpG 69 .....AGISLHELLISLFLFISAPVSAYMLAKAAVLQQLPLEKKTRGKPWEQ.....
VchMrpG 60 .....VIS.RLVGIMLFIFLTAPVAAHLLGKVTQQAGYAFWRNQDAAKQKK.AQK.....
BsuMrpG 64 .....GELSAKILLGILFIFITSPIGGHLICRAAYNSGVKLDERSVQDDYNGIRNFVIK.....
BsuMrpG
PfuMbhC
PfuMbhC .....
BpsMrpG 117 GSN.....
SauMnhG 134 REEHRKKWYQND
RmePhaG 121 ..E.....
PaeMrpG .....
VchMrpG .....
BsuMrpG 118 RKE..DSYL...
BsuMrpG

d

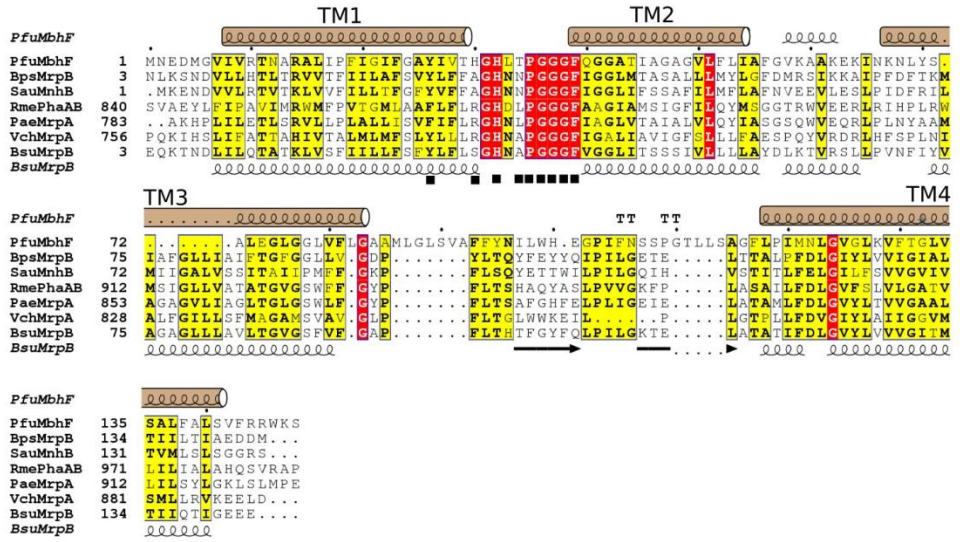
TM1
TM2
TM3
TM4
PfuMbhF
PfuMbhF 1 MNEDMGVIVRTNARALIPFIGIFGAYIVTHGHLTPGGGEQGGATIAGAGVLFLIAFGVKAAKEKINKNLYS.
BpsMrpB 3 NLKSNDVLLHTLTRVVTFIILAFSVYLFFAGHNNPGGGEIGGLMTASALLLMYLGFDMRSIKKAIPFDFTKM
SauMnhB 1 .MKENDVVLRTVTKLVVFILLTFGFYVFFAGHNNPGGGEIGGLIFSSAFILMFLAFNVEEVLESLPIDFRIL
RmePhaAB 840 SVAEYLFIPAVIMRWMFPVTGMLAAFLFLRGHDLPGGGEAAGIAMSIGFILQYMSGGTRWVEERLRIHPLRW
PaeMrpA 783 ..AKHPLILETLSRVLLPLALLISVFIFLRGHNLPGGGEIAGLVTAIALVLQYIASGSQWVEQRLPLNYAAM
VchMrpA 756 PQKIHSLIFATTAHIVTALMLMFSLYLLLRGHNAPGGGEIGALIAVIGFSLLLFAESPQYVRDRLHFSPLNI
BsuMrpB 3 EQKTNDLILQTATKLVSFIILLFSFYLFLSGHNAPGGGEVGGLITSSSIVLLLLAYDLKTVRSLLPVNFIYV
PfuMbhF
TM3
TM4
PfuMbhF 72 .....ALEGLGGLVFLGAAMLGLSVAFFYNILWH.EGPIFNSSPGTLLSAGFLPIMNLGVGLKVFTGLV
BpsMrpB 75 IAFGLLIAIFTGFGGLLV.GDP.....YLTQYFEYYQIPILGETE.....LTTALPFDLGIYLVVIGIAL
SauMnhB 72 MIIGALVSSITAIIPMFF.GKP.....FLSQYETTWILPILGQIH.....VSTITLFELGILFSVVGVIV
RmePhaAB 912 MSIGLLVATATGVGSWFF.GYP.....FLTSHAQYASLPVVGKFP.....LASAILFDLGVFSLVLGATV
PaeMrpA 853 AGAGVLIAGLTGLGSWLF.GYP.....FLTSAFGHFELPLIGEIE.....LATAMLFDLGVYLTVVGAAL
VchMrpA 828 ALFGILLSFMAGAMSVAV.GLP.....FLTGLWWKEIL.....P.....LGTPLLFDVGIYLAIIGGVM
BsuMrpB 75 AGAGLLLAVLTGVGSFVF.GAP.....FLTHTFGYFQLPILGKTE.....LATATIFDLGVVLVVVGITM
PfuMbhF
PfuMbhF 135 SALFALSVFRRWKS
BpsMrpB 134 TIILTIAEDDM...
SauMnhB 131 TVMLSLSGGRS...
RmePhaAB 971 LILIALAHQSVRAP
PaeMrpA 912 LILSYLGKLSLMPE
VchMrpA 881 SMLLRVKEELD...
BsuMrpB 134 TIIQTIGEEE....
BsuMrpB

e

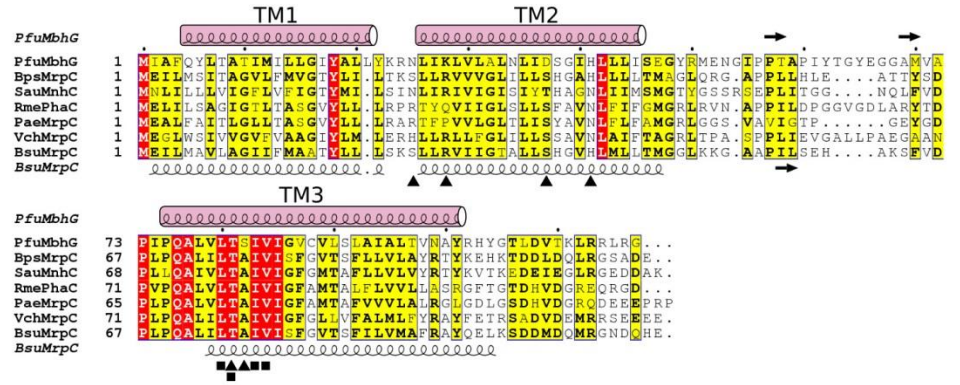
TM1
TM2
TM3
PfuMbhG
PfuMbhG 1 MIAFQYLTATIMILLGIYALLYKRNLIKLVLALNLIDSGIHPLLISEGYRMENGIPPTAPIYTGYEGGAMVA
BpsMrpC 1 MEILMSITAGVLFMVGTYLILTKSLLRVVVGLILLSHGAHLLLLTMAGLQRG.APPLLHLE....ATTYSD
SauMnhC 1 MNLILLLVIGFLVFIGTYMILSINLIRIVIGISIYTHAGNLIIMSMGTYGSSRSEPLITGG....NQLFVD
RmePhaC 1 MELILSAGIGTLTASGVYLLLLRPRTYQVIIGLSLLSFAVNLFIFGMGRLRVN.APPILDPGGVGDLARYTD
PaeMrpC 1 MEALFAITLGLLTASGVYLLLLRARTFPVVLGLTLISYAVNLFLFAMGRLGGS.VAVIGTP.....GEYGD
VchMrpC 1 MEGLWSIVVGVFVAAGIYLMLERHLLRLLFGLILLSSAVNLFAIFTAGRLTPA.SPPLIEVGALLPAEGAAN
BsuMrpC 1 MEILMAVLAGIIFMAATYLLLSKSLLRVIIGTALLSHGVHLMLLTMGGLKKG.AAPILSEH....AKSFVD
BsuMrpC
TM3
PfuMbhG
PfuMbhG 73 PIPQALVLTSIVIGVCVLSLAIALTVNAYRHYGTLDVTKLRRLRG...
BpsMrpC 67 PLPQALLLTAIVISFGVTSFLLVLAYRTYKEHKTDDLDQLRGSADE..
SauMnhC 68 PLLQAIVLTAIVIGFGMTAFLLVLVYRTYKVTKEDEIEGLRGEDDAK.
RmePhaC 71 PVPQALVLTAIVIGFAMTALFLVVLLASRGFTGTDHVDGRGQRGD...
PaeMrpC 65 PLPQALVLTAIVIGFAMTAFVVVLALRGLGDLGSDHVDGRGQDEEEPRP
VchMrpC 71 PLPQALILTAIVIGFGLLVFALMLFYRAYFETRSADVDEMRRSEEEE.
BsuMrpC 67 PLPQALILTAIVISFGVTSFILVMAFRAYQELKSDDMDQMRGNDQHE.
BsuMrpC

f

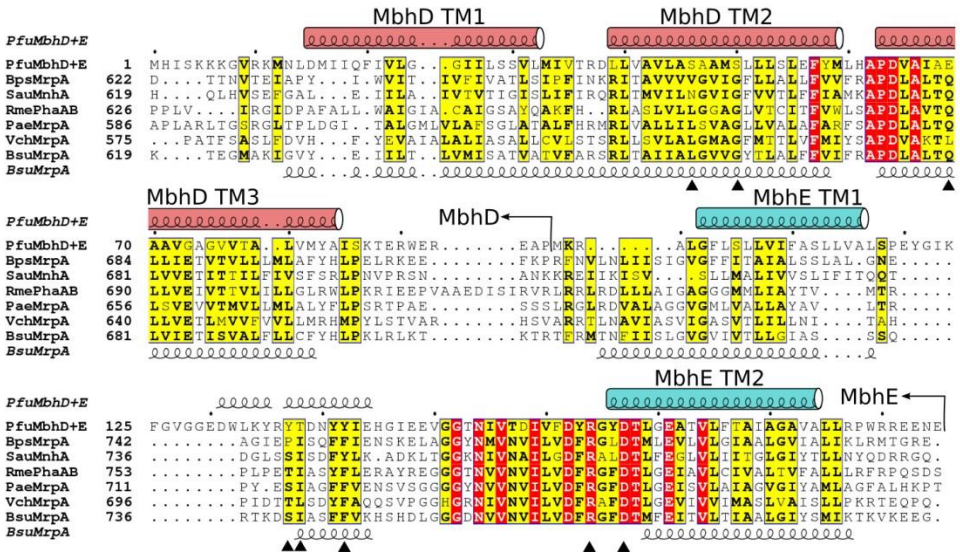
MbhD TM1
MbhD TM2
MbhD TM3
MbhD
MbhE TM1
MbhE TM2
MbhE
PfuMbhD+E
PfuMbhD+E 1 MHISKKKGVRKMNLDMIIQFIVLG..GIILSSVLMIVTRDLLVAVLASAAMSLLLSLEFYMLHAPDVAIAE
BpsMrpA 622 D....TTNVTEIAPY...I.WVIT..IVFIVATLSIPFINKRITAVVVVGVIGFLLALLFVFRAPDLALTQ
SauMnhA 619 H....QLHVSEFGAL...E.IILA..IVTVTIGISLIFIRQRLTMVILNGVIGFVVTLFFIAMKAPDLALTQ
RmePhaAB 626 PPLV....IRGIDPAFALL.WAIGIA.CAIGSAYQAKFH..RLASLVLLGGAGLVTCITFVWLSAPDLAVTQ
PaeMrpA 586 APLARLTGSRGLTPLDGI..TALGMLVLAFSGLATALFHRMRLVALLILSVAGLLVALAIGARFSAPDLALTQ
VchMrpA 575 ...PATFSASLFDVH...F.YEVAIALALIASALLCVLSTSRLLSVLALGMAGFMTTLVFMIYSAPDVAKTL
BsuMrpA 619 K....TEGMAKIGVY...E.IILT..LVMISATVATVFARSRLTAIIALGVVGYTLALFFVIFRAPDLALTQ
BsuMrpA
PfuMbhD+E 70 AAVGAGVVTA..LVMYAISKTERWER.......EAPMKRL.....ALGFLSLLVIFASLLVALSPEYGIK
BpsMrpA 684 LLIETVTVLLLMLAFYHLPELRKEE.........FKPRFNVLNLIISIGVGFFITAIAALSSLAL.GNE.....
SauMnhA 681 LVVETITTILFIVSFSRLPNVPRSN.........ANKKREIIKISV....SLLMALIVVSLIFITQQT.....
RmePhaAB 690 LLVEIVTTVLILLGLRWLPKRIEEPVAAEDISIRVRLRRLRDLLLAIGAGGGMMLIAYTV....MTR.....
PaeMrpA 656 LSVEVVTMVLLMLALYFLPSRTPAE.........SSSLRGLRDVALAGGVGMLVALLAYAV....LTR.....
VchMrpA 640 LLVETLMVVFVVLLMRHMPYLSTVAR.......HSVARRTLNAVIASVIGASVTLILLNI....TAH.....
BsuMrpA 681 LVIETISVALFLLCFYHLPKLRLKT.........KTRTFRMTNFIISLGVGVIVTLLGIAS....SSQ.....
BsuMrpA
PfuMbhD+E 125 FGVGGEDWLKYRYTDNYYIEHGIEEVGGTNIVTDHVFDYRGYDTLGEATVLFTAIAGAVALLRPWRREENE
BpsMrpA 742 ........AGIEPISQFFIENSKELAGGYNMVNVHLVDFRGLDTMLEVLVLGIAALGVIALIKLRMTGRE.
SauMnhA 736 ........DGLSSISDFYLK.ADKLTGGKNIVNAHLGDFRALDTLFEGLVLIITGLGIYTLLNYQDRRGQ.
RmePhaAB 753 ........PLPETIASYFLERAYREGGGTNVVNVHLVDFRGFDTLGEIAVLCIVALTVFALLLRFRPQSDS
PaeMrpA 711 ....PY.ESIAGFFVENSVSGGGGGYNVVNVHLVDFRGFDTLGEISVLAIAGVGIYAMLAGFALHKPT
VchMrpA 696 ........PIDTTLSDYFAQQSVPGGHGRNIVNVHLVDFRAFDTLGEVIVVIMASLVAISLLPKRTEQPQ.
BsuMrpA 736 ........RTKDSIASFFVKHSHDLGGGDNVVNVHLVDFRGFDTMFEITVLTIAALGIYSMIKTKVKEEG.
BsuMrpA

g

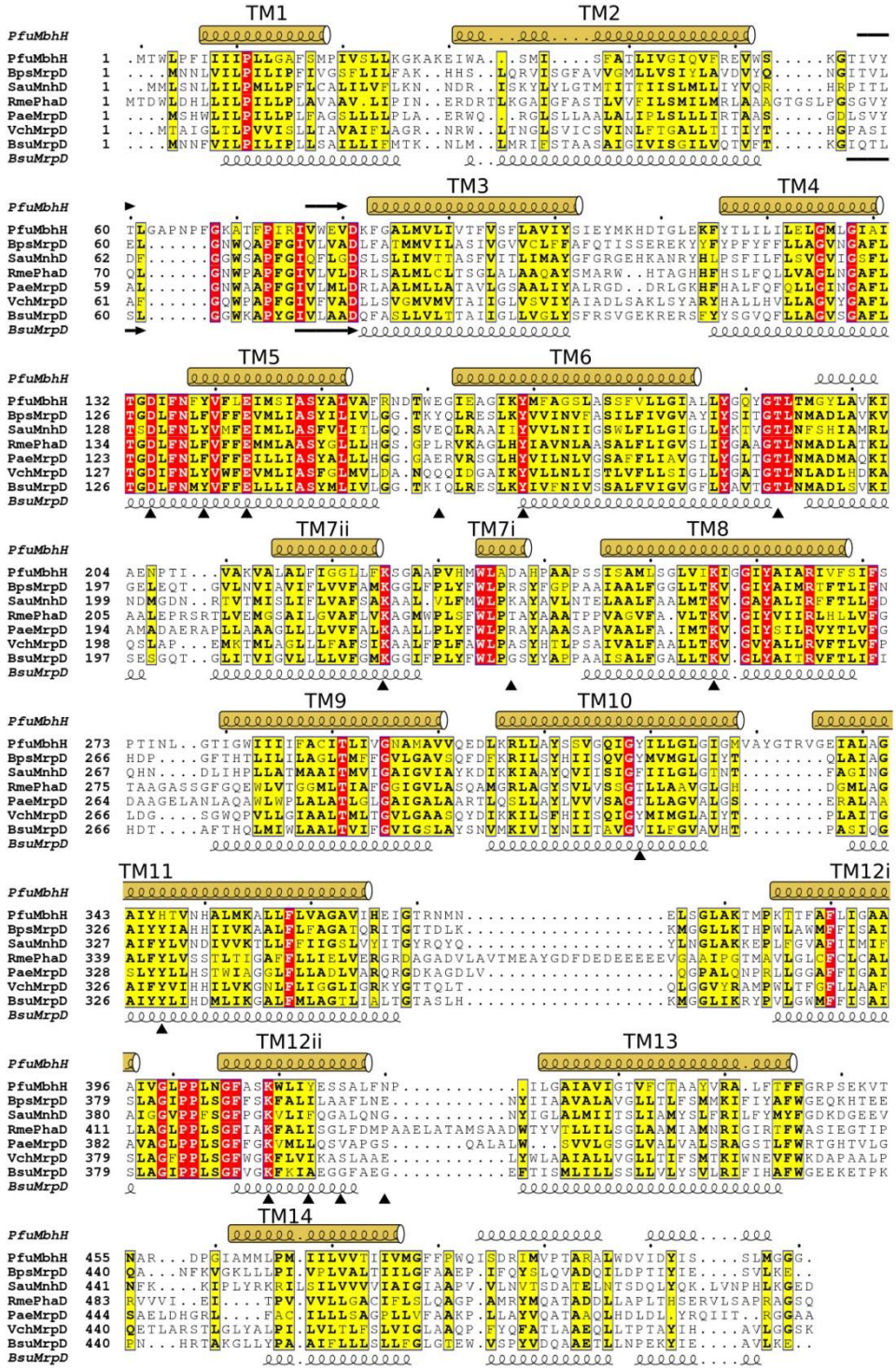
TM1
TM2
TM3
TM4
TM5
TM6
TM7ii
TM7i
TM8
TM9
TM10
TM11
TM12i
TM12ii
TM13
TM14
PfuMbhH
BpsMrpD
SauMnhD
RmePhaD
PaeMrpD
VchMrpD
BsuMrpD
BsuMrpD

Figure SA.14

A detailed comparison of the redox active sites of the MBH and Complex I.

A. The structures are superposed and coloured as in **Figure SA.9B**. In *T. thermophilus* Complex I, the conserved H38 and Y87 bind the quinone headgroup. The H_2-evolving catalytic site in MBH complex, as defined by MbhL E21, C374 and the [NiFe] center, is very close to the quinone headgroup-binding site. Importantly, the three interfacial loops (between the peripheral and membrane arms) in MBH and Complex I show good agreement, and they are all positioned to probe their respective active sites.

B-D. Sequence alignment of the three linker loops of MBH and complex I as shown in (**A**). Protein sequences are Pfu, *Pyrococcus furiosus*; Tth, *Thermus thermophilus*; Ova, *Ovis aries*.

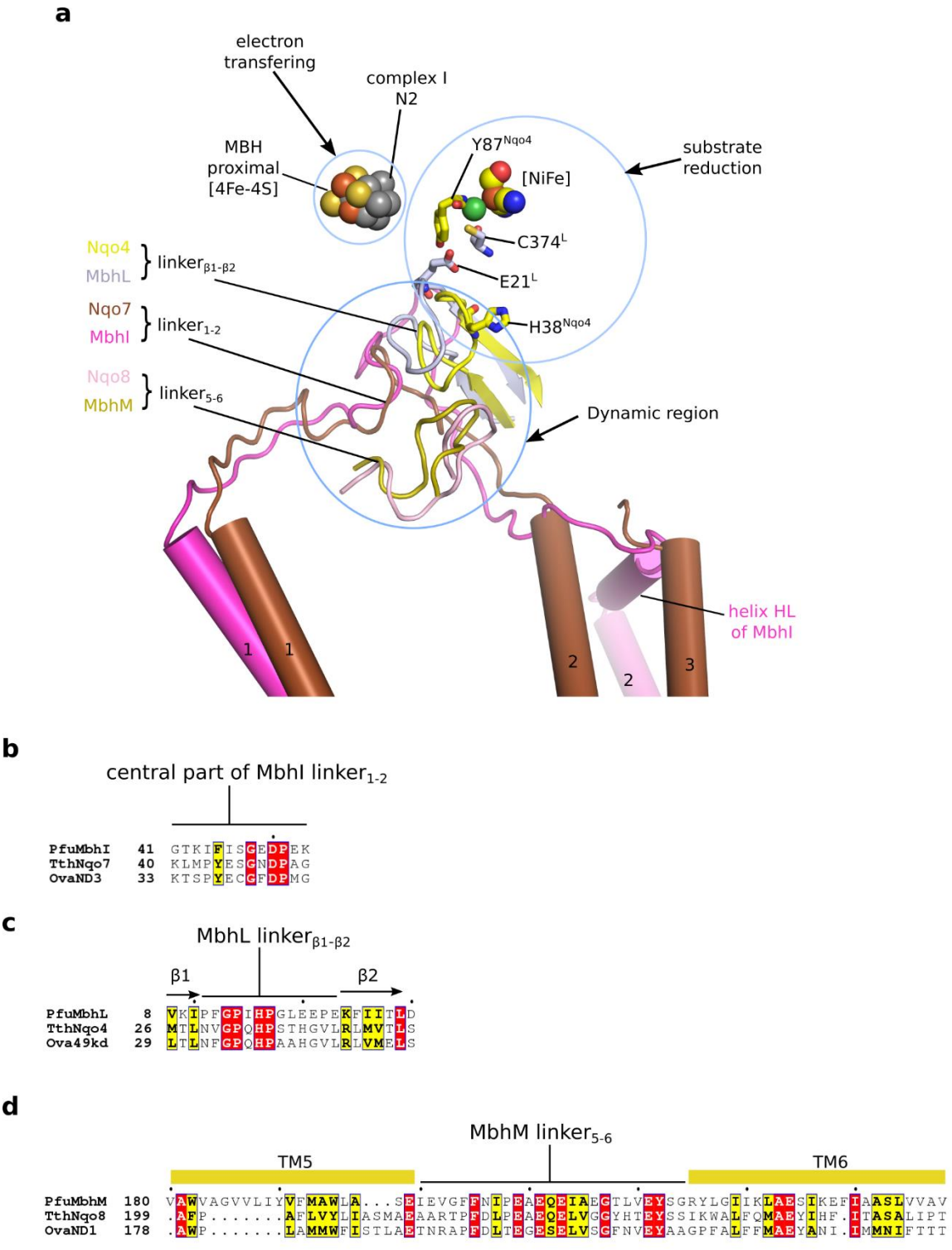
a
electron transfering
complex I N2
MBH proximal [4Fe-4S]
Y87Nqo4
[NiFe]
substrate reduction
C374L
E21L
H38Nqo4
Nqo4
MbhL
linker β1-β2
Nqo7
MbhI
linker 1-2
Nqo8
MbhM
linker 5-6
Dynamic region
helix HL of MbhI
1
1
2
2
3
b
central part of MbhI linker 1-2
PfuMbhI 41 GTKIFISGEDPEK
TthNqo7 40 KLMPYESGNDPAG
OvaND3 33 KTSPYEGGFDPMG
c
MbhL linker β1-β2
β1
β2
PfuMbhL 8 VKIPFGPIHPGLEEPEKFIITLD
TthNqo4 26 MTLNVGPQHPSTHGVLRLMVTLS
Ova49kd 29 LTLNFGPQHPAAHGVLRLVMELS
d
MbhM linker 5-6
TM5
TM6
PfuMbhM 180 VAWVAGVVLIYVFMAWLA...SEIEVGFFNIPEAEQEIAEGTLVEYSGRYLGIIKLAESIKEFIAASLVVAV
TthNqo8 199 .AFP.....AFLVYLIASMAEAARTPFDLPEAEQELVGGYHTEYSSIKWALFQMAEYIHF.ITASALIPT
OvaND1 178 .AWP.....LAMMWFISTLAETNRAPFDLTEGESELVSGFNVEYAAGPFALFFMAEYANI.IMMNIFTTT

APPENDIX B

THE PYROCOCCUS FURIOSUS IRONOME IS DOMINATED BY $[FE_4S_4]^{2+}$ CLUSTERS OR THIOFERRATE-LIKE IRON DEPENDING ON THE AVAILABILITY OF ELEMENTAL SULFUR[6]

[6] Shaik Waseem Vali, Dominik K. Haja, Richard A. Brand, Michael W. W. Adams, and Paul A. Lindahl. Submitted to *The Journal of Biological Chemistry*

Abstract

Pyrococcus furiosus is a hyperthermophilic anaerobic archaeon whose metabolism depends on whether elemental sulfur is ($+S^0$) or is not ($-S^0$) included in growth medium. Under $+S^0$ conditions, expression of respiratory hydrogenases declines and respiratory membrane-bound sulfane reductase and the putative iron-storage protein IssA increases. Mössbauer spectroscopy was used to analyze the iron content of wild-type (WT) and ΔIssA cells grown under $+S^0$ and $-S^0$ conditions. WT-S^0 cells contained ~ 1 mM Fe, with ~ 85% as two types of S = 0 $[Fe_4S_4]^{2+}$ clusters and the remainder mainly high-spin Fe^{II}. WT+S^0 cells contained 5–9 mM Fe, with 75 - 90% as magnetically ordered thioferrate-like (TFL) iron nanoparticles. TFL iron was similar to authentic thioferrates; both consisted of Fe^{III} ions coordinated by an S_4 environment, and both exhibited strong coupling between particles causing applied fields up to 6.0 T to have little spectral effect. At 150 K when magnetic hyperfine interactions were abolished, TFL iron exhibited two doublets that overlapped those of $[Fe_4S_4]^{2+}$ clusters in $-S^0$ cells. This coincidence arose because the coordination environment of TFL iron and cluster iron are similar. The TFL structure was more heterogeneous in the presence of IssA. IssA may coordinate insoluble iron sulfides as TFL iron, formed as a byproduct of anaerobic sulfur respiration under high iron conditions, which thereby reduces its toxicity to the cell. This was the first Mössbauer characterization of the iron-ome of an archaeon, and it illustrates differences relative to the iron content of better-studied bacteria such as *Escherichia coli*.

Introduction

Pyrococcus furiosus is a hyperthermophilic anaerobic archaeon that grows near marine volcanic vents at temperatures approaching 100 °C (1). These cells grow on carbohydrates or peptides and produce acetate, CO_2, and either H_2 or H_2S depending on whether elemental sulfur (S^0) is included in the growth medium. The iron concentration in the organism is high; this d-block transition metal plays critical roles in the cell's metabolism, especially in processes involving redox and energy generation (2). Bioinformatic analysis predicts that there are 178 iron-containing proteins (Table SB.1, (3), 27 of which have been purified (Table SB.2); at least 15 of those purified contain [Fe_4S_4] clusters. This represents 8.4% of the *P. furiosus* genome, which is slightly above average for archaea (7.1%) and well above average for bacteria (3.9%) and eukaryotes (1.1%) (4, 5).

During peptide fermentation, homodimeric aldehyde ferredoxin oxidoreductase (AOR) oxidizes aldehydes derived from amino acids. Each AOR subunit contains an [Fe_4S_4] cluster. Bridging the subunits of the homodimer is a monomeric Fe ion coordinated by His and Glu residues (6). AOR constitutes ~ 1% of the total protein in the cell (7). Formaldehyde ferredoxin oxidoreductase (FOR), pyruvate ferredoxin oxidoreductase (POR), 2-ketoisovalerate ferredoxin oxidoreductase (VOR), 2-ketoglutarate ferredoxin oxidoreductase (KGOR), and indolepyruvate ferredoxin oxidoreductase (IOR) are all [Fe_4S_4] cluster-containing enzymes that catalyze catabolic processes. The latter enzymes catalyze the oxidative decarboxylation of 2-keto acids derived from peptides (8,9,10). Electrons from these catabolic metalloenzymes reduce a monomeric ferredoxin that houses a single $[Fe_4S_4]^{2+/1+}$ cluster ($E^{0'}$ ~ -480 mV vs NHE) coordinated by 3 Cys and 1 Asp residues.

Carbohydrate fermentation involves a modified Embden-Meyerhof pathway that is independent of NAD. Glyceraldehyde-3-phosphate ferredoxin oxidoreductase (GAPOR), another [Fe_4S_4]-containing enzyme, oxidizes glyceraldehyde-3-phosphate to glycerate-3-phosphate and transfers the electrons obtained to the ferredoxin.

Ferredoxin not only receives electrons but it donates them as part of energy generation in the cell; thus, it serves as the electron *currency* for the cell. An evolutionarily ancient membrane-bound respiratory hydrogenase (MBH) is used to oxidize ferredoxin (11). This contains at least three [Fe_4S_4] clusters and a NiFe active-site cluster. Ferredoxin donates electrons to MBH which transfers them, in turn, to protons ($E^{0'}$ = -420 mV at pH 7), forming H_2 as the product. This thermodynamically favorable redox process pumps H^+ ions across the membrane, which are then exchanged with Na^+ ions. This creates a concentration gradient that is used by a Na^+-dependent ATP synthase to generate ATP via chemiosmosis. Ferredoxin also donates electrons to NADH-dependent reduced ferredoxin:$NADP^+$ oxidoreductase 1 (Nfn1) which reduces $NADP^+$ in an electron bifurcation reaction that generates low-potential electrons which can be used in metabolic processes requiring low potentials.

Carbohydrate fermentation can occur with or without S^0, whereas cells grown on peptides require S^0 as there is little growth when it is omitted from the growth medium (12). The metabolism of *P. furiosus* changes significantly when elemental sulfur (S^0) is included in the growth medium (13). Under $+S^0$ conditions, *P. furiosus* shuts-down expression of MBH and of the two NAD(P)-reducing soluble hydrogenases termed SHI and SHII (among other proteins) and up-regulates expression of a membrane-bound sulfane reductase (MBS) (Tables SB.3 and SB.4 (14)). Doing so suppresses production of H_2 and

stimulates H_2S production. MBS uses electrons from ferredoxin to reduce sulfane sulfurs of polysulfides ($E^{0'}$ = -260 mV), generating smaller polysulfide units as illustrated by the following sample reaction.

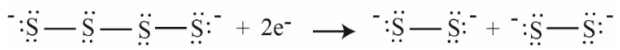

MBS cleaves organic and anionic polysulfides but not to the level of H_2S, which is formed spontaneously from smaller polysulfides (S_n^{2-} where $n \leq 4$). Like MBH, MBS creates a Na^+ ion gradient which is subsequently used, *via* chemiosmosis, for ATP synthesis. MBS is a homolog of MBH and also contains three [Fe_4S_4] clusters. Unlike MBH, it does not contain a NiFe active site (15).

The S^0-dependent shift in metabolism is controlled by transcription factor SurR (16,17). Under $+S^0$ conditions, SurR upregulates iron transport and ISC biosynthesis genes. *P. furiosus* grows better with S° than without it; in fact, the maximal yield (cell mass produced per mole of carbohydrate used) is nearly double that obtained in the absence of S° (herein termed $-S^0$). This implies that more energy can be generated by coupling ferredoxin oxidation to S° reduction than by coupling it to proton reduction, a conclusion substantiated by the finding that MBS contains an additional ion pump compared to MBH (15).

Despite being an anaerobe, *P. furiosus* houses iron-containing proteins that protect it against damage due to reactive oxygen species (ROS). Superoxide reductase catalyzes the reduction of superoxide to H_2O_2 at an active site containing a single Fe^{II} ion. The electrons required for this come from rubredoxin, a protein that houses a mononuclear redox-active Fe^{II}/Fe^{III} ion coordinated by four cysteine residues in a tetrahedral geometry

– an $Fe^{II/III}(S)_4$ site (18). Rubrerythrin catalyzes the reduction of H_2O_2 to water, also using electrons from rubredoxin. It contains an [Fe-O-Fe] center as well as an $Fe^{II/III}(S)_4$ site (19).

P. furiosus contains at least two proteins that store iron, including ferritin and a "miniferritin" DPS-like protein. Ferritin stores thousands of ferric ions within the core of a 24-subunit protein complex as an insoluble Fe^{III} ferrihydrite-type aggregate. The DPS-like protein has a ferroxidase active site ([Fe-O-Fe]) which exhibits peroxidase activity in the presence of H_2O_2. This protein coordinates hundreds of iron ions, obtained from the H_2O_2-dependent oxidation of Fe^{II} (20,21).

Another protein that binds a large amount of iron is IssA. The exact function of the IssA protein is unknown but its expression increases dramatically when cells are grown in $+S^0$ media, but only when iron is present (> 7.4 µM) (22). Vaccaro et al. (23) suggested that IssA stores iron as thioferrates in which Fe^{III} and S^{2-} ions form anionic chains of edge-sharing FeS_4 tetrahedra that are charge-neutralized by cations such as Na^+ or K^+. Using TEM, they detected iron-dense particles 20 – 300 nm in diameter in $+S^0$ *P. furiosus* cells (23). X-ray absorption spectra of the particles indicate a linear polymeric $(FeS_2^-)_n$ structure as in thioferrates; this includes four Fe-S interactions at 2.24 Å, two Fe-Fe interactions at 2.70 Å, and a long-range Fe-Fe interaction at 5.4 Å. The particles exhibit a broad isotropic EPR signal at g = 2.2 that displays anti-Curie Law behavior, also consistent with thioferrates. The EPR signal is observed only above 60 K, similar to the behavior of synthetic thioferrates. Moreover, the iron and sulfur from IssA-associated particles assemble into $[Fe_4S_4]$ clusters. Such clusters can transfer to apo-ferredoxin (in the presence of DTT), indicating that these thioferrate particles can be used in ISC assembly. Purified IssA monomers reportedly contain 38 Fe and 38 S atoms. A 20 nm diameter 3.5 MDa

thioferrate structure is calculated to contain ~ 6400 Fe atoms and ~ 170 IssA monomers. IssA contains only 1 cysteine per monomer raising issues as to how it coordinates such structures.

In this study, we have used primarily Mössbauer (MB) spectroscopy to analyze the iron content of ^{57}Fe-enriched WT and IssAΔ whole *P. furiosus* cells grown on the disaccharide maltose in the presence (+S^0) and absence (-S^0) of elemental sulfur. All ^{57}Fe ions in a sample are detectable by MB spectroscopy, with intensities that are roughly invariant per iron in the sample, regardless of the type of iron center. Thus, MB can be used to evaluate the ironome of these cells, albeit in semi-quantitative terms and only with "coarse-grain" resolution. Using this approach, we have previously evaluated the ironome of *Escherichia coli* (24), *Saccharomyces cerevisiae* (25), and human Jurkat cells (26). This is the first MB study of an archaeon, in this case one that is hyperthermophilic and strictly anaerobic.

Results

WT-S^0 cells harvested while growing exponentially

We began by collecting low-temperature low-field MB spectra of whole WT cells harvested while growing exponentially on maltose with 10 μM ^{57}Fe and without S^0 in the medium. The 5 K 0.05 T MB spectrum was dominated by a broad quadrupole doublet representing ca. 85% of the overall intensity (Figure B.1A). The structured lineshape of the doublet prompted us to decompose it into two partially-resolved sharper doublets, each with isomer shifts δ typical of oxidized S = 0 $[Fe_4S_4]^{2+}$ clusters (Table B.1). The doublets were simulated by the gold and brown solid lines of Figure 1. The quadrupole splitting ΔE_Q associated with the gold doublet was wider than that of the brown doublet, and so we

labeled them *wide* and *narrow* iron sulfur cluster *doublets* (ISC_W and ISC_N). Each doublet represented 35% - 45% of spectral intensity; the exact percentage due to each was difficult to assess because they were not well resolved. Considering that the spectrum represented *all* irons in the cell, including at least 15 different [Fe_4S_4]-containing proteins (Table S2), the ability to decompose all [Fe_4S_4] clusters into two doublets, each with relatively sharp linewidths, was remarkable. One extreme explanation was that 2 of the 15 [Fe_4S_4]-containing proteins in the cell dominated the iron content of the cell, with each protein corresponding to the two doublets. At the other extreme, each [Fe_4S_4]-containing proteins in the cell might have contributed equally to the spectrum but, for some unknown reason, segregated cleanly into these two spectral groups. Neither extreme seems likely but they illustrate the remarkability of the result.

Also remarkable was that δ and ΔE_Q for the two doublets were strongly temperature-dependent. At 150 K (Figure B.1B), ΔE_Q and δ for both doublets declined (Table B.1) but their linewidths did not increase. The temperature dependence of δ is mostly related to the second-order Doppler effect (27). The temperature-dependence of ΔE_Q is generally attributed to changes in the covalency of metal-ligand bonds. This can bring the separation between t_{2g} and e_g atomic orbitals close enough together that orbital populations can be affected by temperature, changing ΔE_Q.

Continuing with the extreme explanations offered above, this result would mean either that both dominant [Fe_4S_4] proteins exhibited this behavior, or that all 15 contributing [Fe_4S_4] proteins did so. This raises an intriguing speculation that $[Fe_4S_4]^{2+}$ clusters in hyperthermophilic organisms might generally possess low-lying excited states.

We wanted to determine whether these doublets arose from diamagnetic iron centers, as would be the case if they arose from $[Fe_4S_4]^{2+}$ clusters. Spectra were collected at 4.2 K and 0, 3, and 6 T applied magnetic fields (Figure B.1, C – E). The solid red lines overlaying the data were simulations that assumed diamagnetism and the δ and ΔE_Q values in Table B.1. The reasonable fits demonstrated that the $ISC_{W/N}$ doublets indeed arose from S = 0 $[Fe_4S_4]^{2+}$ clusters. This conclusion was reinforced by the large number of $[Fe_4S_4]$-containing proteins in these cell (Table SB.2). These spectra also show that virtually all redox-active $[Fe_4S_4]$ clusters in exponentially growing WT-S^0 cells are in the *oxidized* 2+ core state. $[Fe_4S_4]^{2+/1+}$ clusters typically have reduction potentials of ca. -400 mV vs. NHE, suggesting (by considering the Nernst equation) a cellular potential > ca. -340 mV.

After MB spectra were collected, the sample was thawed and, after EPR analysis (see below), the metal content was determined (Table SB.5). We assumed that 70% of the sample volume in the packed MB cup was due to the cells themselves and that the density of the sample was 1.00 g/ml. With these assumptions, we calculated that the sample contained 1.03 mM iron. If 2 $[Fe_4S_4]$-containing proteins dominated this group, their cellular protein concentrations would be ~ 120 µM each. On the other hand, if all 15 $[Fe_4S_4]$ proteins contributed equally, their the average cellular concentration would be ~ 17 µM which seems more likely.

WT-S^0 cells exhibited broad unresolved intensity barely distinguishable from the baseline between ca. -5 and +6 mm/s (Figure B.1A, arrows). This feature represented roughly 15% of the overall intensity and appeared to arise from a paramagnetic iron center. We overlaid the S^0-dependent thioferrate-like (TFL) magnetic material described below onto it, but the mismatch suggested a different type of magnetic iron (called “other

magnetic iron" in Table B.1). By 150 K, the associated magnetic hyperfine interactions collapsed completely into the spectral region occupied by the $ISC_{W/N}$ doublets (Figure B.1B). Importantly, we are not concluding that the absorption necessarily collapsed *into* the $ISC_{W/N}$ doublets at high temperature, only that it occupied/overlapped the same spectral region; more on this distinction below.

A small amount of a high-spin Fe^{II} doublet (~ 5%) was also evident in the 150 K spectrum of WT-S^0 cells (Figure B.1B, double arrow). A similar doublet was probably present in the 5 K spectrum (Figure B.1A), but it could not be distinguished from the "other magnetic" iron. The parameters associated with this doublet are typical of mononuclear and binuclear Fe^{II} sites in proteins with 5 – 6 O/N donor atoms (Table SB.2), as well as any low-molecular-mass Fe^{II} species with a similar ligand environment. There are few if any sulfur donors in the $Fe^{II}(O/N)_{5-6}$ sites. Given the overall iron concentration in the cell, this doublet represented ~ 50 µM $Fe^{II}(O/N)_{5-6}$ total in *P. furiosus* cells.

The 4.2 K 0 T spectrum of WT-S^0 cells in Figure B.1C exhibited two minor features. One was a line at ~ 2.6 mm/s which reflected an $Fe^{II}(O/N)_{5-6}$ doublet. This doublet was simulated by the blue solid line above the spectrum at 15% intensity. The broad non-symmetrical shape of the high-energy line suggested at least two $Fe^{II}(O/N)_{5-6}$ sites. The second minor feature, simulated by the solid green line, was a pattern barely distinguishable from the baseline that suggested a high-spin Fe^{III} species. The putative S = 5/2 species was most evident at 6 T (Figure B.1E) where it represented ~ 15% of overall spectral intensity.

The EPR spectrum of the sample (after thawing the MB sample and transferring it to an EPR tube) exhibited a signal at g = 4.3 which probably originated from the same species (Figure B.2, bottom). It also exhibited an isotropic signal at g = 2.00 but little

intensity at g = 1.94 which is consistent with MB spectra showing that the [Fe_4S_4] clusters in the cell were primarily in the diamagnetic 2+ core oxidation state.

The most surprising aspect of the Figure B.1C spectrum was that the sample used to generate it was identical to that of Figure B.1, A and B - only that it had been stored without thawing in a liquid N_2 dewar for ~ 3 months. Since the $ISC_{W/N}$ doublets were unaffected, iron species other that the clusters affording the $ISC_{W/N}$ doublets (perhaps the "other magnetic" iron) must have reacted slowly in frozen cells to generate the observed high-spin Fe^{II} and Fe^{III} spectral features in Figure B.1, C - E. The S = 5/2 Fe^{III} feature is probably an artefact as we have not observed similar features in other spectra. In contrast, $Fe^{II}(O/N)_{5\text{-}6}$ features were often observed under various conditions, and thus are likely physiologically relevant.

WT+S^0 cells harvested while growing exponentially

Another batch of *P. furiosus* cells was grown in the same medium except under +S^0 conditions. They were also harvested while growing exponentially. The low-temperature low-field MB spectrum of the WT+S^0 cells (Figure B.3A) was dominated by broad absorption that extended from ca. -6 mm/s to +7 mm/s velocity. Given previous studies showing large quantities of TFL material in +S^0 cells, we assigned it to this material. Consistent with that assignment, the EPR spectrum of cells in this state lacked a significant g = 4.3 signal (Figure B.2, top spectrum), indicating the absence of magnetically isolated high-spin S = 5/2 Fe^{III} paramagnetic material in the sample.

The spectrum exhibited two strong absorption lines in the same region of the $ISC_{W/N}$ doublets in WT-S^0 spectra, and this unfortunately created ambiguity for our analysis. It implies that some proportion of the intensity of these two lines arose from the

$ISC_{W/N}$ doublets while the remainder was associated with the TFL material. Based on our simulations and analyses, we estimate that at least 10% and no more than 25% of the spectral intensity arose from the $ISC_{W/N}$ doublets in WT+S^0 spectra. The relative intensity of the two contributions was kept constant in the 3.0 and 6.0 T spectra (Figure B.3, C and D) with 20% of the intensity attributed to the $ISC_{W/N}$ doublets in the 6.0 T spectrum. The solid green lines in Figure B.3, A, C, and D simulated the $ISC_{W/N}$ doublets at the 20% intensity level.

Magnetic hyperfine interactions associated with the TFL material were absent in the WT+S^0 spectrum at 150 K (Figure B.3B), and the intensity associated with this material collapsed into the same region that was occupied by the $ISC_{W/N}$ doublets in WT-S^0 spectra. The intensity of the ISC_W doublet increased from ~ 10% at 5 K to 33% at 150 K. The intensity of ISC_N increased from ~ 10% at 5 K to 65% at 150 K. Thus, 30% of the TFL material collapsed over the ISC_W doublet while 70% collapsed over the ISC_N doublet. None of the TFL material collapsed into features characteristic of Fe^{II} ions.

The 150 K MB spectrum of the WT+S^0 sample did exhibit a minor broad $Fe^{II}(O/N)_{5\text{-}6}$ doublet, representing ~ 4% of spectral intensity (Figure B.3B, arrow). This doublet required two species for fitting, using parameters of mononuclear Fe^{II} species coordinated by 5-6 O/N and no S ligands (Table B.1). These $Fe^{II}(O/N)_{5\text{-}6}$ sites are independent of the TFL material but became apparent once the hyperfine interactions associated with the TFL material collapsed.

We were initially surprised that the TFL magnetic material in WT+S^0 cells had isomer shift and quadrupole splitting parameters (56% δ = 0.37 mm/s and ΔE_Q = 0.75 mm/s; 44% δ = 0.42 mm/s and ΔE_Q = 1.15 mm/s) that were indistinguishable from those

due to the S = 0 $[Fe_4S_4]^{2+}$ clusters in the WT-S^0 cells, given that the low-temperature magnetic properties of the two types of iron species were entirely different. This coincidence probably arose because the local structures of the two types of iron species were remarkably similar. Authentic sodium thioferrate ($NaFeS_2$) exhibits δ = 0.36 mm/s and ΔE_Q = 0.58 mm/s (28), which are similar to those of the TFL material *AND* $[Fe_4S_4]^{2+}$ clusters in these cells. Thioferrates consist of anionic linear chains of $((Fe^{III}S_2)^-)_n$ units, with each Fe^{III} ion coordinated by a tetrahedral environment of sulfide ligands with Na^+ or K^+ counter ions. Likewise, each iron of $[Fe_4S_4]$ clusters are locally coordinated by four sulfur ligands in a tetrahedral environment. The average formal oxidation state of iron in $[Fe_4S_4]^{2+}$ clusters is +2.5, with one delocalized electron shared by two irons in a "mixed-valence" $[Fe^{II}\ Fe^{III}]$ pair (the two pairs of a cluster are then antiferromagnetically coupled to generate the S = 0 system spin). There were clearly no localized $Fe^{II}(S)_4$ sites with sulfur donor sites in the TFL material, since otherwise an intense quadrupole doublet with $\delta \sim 0.7$ mm/s and $\Delta E_Q \sim 3$ mm/s (similar to reduced rubredoxin) would have been observed in the 150 K spectrum of Figure B.3B. On the other hand, some *delocalized* $[Fe^{II}\ Fe^{III}]$ units might have contributed to the TFL structure.

We had hoped that high-field spectra of the WT+S^0 sample would have been sufficient to break the magnetic coupling responsible for the broadness and poor resolution of the magnetic material in low fields, but this was not observed. The spectra at 4.2 K and 0, 3, and 6 T perpendicular applied fields included contributions from both the magnetically-ordered iron and ISCs (Figure B.3, A, C and D). The ISC contribution was calculated as described in *Experimental Procedures*. The known external field and isomer

shift were used to calculate the ISC portion of the spectrum so that in the fitting interaction only the area of this contribution was varied.

Technical Details regarding the physical properties of the TFL material in WT+S^0 cells

The following technical aspects can be skipped without losing the major conclusion that the thioferrates-like material is similar to authentic thioferrates but with some subtle differences. This section provides details of those differences.

The magnetic part of the spectra (Figure B.3A, C and D in red) was modelled with a histogram of hyperfine sextets over a range of effective hyperfine fields in steps of 1 T. The resulting histograms are presented in Figure B.3 E, F and G. Small variations in □□and quadrupole line shift 2□ have been used to approximate the spectral asymmetry of the magnetic part. 2ε is similar to ΔE_Q but it includes an angular dependence, even when the general asymmetry parameter that is absent in ΔE_Q, $\eta = 0$ (27).

These were assumed linear in the effective hyperfine field over the fitted range. The intensities of each sextet were then used to calculate the distribution $P(B_{hf})$. The angle Θ of the hyperfine field B_{hf} with respect to the gamma radiation determines the line intensity ratio A_{23} between line pair 2 and 5 (nuclear transition with $\Delta m = 0$) to 3 and 4 (transitions with $\Delta m = \pm 1$), which can vary between 0 (for Θ = 0; moments parallel to the gamma ray) and 4 (for Θ = 90°) according to the equation

$$A_{23} = \frac{4\sin^2\Theta}{1+\cos^2\Theta}$$

(27). An isotropic distribution of directions yields a ratio of 2, similar to what was observed (Figure B.4). In these experiments, the external magnetic field was perpendicular to the gamma rays. Thus, we can assume rotational symmetry around the field but not around the

gamma ray direction. Useful relations for simple cases of magnetic texture have been described (29, 30).

Several changes are expected when a magnetic field is applied to a magnetically ordered system. First for a ferromagnet or ferrimagnet, the magnetic moments should align parallel to the field. An antiferromagnet will align perpendicular to the field as long as the crystalline anisotropy is not too large. Since the orbital component of the Fe^{III} ions moments is zero (with the ground state configuration $[Ar]3d^5$ having L=0, S=5/2), the crystalline anisotropy is small compared to Fe^{II} (with $[Ar]3d^6$ and L=2, S=2). Then depending on orientation, the external field would add vectorially to the local hyperfine field (which for Fe^{III} is antiparallel to the local moment). If, as we shall see below, moments do not realign in a large magnetic field, either the crystalline anisotropy is large (for example with Fe^{II}) or the magnetic interactions are *frustrated*. Frustration can be caused by competing exchange interactions that cannot all be satisfied, leading to complicated magnetic ground states (31). A Gaussian distribution was assumed for the remaining magnetic part as described by the average value $<B_{hf}>$ and standard deviation □. We also simulated the spectra with an unconstrained histogram distribution and the results were similar though the overall distributions were somewhat more variable from one spectrum to the next.

The indicated effective hyperfine field (Figure B.3, right side) was the vector sum of the true local hyperfine field and the external field. The area of the $ISC_{W/N}$ contribution (green line) was varied to minimize χ^2 error-residuals. The $ISC_{W/N}$ doublets represented 20% of the overall intensity. The calculated distributions of hyperfine fields for all three spectra were centered at $<B_{hf}> \sim 24$ T with a Gaussian standard deviation of $\sigma = 6$ T. The

distribution was essentially invariant up to a 6 T applied field. In addition, the relative intensities of lines 2 (and 5) with respect to lines 3 (and 4) did not change with applied fields, staying essentially equal to 2 up until at least 6 T (Figure B.4). This indicates that the magnetic system is remarkably rigid. In the case of Fe^{III}, this rigidity is unlikely to be due to crystalline anisotropy. A more likely explanation is that it arises from the frustration of the magnetic exchange interactions. Such processes are known for systems with antiferromagnetic interactions dominated by site-disorder or triangular lattices. In the current case, it seems more likely that the origin of the frustration is antiferromagnetic interactions and site disorder, similar to the properties of canonical spin glasses (31), or a disordered superparamagnetic material below the blocking temperature T_{BK}.

In contrast, the equivalent high-field low-temperature spectra of thioferrates exhibits a well-resolved six-line pattern (32). A similar six-line pattern is also observed for thioferrates in spectra collected at zero or low applied field. Thus, the magnetically ordered material in *P. furious*, obtained in WT+S^0 cells, does not have exactly the same magnetic properties as synthetic Na^+/K^+ thioferrates even though the high-temperature MB parameters are similar.

Superparamagnetic materials exhibit anti-Curie Law behavior and can be characterized by its T_{BK}. T_{BK} is operationally defined as the temperature at which half of the spectral intensity exhibits magnetic hyperfine interactions and half is collapsed into quadrupole doublets. To determine this for the TFL magnetic material in *P. furiosus*, we collected spectra at various temperatures (Figure B.5). Temperatures as high as ca. 135 K were required for all magnetic material to collapse into doublets; from this we estimated $T_{BK} \approx 40$ - 50 K. In contrast, all magnetic material in spectra of synthetic thioferrates is

collapsed between 4.2 K and 77 K (28), implying a slightly lower T_{BK}. This is another indication that the magnetic properties of the TFL material in *P. furiosus* differed in subtle ways from synthetic thioferrates.

To summarize these technical comments, the TFL material exhibits some magnetic properties that are similar to authentic thioferrates, but there are some physical/ spectroscopic differences. We are unable to interpret these differences in an unambiguous manner to propose a chemically-defined structure for this novel material, so we can only conclude that it is thioferrate-*like*.

After collecting these spectra, the sample was thawed and the metal contents determined (Table SB.5). The iron concentration in the WT+S^0 sample was 5.25 mM – about 5-fold higher than the WT-S^0 sample. Most or all of this additional iron was due to the TFL iron described above. If the expression levels of the [Fe_4S_4]-containing proteins were unchanged with the added sulfur, ca. 20% of the spectral intensity should have been $ISC_{W/N}$ doublets. This is within our estimate of 10% - 20%. Our data (weakly) support a slight decline in the expression levels of the [Fe_4S_4]-containing proteins when S^0 is included in the medium. Also noteworthy is that WT+S^0 cells contained significantly higher concentrations of Cu, Mn, and Zn than WT-S^0 cells (Table SB.5) indicating a widespread S^0-dependent shift in metal-associated processes.

WT Cells harvested in stationary state

We next collected MB spectra of WT cells grown as above, with and without S^0, but harvested at stationary state. Both 5 K and 150 K MB spectra of WT-S^0 cells (Figure B.6, A and B) were dominated by $ISC_{W/N}$ doublets that collectively accounted for ca. 75% of spectral intensity. Also evident were overlapping doublets due to at least two types of

$Fe^{II}(O/N)_{5-6}$ species. Their collective intensity was ca. 23%, significantly greater than for samples harvested during exponential growth. No magnetic material was evident and the only intense feature in the corresponding EPR spectrum was an isotropic signal at g = 2.00.

A minor $Fe^{II}(S)_4$ species was evident in the 150 K spectrum (Figure B.6B), as indicated by the arrow which highlights the low-energy line of the corresponding doublet. The solid green line simulates this species using parameters in Table B.1. The doublet represented only ~2% of spectral intensity but we observed it in multiple spectra. Such doublets are typical of Fe^{II} ions coordinated by a tetrahedral environment of sulfur donors. *P. furiosus* contains 2 proteins with such $Fe^{II}(S)_4$ sites, rubredoxin and rubrerythrin (Table SB.3).

The 5 K spectrum of WT+S^0 stationary state cells (Figure B.6C) was similar to that of exponentially growing WT+S^0 cells in that it was dominated by a broad feature spanning from -6 mm/s to +7 mm/s. This feature was assigned to the TFL material. Two intense lines near the center of the spectrum had parameters of $ISC_{W/N}$ doublets; they collectively represented no more than ~ 25% of spectral intensity as some portion of this was due to TFL material (Figure B.6C).

The magnetic hyperfine interactions associated with the TFL material were abolished at 150 K (Figure B.6D), with the intensity from this material collapsing over the $ISC_{W/N}$ doublets. As was observed with high-temperature spectra of exponentially grown cells, the ISC_N doublet became relatively more intense than the ISC_W doublet indicating that the TFL magnetic material collapsed mainly over the ISC_N doublet. A broad $Fe^{II}(O/N)_{5-6}$ doublet was also evident in the 150 K spectrum (arrow in Figure B.6D). Its

intensity (~ 4%) was similar for the WT+S^0 sample harvested under exponential conditions but less than for the WT-S^0 sample harvested in stationary state.

After these spectra were collected, samples were thawed and analyzed for metal content. The iron concentrations in WT-S^0 and WT+S^0 cells were 660 µM and 8700 µM, respectively (Table SB.5). If the average expression level of [Fe_4S_4]-containing proteins remained unchanged with the addition of elemental sulfur, ~ 7% of the spectral intensity of Figures B.6, C and D would be due to $ISC_{W/N}$. Our fitting analysis suggests slightly higher percentage range, namely 10% - 25%.

ΔIssA cells

The gene encoding the IssA protein is highly expressed under +S^0 conditions and IssA is thought to be intimately involved in forming TFL nanoparticles. To investigate this further, we grew cells that lacked the gene encoding this protein, the ΔIssA strain, to determine whether it could form TFL iron. We first grew the deletion strain on the same medium as for WT-S^0 cells, and harvested cells during exponential growth as a control. Their 10 K 0.05 T MB spectrum (Figure B.7A) was dominated by the $ISC_{W/N}$ doublets (~80% total). The spectrum also exhibited a broad doublet due to at least 2 $Fe^{II}(O/N)_{5-6}$ species, representing 12% of the overall intensity (double arrows on the right), and to a minor $Fe^{II}(S)_4$ doublet representing ~ 3% of the intensity (single arrows). The 150 K spectrum (Figure B.7B) exhibited the same features, with the temperature-dependence of the $ISC_{W/N}$ doublets visually apparent and both Fe^{II} doublets better resolved. The 4.2 K 6.0 T spectrum (Figure B.7C) was simulated assuming that the $ISC_{W/N}$ doublets were diamagnetic, confirming that they arose from S = 0 $[Fe_4S_4]^{2+}$ clusters.

ΔIssA+S^0 cells were grown and harvested similarly. Their low-temperature MB spectra exhibited an intense six-line spectra at all applied fields (Figure B.8, A – C). Most or all of the spectral intensity arose from the TFL material. The peaks were better resolved than the corresponding spectral features in the WT+S^0 spectra, implying some IssA-dependent structural differences. Surprisingly, the positions of the lines were *unaffected* by applied fields as high as 6.0 T, though the linewidths broadened with increasing field. This implied that the magnetic coupling between particles in the material was significantly stronger than the applied fields and could not be broken at 6 T.

Technical Details regarding the Physical properties of the TFL material in ΔIssA+S^0 cells

Again, the following are technical details that can be skipped without loss of continuity. There were several differences in the magnetism of the ΔIssA+S^0 sample compared to the WT+S^0 exponential sample. Specifically, the extent of broadening of the distribution with external field was greater, and there was a gradual change in the relative line intensity A_{23} (Figure B.4).

Antiferromagnets orient perpendicular to an external field when the crystalline anisotropy is not excessive. In that case all moments would be in a plane that includes the gamma rays. Kuncser et al. (29,30) has given several expressions for A_{23} in different cases. Using their result for moments in a plane with the gamma ray (see Ref 30, Eq. 7'), we obtain $A_{23} = 4/3 = 1.33$, which is about what is observed for an external field of 6 T. Thus, the interactions appear to be strongly antiferromagnetic but with less crystalline anisotropy or frustration than in the WT+S^0 exponential sample.

We also collected low-field spectra at increasing temperatures (Figure B.9) to observe the loss of magnetic hyperfine interactions. Both with Gaussian and Histogram

models were fitted to the spectra. Average results for the two methods (average B_{hf}, width of the distribution $P(B_{hf})$) were similar. Fits assuming the Gaussian model broadened dramatically at 55 K, caused by a strong increase of a low field component. T_{BK} was ~ 50 K, similar to that obtained for the TFL nanoparticles in WT+S^0 cells. Determining the magnetic component for temperatures above 55 K was difficult due to overlap with the $ISC_{W/N}$ components. However, the transition with increasing temperatures was similar to the superparamagnetism observed in fine grains (33). The linewidths for $ISC_{W/N}$ components remained remarkably sharp with increasing temperatures (Table B.1).

In summary, these technical details describe how the TFL nanoparticles in ΔIssA+S^0 cells are somewhat different from those in WT+S^0 cells. Again, we are unable to interpret those differences in unambiguous chemical/structural terms apart from concluding that the material is more crystalline/homogenous in the absence of IssA.

After spectra were collected, the sample were thawed and cellular metal and overall protein concentrations were determined; the protein concentrations in ΔIssA-S^0 and ΔIssA-S^0 samples were 78 ± 3 mg/ml and 36 ± 2 mg/ml, respectively. Metal concentrations are in Table SB.5.

Growth Experiments

Two roles have been proposed for IssA; that it is involved in Fe storage, or that it serves to detoxify insoluble FeS clusters (22,23). In order to test the role of IssA in Fe storage, WT cells were harvested after growth under +S^0 and -S^0 conditions, and ΔIssA under +S^0 conditions. The harvested cells were washed and used to inoculate iron-depleted medium; if IssA binding of TFL aggregates serves to increase the bioavailability of the iron, only WT+S^0 cells should have grown in this iron-depleted medium. However, there was no

growth in any of the iron-depleted medium, no matter what cells were used to inoculate the medium (data not shown).

To test whether IssA is used to detoxify insoluble Fe/S aggregates, WT and ΔIssA strains were grown with and without adding 50 μM iron in both 10 mM sodium sulfide medium (low IssA expression, Figure B.10A) and 1 g/l S^0 medium (High IssA expression, Figure B.10B). Under low sulfide concentrations, all strains grew to similarly high cell protein concentrations in culture (~90 μg/ml), suggesting that high iron concentrations by themselves are not toxic to the cell. On the other hand, under + S^0 (high sulfide) conditions, increasing the Fe concentration led to a significant decrease in growth in both WT and ΔIssA strains. Additionally, the ΔIssA strain only reached half the cell protein concentration as WT under normal (10 μM) Fe conditions, suggesting that IssA sequesters iron, in the presence of sulfur, that would otherwise be toxic.

Discussion

Our results demonstrate that the iron content or ironome of *P. furiosus* cells changes dramatically when elemental sulfur is added to the growth medium. Under -S^0 conditions, most of the iron in the cell is S = 0 $[Fe_4S_4]^{2+}$ clusters. Under +S^0 conditions, the cell imports ~ 5 times more iron, with 75-90% eventually forming TFL aggregates. Some of the iron in WT+S^0 cells must have been in the form of $[Fe_4S_4]^{2+}$ clusters, but quantifying how much was in this form proved difficult because the MB spectral features of TFL iron were indistinguishable from those of $[Fe_4S_4]^{2+}$ clusters at high temperatures, and at low temperatures, the contribution of diamagnetic $[Fe_4S_4]^{2+}$ clusters was obscured by the dominating magnetic features of the TFL aggregates. Simulations of the low-temperature spectral pattern of the ΔIssA+S^0 cells indicated that the $[Fe_4S_4]$ contribution was negligible.

All things considered, we tentatively conclude that the overall expression level of [Fe_4S_4]-containing proteins *decreases* somewhat under $+S^0$ conditions. This supports a shift in cellular metabolism when elemental sulfur is present. [Fe_4S_4]-containing hydrogenases are down-regulated under $+S^0$ conditions (13), and cells grow faster under $+S^0$ conditions as long as sufficient iron is included in the growth media. We also found that concentrations of other metals (Cu, Mn, Zn) were significantly higher in cells grown under $+S^0$ conditions, again indicating major metal-associated metabolic changes.

We characterized the TFL iron in $+S^0$ cells. This material is closely related to authentic thioferrates in that both synthetic thioferrates and the TFL iron consist predominantly of Fe^{III} ions coordinated to four sulfide ions in a tetrahedral geometry. Neither form of iron contains *localized* $Fe^{II}(S)_4$ units, but we cannot exclude the possibility that TFL iron includes some *delocalized* [Fe^{II} Fe^{III}] units. This situation is found in [Fe_4S_4] clusters which have virtually the same δ and ΔE_Q values as TFL iron.

At low temperatures, authentic sodium thioferrate ($NaFeS_2$) exhibits a well-resolved sextet including magnetic hyperfine interactions of magnitude 270 kG (28). This hyperfine field is unusually small for ferric ions due to a high degree of covalency with sulfur. Using MB spectroscopy, Zink and Kargony (32) examined authentic $KFeS_2$ at variable applied perpendicular fields up to 5 T. At all applied fields, synthetic thioferrates displayed a sextet that was not strongly affected by the field. Similarly, the TFL material in both WT+S^0 and ΔIssA+S^0 cells was not strongly affected by applied fields up to 6 T. This suggests even stronger interactions in TFL iron than in synthetic thioferrates. The spectra again show line-splittings characteristic of magnetic ordering including line

broadening typical of a continuous distribution of hyperfine fields. ΔIssA+S^0 spectra were analyzed assuming no ISC contribution.

One of the most surprising conclusions from this work is that the IssA protein is NOT required for forming TFL particles as these particles formed in *P. furiosus* cells lacking IssA. In fact, the spectral properties of TFL particles in the absence of this protein were closer to synthetic thioferrates as they exhibited a well-resolved six-line pattern at 5 K. The poorer spectral resolution associated with the TFL material in WT+S^0 cells may be due to a more heterogeneous distribution of TFL structures. We considered that IssA disrupts the thioferrate structure, perhaps making the material more bioavailable to the cell, but it does not appear to do so.

We also examined the temperature-dependence of hyperfine interactions, and used both Gaussian and Histogram models to fit the spectra. Average results for the two methods (average $<B_{hf}>$, width of the distribution P(Bhf)) were similar. Fits assuming the Gaussian model broadened dramatically at 55 K, caused by a strong increase of a low-field component. Determining this component for temperatures above 55 K was made difficult by the overlap with the $ISC_{W/N}$ components. However, the transition with increasing temperatures was similar to the superparamagnetism of fine grains (33).

By 77 K, these interactions are fully abolished in synthetic thioferrates whereas some interactions remained at this temperature in the *P. furiosus* TFL aggregates. T_{BK} of the TFL material is thus slightly higher than for authentic thioferrates. T_{BK} reflects the size of the magnetically interacting particles, suggesting somewhat larger particles for TFL material in +S^0 *P. furiosus* cells.

Exponentially growing *P. furiosus* -S^0 cells contained only 2 - 5% high-spin $Fe^{II}(O/N)_{5-6}$ sites. In contrast, *E. coli* and *B. subtilis* (Gram negative and positive bacteria) contain substantially higher concentrations of such species (24). The percentage of $Fe^{II}(O/N)_{5-6}$ in *P. furiosus* -S^0 cells increased as they shifted from exponential to stationary state. We hypothesize that imported Fe^{II} is used to assemble and install ISCs into proteins and to metallate proteins with mononuclear Fe and Fe-O-Fe active sites. Perhaps the rates of these assembly and metallation activities decline in stationary state, causing the Fe^{II} feedstock to accumulate. Under +S^0 conditions, the demand for imported Fe^{II} may be greater (for use in generating large amounts of TFL iron), causing the level of Fe^{II} in such cells to remain low under stationary state conditions.

P. furiosus –S^0 cells also contain a small percentage contribution of $Fe^{II}(S)_4$ sites, corresponding to roughly 10 – 40 μM cellular iron. A similar concentration might be present in +S^0 cells but such sites could not be detected (likely due to the higher concentration of cellular iron). Table B.S2 indicated just two proteins that contain such sites, namely rubredoxin and rubrerythrin. This suggests an average cellular concentration of roughly 10 μM each for these proteins.

The TFL material was thought to store iron, coordinated by IssA protein in large assemblies reminiscent of how Fe^{III} is stored in ferritins (23), but other possibilities should now be considered. It seems unlikely that +S^0 cells would store huge amounts of iron, while -S^0 cells would store none, even when both are grown under the same iron-replete conditions. Our experiments have shown that cells in which iron is stored as IssA-bound thioferrate cannot use it as an iron source when transferred to iron-depleted medium. In contrast, *E. coli* cells accumulate large amounts of iron as Fe^{II} (perhaps for storage), yeast

accumulates Fe^{III} polyphosphate in vacuoles (34), and human cells store Fe^{III} as nanoparticles in ferritin cores (26). As a strict anaerobe, *P. furiosus* may not need to store much iron since Fe^{II} dominates the environment under anaerobic conditions and is far more soluble (and thus more bioavailable) than Fe^{III} under the more common aerobic conditions.

Clarkson et al. suggested that IssA is used to sequester insoluble iron sulfides that may be toxic to the cell, as IssA expression is sulfide specific and dependent on the presence of iron (22). The growth experiments conducted in this study support this hypothesis, as high Fe concentrations had no effect on growth of either the parent or ΔIssA in the absence of sulfide, and while iron was still predominantly stored as TFL material in the absence of IssA, the ΔIssA strain showed a significant negative growth phenotype compared to the parent under high sulfide and high Fe conditions.

In light of this, we tentatively propose a new role of TFL iron in the metabolism of *P. furiosus* (Figure B.11). Cells grown under $-S^0$ conditions use membrane-bound hydrogenase as a redox-dependent proton pump to generate a Na^+ ion gradient that is subsequently used to generate ATP via chemiosmosis. Here, H^+ ions are used as the terminal electron acceptor in the electron transport chain, using reducing equivalents that originated from the oxidation of either peptides or carbohydrates and then channeled through ferredoxin. Imported Fe^{II} is used to generate $[Fe_4S_4]$ clusters, among other processes, and these are installed into various apo-proteins including hydrogenases.

Under $+S^0$ conditions, the expression level of membrane-bound MBH decreases, the expression level of membrane-bound MBS increases (Table SB.3), and the rate of Fe^{II} import increases. Using reducing equivalents also obtained from peptides or carbohydrates (and also trafficked through the ferredoxin), sulfane sulfur reductase catalyzes the

reduction of imported polysulfides. Thus, polysulfides serve as the terminal electron acceptor in this form of anaerobic respiration, replacing protons under $+S^0$ conditions. We speculate that free short polysulfide chains are toxic to the cell, and that they react with Fe^{II} to generate the TFL material which, when bound to IssA, is less toxic to the cell. In essence, TFL iron might be a waste product of S^0-dependent anaerobic respiration. As the cell grows, its volume increases along with an increasing concentration of the TFL iron such that the net balance of the opposing processes results in 5 – 9 mM cellular iron concentration. The rate of $[Fe_4S_4]$ synthesis may decline under $+S^0$ conditions because demand is reduced. It is intriguing to consider that this may have been an ancient respiratory pathway that dominated the early Earth in locations where elemental sulfur and ferrous ions were abundant but O_2 pressures were low.

Experimental Procedures

Cell growth

Strains used in this study are listed in Table SB.6. Cultures for MB experiments were grown in defined maltose media composed of 1× base salts, 1× trace minerals, 1× vitamin solution, 2× 19-amino-acid solution, 0.5% (wt/vol) maltose, 0.1% (wt/vol) yeast extract, 10 µM sodium tungstate, and 0.25 mg/ml resazurin, with added cysteine at 0.5 g/l, sodium bicarbonate at 1 g/l, and 1 mM sodium phosphate buffer (pH 6.8). The 5× base salts stock solution contained (per liter) 140 g of NaCl, 17.5 g of $MgSO_4 \cdot 7H_2O$, 13.5 g of $MgCl_2 \cdot 6H_2O$, 1.65 g of KCl, 1.25 g of NH_4Cl, and 0.70 g of $CaCl_2 \cdot 2H_2O$. The 1000× trace mineral stock solution contained (per liter) 1 ml of HCl (concentrated), 0.5 g of Na_4EDTA, 0.05 g of H_3BO_3, 0.05 g of $ZnCl_2$, 0.03 g of $CuCl_2 \cdot 2H_2O$, 0.05 g of $MnCl_2 \cdot 4H_2O$ 0.05 g of $(NH_4)_2MoO_4$, 0.05 g of $AlK(SO_4) \cdot 2H_2O$, 0.05 g of $CoCl_2 \cdot 6H_2O$, and 0.05 g of $NiCl_2 \cdot 6H_2O$.

The 200× vitamin stock solution contained (per liter) 10 mg each of niacin, pantothenate, lipoic acid, *p*-aminobenzoic acid, thiamine (B_1), riboflavin (B_2), pyridoxine (B_6), and cobalamin (B_{12}) and 4 mg each of biotin and folic acid. The 25× 19-amino-acid solution contained (per liter) 3.125 g each of arginine and proline; 1.25 g each of aspartic acid, glutamine, and valine; 5.0 g each of glutamic acid and glycine; 2.5 g each of asparagine, histidine, isoleucine, leucine, lysine, and threonine; 1.875 g each of alanine, methionine, phenylalanine, serine, and tryptophan; and 0.3 g tyrosine. ^{57}Fe was added from a 50 μM stock solution prepared by dissolving 6 mg of elemental ^{57}Fe in 200 μl of a 1:3 HNO_3:HCl mixture. The $+S^0$ conditions contained added S^0 at 3 g/liter.

500 mL cultures were grown anaerobically in 1 liter culture bottles at 90 ℃ with shaking. Cells were harvested at the desired timepoints by centrifugation at 18,000×g for 10 minutes in a Beckman-Coutler Avanti J-30i centrifuge. The cell pellets were washed 3× with 2× base salts containing 50 μM sodium dithionite. Cells were loaded into MB cups and frozen at -80 ℃.

For additional growth experiments, the medium was prepared as described above but with the following substitutions: yeast extract and Fe^{57} were omitted from the medium, $FeCl_3$ was added from a 10 mM stock solution, and 50 mM 3-(N-morpholino)propanesulfonic acid (MOPS) was added. For FeS toxicity experiments, sulfide (as Na_2S) or S^0 were added as indicated. Strains were grown in 50 mL culture bottles at 90 ˚C with shaking. For iron bioavailability experiments, cultures were first grown in medium containing 10 μM iron with (WT and ΔIssA) and without (WT only) 3 g/L added S^0. Cultures were harvested by centrifugation at 18,000×g for 10 min in a Beckman Coulter Microfuge 22 Centrifuge. Cell pellets were washed 3× in 20 mM imidazole pH 6.5

containing 30 mM $MgCl_2 \cdot 6H_2O$, 0.5 M KCl, 2 mM cysteine-HCl, 2 mM dithionite, and 2 mM dithiothreitol and resuspended in the same buffer. Cell suspensions were used to inoculate defined medium containing an additional 30 μM bathophenanthroline disulfonic acid. For both growth experiments, 1 ml culture samples were taken at desired time intervals, and cell protein was measured using a standard Bradford protein assay.

Mössbauer and EPR Spectroscopies

Low-field MB spectra were collected using a model MS4 spectrometer (SEE Co., Edina MN). High-field spectra were collected at 4.2 K using a model L: He-6T spectrometer. Spectra were analyzed using WMOSS software. In spectra that contains both TFL iron and ISC doublets, the doublets were simulated using a spin Hamiltonian model (SpinHam option in WMOSS) using parameters obtained from spectra that did not contain TFL iron. Then, the area of the doublets was allowed to vary in the WinNormos program keeping all other parameters (including hyperfine) constant. Isomer shifts are reported relative to □-Fe foil at room temperature. Following MB analysis, samples were thawed in an anaerobic glovebox, transferred into EPR tubes, and refrozen. Continuous-wave X-band EPR spectra were collected using a Bruker Elexsys E500A spectrometer with a cryogen-free cooling system.

Metal and Protein Analyses

After spectra were collected, samples were thawed and transferred quantitatively to pre-weighed 15 ml Falcon tubes. Samples were resuspended in 5 mg deionized H_2O per gram of cells. Two mg of 0.5 mm diameter glass beads (Sigma) were added per mg of resuspended cell pellet, and the mixture was vortexed 3× for 30 s followed by 1 min on ice. The resulting lysate was centrifuged at 14000×g and the protein concentration of the

supernatant was determined using the Pierce BCA Protein Assay Kit (Thermoscientific). To the same supernatant was added an equal volume of trace-metal grade nitric acid, and the solution was sealed and heated overnight at 80 ^{o}C. Samples were diluted with distilled deionized water and analyzed by ICP-MS (Agilent 7700x).

Data Availability Statement

All data are contained within the manuscript and SI.

Acknowledgments

This work was supported by the National Institutes of Health (GM127021 to PAL), the National Science Foundation (MCB-1817389), the Robert A. Welch Foundation (A1170), and the Division of Chemical Sciences, Geosciences and Biosciences, Office of Basic Energy Sciences of the Department of Energy (DE-FG02-95ER20175 to MWWA). The content is solely the responsibility of the authors and does not necessarily represent the official views of the National Institutes of Health, the National Science Foundation, the Welch Foundation or the Department of Energy. We thank Dr. Francis Jenney for the gift of ^{57}Fe.

Conflict of Interest

The authors declare that they have no conflicts of interest with the contents of this article.

Footnotes

To whom corresponding should be addressed: Paul A. Lindahl, Department of Chemistry, Texas A&M University, College Station TX 77843-3255. Phone, 979-845-0956 ; Fax, 979-845-4719, email: Lindahl@chem.tamu.edu.

[1]Texas A&M University, Department of Biochemistry and Biophysics, College Station, TX 77843 USA.

[2]Department of Biochemistry and Molecular Biology, University of Georgia, Athens GA 30602 USA.

[3]Faculty of Physics, University of Duisburg-Essen, 47057 Duisburg, Germany and Institute of Nanotechnology, Karlsruhe Institute of Technology, 76344 Eggenstein-Leopoldshafen, Germany.

[4]Texas A&M University, Department of Chemistry, College Station, TX 77843 USA.

[5]The abbreviations used are: EPR, electron paramagnetic resonance; ISC, iron sulfur cluster; MB, Mössbauer; $+S^0$, growth that includes elemental sulfur; $-S^0$, growth the excludes elemental sulfur; T_{BK}, Blocking temperature; TFL, thioferrate-like; WT, wild type.

References

1. Fiala, G., and Stetter, K.O. (1986) *Pyrococcus furiosus* sp. nov represents a novel genus of marine heterotrophic archaebacteria growing optimally at 100°C. *Arch. Microbiol.* **145**, 56–61.

2. Cvetkovic, A., Menon, A.L., Thorgersen, M.P., Scott, J.W., Poole, F.L., Jenney, F.E., Lancaster, W.A., Praissman, J.L., Shanmukh, S., Vaccaro, B.J., Trauger, S.A., Kalisiak, E., Apon, J.V., Siuzdak, G., Yannone, S.M., Tainer, J.A., Adams, M.W.W. (2010) Microbial metalloproteomes are largely uncharacterized. ***Nature*** **466**, 779-U18 **DOI:** 10.1038/nature09265

3. Lancaster, W.A., Praissman, J.L., Poole, F.L., Cvetkovic, A., Menon, A.L., Scott, J.W., Jenney, F.E., Jr., Thorgersen, M.P., Kalisiak, E., Apon, J.V., Trauger, S.A., Siuzdak, G., Tainer, J.A., Adams, M.W.W. (2011) A computational framework for proteome-wide pursuit and prediction of metalloproteins using ICP-MS and MS/MS data. *BMC Bioinformatics*, **12**, 64 DOI: 10.1186/1471-2105-12-64.

4. Andreini, C., Banci, L., Bertini, I., Elmi, S. Rosato, A. (2007) Non-heme iron through the three domains of life. *Proteins- Structure and Bioinformatics* **67**, 317-324.

5. Robb, F.T., Maeder, D.L., Brown, J.R., DiRuggiero, J., Stump, M.D., Yeh, R.K., Weiss, R.B., and Dunn, D.M. 2001. Genomic sequence of hyperthermophile, Pyrococcus furiosus: Implications for physiology and enzymology. Methods Enzymol. 330: 134–157.

6. Mukund, S. and Adams, M.W.W. (1991) The novel tungsten-iron-sulfur protein of the hyperthermophilic archaebacterium, *Pyrococcus furiosus*, is an aldehyde

ferredoxin oxidoreductase. Evidence for its participation in a unique glycolytic pathway. *J. Biol. Chem.* **266**, 14208-14216

7. Mukund S., and Adams M.W.W. (1990) Characterization of a tungsten-iron-sulfur protein exhibiting novel spectroscopic and redox properties from the hyperthermophilic archaebacterium *Pyrococcus furiosus*. *J. Biol. Chem*. **265**, 11508-11516.
8. Ozawa, Y., Nakamura, T., Kamata, N., Yasujima, D., Urushiyama, A., Yamakura, F., Ohmori, D., and Imai, T. (2005) *Thermococcus profundus* 2-ketoisovalerate ferredoxin oxidoreductase, a key enzyme in the archaeal energy-producing amino acid metabolic pathway. *J. Biochemistry* **137**, 101-107.
9. Heider, J., Mai, X., and Adams, M.W.W. (1996) Characterization of 2-ketoisovalerate ferredoxin oxidoreductase, a new and reversible coenzyme A-dependent enzyme involved in peptide fermentation by hyperthermophilic archaea. *J. Bacteriol.* **178**, 780-787.
10. Ma, K., Hutchins, A., Sung, S.J.S., and Adams, M.W.W. (1997) Pyruvate ferredoxin oxidoreductase from the hyperthermophilic archaeon, *Pyrococcus furiosus*, functions as a CoA-dependent pyruvate decarboxylase. *Proc. Natl. Acad. Sci. USA* **94**, 9608-9613.
11. Yu, H.J., Wu C.-H., Schut, G.J., Haja, D.K., Zhao, G.P., Peters J.W., Adams M.W.W., and Li, H.L. (2018) Structure of an ancient respiratory system. *Cell*, **173**, 1636–1649.

12. Adams, M.W.W., Holden, J.F., Menon, A.L., Schut, G.J., Grunden, A.M., Hou, C., Hutchins, A.M., Jenney, F.E., Kim, C., Ma, K.S., Pan, G.L., Roy, R., Sapra, R., Story, S.V., Verhagen, M.F.J.M. (2001) Key role for sulfur in peptide metabolism and in regulation of three hydrogenases in the hyperthermophilic archaeon *Pyrococcus furiosus*. *J. Bacteriol*. **183**, 716-724.

13. Schut, G.J., Bridger, S.L., and Adams, M.W.W. (2007) Insights into the metabolism of elemental sulfur by the hyperthermophilic archaeon *Pyrococcus furiosus*: characterization of a coenzyme A-dependent NAD(P)H sulfur oxidoreductase. *J. Bacteriol*. **189**, 4431–4441.

14. Schut, G.J., Brehm, S.D., Datta, S., and Adams, M.W.W. (2003) Whole-genome DNA microarray analysis of a hyperthermophile and an archaeon: *Pyrococcus furiosus* grown on carbohydrates or peptides. *J. Bacteriol*. **185**, 3935-3947.

15. Wu, C.-H., Schut, G.J., Poole, F.L., Haja, D.K., Adams, M.W.W. (2018) Characterization of membrane-bound sulfane reductase: A missing link in the evolution of modern day respiratory complexes. *J. Biol. Chem*. **293**, 16687-16696.

16. Lipscomb, G.L., Keese, A.M., Cowart, D.M., Schut, G.J., Thomm, M., Adams, M.W.W., Scott, R.A. (2009) SurR: a transcriptional activator and repressor controlling hydrogen and elemental sulphur metabolism in *Pyrococcus furiosus*. *Mol. Microbiol*. **71**, 332-349.

17. Lipscomb, G.L., Schut, G.J., Scott, R.A., Adams, M.W.W. (2017) SurR is a master regulator of the primary electron flow pathways in the order Thermococcales. *Mol. Microbiol*. **104**, 869-881.

18. Jenney, F.E., Adams, M.W.W. (2001) Rubredoxin from *Pyrococcus furiosus* in Hyperthermophilic Enzymes Pt. C *Methods in Enzymology* **334**, 45-55.

19. Weinberg, M.V., Jenney, F.E., Jr., Cui, X., and Adams, M.W.W. (2004) Rubrerythrin from the hyperthermophilic archaeon *Pyrococcus furiosus* is a rubredoxin-dependent, iron-containing peroxidase. *J. Bacteriol.* **186**, 7888-7895.

20. Strand, K.R., Sun, C.J., Jenney, F.E., Schut, G,J,, and Adams M.W.W. (2010) Oxidative stress protection and the repair response to hydrogen peroxide in the hyperthermophilic archaeon *Pyrococcus furiosus* and in related species. *Arch. Microbiol*. **192**, 447-459.

21. Ramsay, B., Wiedenheft, B., Allen, M., Gauss, G.H., Lawrence, C.M., Young, M., and Douglas, T. (2006) Dps-like protein from the hyperthermophilic archaeon *Pyrococcus furiosus*. *J. Inorg. Biochem*. **100**, 1061–1068.

22. Clarkson, S.M., Newcomer, E.C., Young, E.G., and Adams, M.W.W. (2010) The elemental sulfur-responsive protein (SipA) from the hyperthermophilic archaeon *Pyrococcus furiosus* is regulated by sulfide in an iron-dependent manner. *J. Bacteriol*. **192**, 5841–5843.

23. Vaccaro, B.J., Clarkson, S.M., Holden, J.F., Lee, D.W., Wu, C.H., Poole, F.L., Cotelesage, J.J.H., Hackett, M.J., Mohebbi, S., Sun, J.C., Li, H.L., Johnson, M.K., George, G.N., and Adams, M.W.W. (2017) Biological iron-sulfur storage in a thioferrate-protein nanoparticle. *Nature Comm.* **8**, 16110; **DOI:** 10.1038/ncomms16110

24. Wofford, J.D., Bolaji, N., Dziuba, N., Outten, F.A. and Lindahl P.A. (2018) Evidence that a respiratory shield in *Escherichia coli* protects a low-molecular-mass Fe^{II} pool from O_2-dependent oxidation. *J. Biol. Chem.* **294**, 50-62.

25. Holmes-Hampton, G.P., Jhurry, N.D., McCormick, S.P., and Lindahl, P.A. (2013) Iron content of *Saccharomyces cerevisiae* cells grown under iron-deficient and iron-overload conditions. *Biochemistry* **52**, 105-114.

26. Jhurry, N.D., Chakrabarti, M., McCormick, S.P., Holmes-Hampton, G.P., and Lindahl P.A. (2012) Biophysical investigation of the ironome of human Jurkat cells and mitochondria. *Biochemistry* **51**, 5276-5284.

27. Gütlich, P., Bill, E., and Trautwein, A.X. (2011) Mössbauer Spectroscopy and Transition Metal Chemistry: Fundamentals and Applications. Springer Verlag, Berlin and Heidelberg, Germany.

28. Taft, C.A. (1977) Mössbauer studies of $NaFeS_2$: magnetic hyperfine fields and covalency in $MFeS_2$ compounds (M = Na, K, Rb, Cs). *Le Journal de Physique* **38**, 1161-1162.

29. Kuncser, V., Keune, W., Vopsaroiu, M., Bissell P.R. (2002) The "in-plane" angular spin distribution in layered systems as obtained by Fe-57 Mössbauer spectroscopy. *Nucl. Instr. and Meth. B* **196**, 135

30. Kuncser, V., Keune, W., Vopsaroiu, M., Bissell P.R. (Erratum) (2006) The 'in-plane' angular spin distribution in layered systems as obtained by Fe-57 Mössbauer spectroscopy (vol 196, pg 135, 2002) *Nucl. Instr. and Meth. B*, **245**, 539-542.

31. Ramirez, A.P. (1994) Strongly geometrically frustrated magnets. *Annual Review of Materials Science*, **124**, 453-480.

32. Zink J. and Kagorny K. (1988) Mössbauer spectroscopic investigations of the magnetic properties of potassium thioferrate-III. *J. Phys. Chem. Solids* **49**, 1429-1434.

33. Mørup, S., Topsøe, H., Lipka, J. (1976) Modified theory for Mössbauer spectra of superparamagnetic particles: Application to Fe_3O_4. *Journal de Physique Colloques*, **37** (C6), C6-287-C6-290. 10.1051/jphyscol:1976658 .

34. Cockrell A.L., Holmes-Hampton G.P., McCormick S.P., Chakrabarti M., and Lindahl P.A. (2011) Mössbauer and EPR Study of Iron in Vacuoles from Fermenting *Saccharomyces cerevisiae*. *Biochemistry*, **50**, 10275-10283.

35. Aono, S., Bryant, F.O., and Adams, M.W.W. (1989) A novel and remarkably thermostable ferredoxin from the hyperthermophilic archaebacterium *Pyrococcus furiosus*. *J. Bacteriol.* **171**, 3433-3439.

36. Heltzel A., Smith E.T., Zhou Z.H., Blamey J.M., Adams M.W.W. (1994) Cloning, expression, and molecular characterization of the gene encoding an extremely thermostable [4Fe-4S] ferredoxin from the hyperthermophilic archaeon *Pyrococcus furiosus*. *J. Bacteriol*. **176**, 4790–4793.

37. Tatur, J., Hagen, W.R., and Matias, P.M. (2006) A highly thermostable ferritin from the hyperthermophilic archaeal anaerobe *Pyrococcus furiosus*. *Extremophiles* **10**, 139-148.

38. Ebrahimi, K.H., Hagedoorn, P.L., Hagen, W.R. (2010) Inhibition and stimulation of formation of the ferroxidase center and the iron core in *Pyrococcus furiosus* ferritin. *J. Biol. Inorg. Chem.* **15**, 1243-1253.

39. Roy, R., Mukund, S., Schut G.J., Dunn D.M., Weiss, R., and Adams M.W.W. (1999) Purification and molecular characterization of the tungsten-containing formaldehyde ferredoxin oxidoreductase from the hyperthermophilic archaeon *Pyrococcus furiosus*: the third of a putative five-member tungstoenzyme family. *J. Bacteriol.* **181**, 1171-1180.

40. Hu Y.L., Faham S., Roy R., Adams M.W.W., and Rees D.C. (1999) Formaldehyde ferredoxin oxidoreductase from *Pyrococcus furiosus*: The 1.85 Å resolution crystal structure and its mechanistic Implications. *J. Mol. Biol.* **286**, 899-914.

41. Roy, R., and Adams, M.W.W. (2002) Characterization of a fourth tungsten-containing enzyme from the hyperthermophilic archaeon *Pyrococcus furiosus*. *J. Bacteriol.* **184**, 6952-6956.

42. Mukund S., and Adams M.W.W. (1995) Glyceraldehyde-3-phosphate ferredoxin oxidoreductase, a novel tungsten-containing enzyme with a potential glycolytic role in the hyperthermophilic archaeon *Pyrococcus furiosus*. *J. Biol. Chem.* **270**, 8389-8392.

43. Mai, X., and Adams, M.W.W. (1994) Indolepyruvate ferredoxin oxidoreductase from the hyperthermophilic archaeon *Pyrococcus furiosus*. A new enzyme involved in peptide fermentation. *J. Biol. Chem.* **269**, 16726-16732.

44. Mai X. and Adams M.W.W. (1996) Characterization of a fourth type of 2-keto acid-oxidizing enzyme from a hyperthermophilic archaeon: 2-ketogluatarate ferredoxin oxidoreductase from *Thermoccoccus litoralis*. *J. Bacteriol.* **178**, 5890-5896.

45. Heider, J., Mai, X.H., and Adams, M.W.W. (1996) Characterization of 2-ketoisovalerate ferredoxin oxidoreductase, a new and reversible coenzyme A-dependent enzyme involved in peptide fermentation by hyperthermophilic archaea. *J. Bacteriol*. **178**, 780-787.

46. Sapra, R., Verhagen, M.F.J.M., and Adams, M.W.W. (2000) Purification and characterization of a membrane-bound hydrogenase from the hyperthermophilic archaeon *Pyrococcus furiosus*. *J. Bacteriol.* **182**, 3423-3428.

47. Yu, H, Haja, D.K., Schut, G.J., Wu, C.H., Meng, X. Zhao, G., Li, H. Adams, M.W.W. (2020) Structure of the respiratory MBS complex reveals iron-sulfur cluster catalyzed sulfane sulfur reduction in ancient life. Nature Commun. 11, **Article Number:** 5953 **DOI:** 10.1038/s41467-020-19697-7

48. Nguyen, D.M.N., Schut, G.J., Zadvornyy, O.A., Tokmina-Lukaszewska, M., Poudel, S., Lipscomb, G.L., Adams L.A., Dinsmore, J.T., Nixon, W.J., Boyd, E.S., Bothner, B., Peters, J.W., and Adams M.W.W. (2017) Two functionally distinct NADPC-dependent ferredoxin oxidoreductases maintain the primary redox balance of *Pyrococcus furiosus*. *J. Biol. Chem.* **292**, 14603–14616.

49. Hagen, W.R., Silva, P.J., Amorim, M.A., Hagedoorn, P.A., Wassink, H., Haaker H., and Robb, F.T. (2000) Novel structure and redox chemistry of the prosthetic groups of the iron-sulfur flavoprotein sulfide dehydrogenase from *Pyrococcus furiosus*; evidence for a [2Fe-2S] cluster with $Asp(Cys)_3$ ligands. *J. Biol. Inorg. Chem.* **5**, 527-534.

50. Charon, M.H., Volbeda, A., Chabriere, E., Pieulle, L., and Fontecilla-Camps, J.C. (1999) Structure and electron transfer mechanism of pyruvate:ferredoxin oxidoreductase. *Curr Opin Struct Biol* **9**, 663–669.

51. Blamey, J.M. and Adams, M.W.W. (1993) Purification and characterization of pyruvate ferredoxin oxidoreductase from the hyperthermophilic archaeon *Pyrococcus furiosus*. *B.B.A.-Protein Struct. M.* **1161**, 19-27.

52. Kurihara, K., Tanaka, I., Chatake, T., Adams, M.W., Jenney, F.E, Jr, Moiseeva N., Bau R, Niimura N. (2004) Neutron crystallographic study on rubredoxin from *Pyrococcus furiosus* by BIX-3, a single-crystal diffractometer for biomacromolecules. *Proc. Natl. Acad. Sci. U.S.A.* **101**, 11215–11220.

53. Bryant, F.O., and Adams, M.W.W. (1989) Characterization of hydrogenase from the hyperthermophilic archaebacterium, *Pyrococcus furiosus*. *J. Biol. Chem.* **264**, 5070-5079.

54. Ma, K., Weiss, R., and Adams, M.W.W. (2000) Characterization of hydrogenase II from the hyperthermophilic archaeon *Pyrococcus furiosus* and assessment of its role in sulfur reduction. *J. Bacteriol.* **182**, 1864-1871.

55. Yeh, A.P., Hu, Y., Jenney, F.E., Adams, M.W.W., and Rees, D.C. (2000) Structures of the superoxide reductase from *Pyrococcus furiosus* in the oxidized and reduced states. *Biochemistry* **39**, 2499-2508.

56. Clay, M.D., Jenney, F.E., Jr., Hagedoorn, P.L., George, G.N., Adams, M.W. W., and Johnson, M.K. (2002) Spectroscopic studies of *Pyrococcus furiosus* superoxide

reductase: Implications for active-site structures and the catalytic mechanism. *J. Am. Chem. Soc.* **124**, 788-805.

57. Jenney, F.E., Jr., Verhagen, M.F.J.M., Cui, X., and Adams, M.W.W. (1999) Anaerobic microbes: oxygen detoxification without superoxide dismutase. *Science* **286**, 306-309.

58. Sevcenco, A.M., Bevers, L.E., Pinkse, M.W.H., Krijger, G.C., Wolterbeek, H.T., Verhaert, P.D.E.M., Hagen, W.R., and Hagedoorn, P.L. (2010) Molybdenum incorporation in tungsten aldehyde oxidoreductase enzymes from *Pyrococcus furiosus*. *J. Bacteriol*. **192**, 4143-4152.

59. Lipscomb, G.L., Stirrett, K., Schut, G.J., Yang, F., Jenney, F.E. Jr, Scott, R.A., Adams M.W.W, Westpheling, J. (2011) Natural competence in the hyperthermophilic archaeon *Pyrococcus furiosus* facilitates genetic manipulation: construction of markerless deletions of genes encoding the two cytoplasmic hydrogenases. *Appl Environ Microbiol*. **77**, 2232-2238.

60. Bridger, S.L., Clarkson, S.M., Stirrett, K., DeBarry, M.B., Lipscomb, G.L., Schut G.J., Westpheling, J., Scott, R.A., Adams, M.W.W. (2011) Deletion strains reveal metabolic roles for key elemental sulfur-responsive proteins in *Pyrococcus furiosus*. *J Bacteriol*. **193**, 6498-6504.

Table B.1: Mössbauer parameters used in simulations (averaged), LT, low temperature; HT, high temperature.

	ISC_W	**ISC_N**	**Magnetic (S^0-dependent)**	**Magnetic (other)**	**Fe(S_4)**	**Fe^{II}(O/N)**	**S = 5/2 Fe^{III}**
δ (mm/s)	0.45 ± 0.04 (LT) 0.43 ± 0.03 (HT)	0.43 ± 0.03 (LT) 0.38 ± 0.05 (HT)			0.65 ± 0.04	1.3 ± 0.1 (LT) 1.2 ± 0.1 (HT)	0.50±0.02
ΔE_Q (mm/s)	1.35 ± 0.05 (LT) 1.15 ± 0.1 (HT)	0.83 ± 0.06 (LT) 0.75 ± 0.07 (HT)			3.0 ± 0.05	2.6 ± 0.1 (LT) 2.7 ± 0.1 (HT)	0.45±0.02
Γ (mm/s)	0.34 ± 0.06 (LT) 0.35 ± 0.05 (HT)	0.47 ± 0.04 (LT) 0.45 ± 0.04 (HT)			0.43 ± 0.03	0.5 ± 0.1 (LT) 0.5 ± 0.1 (HT)	0.50±0.05
D; E/D							0.5; 0.33
A_x; A_y; A_z							-212 KG
η							2.5±0.5
g_x, g_y, g_z							2.0
Figure B.1	45% (LT) 35% (HT) 43% (Post Storage)	35% (LT) 60% (HT) 33% (Post Storage)		~14-15% (LT)		4-5% (LT) 4-5% (HT) 8% (Post storage)	16% (Post storage)
Figure B.3	10% (LT) 33% (HT)	10% (LT) 65% (HT)	78% (LT)			2% (LT) 2% (HT)	

Figure B.6	**+S^0** 10% (LT) 35% (LT) **-S^0** 52% (LT) 42% (HT)	 10% (LT) 63% (HT) 23% (LT) 33% (HT)	77% (LT)		 2% (LT) 2% (HT)	 3% (LT) 3% (LT) 23% (LT) 23% (HT)	
Figure B.7	49% (5 K) 44% (150 K)	36% (5 K) 41% (150 K)			3% (LT) 3% (HT)	12% (5 K) 12% (150 K)	

Figure B.1

Mössbauer spectra of WT *P. furiosus* cells grown under -S^0 conditions and harvested during exponential growth. A, 5 K, 0.05 T; B, 150 K, 0.05 T; C, 4.2 K, 0 T; D, 4.2 K, 3.0 T; and E, 4.2 K, 6.0 T. The field was applied parallel (A and B) and perpendicular (C – E) to the gamma radiation.

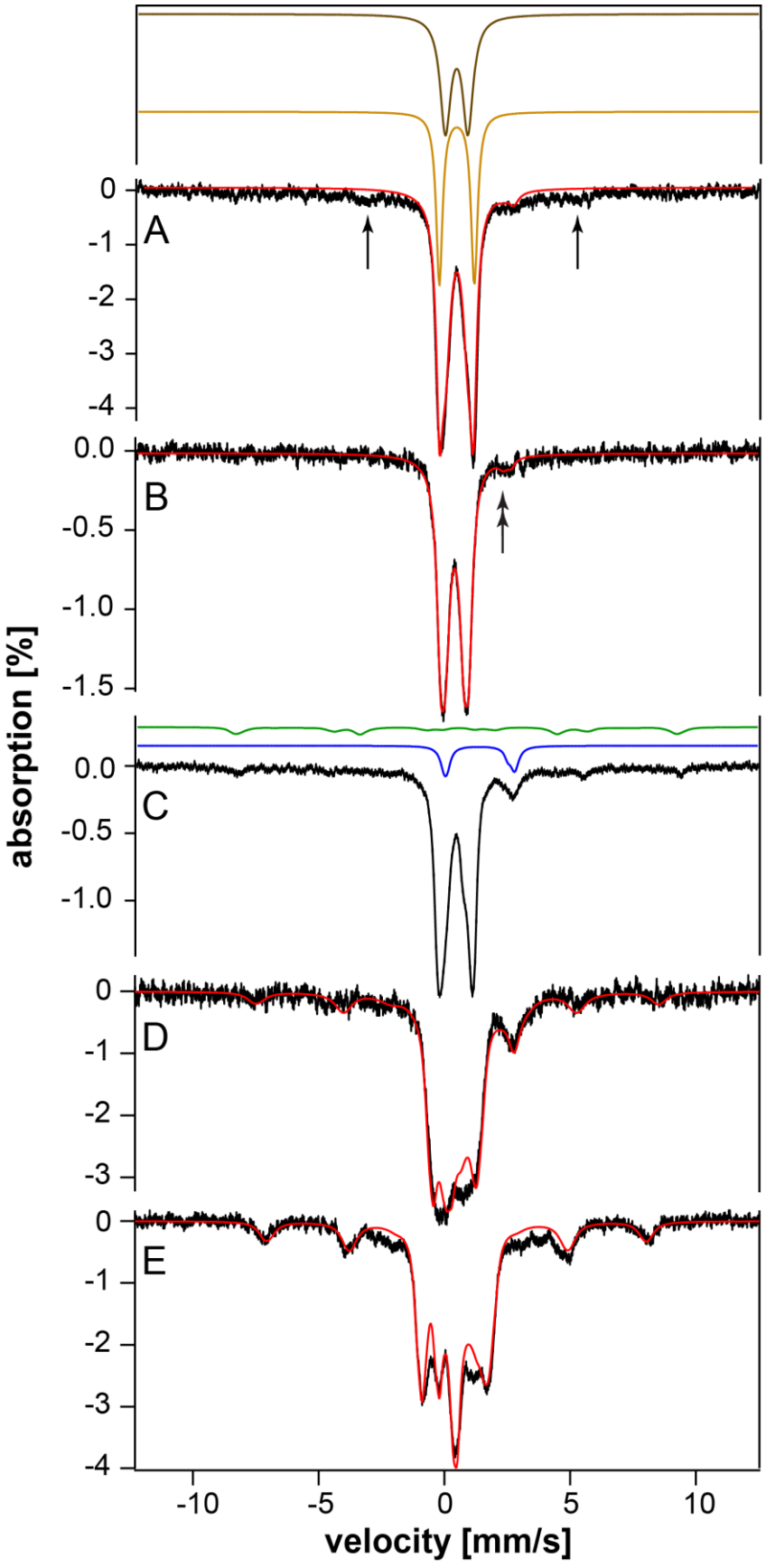
A
B
C
D
E
absorption [%]
velocity [mm/s]
0
-1
-2
-3
-4
0.0
-0.5
-1.0
-1.5
-10
-5
0
5
10

Figure B.2

EPR spectra of WT cells grown under $+S^0$ (top) and $-S^0$ (bottom) conditions. EPR conditions: T, 4 K; frequency, 9.36 GHz; microwave power, 0.2 mW; modulation amplitude 10 G; modulation frequency 100 KHz; sweep time 300s

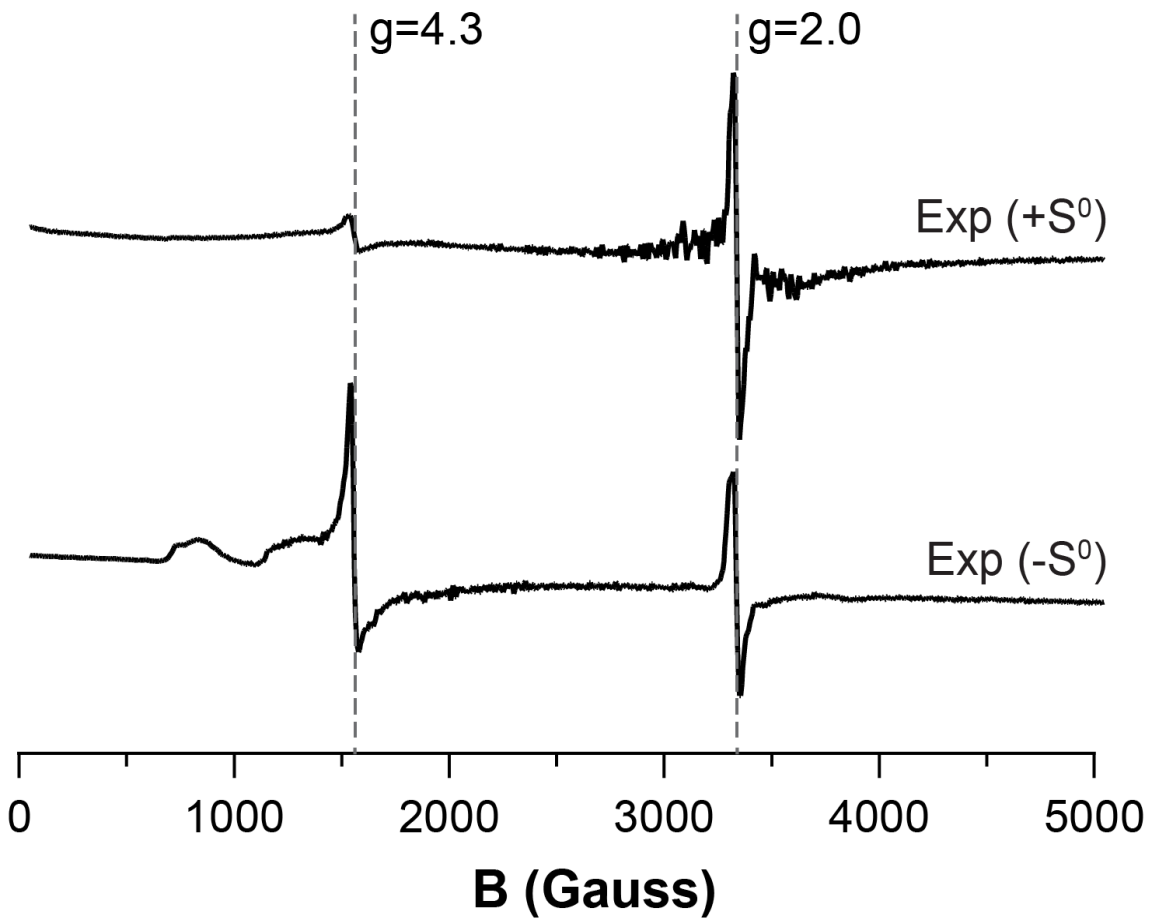
g=4.3
g=2.0
Exp (+S0)
Exp (-S0)
0
1000
2000
3000
4000
5000
B (Gauss)

Figure B.3

Mössbauer spectra of the WT+S^0 sample grown with 10 µM ^{57}Fe and S^0 in the medium, and harvested during exponential phase. A, 5 K 0.05 T; B, 150 K; C, 4.2 K and 3 T; D, 4.2 K and 6.0 T. The applied magnetic field was perpendicular to the gamma radiation. The red lines in A, C, and D are simulations of the magnetically ordered iron using the continuous distribution of hyperfine fields in E (0.05 T), F (3 T) and G (6T). Green solid lines are simulations to WCD and NCD contributions assuming 20% spectral intensity.

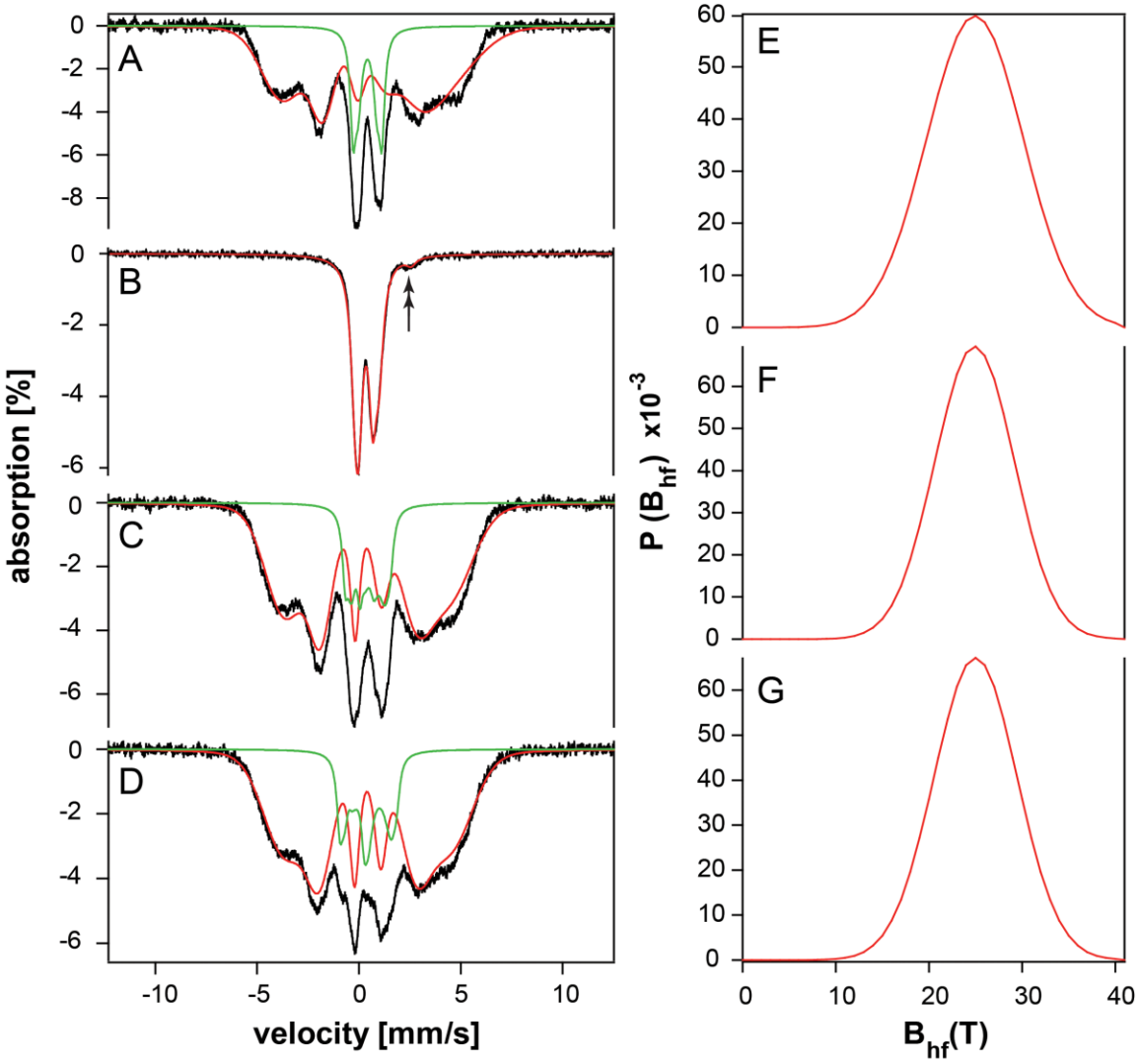
A
B
C
D
E
F
G
absorption [%]
velocity [mm/s]
P (B_hf) x10^-3
B_hf(T)

Figure B.4

Plot of A23 vs external field for WT+S^0 exponential cells (blue line) and ΔIssA+S^0 exponential cells (red line).

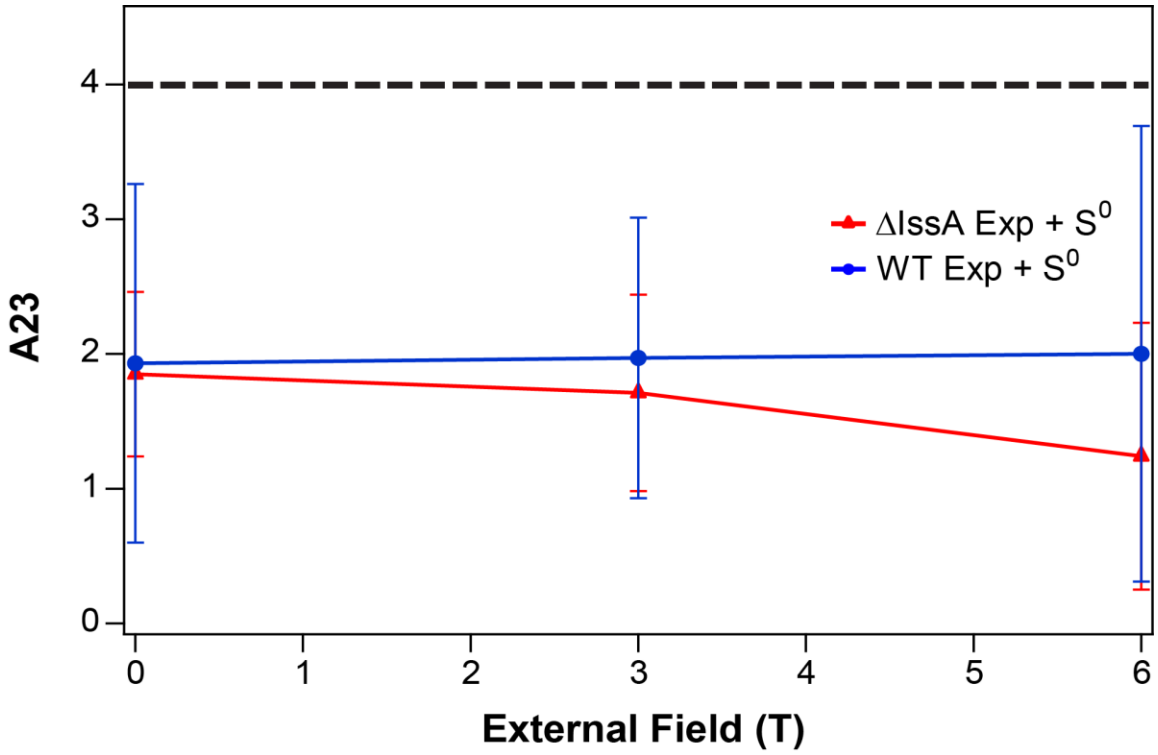
A23
External Field (T)
ΔIssA Exp + S0
WT Exp + S0
0
1
2
3
4
5
6

Figure B.5

Low-field (0.05 T) Mössbauer spectra of exponentially harvested WT+S^0 cells collected at increasing temperatures.

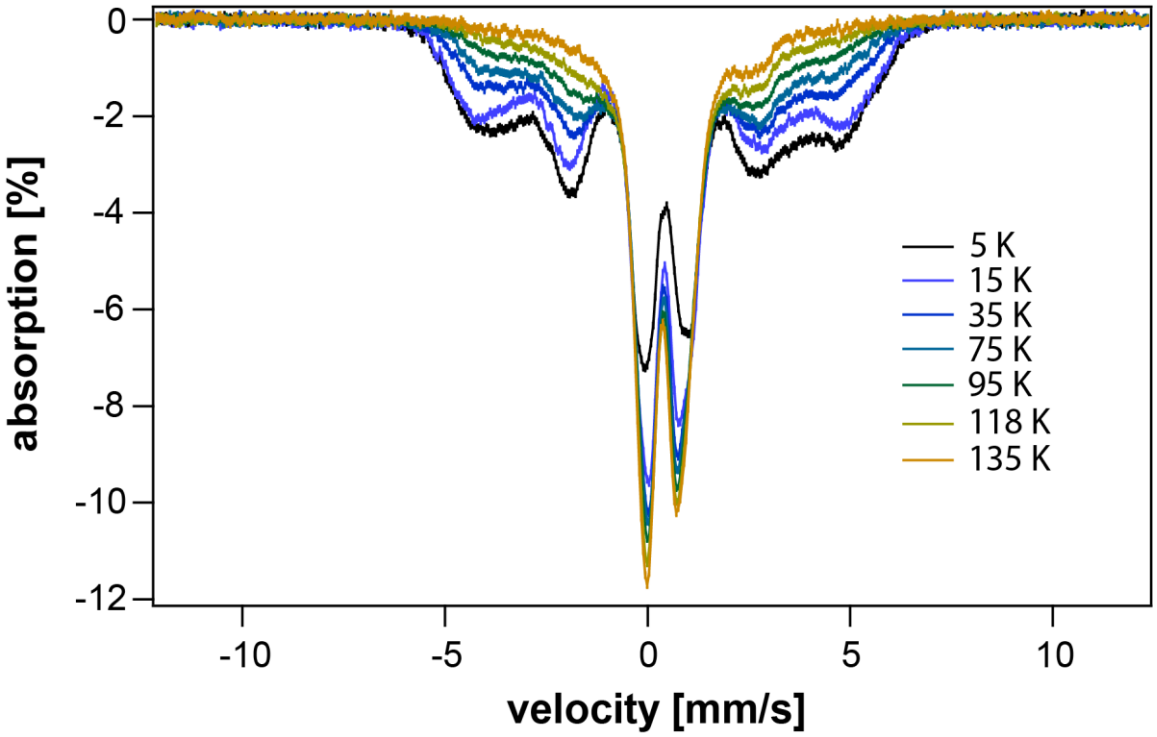
0
-2
-4
-6
-8
-10
-12
absorption [%]
-10
-5
0
5
10
velocity [mm/s]
5 K
15 K
35 K
75 K
95 K
118 K
135 K

Figure B.6

Low-field (0.05 T) Mössbauer spectra of WT-S^0 (A and B) and WT+S^0 (C and D) harvested after cells had reached stationary state. A and C, 5 K; B and D, 150 K

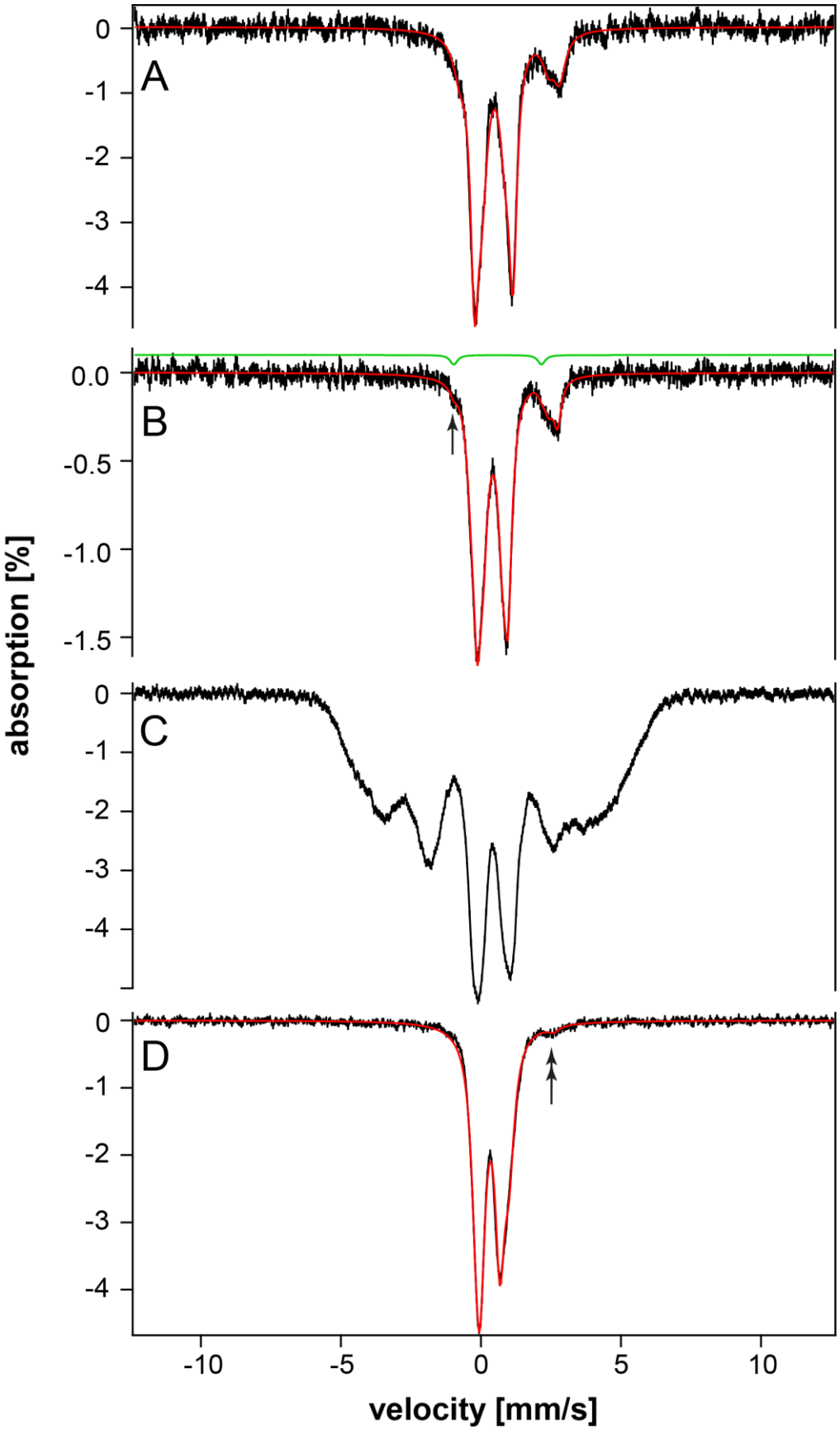
A
B
C
D
absorption [%]
velocity [mm/s]
0
-1
-2
-3
-4
0.0
-0.5
-1.0
-1.5
-10
-5
0
5
10

Figure B.7

Mössbauer Spectra of ΔIssA-S^0 cells. A, 10 K and 0.05 T; B, 150 K and 0.05 T; C, 4.2 K and 6.0 T.

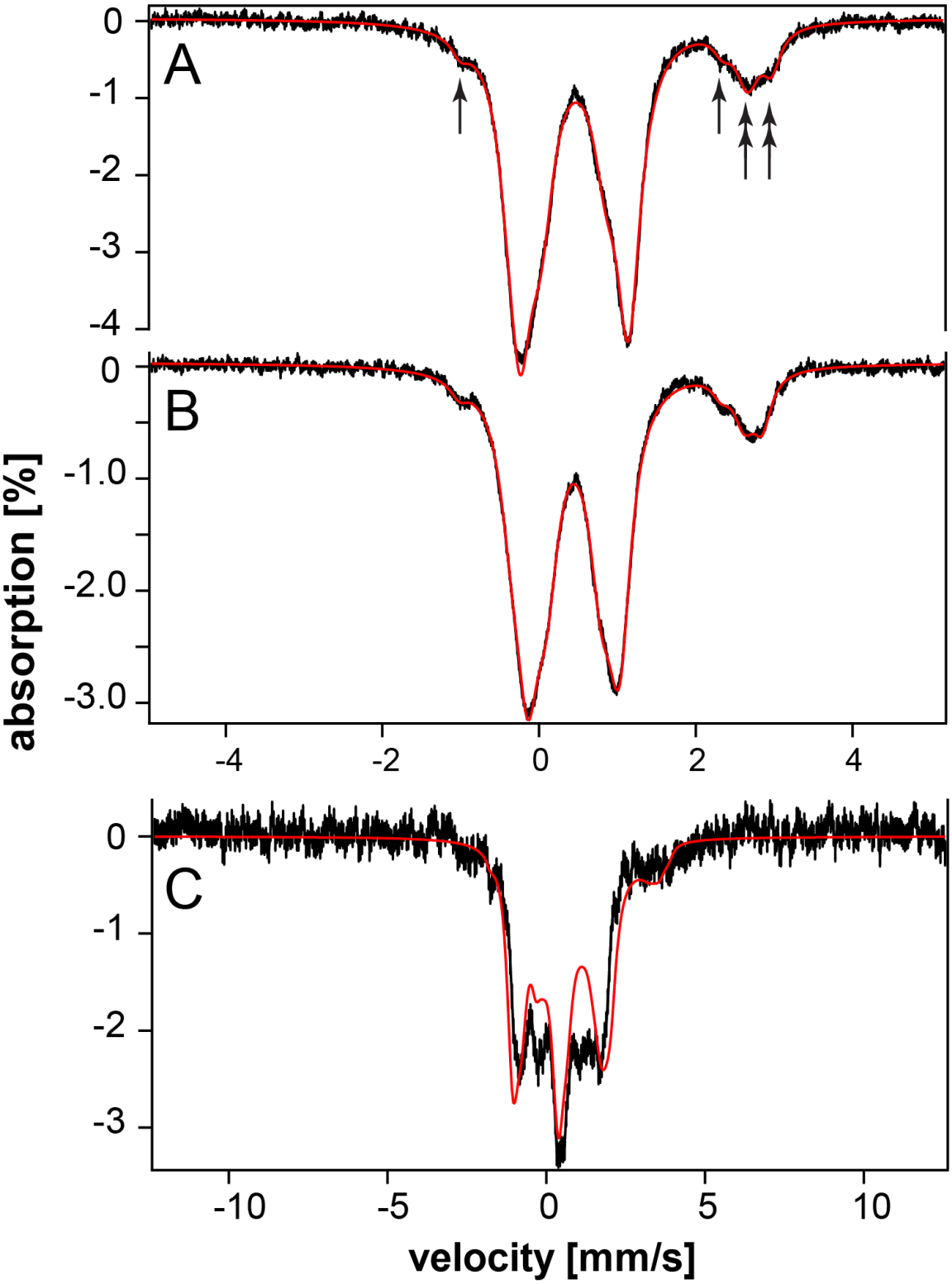
A
B
C
absorption [%]
velocity [mm/s]
0
-1
-2
-3
-4
-1.0
-2.0
-3.0
-10
-5
5
10

Figure B.8

4.2 K Mössbauer spectra of ΔIssA+S^0 cells at A, 0; B, 3.0; and C, 6.0 T. Free-histogram distributions are shown in D (0 T), E (3 T) and F (6 T).

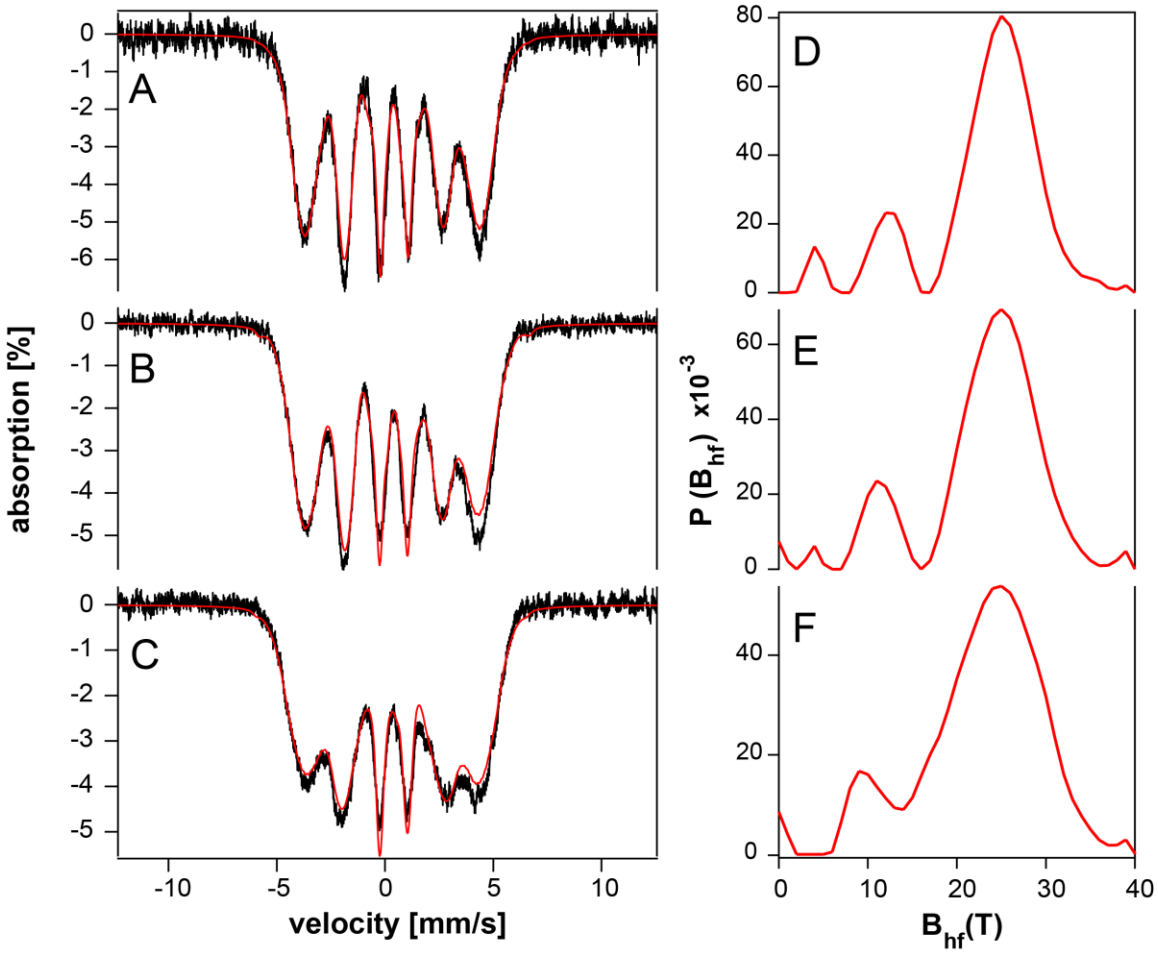
A
B
C
D
E
F
absorption [%]
velocity [mm/s]
P (B_hf) x10^-3
B_hf(T)

Figure B.9

Variable Temperature 0.05 T Mössbauer spectra of ΔIssA+S^0 cells. Right column shows the B_{hf} distribution used to obtain the fit. A and I, 5K; B and J, 10K; C and K, 25K; D and L, 40K; E and M, 55K; F and N, 70K; G and O, 100K; H and P, 120K. Solid green lines in the left column show contribution from $ISC_{N/W}$ while solid red lines indicate contribution from TFL.

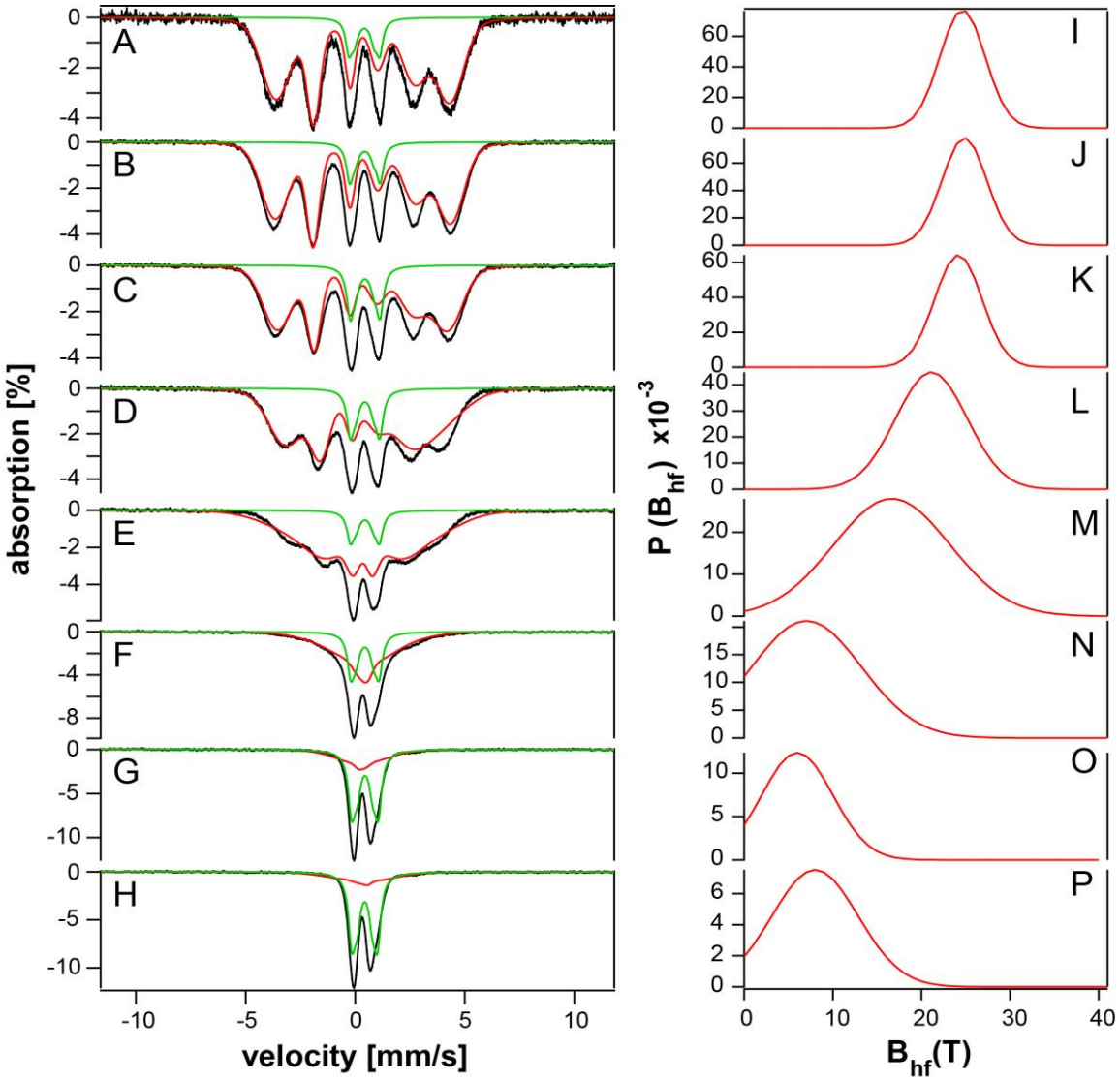
absorption [%]
velocity [mm/s]
A
B
C
D
E
F
G
H
P (B_hf) x10^-3
B_hf(T)
I
J
K
L
M
N
O
P

Figure B.10

Growth of *Pyrococcus furiosus* under 10 mM Na_2S (A) and 1 g/L S^0 (B) conditions. Solid lines, WT; dashed lines, ΔIssA; (■), 10 μM Fe; (●), 50 μM Fe. Error bars represent standard deviation of biological triplicate samples.

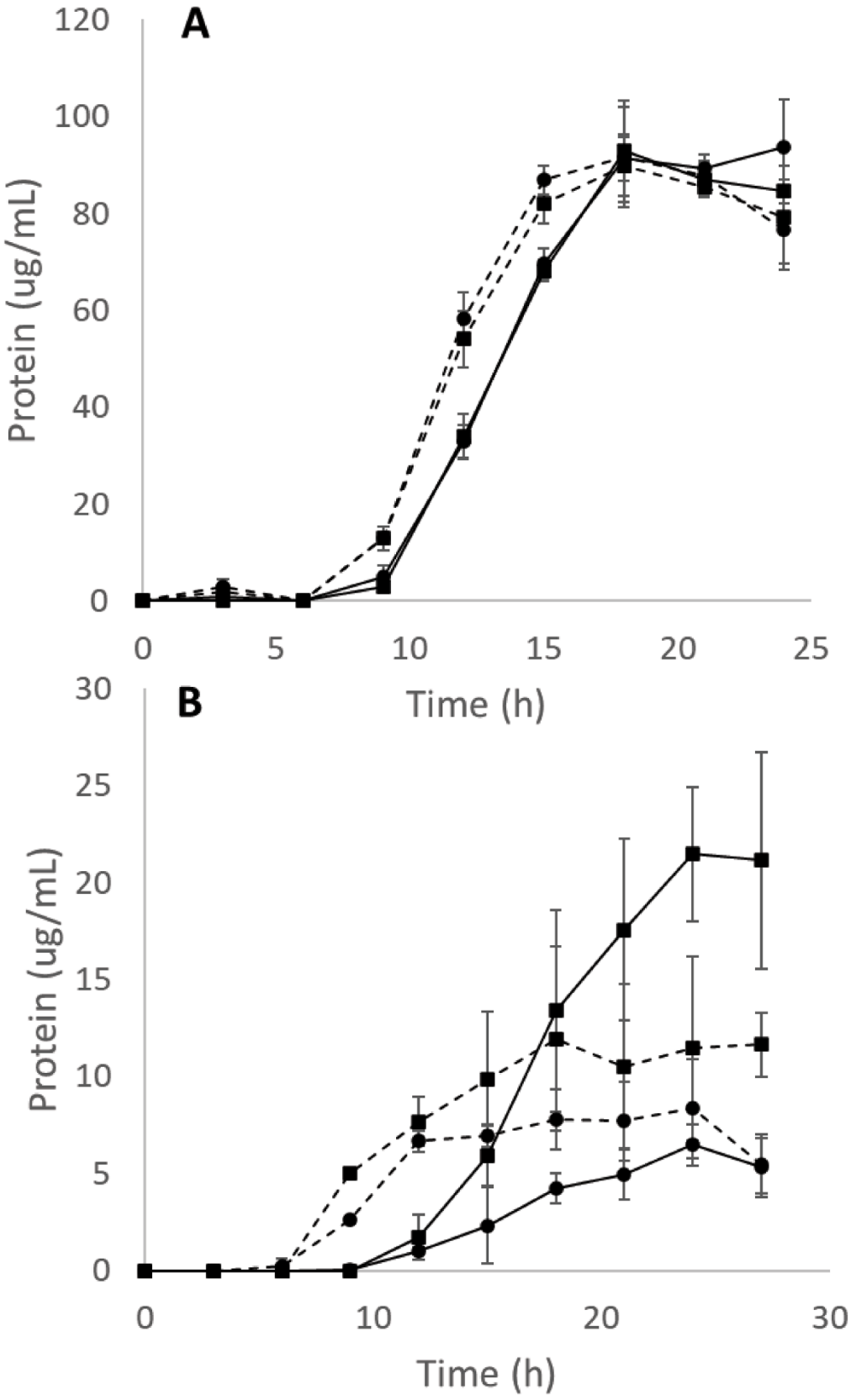
A
120
100
80
60
40
20
0
Protein (ug/mL)
0
5
10
15
20
25
Time (h)
B
30
25
20
15
10
5
0
Protein (ug/mL)
0
10
20
30
Time (h)

Figure B.11

A Model of cellular energy metabolism emphasizing the role of iron and elemental sulfur in *P. furiosus.* See text for details.

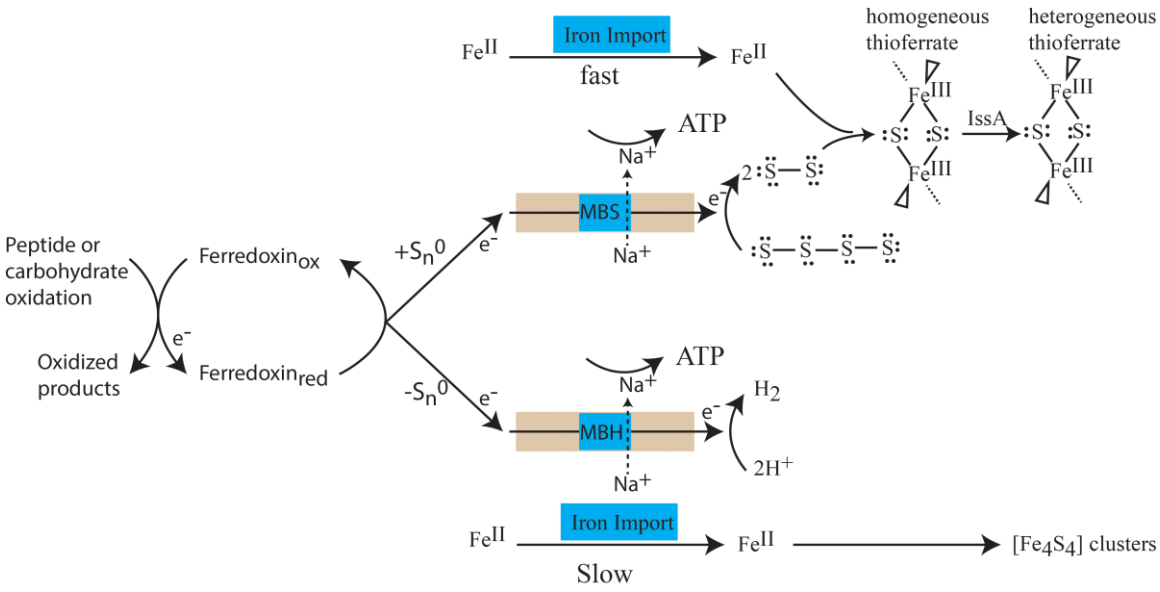
Iron Import
fast
homogeneous thioferrate
heterogeneous thioferrate
IssA
ATP
Na+
MBS
Peptide or carbohydrate oxidation
Ferredoxin ox
Oxidized products
Ferredoxin red
+Sn0
-Sn0
e-
MBH
H2
2H+
Iron Import
Slow
[Fe4S4] clusters

Table SB.1. Iron-containing proteins in *Pyrococcus furiosus* predicted by bioinformatics. Taken from (3).

	GM Number	ORF Number	Annotation
1	PF0754	748906	2-keto acid:ferredoxin oxidoreductase subunitalpha
2	PF1768	1645457	2-keto acid:ferredoxin oxidoreductase subunitalpha
3	PF1771	1647980	2-keto acid:ferredoxin oxidoreductase subunitalpha
4	PF0845	817300	2-keto acid:ferredoxin oxidoreductase subunitalpha
5	PF1767	1644264	2-keto acid:ferredoxin oxidoreductase subunitdelta
6	PF1770	1646824	2-keto acid:ferredoxin oxidoreductase subunitgamma
7	PF1773	1649361	2-keto acid:ferredoxin oxidoreductase subunitgamma
8	PF0139	149451	2-keto acid:ferredoxin oxidoreductase subunitgamma
9	PF0969	928888	2-ketovalerate ferredoxin oxidoreductase subunitalpha-2
10	PF0970	930085	2-ketovalerate ferredoxin oxidoreductase subunitdelta-2
11	PF0938	903832	3-isopropylmalate dehydratase large subunit
12	PF0511	530974	3-methyladenine DNA glycosylase
13	PF0201	214120	aconitate hydratase (aconitase)
14	PF0075	81500	alcohol dehydrogenase
15	PF0608	631178	alcohol dehydrogenase
16	PF0346	358419	aldehyde:ferredoxin oxidoreductase (aor)
17	PF1033	989258	alkyl hydroperoxide reductase
18	PF0722	720985	alkyl hydroperoxide reductase subunit c
19	PF2064	1904500	arylsulfatase regulatory protein, putative
20	PF0077	83155	biotin operon repressor/biotin--[acetyl CoAcarboxylase] ligase
21	PF0860	835631	btpA family protein
22	PF0482	497978	cell division control protein 21
23	PF0302	318028	co-factor modifying protein
24	PF0204	220427	conserved hypothetical protein
25	PF0206	222756	conserved hypothetical protein
26	PF0096	104208	conserved hypothetical protein
27	PF1182	1128650	conserved hypothetical protein
28	PF1489	1391238	conserved hypothetical protein
29	PF1551	1448377	conserved hypothetical protein
30	PF1158	1107110	conserved hypothetical protein
31	PF1061	1016054	conserved hypothetical protein
32	PF0037	43228	conserved hypothetical protein
33	PF1192	1137142	conserved hypothetical protein
34	PF1193	1137512	conserved hypothetical protein
35	PF1199	1141457	conserved hypothetical protein
36	PF1544	1443272	conserved hypothetical protein

37	PF1397	1311770	conserved hypothetical protein
38	PF1049	1002916	conserved hypothetical protein
39	PF1083	1032190	conserved hypothetical protein
40	PF2025	1871822	conserved hypothetical protein
41	PF0144	154650	conserved hypothetical protein
42	PF1638	1529201	conserved hypothetical protein
43	PF0138	148781	conserved hypothetical protein
44	PF0850	824641	conserved hypothetical protein
45	PF1718	1597514	conserved hypothetical protein
46	PF1325	1247070	conserved hypothetical protein
47	PF1285	1211743	conserved hypothetical protein
48	PF1286	1212834	conserved hypothetical protein
49	PF1277	1207631	conserved hypothetical protein
50	PF0913	884008	conserved hypothetical protein
51	PF0914	884391	conserved hypothetical protein
52	PF0843	816518	conserved hypothetical protein
53	PF0846	820618	conserved hypothetical protein
54	PF0849	823503	conserved hypothetical protein
55	PF1389	1302837	conserved hypothetical protein
56	PF1454	1362012	conserved hypothetical protein
57	PF1470	1375936	conserved hypothetical protein
58	PF1190	1136390	conserved hypothetical protein
59	PF1195	1138566	conserved hypothetical protein
60	PF1196	1139695	conserved hypothetical protein
61	PF0689	700021	conserved hypothetical protein
62	PF0695	705210	conserved hypothetical protein
63	PF0741	738742	conserved hypothetical protein
64	PF0723	722156	conserved hypothetical protein
65	PF1934	1783451	conserved hypothetical protein
66	PF1972	1822760	conserved hypothetical protein
67	PF1628	1520292	conserved hypothetical protein
68	PF0342	354894	conserved hypothetical protein
69	PF1605	1496972	conserved hypothetical protein
70	PF0612	633007	conserved hypothetical protein
71	PF1914	1765399	conserved hypothetical protein
72	PF1042	996088	conserved hypothetical protein
73	PF1967	1817174	conserved hypothetical protein
74	PF0602	622998	conserved hypothetical protein
75	PF0631	643597	conserved hypothetical protein
76	PF1782	1655977	conserved hypothetical protein
77	PF2033	1877126	conserved hypothetical protein

78	PF0858	833697	conserved hypothetical protein
79	PF0724	722839	conserved hypothetical protein
80	PF0690	699847	conserved hypothetical protein, possiblethioredoxin/glutaredoxin
81	PF0731	727122	copper-transporting atpase, p-type
82	PF0705	709009	cytochrome c-type biogenesis protein
83	PF1242	1175771	dehydrogenase subunit alpha
84	PF1296	1223405	dihydropteroate synthase
85	PF1941	1793572	dihydropteroate synthase
86	PF0942	908597	dihydroxy-acid dehydratase
87	PF1210	1152634	dipeptide ABC transporter, permease protein
88	PF1797	1669334	d-nopaline dehydrogenase
89	PF1909	1760272	ferredoxin
90	PF2030	1873914	ferredoxin-family protein
91	PF0857	831703	ferrous iron transport protein b
92	PF0751	746296	flavoprotein
93	PF0694	703868	flavoprotein
94	PF1203	1145403	formaldehyde:ferredoxin oxidoreductase
95	PF1480	1385199	formaldehyde:ferredoxin oxidoreductase wor5
96	PF1521	1419794	formate dehydrogenase alpha chain
97	PF0441	457188	galactose-1-phosphate uridylyltransferase
98	PF1910	1760551	glutamate synthase
99	PF0205	221932	glutamate synthase subunit alpha
100	PF1327	1247601	glutamate synthase [NADPH] small chain
101	PF1457	1363259	glutaredoxin/thioredoxin-like protein
102	PF0094	102519	glutaredoxin-like protein
103	PF0464	478142	glyceraldehyde-3-phosphate:ferredoxinoxidoreductase
104	PF2005	1855892	glycerol-3-phosphate dehydrogenase
105	PF1229	1162991	glycosylase putative; mutY-nth family
106	PF1763	1640658	GTP-binding protein, gtp1/obg family
107	PF0925	890633	heme biosynthesis protein
108	PF0647	659796	heme biosynthesis protein
109	PF1332	1253842	H-II alpha (hydrogenase subunit alpha)
110	PF1331	1252601	H-II delta (hydrogenase subunit delta)
111	PF1330	1251888	H-II gamma (hydrogenase subunit gamma)
112	PF1329	1251025	H-II hydrogenase subunit beta
113	PF0008	8548	hit family protein (hit)
114	PF1107	1054030	hit family protein (hit)
115	PF0559	577932	hydrogenase expression/formation regulatoryprotein
116	PF0188	198787	hydrogenase subunit gamma
117	PF1328	1249026	hydrogenase subunit gamma
118	PF1245	1179923	hypothetical d-nopaline dehydrogenase

119	PF1109	1058861	hypothetical protein
120	PF1482	1386082	hypothetical protein
121	PF2060	1899840	hypothetical protein
122	PF1110	1059349	hypothetical protein
123	PF0533	551149	indolepyruvate ferredoxin oxidoreductase subunita
124	PF0534	551790	indolepyruvate ferredoxin oxidoreductase subunitb
125	PF1774	1650532	iron (III) ABC transporter, ATP-binding protein
126	PF0911	882732	iron (III) ABC transporter, ATP-binding protein
127	PF0851	825121	iron-dependent repressor
128	PF0660	671023	iron-sulfur cluster binding protein
129	PF1952	1802989	iron-sulfur protein
130	PF1976	1828270	l-aspartate oxidase (quinolinate synthetase)
131	PF1432	1342256	mbh10 NADH dehydrogenase subunit (like cCoL,EchC, HycH)
132	PF1434	1344050	mbh12 membrane bound hydrogenase alpha (NADHdehydrogenase)
133	PF1436	1345434	mbh14 iron-sulfur protein (like HycF, EchF,CooX)
134	PF0090	97550	molybdenum cofactor biosynthesis protein
135	PF0345	358122	molybdopterin converting factor, subunit 1
136	PF0543	562899	molybdopterin converting factor, subunit 1
137	PF0729	725885	multi domain protein containingcorrinoid/iron-sulfur region
138	PF1444	1352727	NADH dehydrogenase subunit
139	PF1441	1350388	NADH dehydrogenase subunit
140	PF1442	1351020	NADH dehydrogenase subunit
141	PF1901	1751973	oxygen-independent coproporphyrinogen IIIoxidase
142	PF1003	961250	phosphate-binding periplasmic protein precursor(pbp)
143	PF1755	1632493	possible fumarate hydratase (fumarase) alphasubunit
144	PF1754	1632002	possible fumarate hydratase (fumarase) betasubunit
145	PF0692	702081	prismane protein homolog
146	PF1287	1214251	probable ATP-dependent transporter similar toabc
147	PF0742	739367	probable ferritin homolog
148	PF1903	1754483	probable translation initiation factor (if-2homolog)
149	PF1679	1562997	putative 3-isopropylmalate dehydratase largesubunit
150	PF1680	1563488	putative 3-isopropylmalate dehydratase smallsubunit
151	PF0939	904323	putative 3-isopropylmalate dehydratase smallsubunit
152	PF0187	197868	putative cofactor synthesis protein
153	PF0247	256063	putative HTH transcription regulator
154	PF1911	1761982	putative hydrogenase
155	PF1479	1383440	putative oxidoreductase, Fe-S subunit
156	PF0119	123510	putative perplasmic sugar binding protein
157	PF1796	1669077	putative polyferredoxin
158	PF2026	1872873	putative polyferredoxin

159	PF1938	1788984	putative sugar binding protein (malE-like)
160	PF0966	926380	pyruvate ferredoxin oxidoreductase subunitalpha-2
161	PF0967	927581	pyruvate ferredoxin oxidoreductase subunitdelta
162	PF0971	930439	pyruvate ferredoxinoxidoreductase/2-ketovalerate ferredoxin oxidoreductasegamma subunit
163	PF0670	679716	rnase l inhibitor
164	PF1282	1210573	rubredoxin
165	PF1283	1210814	rubrerythrin
166	PF1795	1668574	sarcosine oxidase subunit alpha
167	PF0894	867811	sulfhydrogenase alpha subunit
168	PF0891	864857	sulfhydrogenase beta subunit
169	PF0893	866528	sulfhydrogenase delta subunit
170	PF0892	865732	sulfhydrogenase gamma subunit
171	PF1281	1210188	superoxide reductase
172	PF0752	747589	thioredoxin peroxidase
173	PF1337	1257851	transcriptional activator, putative
174	PF1338	1258479	transcriptional activator, putative
175	PF1194	1138558	transcriptional regulator (furr family)
176	PF1739	1616027	trehalose/maltose binding protein
177	PF0344	356987	tungsten-containing aldehyde ferredoxinoxidoreductase cofactor modifying protein
178	PF1961	1812948	tungsten-containing formaldehyde ferredoxinoxidoreductase wor4

Table SB.2: Characterized iron-containing proteins in *Pyrococcus furiosus*.

Protein	Identifier	Description	Iron Center	Reference
Aldehyde ferredoxin Oxidoreductase (AOR)	PF0346	Oxidizes aldehydes derived from amino acids	1 $[Fe_4S_4]$ per subunit; 1 Fe^{II} per dimer	(4)
DPS-like Protein (miniferritin)	PF1193	Peroxidase activity; $_2O_2$ oxidation of Fe^{II}	[Fe-O-Fe] ferroxidase site; ca. 300 Fe^{III} ions in mineral aggregate	(18,19)
Dehydratase	PF0938 PF1679	Involved in amino acid biosynthesis	Predicted to encode an ISC	(18)
Dipeptide binding protein	PF0357		Predicted to encode an ISC	(18)
Ferredoxin (Fd)	PF1909	Redox currency	$[Fe_4S_4]^{2+/1+}$ cluster coordinated by 3 cys and 1 asp	(34,35)
Ferritin	PF0742	Iron storage	[Fe-O-Fe] ferroxidase site; thousands of Fe^{III} ions in ferrihydrite-like mineral	(36,37)
Formadehyde ferrodoxin oxidoreductase (FOR)	PF1203	Oxidizes aldehydes in the catabolism of amino acids	1 $[Fe_4S_4]$	(38,39)
Formaldehyde ferredoxin oxidoreductase 4 (WOR4)	PF1961	Unknown; maybe involved in S^0 reduction	1 $[Fe_4S_4]$	(40)
Formate dehydrogenase (putative	PF1242 PF1521			
Glyceraldehyde-3-Phosphate ferredoxin oxidoreductase (GAPOR)	PF0464	Involved in the unusual glycolytic pathway in Pf (metabolism of carbohydrates). This converts glyceraldehyde-3-phosphate to glycerate-3-phosphate without generating ATP. Ferredoxin is the electron acceptor in glycolysis; no NAD(P)H is formed.	1 $[Fe_4S_4]$	(41)
Indolepyruvate ferredoxin oxidoreductase (IOR)	PF0533 PF0534	Catalyzes the oxidative decarboxylation of aryl pyruvates generated by the transamination of aromatic amino acids, to the corresponding aryl acetyl-CoA (same as PFOR).	Each tetramer contains 4 $[Fe_4S_4]$ clusters and 1 $[Fe_3S_4]$ cluster	(42)
Iron-sulfur sequestration protein A (IssA)	PF2025	Upregulated when grown on S^0 and iron	Associated with thioferrate aggregates	(20,21)
3-isopropylmalate dehydratase	PF0938 PF0939			(12)
2-ketoglurate ferredoxin oxidoreductase (KGOR)	PF1767 PF1768 PF1769 PF1770	Catalyzes the oxidative decarboxylation of 2-ketoglutarate to succinyl coenzyme A and CO_2 and reduces ferredoxin; involved in biosynthesis not energy (homolog of PFOR).	At least 3 $[Fe_4S_4]$ clusters	(43)

2-ketoisovalerate ferredoxin oxidoreductase (VOR)	PF0968 PF0969 PF0970 PF0971	Catalyzes the oxidative decarbonylation of mainly aliphatic amino-acid derived 2-keto acids.	At least 3 [Fe_4S_4] clusters	(44)

Protein	Identifier	Description	Iron Center	Reference
Membrane-bound hydrogenase (MBH)	PF1423 PF1424 PF1425 PF1426 PF1427 PF1428 PF1429 PF1430 PF1431 PF1432 PF1433 PF1434 PF1435 PF1436	Used in energy generation. Related to Respiratory Complex I	3 [Fe_4S_4] + NiFe site	(45) (9)
Membrane-bound sulfane reductase (MBS)	PF1441 PF1442 PF1443 PF1444 PF1445 PF1446 PF1447 PF1448 PF1449 PF1450 PF1451 PF1452 PF1453	Homolog of MBH complex. Expression increases after S^0 addition. MBX reduces the sulfane sulfur of polysulfides.	3 [Fe_4S_4] clusters	(Yu 2020)
NADH-dependent reduced ferredoxin:$NADP^+$ oxidoreductase 1 (Nfn1)	PF1327 PF1328	Electron bifurcation	1 [Fe_2S_2] + 2 [Fe_4S_4]	(46,47)
NADH-dependent reduced ferredoxin:$NADP^+$ oxidoreductase 2 (NfnII)	PF1910 PF1911	Shuttles electrons between NADPH and Fd. Uprelated under S0 reducing conditions with sugars or peptides as carbon sources.	1 [Fe_2S_2] + 2 [Fe_4S_4]	(46,47)
Prismane protein	PF0692		Predicted to encode an ISC	(18)
Pyruvate ferredoxin oxidoreductase (POR or PFOR)	PF0965 PF0966 PF0967 PF0971	Catalyzes the ferredoxin-dependent oxidative decarboxylation of pyruvate to acetyl-CoA.	3 [Fe_4S_4] clusters	(48,49)
Rubredoxin	PF1282	Donates electrons to rubrerythrin and superoxide reductase. Is involved in an anaerobic ROS detoxification system.	$Fe(cys)_4$	(50)
Rubrerythrin	PF1283	Catalyzes the reduction of H_2O_2 to water using electrons from rubredoxin; involved in anaerobic ROS detoxification.	1 [Fe-O-Fe] and 1 $Fe(cys)_4$	(17)
Soluble Hydrogenase I (SHI)	PF0891 PF0892 PF0893 PF0894	Catalyzes the reversible oxidation of H_2 to generate reduced NAD(P)H	3 [Fe_4S_4] + NiFe site	(51)
Soluble Hydrogenase II (SHII)	PF1329 PF1330 PF1331 PF1332	Catalyzes the reversible oxidation of H_2 to generate reduced NAD(P)H	3 [Fe_4S_4] + NiFe site	(52)
Superoxide reductase	PF1281	Catalyzes the reduction of superoxide to H_2O_2 using rubredoxin as an electron donor.	Mononuclear Fe^{II} with 4 His, 1 Ccys, and 1 Glu ligand.	(53,54,55)
WOR5	PF1480		4 [Fe_4S_4]	(56)

Table SB.3: Proteins upregulated under $+S^0$ conditions (fold change >3). Taken from (12).

Gene	Annotation	Avg_Log2_Ratio	SD	Fold
PF2025	IssA	7.568	0.456	189.852
PF2026	putative polyferredoxin	6.573	1.728	95.265
PF0938	3-isopropylmalate dehydratase large subunit	3.406	0.403	10.603
PF0094	glutaredoxin-like protein	3.333	0.564	10.081
PF1972	ribonucleoside-triphosphate reductase activating protein	3.035	0.185	8.199
PF0723	FTR1 Iron Permease	2.947	0.051	7.711
PF0942	dihydroxy-acid dehydratase	2.699	0.093	6.496
PF0939	putative 3-isopropylmalate dehydratase smallsubunit	2.294	0.186	4.907
PF2030	ferredoxin-family protein	2.098	0.155	4.281
PF0857	ferrous iron transport protein b	2.056	0.022	4.16
PF0075	alcohol dehydrogenase	1.927	0.286	3.803
PF0204	glutamine amidotransferase type-2 domain-containing protein	1.641	0.032	3.12
PF1454	radical SAM containing protein	1.623	0.059	3.082

Table SB.4: Proteins upregulated during -S^0 conditions (fold change > 3). Taken from (12).

Gene	Annotation	Avg_Log2_Ratio	SD	Fold
PF0925	heme biosynthesis protein	-6.012	0.21	64.565
PF1329	H-II hydrogenase subunit beta	-5.935	1.146	61.2
PF1330	H-II gamma (hydrogenase subunit gamma)	-5.891	0.584	59.367
PF2064	arylsulfatase regulatory protein, putative	-5.632	0.288	49.597
PF1521	formate dehydrogenase alpha chain	-5.545	0.1	46.707
PF1331	H-II delta (hydrogenase subunit delta)	-5.208	0.237	36.968
PF0891	sulfhydrogenase beta subunit	-4.391	0.783	20.982
PF1797	d-nopaline dehydrogenase	-4.138	0.993	17.611
PF1332	H-II alpha (hydrogenase subunit alpha)	-3.868	2.406	14.603
PF1482	MoaD/ThiS	-3.786	0.103	13.798
PF1434	mbh12 membrane bound hydrogenase alpha (NADHdehydrogenase)	-3.621	0.074	12.309
PF2060	Radical SAM/SPASM domain protein	-3.617	0.107	12.271
PF1432	mbh10 NADH dehydrogenase subunit (like cCoL,EchC, HycH)	-3.448	0.297	10.914
PF0559	hydrogenase expression/formation regulatoryprotein	-3.133	1.347	8.778
PF0892	sulfhydrogenase gamma subunit	-3.052	0.847	8.295
PF1796	putative polyferredoxin	-3.043	0.025	8.242

PF0893	sulfhydrogenase delta subunit	-3.037	0.521	8.21
PF1436	mbh14 iron-sulfur protein (like HycF, EchF,CooX)	-3.023	0.097	8.132
PF1795	sarcosine oxidase subunit alpha	-2.987	0.113	7.928
PF0741	Thioredoxin	-2.678	0.113	6.4
PF0752	thioredoxin peroxidase	-2.538	1.137	5.81
PF1277	7-carboxy-7-deazaguanine synthase	-2.081	0.138	4.233
PF1003	phosphate-binding periplasmic protein precursor(pbp)	-2.005	0.452	4.015
PF1194	transcriptional regulator (furr family)	-1.992	0.172	3.978
PF0894	sulfhydrogenase alpha subunit	-1.98	0.109	3.947
PF0846	Amidohydrolase	-1.95	0.003	3.864
PF0731	copper-transporting atpase, p-type	-1.896	0.296	3.722
PF0602	flavin reductase family protein	-1.866	0.026	3.645
PF0344	tungsten-containing aldehyde ferredoxinoxidoreductase cofactor modifying protein	-1.837	0.142	3.573
PF0345	molybdopterin converting factor, subunit 1	-1.644	0.216	3.126
PF1158	Elp3/Radical SAM protein	-1.626	0.009	3.088

Table SB.5. Cellular elemental concentrations of samples (μM). Sulfur measurements for the ΔIssA strain were unreliably low and so are not included. Each measurement is n = 1 in which each sample was divided into three aliquots and digested and analyzed independently. The uncertainties are standard deviations for those determinations. Exp, harvested during exponential growth phase; St.St, harvested during stationary growth phase.

Sample	**Fe**	**P**	**S**	**Mn**	**Co**	**Cu**	**Zn**
WT-S^0 (Exp)	1030 ± 10	65500 ± 500	78000 ± 13000	0.065 ± 0.01	7 ± 1	145 ± 1	540 ± 5
WT-S^0 (St.St)	660 ± 10	42600 ± 400	40800 ± 800	0.65 ± 0.05	5 ± 1	23 ± 1	510 ± 10
WT+S^0 (Exp)	5250 ± 60	45900 ± 700	358600 ± 4400	9 ± 0.5	67 ± 1	305 ± 3	4990 ± 60
WT+S^0 (St.St)	8700 ± 300	47100 ± 1500	648000 ± 19000	22 ± 1	115 ± 5	550 ± 20	7400 ± 300
ΔIssA-S^0 (Exp)	1300 ± 300	40000 ± 4100	-	1 ± 1	3 ± 1	32 ± 3	150 ± 20
ΔIssA+S^0 (Exp)	9100 ± 400	78700 ± 1100	-	17 ± 1	44 ± 15	300 ± 50	690 ± 200

Table SB.6. Strains used in this study.

Trivial Name	**Strain Name**	**Description**	**Ref.**
WT	MW0002	Δ*pyrF*	57
ΔIssA	MW0012	Δ*pyrF* Δ*sipA*::*Pgdh pyrF*	58

Supplementary References

57. Lipscomb, G.L., Stirrett, K., Schut, G.J., Yang, F., Jenney, F.E. Jr, Scott, R.A., Adams M.W.W, Westpheling, J. (2011) Natural competence in the hyperthermophilic archaeon *Pyrococcus furiosus* facilitates genetic manipulation: construction of markerless deletions of genes encoding the two cytoplasmic hydrogenases. *Appl Environ Microbiol*. **77**, 2232-2238.

58 . Bridger, S.L., Clarkson, S.M., Stirrett, K., DeBarry, M.B., Lipscomb, G.L., Schut G.J., Westpheling, J., Scott, R.A., Adams, M.W.W. (2011) Deletion strains reveal metabolic roles for key elemental sulfur-responsive proteins in *Pyrococcus furiosus*. *J Bacteriol*. **193**, 6498-6504.

APPENDIX C

PUBLICATIONS OF DOMINIK K HAJA

Accepted publications

Wu, C. -H., **Haja, D. K**., & Adams, M. W. W. (2018). Cytoplasmic and membrane-bound hydrogenases from *Pyrococcus furiosus*. *Enzymes Of Energy Technology, 613*, 153-168

Yu, H., Wu, C. -H., Schut, G. J., **Haja, D. K**., Zhao, G., Peters, J. W., Adams, M. W. W., Li, H. (2018). Structure of an ancient respiratory system. *Cell, 173* (7), 1636-1649

Wu, C. -H., Schut, G. J., Poole, F. L., **Haja, D. K**., & Adams, M. W. W. (2018). Characterization of membrane-bound sulfane reductase: a missing link in the evolution of modern day respiratory complexes. *J. Biol. Chem., 293* (43), 16687-16696

Wu, C. -H., Ponir, C. A., **Haja, D. K**., & Adams, M. W. W. (2018). Improved production of the NiFe-hydrogenase from *Pyrococcus furiosus* by increased expression of maturation genes. *Protein Eng. Des. Sel., 31* (9), 337-344

Haja, D. K., Wu, C. -H., Poole, F. L., Sugar, J., Williams, S. G., Jones, A. K., & Adams, M. W. W. (2019). Characterization of thiosulfate reductase from *Pyrobaculum aerophilum* heterologously produced in *Pyrococcus furiosus*. *Extremophiles, 24* (1), 53-62

Yang, W., Vansuch, G. E., Liu, Y., Jin, T., Liu, Q., Ge, A., Sanchez, M. L. K., **Haja, D. K**., Adams, M. W. W., Dyer, R. B., Lian, T. (2020). Surface-ligand “liquid" to “crystalline" phase transition modulates the solar H2 production quantum efficiency of CdS nanorod/mediator/hydrogenase assemblies. *ACS Appl. Mater. Interfaces*, *12* (31), 35614-35625

Vansuch, G. E., Wu, C. -H., **Haja, D. K**., Blair, S. A., Chica, B., Johnson, M. K., Adams, M. W. W., Dyer, R. B. (2020). Metal-ligand cooperativity in the soluble hydrogenase-1 from *Pyrococcus furiosus*. *Chem. Sci.*, *11* (32), 8572-8581

Haja, D. K., Wu, C. -H., Ponomarenko, O., Poole, F. L., George, G. N., & Adams, M. W. W. (2020). Improving arsenic tolerance of *Pyrococcus furiosus* by heterologous expression of a respiratory arsenate reductase. *Appl. Environ. Microbiol.*, *86* (21)

Yu, H., **Haja, D. K**., Schut, G. J., Wu, C. -H., Meng, X., Zhao, G., Li, H., Adams, M. W. W. (2020). Structure of the respiratory MBS complex reveals iron-sulfur cluster catalyzed sulfane sulfur reduction in ancient life. *Nat. Commun.*, *11* (1)

Clarkson, S. M., **Haja, D. K.**, Adams, M. W. W. (2020). The hyperthermophilic archaeon *Pyrococcus furiosus* utilizes environmental iron sulfide cluster complexes as an iron source. *Extremophiles* Accepted 03/2021

Manuscripts in preparation

Matthew, L. G., **Haja, D. K.**, Pritchett, C., McCormick, W., Adams, M. W. W., Lanzilotta, W. N. (2021). In situ crystallography reveals an unprecedented function for a tungsten-containing oxidoreductase. *J. Mol. Biol in review 12/2020*

Yu, H., Schut, G. J., **Haja, D. K**., Adams, M. W. W., and Li, H. (2021). Evolution of complex I-like respiratory complexes. *JBC in review 02/2021*

Vali, S. W., **Haja, D. K.**, Brand, R., Adams, M. W. W., Lindahl, P. A. (2021). The iron-ome of *Pyrococcus furiosus* is dominated by thioferrate-like iron or [Fe4S4] 2+ clusters depending on elemental sulfur availability: evidence for a novel form of anaerobic respiration *JBC in review 02/2021*

Haja, D. K., Adams, M. W. W. (2021). Sodium ion pumping by Mrp in *Pyrococcus furiosus*. *Extremophiles submitted 03/2021*

Schut, G. J., **Haja, D. K**., XXXXX, Poole, F. L., Li, H., Adams, M. W. W. (2021). BfuABC is a new class of abundant and extremely diverse bifurcating enzymes. *Nat. Chem. Biol submitted 03/2021*

XXXXX, Schut, G. J., **Haja, D. K.**, Poole, F. L., Adams, M. W. W., Li, H. (2021). Structure of the bifurcating NiFe hydrogenase from *Acetomicrobium mobile*. *Nat. Chem. Biol in preparation*

Chica, B., Vansuch, G. E., **Haja, D. K.**, Wu, C.-H., Adams, M. W. W., Dyer, R. B. (2021). Insights into *Pyrococcus furiosus* SHI oxygen tolerance and spectroscopic characterization of photochemical reactivation processes. *Chem. Sci in preparation*

Vansuch, G. E., **Haja, D. K.**, Adams, M. W. W., Dyer, R. B. (2021). Probing exogenous carbon monoxide binding dynamics in soluble hydrogenase-1 from *Pyrococcus furiosus:* native and variant enzymes. *Chem. Comm. in preparation*

Vansuch, G. E., **Haja, D. K.**, Narehood, S. M., Adams, M. W. W., Dyer, R. B. (2021). Time resolved mechanistic studies of soluble hydrogenase-1 from *Pyrococcus furiosus* enzyme variants. *JACS in preparation*